University of Alaska

Coastal Marine Institute

Beaufort and Chukchi Sea Seasonal Variability for Two Arctic Climate States

Principal Investigators:

Andrey Y. Proshutinsky, Woods Hole Oceanographic Institution
Mark A. Johnson, University of Alaska Fairbanks
Tatiana O. Proshutinsky, University of Alaska Fairbanks
James A. Maslanik, University of Colorado at Boulder

Final Report

June 2003

OCS Study MMS 2003-024

CMI contact information

E-mail: cmi@sfos.uaf.edu
Phone: 907.474.7707
Fax: 907.474.7204
Postal: Coastal Marine Institute
School of Fisheries and Ocean Sciences
University of Alaska Fairbanks
Fairbanks, AK 99775-7220

This study was funded in part by the U.S. Department of the Interior, Minerals Management Service (MMS), through Cooperative Agreement No. 1435-01-98-CA-30909, Task Order No. 15174, between the MMS, Alaska Outer Continental Shelf Region, and the University of Alaska Fairbanks.

The Department of the Interior Mission

As the Nation's principal conservation agency, the Department of the Interior has responsibility for most of our nationally owned public lands and natural resources. This includes fostering sound use of our land and water resources; protecting our fish, wildlife, and biological diversity; preserving the environmental and cultural values of our national parks and historical places; and providing for the enjoyment of life through outdoor recreation. The Department assesses our energy and mineral resources and works to ensure that their development is in the best interests of all our people by encouraging stewardship and citizen participation in their care. The Department also has a major responsibility for American Indian reservation communities and for people who live in island territories under U.S. administration.

The Minerals Management Service Mission

As a bureau of the Department of the Interior, the Minerals Management Service's (MMS) primary responsibilities are to manage the mineral resources located on the Nation's Outer Continental Shelf (OCS), collect revenue from the Federal OCS and onshore Federal and Indian lands, and distribute those revenues.

Moreover, in working to meet its responsibilities, the **Offshore Minerals Management Program** administers the OCS competitive leasing program and oversees the safe and environmentally sound exploration and production of our Nation's offshore natural gas, oil and other mineral resources. The MMS **Royalty Management Program** meets its responsibilities by ensuring the efficient, timely and accurate collection and disbursement of revenue from mineral leasing and production due to Indian tribes and allottees, States and the U.S. Treasury.

The MMS strives to fulfill its responsibilities through the general guiding principals of: (1) being responsive to the public's concerns and interests by maintaining a dialogue with all potentially affected parties and (2) carrying out its programs with an emphasis on working to enhance the quality of life for all Americans by lending MMS assistance and expertise to economic development and environmental protection.

OCS Study MMS 2003-024

Final Report

Beaufort and Chukchi Sea Seasonal Variability for Two Arctic Climate States

by

Andrey Y. Proshutinsky[1]
Mark A. Johnson[2]
Tatiana O. Proshutinsky[2]
James A. Maslanik[3]

Principal Investigators

[1]Physical Oceanography Department, MS #29
Woods Hole Oceanographic Institution
Woods Hole, MA 02543

[2]Institute of Marine Science
University of Alaska Fairbanks
Fairbanks, AK 99775-7220

[3]Cooperative Institute for Research in Environmental Sciences
University of Colorado at Boulder
Boulder, CO 80309-0216

E-mail: aproshutinsky@whoi.edu
johnson@ims.uaf.edu
fstop@uaf.edu
james.maslanik@colorado.edu

June 2003

Contact information

e-mail: cmi@sfos.uaf.edu
phone: 907.474.7707
fax: 907.474.7204
postal: Coastal Marine Institute
School of Fisheries and Ocean Sciences
University of Alaska Fairbanks
Fairbanks, AK 99775-7220

Table of Contents

List of Tables

List of Figures

Abstract

This project improves our understanding of the mechanisms affecting the seasonal cycle in the Arctic Ocean and Beaufort Sea, explores the relationship between the seasonal cycle and interannual variability, and advances our previous research that identified two states of wind-driven Arctic Ocean circulation [see Proshutinsky and Johnson 1997]. The present work incorporates more recent observational studies from satellites and other current sources, and includes new modeling work as well. We now recognize associations between the two regimes, and variations in oceanic, atmospheric, and sea ice conditions. This report documents those associations and addresses possible causal mechanisms.

We focus on the two states, termed the anticyclonic circulation regime (ACCR) and the cyclonic circulation regime (CCR), to address differences in the seasonal cycle and the impact seasonal anomalies have on interannual fluctuations. Atmospheric, ice, and oceanic observational data, along with the results of numerical experiments using a coupled sea ice–ocean model, provide evidence that during the ACCR, Arctic atmospheric pressure is higher, wind speed is lower, and winter temperatures are colder, compared with the CCR. When the CCR dominates, precipitation increases over the ocean and decreases over land. During the CCR, summer wind divergence produces more openings in the sea ice, allowing the upper ocean to accumulate heat. This positive heat anomaly extends the ice melt season, increases freshwater content, and leads to generally thinner ice.

In the Beaufort Sea, a reservoir of fresh water stabilizes the upper ocean circulation and helps drive the anticyclonic Beaufort Gyre. During ACCR years, anticyclonic winds allow the Beaufort Gyre to strengthen and accumulate significant amounts of comparatively fresh water. However, when cyclonic (counterclockwise) winds prevail during the CCR years, sea ice and fresh water are exported, exiting through the straits of the Canadian Archipelago to the North Atlantic. This behavior of the Beaufort Gyre has implications far outside the Arctic because the released fresh water in the North Atlantic Ocean can influence deep convection and the global thermohaline circulation. We hypothesize that the storage and release of fresh water in the Beaufort Gyre is linked to global climate through freshwater modulation of deep convection. The accumulation and release of fresh water is regulated by wind-driven and thermohaline forcing through a cascade of oscillations alternating on a decadal cycle that link the Beaufort Gyre, the Arctic Basin, and the Greenland and Labrador Seas.

Introduction

The seasonal variability of the atmosphere, ocean, and ice in high latitudes depends on coupled dynamics and thermodynamics in ways not yet fully understood. Changes of amplitude or timing of the Arctic seasonal cycle can be modulated by interannual variability, implying an important coupling between the seasonal and interannual time scales. The true climatic impact of the seasonal signal on Arctic interannual variability remains unknown. Unresolved issues concerning the evolution of the Arctic seasonal cycle require further investigation in order to advance our understanding of climate variability in the region.

Currently available atlases, manuals, and reference books [Gorshkov 1980; Levitus 1982; Treshnikov 1985; EWG 1997] include information about multi-year mean atmospheric, oceanic, and ice characteristics, or at best, information about the multi-year seasonal cycle. These sources of information do not account for the Arctic seasonal evolution related to different Arctic climatic states that have been demonstrated in recent studies [Mysak et al. 1990; Proshutinsky and Johnson 1997; Mysak and Venegas 1998; and Thompson and Wallace 1998].

More recently, Proshutinsky and Johnson [1997] (hereafter P&J) have found two wind-driven circulation regimes, or two climate states, or two climate modes of the Arctic atmosphere and ocean. They have shown that wind-driven ice motion and upper ocean circulation alternate between anticyclonic and cyclonic states. Shifts between regimes occur at 4- to 9-year intervals, resulting in an average 10- to 15-year period. The anticyclonic circulation regime (ACCR) has been observed in the model results for 1946–1952, 1958–1962, 1972–1979, 1984–1988, and 1998–2001. The cyclonic circulation regime (CCR) prevailed during 1953–1957, 1963–1971, 1980–1983, 1989–1997, and in 2002. (See p. 38 for a complete list of acronyms and abbreviations used in this report and their definitions.)

River runoff, permafrost temperature, ice extent, index of the North Atlantic Oscillation, water temperature in the Iceland Sea, sea ice anomalies in Davis Strait, and other parameters have a similar variability and correlate well with the circulation regimes (see Table 1). Based on results of this study, we expect substantial differences among the seasonal cycles of ice, oceanic, and atmospheric parameters associated with different Arctic climatic states in the entire Arctic Ocean, particularly in the Beaufort and Chukchi Seas.

Table 1. Interpretation of observed and simulated anomalies of environmental parameters in terms of anticyclonic circulation regime (ACCR) and cyclonic circulation regime (CCR) theory. N = negative anomaly, P = positive anomaly, A = anticyclonic circulation, C = cyclonic circulation

Parameter	Anomaly	
	ACCR	CCR
Atmospheric vorticity over the polar cap	N	P
Sea level atmospheric pressure (SLP) over the Arctic Ocean	P	N
Surface wind circulation	A	C
Surface wind speed	N	P
Cloudiness	N	P
Precipitation	N	P
Surface air temperature	N	P
Sea ice extent	P	N
Sea ice thickness	P	N
Sea ice drift	A	C
Duration of ice melt season	N	P
Ocean surface circulation	A	C
Ocean surface water temperature	N	P
Ocean surface water salinity	P	N
Ocean heat content	N	P
Ocean freshwater content	P	N
Storm activity	N	P
River discharge	P	N
Permafrost temperature [Osterkamp et al. 1994]	N	P

Although some modeling studies have reproduced the Arctic ice and ocean seasonal behavior, their real focus was mean Arctic climatic conditions [Hibler and Bryan 1987; Oberhuber 1993; Piacsek et al. 1991]. Semtner's [1987] modeling experiments give a realistic representation of the Arctic's ice–ocean seasonal variability. He concludes that the oceanic heat flux not only governs the wintertime ice extent in the Greenland and Barents Seas, but also regulates the summertime ice extent in the Arctic's marginal seas. According to Semtner, the latter process is related to the dynamics of the intermediate Atlantic water layer. Observations confirm this conclusion [Nikiforov and Shpaikher 1980]. A special investigation of the Arctic Ocean's seasonal climatology was carried out by Häkkinen and Mellor [1992] using a coupled sea ice–ocean model. These authors reproduced the seasonal change of the ice mass, oceanic heat flux to the lower ice surface, and other ice and oceanic parameters quite well.

Our current project is designed to improve understanding of the mechanisms affecting the seasonal cycle, and the relationship between seasonal and interannual variability—processes that were not stressed in the modeling and observational studies mentioned above. Based on P&J results, we recognize differences among seasonal cycles of sea ice, oceanic, and atmospheric parameters associated with the anticyclonic and cyclonic circulation regimes. The coupled ice–ocean models used in this research provide insight into the behavior of the Arctic climate system. The modeling results are used to establish the differences between the cyclonic and ACCR seasonal signals and to evaluate the contribution of seasonal changes to Arctic interannual variability. Satellite-based and other newly available observations are used in this study for analysis and model evaluation.

This report consists of seven sections. Following the introduction, the second section presents evidence supporting two wind-driven circulation regimes of the Arctic Ocean. The seasonal variability of environmental parameters derived from observations and model results are presented in the following two parts. In the fifth section we formulate new hypotheses explaining the role which the Beaufort Gyre may play in Arctic climate variability. An analysis of sea ice conditions 1998–2002 is presented in the sixth part. Major conclusions are given in the final section.

Two Circulation Regimes of the Wind-Driven Arctic Ocean

The major goal of this section is to demonstrate the existence in the Arctic Ocean of two regimes of wind-driven ice and water circulation. This section examines the role of wind-driven variations in the Arctic's ice drift and water currents at seasonal and interannual time scales. Spatial and temporal variability of the Arctic's ice drift and water motion are investigated using a 2-D coupled ice–ocean, vertically integrated, barotropic model. To place these results in historical context, a brief review of both the wind and thermohaline driven Arctic flow is presented. For a review of models developed mainly in the United States and their application to polar oceanography, see Häkkinen [1990].

Historical background

The relative contributions of the wind-driven and thermohaline circulation to the total flow in the Arctic Ocean (Figure 1) are not yet clear. Nansen [1902], Shokalskii [1940], Gordienko and Karelin [1945], Gordienko [1958], and Buinitskii [1951, 1958] assumed that the surface circulation in the Arctic Ocean was driven mainly by inflow of Atlantic water through Fram Strait. From continuity they argued that inflowing water caused an outflow of surface water to the Greenland Sea. These scientists believed the Arctic Ocean circulation was mainly thermohaline-driven and closely linked with the world ocean circulation.

In contrast to the "thermohaline" school, Zubov and Somov [1940], Shuleikin [1941], Shirshov [1944], Treshnikov [1959], and Gudkovich and Nikiforov [1965] believed that the inflow of Atlantic Water into the Arctic Basin was caused by wind-forced outflow of surface water to the Greenland Sea.

A series of 2-D numerical model results corroborated Gudkovich's conclusion [Felzenbaum 1958; Campbell 1965; Galt 1973; Hart 1975; Ponomarev and Felzenbaum 1975; Proshutinsky 1988, 1993] that winds were the major factor driving Arctic Ocean circulation. However, Treshnikov and Baranov [1972] demonstrated that the major features of the Arctic Ocean circulation could be obtained by diagnostic calculations based on observed water temperature and salinity fields (geostrophic circulation). A similar conclusion could be made according to the results of the diagnostic model by Ponomarev [1977] and prognostic models by Semtner [1976] and by Gazova and Ponomarev [1983].

3-D coupled ice–ocean models were presented by Hibler and Bryan [1987], Semtner [1987], Fleming and Semtner [1991], Riendlinger and Preller [1991], Piacsek et al. [1991], Häkkinen and Mellor [1992], Polyakov and Timokhov [1995] and many others. All of these models and numerical experiments were directed to developing new models and describing better observed features of water and ice dynamics but none focused on the variability of wind-driven circulation. Recent papers by Häkkinen [1993, 1995] presented explanations for deep convection in the Greenland Sea and the Great Salinity Anomaly. Many numerical experiments with ice and ice–ocean models have been carried out by Walsh and Johnson [1979], Walsh et al. [1985], Walsh and Chapman [1990], Englebretson and Walsh [1989], Maslanik et al. [1996], and Serreze et. al [1992] showing the dominant role of the atmosphere in sea ice drift. On the other hand, Holland et al. [1996] demonstrated that buoyancy forcing is critical to maintaining mixed-layer circulation.

We assume that both thermohaline and wind-driven forcing are important to the Arctic Ocean's circulation, and agree with Treshnikov and Baranov's [1972] conclusion that the role of individual factors in the circulation cannot be easily evaluated because observed temperature and salinity distributions reflect the combined effects of wind, baroclinicity, and topographic interaction. We believe that there is at present insufficient information for clearly separating the roles of atmospheric and thermohaline forcing in the Arctic Ocean. Through numerical modeling, however, the relative strengths of the circulations arising from atmospheric driving and thermohaline driving can be compared. To do this we used mean winter and summer, 3-D temperature and salinity fields of the Arctic Ocean including the Norwegian, Greenland and Barents Seas. The summer (June–November) and winter (December–May) data were obtained by averaging the observations for the period 1955–1990. For the Arctic Basin, winter information stems mainly from observations in March–May of 1973–1980. The summer data for the Arctic Basin were collected by drifting stations during 1955–1975.

These data were used by Polyakov and Timokhov [1995] to simulate 3-D circulation in the Arctic Ocean for winter and summer conditions. Observed 3-D fields of water density gradients were the only external force which drove their 3-D diagnostic model. For this report we call this the "thermohaline" circulation. Results from their simulations (with a spatial resolution of approximately 55 km) showing the surface thermohaline circulation in the Arctic Ocean [Polyakov and Timokhov 1995] are presented in Figure 2. The simulation reproduced many well-known features of the Arctic Ocean surface circulation such as the Beaufort Sea Gyre, Trans-Arctic Current, the East Greenland Current, and the Norwegian Current. Generally, model results do not show significant seasonal change in the direction of the surface circulation. There is a visible decrease of velocities in winter relative to summer, although in winter the Trans-Arctic Current and the Beaufort Sea Gyre are more pronounced than in summer. While these results demonstrate that the thermohaline circulation is seasonally very stable, note that they were obtained on the basis of averaging about 40 years of data. Year-to-year variability of the Arctic Ocean thermohaline circulation remains poorly known because of lack of data.

Gudkovich [1961a, b] explained the stability of Arctic currents by the presence of strong vertical stratification. In a simple view, the Arctic Ocean's vertical structure is a two-layer fluid with cold, low salinity surface waters and relatively warm, high salinity deep waters. The upper layer responds to wind forcing by turning to the right of the direction of motion; winter anticyclonic flow drives the upper waters to the center of the circulation, raising its sea level while the boundary between the two layers is lowered.

Along the coasts, the sea level is lower but the interface is higher than when undisturbed (Figure 3). In contrast, the summer cyclonic wind circulation lowers sea level in the basin center and elevates the interface while along the coasts the sea level is higher and the interface is depressed. Proshutinsky [1988, 1993] and Doronin and Proshutinsky [1991] showed that the boundary between the two layers varies seasonally by as much as 30 m, and the vertical migration of the Atlantic waters along the shelf breaks reaches tens of meters, in good agreement with observations [Nikiforov and Shpaikher 1980].

Regimes of circulation

References exist in both the meteorological and oceanographic literature describing different periods of the Arctic Ocean climate variability. Nikiforov and Shpaikher, [1980], for example, suggested that a 5–6 year cycle in Arctic Basin circulation was driven by feedback loops between terrestrial hydrologic processes and oceanic deep water formation, ice growth dynamics and thermohaline circulation. Karklin [1977] found that the ice conditions and ice drift in the Arctic seas had a periodicity of 6–7 years. He concluded that long period tides are responsible for these changes in the Arctic. After analyses of hydrologic, sea ice, oceanic and atmospheric data from the Greenland and Labrador Seas and from the Arctic and northern Canada, Mysak et al. [1990] and Mysak [1995] suggested the existence of an interdecadal (15–20 years) Arctic climate cycle linked to the North Atlantic.

By comparing the atmospheric pressure distribution to the observed water currents in the Arctic Basin, Gudkovich [1961a, b] concluded that two types of surface circulation existed (Figure 4). The principal and most valuable aspect of Gudkovich's work was his demonstration of the existence of an anticyclonic circulation system in the Canadian region (Beaufort Gyre) and a cyclonic circulation with its center to the north of the Laptev Sea. The Trans-Arctic Current flows between these two circulation cells. Type A (this is our anticyclonic circulation regime [ACCR]) circulation usually occurs during years when a prominent winter polar high drives the system so that the area of anticyclonic surface circulation increases and the area of cyclonic circulation shrinks. The axis of the Trans-Arctic Current is moved to the northern margins of the Arctic seas and carries ice into the Greenland Sea from the Laptev, East Siberian, and Chukchi Seas.

Type B (this is our cyclonic circulation regime [CCR]) circulation is characterized by contraction of the anticyclonic circulation and expansion of the cyclonic circulation. This circulation arises with the dissipation of the polar high (usually centered over the Beaufort Sea) and the propagation of the Siberian high (northern extension of the Asian high located over Siberia) to the northern margins of the eastern Arctic seas. In this case the Siberian high is responsible for west to east winds over the Siberian seas. The Trans-Arctic Current slows and shifts toward North America, leading to cyclonic surface and ice circulation in the East Siberian and Chukchi Seas.

These observed changes in the ice conditions suggest a high correlation between atmospheric and oceanic circulation in the Arctic. According to Nikiforov and Shpaikher [1980], the coefficient of correlation between ocean and atmospheric circulation may reach 80% for the upper 200-m layer of the ocean. Thorndike and Colony [1982] demonstrated that about 70% of the variance of the daily ice velocity was accounted for by the geostrophic winds and concluded that ocean currents were responsible for only about 15% of the ice motion. They found that about half of the long-term average ice motion is directly related to the wind, the other half being due to the mean ocean currents. These correlations suggest that

atmospheric forcing is a very important factor driving variability in the Arctic Ocean circulation and we will investigate it below using model results and observational data.

2-D coupled ice–ocean model

Model equations

We use a system of equations of motion and continuity written in vector notation and in stereographic polar coordinates:

$$\frac{d\mathbf{U}}{dt} + f\mathbf{k}\times\mathbf{U} = -gDm\nabla\zeta + N_h m^2\nabla^2\mathbf{U} + \frac{c\mathbf{T}_i + (1-c)\mathbf{T}_s - \mathbf{T}_b}{\rho} + Dm\mathbf{P_a} \qquad (1)$$

$$\frac{\partial\zeta}{\partial t} = -m^2\nabla(\mathbf{U}/m) \qquad (2)$$

and the equations of motion and continuity for ice,

$$\frac{d\mathbf{u}_i}{dt} + f\mathbf{k}\times\mathbf{u}_i = -gm\nabla\zeta + \frac{\mathbf{T}_{is} - \mathbf{T}_i}{\rho_i h_i} + \mathbf{F}_i \qquad (3)$$

$$\frac{\partial c}{\partial t} = -m^2\nabla(\mathbf{u}_i c/m) \qquad (4)$$

Here, x, y are the lateral coordinates, with their origin at the North Pole; $\mathbf{U}$ is a vector of volume transport with components U, V along x- and y-directions; t is time; f denotes the Coriolis parameter; $\mathbf{k}$ is a unit vector along the vertical direction; g is an acceleration of gravity; D is total depth ($D = \mathrm{H} + \zeta$); m denotes a map coefficient; ζ denotes free surface elevation; N_h is horizontal eddy viscosity ($= 5\cdot 10^9$ cm^2 s^{-1}); c is ice concentration, $0 \le c \le 1$; $\mathbf{T}_i$ is a vector of ice stress between water and ice; $\mathbf{T}_s$ is a vector of water stress between atmosphere and water; $\mathbf{T}_b$ is a vector of bottom stress; ρ is water density; $\mathbf{P_a}$ is a vector of sea level atmospheric pressure gradient; $\mathbf{u}_i$ is a vector of ice velocity; $\mathbf{T}_{is}$ is a vector of ice stress between atmosphere and ice; ρ_i is ice density; h_i is ice thickness; $\mathbf{F}_i$ is a vector of internal ice forces.

$$\frac{d}{dt} = \frac{\partial}{\partial t} + m\left\lfloor\frac{U}{D}\frac{\partial}{\partial x} + \frac{V}{D}\frac{\partial}{\partial y}\right\rfloor$$

In the above operator only the first order nonlinear terms are retained. The stereographic polar coordinate system used in (1) – (4) is very close to the rectangular system of coordinates except for the map coefficient m that describes a correction from a spherical to polar stereographic projection. Its value changes from 1 at 90 °N to 1.071 at 60 °N.

The interaction of water and atmosphere is described by

$$\mathbf{T}_s = \rho_\alpha R_\alpha \mathbf{W}|\mathbf{W}| \qquad (5)$$

where $\mathbf{W}$ is a vector of surface wind and ρ_α and R_α are air density and friction coefficient between air and water respectively.

The surface wind was determined from geostrophic relationships with consideration of the transitional coefficient C_α and angle of deviation of surface wind from the thermohaline direction A_α. Implemented in the model calculations is the algorithm in which

$$C_\alpha = 0.7 \quad \text{if} \quad \mathbf{W} < 15\ m\ s^{-1}$$
$$A_\alpha = 30° \quad \text{if} \quad \mathbf{W} < 15\ m\ s^{-1}$$
$$C_\alpha = 0.8 \quad \text{if} \quad \mathbf{W} > 15\ m\ s^{-1}$$
$$A_\alpha = 20° \quad \text{if} \quad \mathbf{W} > 15\ m\ s^{-1}$$

The surface wind transitional coefficients and turning angles are based on the model calibration, and diagnostic and prognostic simulations of the ice drift and storm surges in the Kara, Laptev, East Siberian, and Chukchi Seas [Proshutinsky 1978, 1986, 1993].

The air–water drag coefficient is a function of the wind speed [Proshutinsky 1978, 1986, 1993].

$$R_\alpha = \left(1.1 + 0.04|\mathbf{W}|\right) \cdot 10^{-3}$$

Bottom stress is described by

$$\mathbf{T}_b = \rho R_b \frac{|\mathbf{U}|\mathbf{U}}{D^2} \tag{6}$$

where R_b is a bottom friction coefficient ($= 2.6 \cdot 10^{-3}$).

The interaction of ice and atmosphere is described by

$$\mathbf{T}_{is} = \rho_\alpha R_{i\alpha} \mathbf{W}|\mathbf{W}| \tag{7}$$

In a first approximation the ice–atmosphere drag coefficient, $R_{i\alpha}$, is equal to the air–water friction coefficient, R_α.

The interaction of ice and water is described by

$$\mathbf{T}_i = \rho R_i \left|\mathbf{u}_i - \frac{\mathbf{U}}{D}\right| \left(\mathbf{u}_i - \frac{\mathbf{U}}{D}\right) \tag{8}$$

The ice–water drag coefficient R_i ($= 5.5 \cdot 10^{-3}$) was estimated by McPhee [1986].

To describe internal ice forces the nonlinear viscous constitutive law proposed by Rothrock [1975] is used:

$$\mathbf{F}_i = \eta m^2 \nabla^2 \mathbf{u}_i + \Lambda m^2 \nabla\left(\nabla \mathbf{u}_i\right) - m \nabla p \tag{9}$$

Here

$$\nabla(\nabla \mathbf{u}_i) = grad(div \mathbf{u}_i)$$

Rothrock [1975] suggested that the tensile stress in ice is negligible compared to compressive stress. Pressure (p) in (9) is given by:

$$p = -A_p m \nabla \mathbf{u}_i \quad \text{if} \quad \nabla \mathbf{u}_i < 0$$
$$p = 0 \quad \text{if} \quad \nabla \mathbf{u}_i \geq 0 \tag{10}$$

In the above equations both bulk (Λ) and shear (η) viscosity coefficients are taken to be equal ($= 10^7$ cm^2 s^{-1}); A_p ($= 10^8$ cm^2 s^{-1}) is the ice pressure coefficient.

The magnitude of the horizontal frictional coefficients used in (1) and (9) should result in numerical stability and reasonable reproduction of the turbulent processes in the water and ice. Horizontal eddy viscosity $N_h = 5 \cdot 10^9$ cm^2 s^{-1} is taken close to the threshold of numerical stability $N_h = 5 \cdot 10^8$ cm^2 s^{-1} [Kowalik 1981].

Initial and boundary conditions

Initially, the dependent variables in the integration domain are taken as zero:

$$\zeta(x,y)_{t=0} = 0 \tag{11}$$

$$\mathbf{U}(x,y)_{t=0} = 0 \tag{12}$$

$$\mathbf{u}_i(x,y)_{t=0} = 0 \tag{13}$$

Along the solid boundary (S) we assume a no-slip condition for water transport and ice velocity

$$\mathbf{U}(x,y,t)_S = 0 \tag{14}$$

$$\mathbf{u}_i(x,y,t)_S = 0 \tag{15}$$

In ice-free areas, equations (1) and (2) are solved subject to the boundary condition at the bottom (5), $\mathbf{T}_i = 0$, and $c = 0$.

Under the shore-fast ice the same equations are used, with ice velocity set to zero and compactness, c, equal to 1. In the areas covered by pack ice, the full system of equations (1) – (8) was used to obtain a solution. A series of numerical experiments has been carried out with different versions of the model in order to study the effects of internal ice stresses, ice distribution, ice–water friction and ice thickness, but are not reported here.

In this report, we discuss results from only one numerical experiment where the ice thickness and ice concentration were prescribed explicitly. We solved only the dynamical ice equations without effects of ice formation and ice melting. We have artificially prescribed seasonal variability of ice concentration and ice thickness as external parameters. In winter the concentration of pack ice was prescribed as 0.95. For the summer period (from June to November) the concentration of pack ice was prescribed as 0.90. There is no fast ice in the Arctic Ocean in summer. In summer its area of occupation was prescribed with pack

ice having 0.2 concentration. The ice thickness is prescribed as shown in Figure 5 and does not change throughout the simulations.

If sea level is known in the vicinity of the open boundary (along the first line parallel to the open boundary), the linear hyperbolic problem is solved (horizontal friction and advective terms in (1) are omitted). This procedure yields a unique solution for the volume transport with sea level defined at the open boundary, [e.g., Kowalik and Murty 1993]. With the above restriction, the open boundary conditions pertinent to equation (1) to (2) can be stated as follows:

$$\zeta_O = \zeta(x,y,t) \tag{16}$$

$$\mathbf{U}(x,y,t)_O = \mathbf{U}(x,y,t) \tag{17}$$

If the sea level along the open boundary is not known, a radiation condition is prescribed as

$$\mathbf{U} = \pm \zeta_{in} (gH)^{-2} \tag{18}$$

where ζ_{in} is sea level along the first line parallel to the open boundary.

For ice cover at the open boundary the following conditions are prescribed

$$\frac{\partial \mathbf{u}_i}{\partial n} = 0 \tag{19}$$

$$\frac{\partial c}{\partial n} = 0 \tag{20}$$

where n is a normal to the open boundary.

Along the open boundaries in the North Pacific we prescribe sea level (1.5 m). Along the open boundaries in the North Atlantic we prescribe the radiation condition (18). These conditions establish the sea slope between the Pacific and Atlantic Oceans which forces the mean inflow from the Bering Sea into the Arctic Ocean (about 1 Sv; 1 Sv = 10^6 m^3 s^{-1}), a stable circulation in the northern Bering Sea and the Chukchi Sea [Proshutinsky 1986], and apparently plays a significant role in formation of the Trans-Arctic Current which ultimately flows out Fram Strait. Recent estimates [Roach et al. 1995] give an average permanent transport in the Bering Strait of about 0.8 Sv, close to that obtained in the model. To include river runoff we prescribe water transport (**U** or **V**) for model rivers (Mackenzie, Kolyma, Indigirka, Lena, Khatanga, Yenisey, Ob and Pechora), although river input does not have a significant influence on the results presented here.

Note that the ocean boundary in the Pacific is near 50 °N, well south of Bering Strait. In the Atlantic, the open boundary is south of Greenland, well away from Fram Strait. Thus, the main ports (Bering Strait, Fram Strait, Canadian Archipelago) are not directly prescribed but respond to the model dynamics.

Data for model

To define the model's 55.5-km spatial grid, we sub-sampled the 14-km spatial grid and bathymetry prepared by Kowalik and Proshutinsky [1994] for their tidal model of the Arctic Ocean. Figure 1 shows the computational domain. In the central Arctic Ocean the free-drift ice motion is expected because of the distance from lateral boundaries. We might anticipate smaller errors in this region than in the other regions because of free-drift ice motion without coastal influence, although small errors may be offset by the possibly large errors in the atmospheric pressure fields, hence surface winds, in the central Arctic. Coastal regions have lateral effects on ice drift, so internal ice forces and variations of sea level are important. The southern parts of the Chukchi Sea and northern parts of Fram Straight are under the influence of permanent currents (Bering Straight current in the Chukchi Sea and the East Greenland Current in the Greenland Sea). In the Lincoln Sea (north of Greenland), where the ice is much thicker (Figure 5) than in the other regions, large internal ice stresses are expected and buoy behavior may be different. The ice thickness distribution in Figure 5 is combined from different sources and was published by Kowalik and Proshutinsky [1994]. They used information from Bourke and Garrett [1987], Hibler [1989] and Romanov [1992]. Figure 5 shows the average winter ice cover with three areas clearly delineated: the ice-free region in the North Atlantic, the Greenland and Barents Seas, and the pack ice region in the Arctic Ocean, as well as shore-fast ice along the coasts.

The atmospheric pressure fields were obtained from the National Center for Atmospheric Research's (NCAR) CD-ROM [1990] containing a selected subset of the National Meteorological Center (NMC) northern hemisphere octagonally gridded daily surface pressure data. The horizontal resolution of the NCAR data is about 350 km. These data have been widely used for Arctic Ocean modeling by Serreze et al. [1989], Häkkinen [1993, 1995], Maslanik et al. [1996], and many others; their quality and accuracy were discussed by Trenberth [1992].

Results

The ice–ocean model was initialized from rest on 1 January 1946, and run for 56 years until 31 December 2002, using daily surface winds computed from NCAR's atmospheric pressure fields, the mean annual river run-off, and an imposed sea level slope between the Pacific and Atlantic Oceans to provide reasonable inflow (1 Sv) from the Pacific. The barotropic model spin-up takes about four months.

Comparison of modeled ice motion and buoy drift data

We have compared data from modeled ice motion with data from 630 drifting surface buoys [Thorndike et al. 1982] and 31 "North Pole" stations having durations from days to several years during the period from 1950 to 2000. From the buoy positions we calculated velocity vectors and averaged them over one day for comparison to the modeled ice drift. Figure 6 shows generally good agreement between the modeled and observed one-day averaged buoy velocities. Correlation coefficients between the simulated and observed buoy drift velocities average more than 0.7. The temporal variability of the coefficient of correlation in the central Arctic varies between 0.6 and 0.8. For the marginal seas there is insufficient buoy information for robust statistics. In the vicinity of Fram Strait the correlation is quite good between April and August. At this time of the year, the wind speed in the region is smaller than average and the East Greenland Current dominates surface transport. The direction of the modeled ice drift is reproduced very well.

A second approach to test how well the model simulates ice motion utilizes the empirical relationship described by Thorndike and Colony [1982] for ice drift and thermohaline winds in the Arctic Ocean using 1979 and 1980 data from an array of surface drifting buoys. The relationship between the ice velocity **u**, the geostrophic wind **G**, and the mean ocean current **c** was examined in the form

$$\mathbf{u} = A\mathbf{G} + \mathbf{c} + \varepsilon \tag{21}$$

where A is a complex constant and the vectors **u**, **G**, **c** and ε are thought of as complex numbers. The complex coefficient A involves a scaling factor $|A|$ and a turning angle θ.

$$A = |A| e^{-i\theta}$$

Thorndike and Colony [1982] showed that, in the absence of a steady ocean current, sea ice moves about 8° to the right of the thermohaline wind at 0.008 times its speed (i.e., $\theta = 8°$, $|A| = 0.008$). Although the model is simple, it describes 70% of the variance of the ice velocity, leaving residuals with a standard deviation of 0.04 m s^{-1} [Thorndike and Colony 1982].

To estimate ice drift from the Thorndike and Colony model, thermohaline winds were calculated from the NCAR data and ice drift velocities were computed using the equation (21) without regard to ocean currents. Velocities from the Thorndike and Colony model and from our model show very good overall agreement. Coefficients of correlation between our model ice drift and ice drift calculated from the Thorndike and Colony model are higher than 0.9 in the center of the Arctic Ocean. This second approach again confirms that our model ice drift is reasonable. However, note that the correlation coefficients decrease toward land and reach a minimum in the Bering Strait, the mouths of rivers, and in Fram Strait. Decreasing coefficients near coasts can be explained by the influence of internal ice forces which are included in our model but are not taken into account in the Thorndike and Colony model. Further, in Bering and Fram Straits, and at the river mouths, our model includes permanent ocean currents generated by the sea level slope between the Pacific and Atlantic Oceans and by river runoff respectively, none of which are included in the Thorndike and Colony model.

We also have compared simulated and observed sea level at stations along the Arctic Ocean coastline (Figure 7). Coefficients of correlation between observed and simulated sea level are higher than 0.7. The good agreement between modeled and observed parameters confirms a generally accurate reproduction of ice and water circulation, and further validates the two-regime theory.

Interannual variability

Simulated sea level is used in this paper as an integral measurement (index) describing variability of the Arctic Ocean circulation. Year-to-year and seasonal fluctuations of the sea level are natural indicators of large-scale circulation and the interaction between the atmosphere and ocean. In Figure 8, a yearly history of the simulated sea level heights in the Arctic Ocean is shown. To determine the variability of the Arctic Ocean's wind-driven circulation we examined the simulated sea level slope near the center of the Arctic Basin as a measure of cyclonicity and anticyclonicity by calculating the difference between sea level at the center of a closed circulation cell and sea level at the periphery of this circulation, then divided this difference by the distance between the center and periphery (Figure 9). This was done by visually locating the maximum or minimum of the sea level in the central Arctic (see Figure 8), then searching for the last closed isoline around that maximum or minimum to determine the gradient. While the magnitude of the gradient is somewhat sensitive to the shape of the last closed isoline, the sign is not. Positive values correspond to a raised central sea surface and anticyclonic water circulation. Negative values correspond to lowered central sea surface and cyclonic water circulation. A time series of the sea surface height gradients from 1946 through 2002 is presented in Figure 10. Spectral analysis of this time-series gives a peak at about the 15 year period, although it is not particularly well resolved by the 56 year-long data.

Two major regimes describe the modeled wind-driven ice circulation in the Arctic Ocean. One regime is characterized by anticyclonic circulation during 1946–1952, 1958–1963, 1972–1979, 1984–1988, and 1998–2001. A second regime is characterized by cyclonic circulation as observed in the model during

1953–1957, 1964–1971, 1980–1983, 1989–1997, and in 2002. The circulation has been averaged over each multi-year interval (Figures 11 and 12). Year 2002 was not taken into account because it represents only one year. Regime shifts between cyclonic and anticyclonic flow occur at 4 to 9 year intervals resulting in an average ten to fifteen year period.

Here we present new results of the circulation regime definition based on EOF (empirical orthogonal function) analysis of the simulated sea surface height (SSH) time series. The expansion coefficients time series for the first EOF mode is shown in Figure 13 (lower panel). The first EOF pattern of the simulated annual mean SSH accounts for 43% of the SSH anomaly variance (Figure 13, top panel). The second and third modes (not shown) represent 26% and 8% of the SSH anomaly variance, respectively, and are not discussed further.

The first EOF mode of SSH variability we call the Arctic Ocean Oscillation (AOO). This pattern is very similar to Figure 10. The SSH anomaly for years with a negative AOO index (Figure 13, lower panel) corresponds to the ACCR, and the SSH anomaly with a positive AOO index corresponds to the CCR. The AOO correlates very well with the time series of sea level gradients (bars in Figure 13), which is consistent with our empirical definition of two circulation regimes based on simulated sea level gradients.

The annual cycle

The annual cycle has been examined with respect to the two general wind-driven circulation regimes. We have averaged into monthly bins ice motion from each ACCR, and also motion from each CCR based on the results of Figure 10. In the anticyclonic regime, strong anticyclonic circulation dominates for about 10 months from October to July. In years with a cyclonic regime, summer circulation, characterized by weak cyclonic circulation, dominates the annual cycle.

Correctly simulating the annual cycle requires that, at least, the observed and modeled transports through Bering and Fram Straits agree. In Bering Strait, the summer (May to September) inflow to the Arctic Ocean increases, according to Coachman and Aagaard [1988] and Roach et al. [1995]. These observations show that the winter transport is lower than in summer and has two local maxima in January and November. This pattern of seasonality of transport through Bering Strait is duplicated by the model (Figure 14). Furthermore, the agreement between the simulated and observed [Coachman and Aagaard 1988; Roach et al. 1995] transport in the Bering Strait lends support to the Coachman et al. [1975] concept of the wind-driven nature of transport variability through Bering Strait. In Fram Strait, the model shows increased ice transport during winter and slow ice flow in summer. This is in agreement with observed seasonal variability of surface velocities there [Vinje and Finnekåsa 1986].

Questions

Three fundamental questions are posed: 1) Do the modeled regimes exist in the real ocean? 2) What factors drive them and how are transitions made between the two regimes? 3) What are the implications of the existence of these two regimes for the circulation of the Arctic and its environmental conditions?

1) Do these regimes exist?

We have demonstrated that the cyclonic and anticyclonic regimes are driven by atmospheric winds. By comparing the model ice velocities with velocities from individual drifting buoys and with the buoy motion model presented by Thorndike and Colony [1982], we have demonstrated that the model reproduces well the large scale ice circulation of the Arctic Ocean. However, our model is wind-driven only; the thermohaline circulation is not included. Assuming linear processes in the ocean, we can sum the modeled thermohaline and the wind-driven circulations to represent the total flow, recognizing that the observed temperature and salinity fields used in the model already reflect to some extent wind driving

as well. The average thermohaline circulation is anticyclonic (Figure 2), so adding to it the wind-driven anticyclonic flow reinforces the anticyclonic surface motion (Figure 15). Conversely, adding the cyclonic wind-driven regime to the anticyclonic thermohaline circulation weakens and may even reverse the total flow (Figure 16).

Monthly averages of the total circulation (mean thermohaline plus monthly-averaged wind-driven) show better agreement with the buoy velocities in certain regions than the wind-driven regime alone. We present summed surface motion vectors for specific months from an anticyclonic regime (1987) (Figure 17) and from a cyclonic regime (1992) (Figure 18) for comparison to observed buoy motions. In 1987, only anticyclonic ice drift is observed for July and August. In contrast, during July 1992 there is a major cyclonic cell centered over the pole and a small, anticyclonic cell depicting the Beaufort Gyre. By August, the anticyclonic circulation cell has practically disappeared. In all cases, there is generally good agreement with the buoy vectors. This study is in agreement with other results [Serreze et al. 1989, 1990] documenting cyclonic ice motion in the Canadian Basin during summer.

The time series of sea-level gradients computed in this study are compared to the ice extent in the Bering Sea, temperature anomalies of the intermediate, cold layer near Kamchatka, and salinity variations in the near shore Gulf of Alaska (Figure 19). The sea ice extent in the Bering Sea has been presented by Niebauer [1988], the temperature anomaly in the intermediate, cold layer from southeast Kamchatka is from Davydov [1989], and the salinity anomalies in the Gulf of Alaska are from Royer [1996]. These time series show periods of variation similar to the two regimes of Arctic circulation. After about 1970 when sea ice extent could be computed from satellite data, increased Bering Sea ice cover corresponds quite well to periods of anticyclonic circulation. Temperature in the intermediate, cold layer near Kamchatka is cool during the anticyclonic regimes, and salinity in the Gulf of Alaska increases during the anticyclonic regimes.

2) What drives these regimes?

There are at least two possible driving mechanisms related to this 10–15 year oscillation in the Arctic. The first mechanism proposed by Nikiforov and Shpaikher [1980] considers the Arctic to be a self-regulated, closed system. They speculated that atmospheric circulation, river runoff, freshwater input, ice thickness, ocean–atmosphere heat flux, and changes in the thickness of the warm Atlantic layer along the periphery of the Arctic are linked. They suggested the following mechanism:

Anticyclonic atmospheric circulation is associated with negative precipitation anomalies that result in reduced river discharge, less freshwater in the near-shore surface layer, and increased surface salinity. Anticyclonic winds upwell the warm Atlantic layer around the periphery so that increased heat flux, combined with the greater surface salinity, reduces sea ice thickness and extent. Positive SST (sea surface temperature) anomalies initiate local cyclonic atmospheric circulation. Cyclonic atmospheric circulation is associated with increased precipitation and freshwater discharge to the shelf regions. Salinity is lowered and vertical stratification is increased. The cyclonic atmospheric circulation drives downwelling along the continental shelf and reduces the heat flux from the warm Atlantic layer to the atmosphere, increasing ice thickness and extent. The atmosphere cools due to the reduced heat flux and anticyclonic atmospheric circulation is enhanced.

There are some problems with this theory because our results show (see sections below) that the observed river runoff increases during the anticyclonic circulation and decreases during cyclonic circulation regimes.

We speculate that shifts between regimes may be triggered by cold and warm SSTs in the far northern North Atlantic. Warm SST anomalies drive the formation of a tongue of low atmospheric pressure toward the Arctic that may develop into broad cyclonic atmospheric circulation. If the Atlantic layer water

temperature anomaly is negative, then high atmospheric pressure sets up anticyclonic atmospheric circulation. Large SST anomalies reported by Hansen and Bezdek [1996] appeared to precede changes in the two regimes discussed here (Figure 19). Cold SST anomalies appear before the change to an anticyclonic regime and a warm SST anomaly appeared prior to the change to a cyclonic regime. Although the timing of these events may be coincidental, it is tempting to suggest them as causal mechanisms.

3) What are the implications on Arctic circulation and environmental parameters?
One of the important implications is that during the years of anticyclonic surface circulation the core of the Trans-Arctic Current is intensified and shifted towards Siberia. This shift enhances ice removal from the East Siberian, Laptev, and Kara Seas where ice is generally thinner. A discharge of thinner ice may reduce the total freshwater discharge through Fram Strait. Conversely, during years of cyclonic circulation, the core of the Trans-Arctic Current shifts toward Canada and Greenland, increasing flow of older, thicker ice out of the Arctic so that we might expect a freshening in the Greenland Sea and possible formation of a salinity anomaly.

Another implication is that our knowledge about the Arctic is biased toward the ACCR. We have already shown that much of the Arctic data were collected during years with wind-driven anticyclonic circulation. For example, some of largest data sets were obtained during expeditions between 1972 and 1980. Figure 20 shows locations of hydrographic stations in the Arctic Ocean for different decades [EWG 1997].

Beaufort and Chukchi Sea Seasonal Variability in Two Climate States

Regional characteristics

The Chukchi and Beaufort Seas are under significant influence of the Pacific oceanic water and atmospheric air masses. The Chukchi Sea is unique among the Arctic shelf seas in that its circulation and physical properties are strongly influenced by waters of Pacific Ocean origin. The mean pressure gradient between the Pacific and Arctic Ocean, referred to herein as the secular pressure gradient, forces a northward flow through Bering Strait and across the Chukchi shelf [Gudkovich 1961b; Coachman et al. 1975; Nikiforov and Shpaikher 1980]. The sea level gradient between these two basins in on the order of 10^{-6} and is attributed to the water density difference between the North Pacific and the Arctic Ocean [Coachman et al. 1975]. This pressure gradient is substantial because the mean northward flow persists throughout the year [Weingartner et al. 1998; Weingartner and Proshutinsky 1998], even though the average winds are northeasterly and tend to establish an opposing flow.

Although the Chukchi Shelf is shallow and flat, the bathymetric relief is large relative to the total depth; for example, broad areas of Hanna and Herald Shoals have depths less than 30 m. Bathymetric variations play a crucial role in "steering" both the mean and varying components of the circulation field. The bathymetry causes a splintering of the Bering Strait throughflow into three branches having distinctly different water mass properties. The differences in water masses and their circulation patterns greatly affect regional productivity patterns and the distribution and abundance of marine organisms. One branch consisting of the high-salinity nutrient-rich (Bering Shelf Water) fraction of the inflow flows north-westward through Hope Valley and then northward through Herald Valley in the western part of the basin [Coachmen et al. 1975]. A second branch transports the low salinity and nutrient-poor (Alaska Coastal Water) fraction of the Pacific inflow across the Chukchi shelf [Coachmen et al. 1975; Walsh et al. 1989] in a relatively swift coastal current (Alaska Coastal Current). A third branch carries a mixture of these two water masses northward through the depression to the east of Herald Shoal.

Investigation of the Beaufort Sea has a relatively long history and can be subdivided into studies of the coastal and studies of the open sea (Beaufort Gyre). The investigation of coastal Beaufort Sea processes was motivated by oil and gas companies in the early 1960s. Major accomplishments of the coastal Beaufort Sea studies have been published in numerous reports of the Minerals Management Service, manuals, and scientific papers (The Alaskan Beaufort Sea: Ecosystems and Environments [Barnes et al. 1984], Climatic Atlas of the Outer Continental Shelf Waters and Coastal Regions of Alaska [Brower et al. 1977]; The Coast and Shelf of the Beaufort Sea [Reed and Sater 1974], etc.)

The Beaufort Gyre is one of the most hostile and inaccessible areas of the globe. Most of it has never been measured or observed. The region's harsh climate and winter darkness deterred potential explorers because the dense and thick drifting sea ice of the Arctic Ocean made this area inaccessible not only to those seeking a navigable northern passage to the Orient, but also to scientific expeditions. It was not until the late 19th century, when new motives of scientific discovery and the symbolic conquest of the Pole began to supplant the primary commercial motives of hunters and passage-seekers, and when steam-powered ships replaced sailing vessels, that the exploration of the central Arctic began in earnest.

The first oceanographic observations made from ice floes by U.S. aircraft in 1951 and 1952 [Worthington 1953] indicated that the circulation of the Atlantic waters in the Arctic Ocean was more complicated than the cyclonic system suggested by Nansen [1902]. Worthington discovered a large anticyclonic gyre (Beaufort Gyre) in the northern parts of the Beaufort Sea. Since 1951, there have been several expeditions sampling water characteristics and bottom sediments in the region. They include: manned drifting stations T3 (1958 and 1965–70), ARLIS (1960–61), AIDJEX (1975–1976), North Pole (1950–1991), SHEBA (1997–1998); buoys SALARGOS (1985–1993), IOEB (1996–1998), IABP (1979-present); airborne surveys (SEVER, 1972–1986); submarine surveys (SCICEX, 1993–1998); and satellite-based observations (1972-present). (See p. 37 for a complete list of acronyms and definitions.)

In 1954, Treshnikov, using Russian airborne surveys, determined the boundaries of the Beaufort Gyre. Gudkovich [1966] calculated the period of sea ice circulation in the Beaufort Gyre (3.5 years) by analyzing Russian drifting station tracks. In 1966, Hunkins presented clear evidence of a clockwise spiral structure (Ekman spiral) of ocean currents in the upper layers of the Canadian Basin, and in 1974 he discovered subsurface eddies after extensive observations during the AIDJEX program. After AIDJEX, the first phase of Beaufort Gyre exploration was completed and routine observations have been performed since 1978. This routine work brought new discoveries in the beginning of the 1990s: warming of the Atlantic water layer and sea ice thinning relative to the 1970s, and a change in the rate of bioproductivity [Carmack et al. 1995; Rudels et al. 1994; Swift et al. 1997; Rothrock et al. 1999; Melnikov 2000].The multi-year hydrological regime of the Chukchi Sea and the Beaufort Sea (atmospheric and oceanic conditions) is presented in some atlases [e.g., Gorshkov 1980; Levitus 1982; Treshnikov 1985; EWG 1997].

Most expeditions have obtained information describing some oceanic and biologic parameters from the uppermost layers of the ocean and along the southern periphery of the Beaufort Gyre. However, the central and northern parts of the Gyre are still poorly investigated. Ocean currents, ocean structure, and oceanic biological components deeper than the upper layer are not known. Spatial and temporal variability of the Beaufort Gyre dynamics, sea ice parameters, bottom structure and sediments, biological productivity, and paleoceanography remain unknown in this area. In this situation, in order to analyze the variability of the central Beaufort Sea and many coastal regions we have used results from numerical modeling under specially designed numerical experiments.

Seasonal cycle of the atmospheric and terrestrial parameters

Observational data form the basis for this section. Assuming that the sea level atmospheric pressure (SLP), winds, surface air temperature (SAT), precipitation, and cloudiness are different for the CCR and ACCR, we have averaged them separately over years with either the cyclonic or anticyclonic regimes. Resulting seasonal cycles of the atmospheric parameters are discussed below. In our analyses, we usually discuss general characteristics of the regime for the entire Arctic Ocean and for some of its regions and then we describe regional characteristics of the Beaufort and Chukchi Seas with more details. Eight geographical zones based on climatologic subdivision of the Arctic are used for the analysis of the atmospheric parameters and are shown in Figure 1 (hereafter we will refer to these regions as climatic regions).

Sea level atmospheric pressure and geostrophic winds

We used two data sets. The first data set covers 1946-present and is based on the National Meteorological Center northern hemisphere octagonally gridded daily sea level atmospheric pressure from 1946 to present. This data set is used to analyze SLP and other parameters of the entire Arctic Ocean for about a 50-year period. The second data set covers 1979 to the present and is used because the areal coverage and quality of this data set are much better than for the earlier period. These data are based on the observations provided by the International Arctic Buoy Programme, which has maintained a network of buoys drifting on the pack ice of the Arctic Ocean since 1979. These buoys carry instruments for measuring sea level atmospheric pressure, surface air temperature, and several other geophysical quantities. Seasonal variability of SLP and computed geostrophic winds for the two circulation regimes for the entire Arctic Ocean are presented in Figures 21 and 22. A center of high SLP is located over the Beaufort Sea during the mean ACCR year, except in August and September. Anticyclonic winds prevail from October through July. In August and September the atmospheric circulation becomes cyclonic. When the CCR dominates in the Arctic, the Icelandic Low is intensified and a tongue of low SLP propagates to the north (Figure 22). From June through September the center of low pressure is located in the vicinity of the North Pole, where it generates cyclonic winds. Even in October and December the isobars have a cyclonic curvature in the central Arctic. The center of high SLP is well developed over the Beaufort Sea in January, April, and November only. Detailed analysis of the SLP during anticyclonic and cyclonic circulation years is presented in Johnson et al. [1999]. Figure 23 shows that during ACCR, the SLP is overall higher than during CCR everywhere in the eight climatic regions; the maximum difference between anticyclonic and cyclonic circulation regimes is in the central Arctic region. In August the SLP is lower by about 8 hPa during the CCR, compared with the ACCR, in this region. Figure 24 shows seasonal variability of geostrophic winds: in general, wind speed is higher for CCR, especially in summer, than for ACCR. The largest difference is in the Greenland Sea region (1 m s^{-1}) and in the central Arctic and Western regions (0.6 m s^{-1}).

The Beaufort and Chukchi Sea regional characteristics of the SLP and geostrophic wind averaged for the cyclonic and anticyclonic regimes are shown in Figures 25–36.

In January SLP fields over the Beaufort and Chukchi Seas do not change significantly from regime to regime. A center or a ridge of relatively high SLP is located over the Beaufort Sea during all regimes and a generally anticyclonic (clockwise) wind dominates. The Aleutian Low is well pronounced in January and it generates a significant SLP gradient in the area of the Bering Strait and relatively strong northeast and east winds along southern parts of the Beaufort and Chukchi Seas. The northern parts of the region (box limited by dotted line in Figures 25–36) are under the influence of the west northwest winds. The central part of the region has relatively weak winds because it is under the influence of the high SLP with very small horizontal SLP gradients. SLP is generally higher for the ACCR than for the CCR. Wind speed is higher during ACCR (about 0.7 m s^{-1}). Note that a 1 m s^{-1} wind speed difference could result in about 50 km per month difference in the location of the sea ice edge. SLP distribution and wind patterns for all

regimes during February–May are more or less similar to January characteristics; SLP for ACCR is usually higher than for CCR years and wind speed is higher for ACCR years, which contradicts the conclusion made for the entire Arctic Ocean. This is probably because the Beaufort and Chukchi Seas are also influenced by the Pacific Ocean and especially by the Aleutian Low during winter.

From June through September a cyclonic circulation pattern becomes dominant in the Beaufort and Chukchi Seas after 1979. Starting from October, the circulation regime changes again and reflects the more winter situation when anticyclonic winds and high SLP dominate over the Beaufort and Chukchi Seas.

Surface air temperature and cyclonic activity

The daily 2-meter air temperature (hereinafter air temperature) data used in this analysis are derived from buoys, manned drift stations, and all available land stations [Martin and Munoz 1997]. The seasonal variability of air temperature is presented in Figure 37. A mean winter during ACCR is colder than a mean winter of CCR everywhere in the Arctic. The air temperature difference between mean anticyclonic and CCR winters tends to decrease from regions adjacent to the North Atlantic toward the Pacific Ocean, reaching its minimum in the Pacific region. The maximum temperature difference of 9 °C is in March in the central Arctic region. The anticyclonic and CCR summer air temperatures are practically equal except in the Franz Josef Land region where air temperature during CCR is lower than during ACCR. Arctic warming during the CCR is related to advection of heat from the North Atlantic due to atmospheric circulation. The link between penetration of cyclones into the Arctic and the Arctic heat regime was pointed out by Russian climatologists Vize [1944] and Berg [1947], who explained significant Arctic warming in the late 1930s as being a result of enhanced cyclonic activity. Vitels [1948] demonstrated that in the 1920s and 1930s shifts in the atmospheric circulation were related to a change of cyclonic activity in the Kara and Barents Seas. He showed that in the 1930s the number of cyclones crossing Europe decreased by 10%, and their trajectories moved to the north, leading to warming in the Arctic. According to P&J, the 1990s are CCR years; the recent increase in the number of cyclones penetrating into the Arctic through the Norwegian and Greenland Seas has been shown by Serreze et al. [1997]. Enhanced cyclonic activity may cause increased cloudiness associated with a warmer Arctic winter during CCRs compared with ACCR years.

Regional characteristics of the monthly mean air temperature regime over the Beaufort and Chukchi Seas are presented in Figures 38–49. Seasonal variability of air temperature for the region under research is in good agreement with the variability described above for the entire Arctic Ocean. During ACCR a colder air temperature prevails and during CCR air temperature is higher than during ACCR. Summer air temperature is close to 0 °C for both circulation regimes.

The cyclonic (or storm) activity for the southern Beaufort Sea was analyzed recently by Hudak and Young [2002]. Storm analysis was done for the 1970–1995 time period for months June to November inclusive. On average, there were 14 storms per storm season, with a standard deviation of 5. The years 1976 to 1982 were the stormiest, with an average of 19 storms per storm season. They did not find any discernible trend in the storm frequency over the 25-year period. By month, October had the highest storm frequency, with July the lowest. We have averaged their data (number of storms) for the periods of cyclonic and anticyclonic regimes and found that during the 1980–1983 CCR there were 72 storms (18 per season), during the 1984–1988 ACCR there were 62 storms (12.4 per season), and during the 1989–1995 CCR there were 87 storms (12.4 per season). Data provided above generally show that the number of cyclones crossing the Chukchi and Beaufort Seas during cyclonic circulation regime is greater than during ACCR.

Cloudiness

There is a significant lack of cloudiness data in the Arctic. Some cloud coverage data are available from Gorshkov [1980]. The existing observational data from the Arctic Ocean are based on daily reports from Russian drift stations that operated from 1950 through 1991. These observations mostly covered the central Arctic region. Polar cloudiness is not well modeled either [Curry et al. 1996]. Walsh and Chapman [1998] recently analyzed observational data from Russian drift stations and modeling data from the U.S. National Centers for Environmental Prediction and the European Center for Medium-Range Weather Forecasting, and concluded that the results from various sources, including the reanalyses, indicate that clouds warm the Arctic surface when integrated over the annual cycle, but reanalyses are less successful in capturing the annual cycle of the effects of Arctic clouds. Figure 15(c) in Walsh and Chapman [1998] shows annual cycles of mean SAT with cloudy skies and clear skies derived from the Arctic and Antarctic Research Institute observations. The difference between the two curves and their seasonal variability is similar to that from data reflecting SAT during the ACCR and CCR (Figure 37). If clouds lead to warming in the Arctic, then during CCR the Arctic sky will be, in general, more cloudy. Unfortunately we do not have any specific information about cloudiness over the Beaufort and Chukchi Seas and assume that it's seasonal variability is similar to the seasonal variability of cloudiness over the Arctic Ocean for the CCR and ACCR respectively.

Precipitation and river runoff

Our analysis of seasonal variability of precipitation in the Arctic is based on the former Soviet Union's monthly precipitation archive (1891–1993). This archive, compiled by Groisman of the University of Massachusetts, consists of measurements from 622 stations covering the territory of the Former Soviet Union. These data were provided by the Earth Observing System Distributed Active Archive Center at the National Snow and Ice Data Center (NSIDC), University of Colorado, Boulder, Colorado (http://nsidc.colorado.edu/data/nsidc-0059.html). Figures 50 and 51 show that when CCR dominates over the Arctic Ocean, precipitation increases over the ocean ($\varphi \geq 70\,^{\circ}\mathrm{N}$, φ is latitude) for all seasons, and decreases over the land ($55\,^{\circ}\mathrm{N} \geq \varphi \geq 70\,^{\circ}\mathrm{N}$) only in summer. During ACCR, the opposite situation occurs.

The SLP patterns show that when the pressure over the pole is low (high), the SLP over the surrounding land masses is generally high (low), particularly in the earlier part of the record (1946 through 1972) which is consistent with the "seesaw" identified by Lorenz [1951], Kutzbach [1970], Wallace and Gutzler [1981], and Trenberth and Paolino [1981]. The transient SLP pattern over northern Siberia varies out-of-phase with the SLP over the Arctic Ocean, and approximately covers the drainage area of the Siberian rivers. The transient SLP over western Canada extends over the drainage basin of the Mackenzie River. Because low SLP may be associated with more cyclonic activity, more storms, and more precipitation [Serreze et al. 1997], one might expect precipitation to vary with the two regime signal. One measure of this is river discharge which integrates precipitation over the drainage basin.

River discharge data for the Siberian rivers were obtained from ftp://ncardata.ucar.edu/datasets/ds553.1, and the Mackenzie River from the Normal Wells Station, Canada (courtesy of J. Walsh). Unfortunately, prior to 1966, the Mackenzie River data have many missing values and are not used here. The three-year smoothed Mackenzie River discharge time series is shown in Figure 52.

River runoff is related to precipitation. Siberian river discharge is higher in ACCR years and lower in CCR years. Figure 53 shows river runoff for the largest Siberian rivers depending on circulation regime. Figure 52 shows interannual variability of the Mackenzie River runoff and confirms our general rule: River runoff increases during ACCR and decreases during CCR.

Snow melt

Yearly snow melt onset dates over Arctic sea ice are derived from Scanning Multichannel Microwave Radiometer (SMMR) and Special Sensor Microwave/Imager (SSM/I) brightness temperatures [Drobot and Anderson 2001]. The introduction of liquid water to snow results in a sharp increase in the emissivity and hence brightness temperature of the snowpack. Snow melt onset is defined as the point in time when microwave brightness temperatures increase sharply due to the presence of liquid water in the snowpack. Data span the years 1979 through 1998, and are in a polar stereographic grid at 25-km resolution. Figure 54 shows days of onset of melt over sea ice averaged for ACCR and CCR years. All regimes except the last one (for which we do not have enough data) show that surface melt onsets are earlier in CCR than in ACCR. This time difference can reach up to an average of 6 days for the area under research.

Arctic ice and ocean seasonal cycles

In this section, we present the seasonal cycles of Arctic ice and ocean in years attributed to anticyclonic and cyclonic circulation regimes. Modeling results provide the basis for this analysis because of the lack of observational information. Based on P&J and observations, 1987 and 1992 have been chosen for modeling as "typical" years representing environmental conditions for the anticyclonic and cyclonic climate regimes, respectively. The analyses of the oceanographic and atmospheric information use different geographic regions. In the previous section, climatic Arctic regions were specified. For analysis of the oceanographic parameters we use a regionalization associated with Arctic Ocean bottom topography (Figure 55).

Design of numerical experiments

The 3-D coupled ice–ocean model of Polyakov et al. [1998] takes into account ice and ocean dynamics and thermodynamics. Forcing is specified via atmospheric parameters, river discharge, heat, salt, and water transport through open boundaries. The ice dynamic model uses an elastic–plastic constitutive law. Ice mass and concentration are described by distribution functions. The ice thermodynamic model is applied individually to each of the six ice-thickness categories. Advection of the ice partial mass and concentration is parameterized by a fourth-order accuracy algorithm. The ocean is described by a 3-D time-dependent, baroclinic, z-coordinate free-surface model with 29 levels (2.5, 5, 10, 15, 20, 25, 30, 40, 50, 60, 75, 100, 150, 200, 250, 300, 400, 500, 600, 750, 1000, 1500, 2000, 2500, 3000, 3500, 4000, 4500, and 5000 m). Thermodynamic coupling between the ice and ocean models is achieved in several ways. The influence of the ocean on the ice is due to oceanic heat flux that depends on both dynamic and thermodynamic factors. The dynamic factor depends on the vertical shear of ocean currents and buoyancy, and the thermodynamic factor depends on the vertical gradient of water temperature under the ice cover. Ice melting/freezing affects the upper ocean via changes of the surface salinity and temperature. The temperature and salinity in the upper ocean cell are defined as weighted averages of the temperature and salinity of the water column under ice and in leads. The surface layer in the leads is allowed to warm above the freezing point.

The numerical model domain with horizontal resolution of 55.56 km is shown in Figure 55. This resolution is too coarse for the complex geometry of the Canadian Archipelago to be fully included and this region is excluded from our consideration here, although three open boundaries exist at the straits to make the flow more realistic.

The model is initialized with multi-year mean winter ocean temperature and salinity data [Polyakov and Timokhov 1994]. The transports at oceanic open boundaries are specified as 7 Sv out at the Denmark Strait, 8 Sv in at the Norwegian Sea, and 1 Sv in at the Bering Strait. The straits of the Canadian Archipelago are open for free water exchange. The monthly river discharges are obtained from Treshnikov [1985], Carmack [1990], and Pavlov et al. [1994]. At the river mouths the salinity is

prescribed as 0 psu, and the monthly mean water temperature is taken from Gorshkov [1980]. The air humidity, assumed to be spatially and temporally constant, equals 80%. The monthly ice/snow albedo [Maykut and Untersteiner 1971] and precipitation values [Parkinson 1978] are spatially constant. The daily wind stresses are computed from SLP [NCAR 1990], and their seasonal variability in 1987 and 1992 is depicted in Figures 56 and 57. The monthly climatic SAT and cloudiness are taken from Gorshkov [1980]. The daily SAT data for 1987 and 1992 are derived from buoys, manned drift stations, and all available land stations [Martin and Munoz 1997]. The initial ice thickness is from Romanov [1992]. The initial ice extent corresponds to climatic mean January and ice concentration is 98.

Four 15-year integrations of the coupled model have been carried out. The first two model runs (denoted as W-87 and W-92) use daily SLP and surface daily winds for 1987 and 1992, respectively. The river runoff, heat, salt, water transport through the open boundaries, and atmospheric climatology are specified as discussed above. Thus, differences in the model results for W-87 and W-92 are due only to peculiarities of the atmospheric dynamics. Two additional model runs (denoted as WT-87 and WT-92) take into account daily SAT instead of the climatologic monthly means used in experiments W-87 and W-92.

The experiments have shown that an increase or decrease of ice thickness due to attainment of a quasi-steady state is accompanied by the addition of salt or fresh water into the upper ocean. To prevent either salt accumulation or freshening in the experiments, the ocean temperature and salinity have been returned to their initial distributions on the first of January during the first five years of model integration. The results are presented for the last year of each 15-year integration, when the ice mass is in equilibrium and the deep ocean is still slowly evolving.

Repeated prescribed forcing for a particular year (1987 or 1992) has both advantages and disadvantages. This approach allows exhibition of tendencies hidden in the forcing fields. It works like a photographic developing solution: The longer the print is in the solution the sharper the details of the composition. However, as in photography, an over-long development produces a completely black image; in these experiments lengthy integration might lead to unreal values for the oceanographic parameters. The duration of each circulation regime is about 4–9 years, which is the same order of magnitude as the 10 years of fully prognostic model integrations used here. We believe that our modeling results reveal anomalies in the responses of the ice and ocean to the different atmospheric circulation regimes, yet they show ice–ocean climatic states in agreement with observations.

Seasonal cycle of the ice cover

Systematic observations of the Arctic ice drift started in 1978 [Thorndike et al. 1982]. Figure 58 shows seasonal variability of ice drift speed derived from drifting-buoy observations (1978–2000) averaged over all years of the ACCR and CCR. During the CCR the ice drift velocities are generally higher than during the ACCR in the Pacific region, the central Arctic Basin and the Greenland Sea. In the Beaufort Sea, Siberian region, and Franz Josef Land region, the ice drift velocities are lower during CCR than during ACCR although CCR wind is stronger than ACCR wind (Figure 24). An explanation for this which addresses the combined influences of wind and density-driven ocean currents is offered later.

Computed (WT experiments) and observed monthly ice drift are presented in Figures 59 and 60 for 1987 (ACCR) and in Figures 61 and 62 for 1992 (CCR), respectively. The correlation coefficients between the simulated and observed buoy drift velocities are, overall, higher than 0.7. The correlation is higher in the central Arctic, while at the basin peripheries the correlation is lower. This is similar to results discussed by Lemke [1997], P&J, and Steele et al. [1997].

Both observations and modeling results provide evidence that in 1987, with prevailing anticyclonic winds (Figure 56), strong anticyclonic ice drift dominated the Arctic Ocean during all months except September (Figures 59 and 60). In 1992 (CCR), from May through September, cyclonic ice drift dominated; during winter of this CCR year the anticyclonic ice drift prevailed (Figures 61 and 62). The difference between the summer and winter Arctic ice drift has been previously discussed by Gudkovich [1961a], who related strengthened winter and weakened summer ice drift to the intensity and location of the polar high. Analyzing SLP charts and drift patterns of manned polar stations, Gudkovich pointed out that the summer ice drift and surface water circulation may even alternate between anticyclonic and cyclonic. Serreze at al. [1989] using drifting buoy data for 1979–1985 demonstrated that, indeed, in late summer to early autumn, the ice motion can become cyclonic. According to P&J, in ACCR years the winter processes are enhanced in the Arctic; during CCR years, summer processes are enhanced. Thus, in terms of seasonal variability presented in the atlases, manuals, and reference books, the difference between ice drift patterns of the two climate regimes is the difference between durations of "summer" and "winter" processes. In ACCR years, the "winter" processes with anticyclonic ice drift dominate; the "summer" processes with cyclonic ice drift prevail during CCR years. Observations and modeling results presented in this paper are consistent with this theory.

At temporal scales longer than one month, the ice drift patterns for the Beaufort and Chukchi Seas are less influenced by direct wind forcing because of the relatively strong thermohaline or permanent ocean circulation. Circulation of the Chukchi Sea depends significantly on the dynamics of inflow from the Bering Sea (see sections above) and the circulation of the Beaufort Sea is influenced by relatively strong anticyclonic circulation of the Beaufort Gyre supported by the salinity minimum in the center of the Beaufort Sea. Origination of this salinity minimum and its variability in space and time will be discussed later. This dependence on the geostrophic or thermohaline or "permanent" currents in the Beaufort and Chukchi Seas is well pronounced in the sea ice concentration fields and sea ice extent.

The monthly mean ice concentration for each Arctic climatic region, averaged over all CCR and ACCR years is presented in Figure 63. This information is derived from satellite observations [National Snow and Ice Data Center 1989]. In summer, ice concentration is lower during CCR than during ACCR, except in the Beaufort and Greenland Seas. This fact will be explained later after analysis of numerical experiments.

The major difference between anticyclonic and cyclonic regime ice concentration in the central Arctic Ocean occurs in summer, which corroborates our conclusion about the importance of summer processes in the Arctic (Figure 64). Satellite information used by Comiso and Kwok [1996], Maslanik et al. [1996], and our analysis of the satellite data from the National Snow and Ice Data Center, show a wide ice-free zone that reaches to approximately the 20-meter isobath in the East Siberian and Laptev Seas in summer 1992 (CCR). Summer reduction (up to 60%) of ice concentration in 1992 (CCR) to the north of the Laptev Sea, is well pronounced. According to observations by Gloersen et al. [1992] and our analysis, there was no such reduction of ice concentration in 1987 (ACCR). The summer wind divergence during 1992 (CCR) leads to the significant decrease of ice concentration in the Eurasian Basin and the Laptev and East Siberian Seas. The model results in 1992 reproduce, very well, anomalies observed in this portion of the Arctic (Figure 65). The similarity in ice concentration between the W and WT experiments suggests that the daily air temperature used in the WT experiments does not much influence sea ice conditions there.

The seasonal variability of computed ice concentration for different regions of the Arctic Ocean is shown in Figure 65. Total ice concentration integrated over an entire CCR year is less than in an ACCR year. The maximum difference (about 30%) between ice concentrations in 1987 and 1992 is in summer to the north of the Laptev Sea (Region 3). There is a slight decrease of ice concentration in Region 4 in the summer of 1992 (cyclonic regime) relative to 1987 (anticyclonic regime). Ice is more compact in Regions

1, 2, and 5 in 1992 (cyclonic regime) than in 1987 (anticyclonic regime). This is a direct consequence of the ice advection from Regions 3 and 4 into Regions 1, 2, and 5 under the influence of summer cyclonic winds in 1992. Ice exhibits interesting behavior in Region 6 (the Greenland Sea): Our model results show an increase of sea ice concentration in winter 1992 relative to winter 1987, and the opposite tendency in summer, suggesting that in 1992 more ice is transported from the Arctic Ocean to the Greenland Sea in winter, and more ice is melted in the Greenland Sea in summer.

Seasonal variability of the observed sea ice concentration for different circulation regimes in the Beaufort and Chukchi Sea region is presented in Figures 66–78. The interannual variability of sea ice concentration is very large and not only wind is responsible for this parameter. Inflow of warm waters from the Bering Sea also plays an important role in the average sea ice concentration in this area. The heat flux from the Bering Sea is responsible for the sea ice melt and a support of open water in the Bering Strait and Southern Chukchi Sea during early spring and late fall (Figures 71 and 76).

Observational analyses based on sea ice composites

To provide an independent data set to contrast with the model output and to identify additional detail within the Arctic Basin and peripheral seas, remotely sensed imagery was used to study spatial patterns of sea ice cover and ice drift during the two circulation regimes. To accomplish this, the record of passive microwave-derived ice concentrations and ice type (first-year and multi-year ice) and the blended ice motion fields were used to generate composites of each parameter (first-year ice concentration, multi-year ice concentration and ice velocity) for years designated as being predominantly cyclonic or anticyclonic during 1979–2000, the period of available data. These composites thus represent average ice concentration, ice type, and ice velocity for the two regimes, as estimated from remotely-sensed data (and, in the case of ice motion, from a combination of remotely-sensed imagery and drifting buoy locations).

The remotely-sensed data were studied in combination with NCEP sea level pressures and 2-m air temperatures. To facilitate this analysis, the sea ice data and the NCEP fields were mapped to a common earth coordinate system.

The sea level pressure and air temperature data were obtained from the NCEP Reanalysis Project and provided by the NOAA-CIRES Climate Diagnostics Center, Boulder, Colorado, from their web site at http://www.cdc.noaa.gov. A description of the NCEP/NCAR Reanalysis Model can be found at http://dss.ucar.edu/pub/reanalysis/rean_model.html.

The NCEP data is on a 2.5 degree grid, and for easier comparisons, the EASE-Grid, an equal area polar projection, was chosen. The NCEP data was re-gridded and interpolated to a 25-km resolution EASE-Grid. More information on the EASE-Grid can be found at http://nsidc.org/data/ease/index.html.

The ice concentrations were calculated from SSM/I and SMMR brightness temperature using the NASA TEAM algorithm at http://www.nsidc.colorado.edu/data/docs/daac/nsidc0051_gsfc_seaice.gd.html. The brightness temperature data, obtained from the National Snow and Ice Data Center, is on a polar stereographic projection at approximately 25-km resolution, and was re-projected to the EASE-Grid. Both total and multi-year ice concentrations were produced.

Ice velocity information was obtained from the AVHRR Polar Pathfinder program. These data were produced from the passive microwave instruments, SSM/I and SMMR, and AVHRR and cover a time span from 1978 to 2000. Ice divergences were computed from the ice velocity data.

The cyclonic years used in these comparisons were 1980–1983 and 1989–1997 and the years for anticyclonic were 1984–1988 and 1998–2000. For each of the data types, full cyclonic and anticyclonic

means were made and differences calculated. The differences between regimes are calculated as ACCR minus CCR.

Patterns of ice motion (Figures 79 and 80) and ice concentration (Figures 81–83) seen in the remotely-sensed data are consistent with the atmospheric circulation depicted in the NCEP SLP fields for anticyclonic and cyclonic years (Figures 84–86). While the basic ice drift patterns generally appear fairly similar qualitatively during the cyclonic and anticyclonic years, comparing the ice velocity differences (anticyclonic minus cyclonic, Figure 87) in conjunction with the SLP differences highlights the notable effects of the changes in regime. Ice drift is more rapid in the Beaufort Sea in keeping with the increased SLP differential from the central Arctic to Alaska and western Canada. The strength of the Transpolar Drift Stream is decreased, reflecting the higher pressure and anticyclonic tendency in the central Arctic.

Differences in total ice concentration (Figures 81–83) averaged over the entire year, and ice concentration during the month of September only (Figures 88–90), point out distinct characteristics of the anticyclonic versus cyclonic regimes. For example, the difference map of total ice concentration (anticyclonic minus-cyclonic, Figure 83) suggests a tendency for a consolidation of the ice pack, with increased concentrations in the Arctic Basin and decreasing concentration in areas such as southern and eastern Baffin Bay, the East Greenland Sea, and the Laptev and Barents Seas. This translates into a net decrease in ice extent in the Arctic Ocean over these areas, with possible implications for a variety of processes such as turbulent heat fluxes within the central Arctic, and effects on ocean surface-layer salinity in the North Atlantic. Within the Arctic Basin, concentrations tend to be greater in the southern Beaufort and East Siberian Seas during the anticyclonic regime. In September (Figures 88–90), the differences in total ice concentration between the two regimes are most clearly seen as a decrease in concentration in most of the Beaufort and Chukchi Seas (and the western hemisphere portion of the Arctic Basin as a whole), with increases in the East Siberian and Laptev Seas, and the eastern Arctic as a whole, with the exception of portions of the Kara Sea.

Comparison of multi-year ice concentration (Figures 91–93) between the two regimes also shows distinct differences. The anticyclonic regime (Figure 92) appears to favor increased multi-year ice concentration over nearly the entire Arctic Basin with the exception of narrow zones along the marginal ice zones in the Beaufort and Barents Seas. The contrast in amount of multi-year ice is particularly notable in the East Siberian Sea. The increases in the central Arctic during anticyclonic circulation appear consistent with the ice drift patterns that show decreasing advection out of this region and decreased ice transport from the Arctic Basin via the Transpolar Drift Stream. Given that multi-year ice is typically thicker than first-year ice, and bearing in mind the results given above regarding total ice concentration, one interpretation of these data is that the anticyclonic regime favors retaining a thicker, more compact ice cover in the Arctic Basin, with a decrease in ice extent in the eastern Arctic. Hence, it is interesting to note that statistics of ice thickness compiled from upward-looking sonar or other means will be affected by the location of measurements used in the sample. In terms of regional ice prediction, we find that ice severity in the Beaufort Sea [Barnett 1980] depends strongly on multi-year ice concentration and the location of the contour of 50% multi-year ice (Figures 91–92). The difference map for multi-year ice concentration (Figure 93), with the sharp boundary between decreased and increased multi-year ice, suggests that the relationship between ice severity and anticyclonic/cyclonic circulation is likely to be complex. This is in keeping with our findings that, when included in a step-wise regression modeling of ice severity, the circulation regime does not contribute significantly to improving the ice-severity prediction for the sea route from Prudhoe to Bering Strait.

Patterns of ice divergence (Figures 94–95) appear similar in the different circulation regimes, with considerable spatial variability along with some regions of coherent zones of divergence and convergence. The difference field (Figure 96) is consistent with the differences in ice motion and SLP. While spatial variations are large, the differences highlight some particular areas of action. For

example, the anticyclonic regime favors increased ice export west of Banks Island, which appears as a region of increased divergence in the anticyclonic-minus-cyclonic divergence map. Concurrently, the increased westward ice transport in the Beaufort Sea yields a larger area of convergence in the Chukchi Sea during anticyclonic circulation. These areas tend to correspond to regions where total ice concentration showed an increase during anticyclonic circulation. Such regions include the Chukchi Sea off the western Alaskan coast, and near the New Siberian Islands. The increased divergence west of Banks Island appears as a small area of decreased ice concentration, suggesting that the Banks Island Polynya should be more prevalent during anticyclonic periods, but with greater concentration and less divergence off the Barrow, Alaska coast. Other areas show less correspondence between divergence and changes in ice concentration. One such area is in the East Siberian Sea, where ice concentrations are, in general, lower during anticyclonic circulation, but where divergence is only slightly greater. This may indicate that thermodynamic processes such as increased melt or reduced ice growth may be contributing to the differences in ice concentration between the two circulation regimes.

In summary, the analysis of remotely-sensed fields indicates that the anticyclonic and cyclonic regimes differ substantially in their effects on total ice concentration, multi-year ice concentration, ice motion, deformation, and ice extent. These results have a variety of implications for regional and long-term ice prediction, assessment of the sea ice record as an indicator of climatic change, and estimation of the role of sea ice on climate variability under different atmospheric circulation regimes.

Ice thickness

The seasonal range of the computed ice thickness (Figures 97 and 98) is 20–30 cm in the central Arctic (Region 4). It reaches 50 cm and more in Regions 1, 2, 5, and 6, and more than 1 m in the Laptev Sea (Region 3) and other Arctic marginal seas. These model results correspond well to observational data [Romanov 1992; Maykut and McPhee 1995] and modeling [Steele et al. 1996]. The range of the seasonal signal is about the same for both circulation regimes, although the annual mean ice thickness is very different (Figure 98). In general, the sea ice is much thicker during the ACCR than during the CCR.

The ice thickness difference between 1987 (ACCR) and 1992 (CCR) varies from 20–40 cm in Regions 1 and 5, and 60–110 cm in Region 6, to 90–110 cm in Regions 2 and 4, and up to 110–160 cm in Region 3. The ice thickness distribution function (not shown) corroborates the finding of thinner ice in 1992 than in 1987. The computed ice thickness distribution for Region 3 (Laptev Sea) is anomalous in 1992. In summer, the Laptev Sea is about 50% free of ice. In winter, the multi-year thick ice which is typical for this area [Romanov 1992] is replaced by the first-year thinner ice. In 1987 (ACCR), the ice consists of 90% multi-year ice and 6% leads in summer, and 93% multi-year ice and 5% first-year thin and intermediate ice in winter. In the Canadian Basin, off the Canadian Archipelago, and at the strait between Franz Josef Land and Spitsbergen, the ice conditions are heavier (ice is thicker and ice concentration is higher) in 1992 than in 1987 due to advection of thick ice from the central Arctic to its peripheries (see Figure 99) for the computed spatial distribution of ice thickness).

The Beaufort and Chukchi Sea seasonal variability of sea ice thickness for the CCR and ACCR years is presented in Figures the 100–111. Each figure shows the horizontal distribution of sea ice thickness, prevailing direction and speed of the sea ice drift, mean sea ice thickness in the area, and a distribution of sea ice thickness along an approximately 1000-km section (from Barrow to the North). There is a significant reduction in sea ice thickness during the year of the CCR. This reduction is a result of the unusual sea ice drift. One can see the ice build up and the respective sea ice thickness increase in the eastern part of the Beaufort Sea. We did not include this area in the analysis of the mean sea ice thickness of the Beaufort and Chukchi Seas intentionally. This local area with sea ice build up is relatively small but, because of the large value of the sea ice thickness, it compensates for the reduction of sea ice in the

other areas of the Arctic Ocean (see also Figure 99). These results are in good agreement with the results recently reported by Holloway and Sou [2001].

Seasonal cycle of the ocean

Oceanic circulation

The general ocean surface circulation including the anticyclonic Beaufort Gyre, the East Greenland Flow, and the Norwegian Current (with North Cape and Spitsbergen branches) is well reproduced by the model for the ACCR year (1987). The surface water circulation in this year is similar to the pattern of ice drift (Figure 59). The differences between the surface water and ice drift velocities are small (Figure 112). In the central Arctic the summer difference is less than 1 cm s^{-1}; at the continental slope of the Chukchi Sea the difference is about 2–3 cm s^{-1}, implying the relatively strong contribution of the density-driven component to the formation of oceanic surface circulation.

In the CCR year 1992, an anticyclonic oceanic surface circulation dominates in winter and agrees with the ice drift pattern (Figure 61). In summer 1992, the surface currents differ substantially (up to 2–3 cm s^{-1}) from the ice drift. Density distribution maintains an anticyclonic rotation in the surface layer. By contrast, wind stresses transmitted to the ocean by ice drift generate a cyclonic motion. Thus, density- and wind-induced forces act in opposition. The monthly ice drift speed derived from buoy observations in the Beaufort Sea and depicted in Figure 58 corroborates that the ice circulation is weaker in 1992 compared with 1987 because these winds act against ocean density-driven currents. Details for the Beaufort and Chukchi Seas are shown in Figure 113.

Below the surface, at a depth of 25–50 m, the computed circulation remains anticyclonic in both 1987 and 1992. The seasonal signal decays toward the bottom, and at 300-m depth the difference between the summer and winter simulated circulations is negligible. The kinetic energy of wind, computed ice drift, and currents at depths of 2.5, 50, and 300 m is depicted in Figure 114. There is substantial decay of the seasonal signal with depth. Note also higher kinetic energy of ice drift and oceanic surface currents in 1987 (ACCR) than in 1992 (CCR) even though the kinetic energy of summer winds in 1992 is overall higher than in 1987.

Water temperature and salinity

Seasonal variability of the simulated water temperature and salinity is depicted in Figure 98. In general, ice concentration controls the sea surface temperature (SST) in ice-covered regions of the central Arctic, where the solar radiation and atmospheric heat may be effectively absorbed by the upper ocean in leads. Therefore, the evolution of the temperature in the 50-m upper ocean follows the variability of ice concentration, reaching its maximum in August and minimum in May (Figure 98). In winter the Arctic SST is near the freezing point. The seasonal cycle of the salinity in the central Arctic is mainly determined by the annual variability of ice mass, with a minimum in September and a maximum in May (Figure 98). There is a tendency for a weaker seasonal signal in salinity when ice is more compact. The summer decrease of ice concentration in the center of the cyclonic circulation to the north of the Laptev Sea and surrounding areas causes accumulation of solar radiation and warming of the upper ocean. This process leads to additional ice melt and freshening of the surface water. In winter, there is intense ice production and salinification there. Thus, both summer and winter processes are responsible for the stronger seasonal signal in 1992 (CCR) than in 1987 (ACCR) in Region 3. The seasonal variability of the computed temperature and salinity in Region 2 (off the Chukchi Sea slope) differs from that in other regions (Figure 98). In 1992 (CCR) the water in this region is colder in winter and warmer in summer than in 1987 (ACCR). Water salinity is higher there in 1992 than in 1987 here. This anomaly will be discussed in the last section of our report. Seasonal variability of the water temperature and salinity for ACCR and CCR years for the Beaufort and Chukchi Seas is shown in Figures 115–118 in detail.

Differences between ACCR and CCR years in these parameters are shown in Figures 119–122. Differences are very small in winter but increase significantly in summer when sea ice melts and solar radiation warms up the surface layer. These differences are regulated by the location of the sea ice edge and sea ice concentration as it is described above.

Water heat content

The seasonal change of the heat content of the 50-m upper Arctic Ocean for the regions with depth deeper than 200 m has been estimated by the formula:

$$Q = \int_0^h c_p \rho \left(T - T_{fr}\right) dz \qquad (22)$$

where h = 50 m; c_p (= $4.19 \cdot 10^6$ $\mathrm{Jm^{-3}\ grad^{-1}}$) is the volumetric heat capacity of water; ρ is the water density; T is the water temperature; and T_{fr} is the freezing temperature at a given salinity [Treshnikov and Baranov 1972]. The heat content for 1987 and 1992 is depicted in Figure 123. Summer leads in the central Arctic in 1992 cause warming and accumulation of heat in the upper ocean. Both WT-92 and W-92 experiments show that this process results in extra ice melt and water freshening (Figure 98). This water freshening in the central Arctic during CCR years provides an extra freshwater export from the Arctic Ocean to the Greenland Sea. There is a significant influence of the SAT on the formation of the salinity anomalies in the upper Arctic Ocean under CCR.

Tendencies of Interannual Variability

Observations and numerical experiments show substantial differences in the seasonal cycle in CCR and ACCR years. In this section we analyze results of numerical experiments to show how these differences affect the interannual response of the Arctic ice and ocean to atmospheric forcing. Our approach with repeated prescribed forcing for a particular year does not allow us to study real interannual variability of the ice and ocean. However, this approach may be successful in exhibiting tendencies hidden in the forcing fields. Thus, this analysis focuses only on trends and anomalies of the ice and ocean parameters.

Sea ice

The computed basin-averaged ice mass in 1987 (ACCR) remains close to that of Romanov [1992] during all 15 modeling years (Figures 124 and 125). During the CCR year 1992, summer winds flush multi-year ice from the East Siberian and Laptev Seas and significantly decrease sea ice concentration in the Eurasian Basin, resulting in leads in the ice cover. During the following winter first-year ice appears in the ice-free areas. Repetition of this process over several years of a cyclonic regime results in thinner ice by more than 0.5 m in the central Arctic and about 1 m in the northern parts of the marginal seas in 1992 compared with 1987 (Figures 98 and 99). The mean ice mass in the central Arctic differs by about 0.28×10^{16} kg between 1987 (ACCR) and 1992 (CCR) (Figure 125). Regional variations of ice mass are substantial as well (Figure 124, top panels). The area of thin ice moves with time from the "eye" of the ice divergence (Region 3, Figure 55) toward the basin's peripheries. After several years thick ice in Region 3 is replaced by thinner ice. This process, with some time lag, occurs in the adjacent regions as well. Therefore, after 3–4 years of the cyclonic regime (1992) the ice mass drops in the central Arctic, and the ice thickness in Fram Strait decreases (Figure 124), reducing ice transport into the Greenland Sea. The resulting pattern of mean ice thickness depicted in Figure 99 shows thinner ice in 1992 (CCR) than in 1987 (ACCR) in the central Arctic, except for a relatively narrow strip of very thick ice, up to 8–9 m, along the Canadian Archipelago. Multi-year behavior of sea ice mass, heat, and freshwater content in the

Laptev and Beaufort Seas is shown in Figure 124. Sea ice mass reduction in the Beaufort Sea is related more to the melting processes than to the decrease of sea ice concentration. Heat accumulation in the water and freshwater content in the upper ocean do not change significantly from regime to regime in the Beaufort Sea (see also Figures 115–122) because maximum changes occur mainly in the Chukchi Sea, and in the Beaufort part of the area changes are not pronounced. This is because during ACCR and CCR wind tends to drive sea ice toward or parallel to the coastline and sea ice concentration along Alaskan coast does not change (averaged for period of 4 to 9 years); but interannual variability could be considerable.

Temperature, salinity, and heat/freshwater content of the upper ocean

The ocean responds to the wind anomalies much slower than does the ice cover. Time evolution of the computed heat and freshwater content in the upper 50-m layer of the Arctic Ocean is depicted in Figure 125 (the freshwater balance is determined following Steele et al. [1996]). During the first five years the difference between the oceanic responses in 1987 and 1992 is negligible due to restoration of the water temperature and salinity. After this restoring period, anticyclonic ice and ocean surface circulation in 1987 results in salinification and cooling of the upper ocean for about 5–7 years; after that the upper ocean oscillates around its equilibrium state. The seasonal change of the heat content increases slightly (Figure 125), whereas the amount of fresh water revolving in the seasonal cycle remains practically the same throughout the 10 years of the modeled anticyclonic state. In the year with a cyclonic regime (1992) the additional heat supply from the atmosphere into the water encourages ice melt and freshening of the upper ocean. The oceanic heat and freshwater content increase with time, although, as for 1987, the amount of fresh water involved in the seasonal cycle remains unchanged (Figure 125).

Regionally, the time evolution of the 50-m upper ocean layer varies substantially (Figure 123 and 124). To the north of the Laptev Sea (Region 3) slight warming and salinification of the upper ocean under the ACCR (1987) contrasts with the sharp increase in heat content and freshening in the cyclonic regime (1992). The interannual variability of freshwater content in the central Arctic (Regions 4 and 5) is similar to that in Region 3, although the temperatures in Regions 4 and 5 are different. The profound drop of the heat content in Region 4 during the first several years of the freely evolving system in 1987 (ACCR) leads to a big difference between the heat content in 1987 and 1992; by the end of the simulation this difference is small. In the Nansen Basin (Region 5) the heat content in 1987 (ACCR) even exceeds that in 1992 (CCR), except for the last couple of years of integration. In the Beaufort Sea (Region 1) the interannual variability of the upper ocean incorporates, to some extent, the features of the adjacent Regions 3 and 4. Off the Chukchi Sea slope (Region 2) both the seasonal and interannual variability of the upper ocean differ from that in other regions. In 1987 (ACCR) the upper ocean is, on average, warmer than in 1992 (CCR). One of the possible reasons for heating and salinification of the upper ocean over the Chukchi Cap may be upwelling of intermediate waters to the surface. The vertical thermohaline structure in the Arctic in 1987 remains almost unchanged relative to its initial distribution from Polyakov and Timokhov [1994]. Salinification and warming of the upper ocean over the Chukchi Cap in the 1990s (CCR) was recorded by McPhee [1999] during the SHEBA expedition. Time evolution of the freshwater content to the north of the Chukchi Sea is similar in 1987 and 1992, and the salinity is higher in 1992 than in 1987. In the Greenland Sea (Region 6) the most pronounced features are a strong seasonal variability of the heat content in both 1987 and 1992 and substantially fresher water in the surface layer under the cyclonic regime (1992). The transport of extra ice and fresh water from the central Arctic into the Greenland
Sea in 1992 (CCR) establishes a strong vertical stratification in the GIN Sea (Greenland, Iceland, and Norwegian Seas).

Inflow/outflow

The water exchange in the upper 200-m layer between the Arctic Ocean and the Greenland, Barents, and Kara Seas is shown in Figure 126. In 1987, the annual equilibrium water outflow from the Arctic Ocean into the Greenland Sea through Fram Strait is about 1.1 Sv distributed equally in 0–50 and 50–200-m layers. Prevailing winds cause more intense outflow from the Arctic into the Greenland Sea through Fram Strait under the cyclonic regime (1992). This outflow is balanced by inflow of warm and salty Atlantic water through the Kara and Barents Seas (mostly the latter); the major portion of this inflow is concentrated in the deeper 50–200-m layer (Figure 126). A recent modeling study by Zhang et al. [1998] pointed out that an increase of the temperature and salinity in the upper Eurasian Basin in the 1990s (CCR years) is due to increased incoming warm and salty Atlantic water through Fram Strait, and most significantly, via the Barents Sea. Our modeling results show a substantial increase of Atlantic Water transport from the Barents Sea during CCR (1992) too. However, there are some doubts that intensified Atlantic Water inflow caused the observed salinification of the surface layer in the Eurasian Basin in the 1990s.

Nikiforov and Shpaikher [1980] demonstrated that salinification and freshening of the upper ocean in this region of the Arctic is closely related to atmospheric circulation. In years with reduced atmospheric surface pressure, prevailing offshore winds move fresh surface water, formed by Siberian river discharge and ice melt, from the Laptev and East Siberian Seas northward. This surface water is replaced by saltier underlying water via upwelling along the continental slope. The positive salinity anomalies to the north of the Laptev Sea reached 2–3 psu [Nikiforov and Shpaikher 1980]. The same phenomenon was recorded during Russian oceanographic surveys in the 1970s. In 1979, the transition year from ACCR to CCR, the observations showed a remarkable increase of water salinity (up to 3 psu) at the continental slope of the Laptev Sea. This anomaly is as large as observed in the 1990s [Steele and Boyd 1998].

Freshwater pathways

Two major processes seem to establish the observed salinity anomalies of the upper ocean in the Arctic. Under the CCR, additional ice melt causes freshening of the upper ocean in the Eurasian and Canadian Basins, whereas the redistribution of the Siberian rivers' outflow, under prevailing winds in the cyclonic years, may result in salinification of the upper mixed layer in the Nansen Basin. Under the ACCR the redistribution of the river outflow and summer ice melt lead to opposite salinity anomalies. Our model seems to reproduce, quite well, the annual cycle of fresh water involved in the ice freezing/decay under the two climatic states. But the salinification of the surface layer in the Nansen Basin, associated with the northeastward outflow of the Siberian rivers under the cyclonic regime, is not captured by the model. A possible reason for this model behavior may reside in the fact that we used atmospheric conditions for one particular year (1992), whereas the observed salinity anomaly of the 1990s was perhaps formed in one of the previous or succeeding years of the cyclonic regime. Recent observations by Guay at al. [1998] support this conclusion. Summer measurements of temperature, salinity, and dissolved barium were obtained from the Laptev Sea and neighboring areas of the Nansen, Amundsen, and Makarov Basins in 1993, 1995, and 1996. The tracer fields exhibited significant interannual variability during these years. Guay at al. [1998] have demonstrated that under the influence of local winds, fresh shelf waters formed by river outflow can move from the Laptev shelf either northward beyond the shelf break into adjacent deep-water areas (Region 3), or eastward into the East Siberian Sea and farther into the Arctic interior along the Mendeleyev Ridge. We plan experiments with the atmospheric conditions for the period 1979–1996 to clarify this situation.

Mackenzie River discharge may also be an important source of surface salinity anomalies in the Canadian Basin under the two circulation regimes. In ACCR years, Mackenzie River fresh waters become entrained into the Beaufort Gyre, causing freshening of the surface layer in Region 2 (Region 1 does not show the same response due to the large area of the region to the north where the 1992 processes are under the

direct influence of openings in the ice cover). In the CCR years, these waters flow to the east and leave the Arctic Ocean through the straits of the Canadian Archipelago. Thus, different regimes may cause substantial changes in the pathway of the Mackenzie River freshwater discharge.

The Role of the Beaufort Gyre in Arctic Climate Variability: Seasonal to Decadal Climate Scales

The present state of the Arctic Ocean and its influence on the global climate system strongly depend on the Arctic Ocean freshwater budget [Aagaard and Carmack 1989, hereinafter A&C] because fluctuations in freshwater export can significantly influence the depth and volume of deep water formation in the North Atlantic and ultimately the strength of the global thermohaline circulation. The traditional approach for the investigation of the freshwater budget of the Arctic Ocean has been to perform a detailed analysis of its major components, including river runoff, the inflow of waters from the Atlantic and Pacific Oceans, the outflows through Fram Strait and the Canadian Archipelago, the atmospheric moisture flux and the annual cycle of ice formation and melt. For a more comprehensive overview, see Lewis et al. [2000]. Significantly less attention has been paid to the analysis of the processes involved in the storage of fresh water in the Arctic Ocean and its temporal variability. The regional differences in freshwater storage (e.g., ice thickness distribution and ocean salinity) are substantial [A&C; Steele et al. 1996].

The freshwater storage in the ocean results in persistent salinity anomalies. One of these persistent anomalies is located in the Beaufort Gyre, denoted by a salinity minimum at depths from 5 through 400 m (Figure 127). This anomaly drives the thermohaline circulation of the Arctic Ocean anticyclonically. Figure 128b shows the dynamic topography relative to 200 db and is calculated based on temperature and salinity data from the Environmental Working Group Atlas of the Arctic Ocean. The freshwater budget of the Arctic Ocean and the freshwater flux to the North Atlantic depend significantly on the intensity of this salinity anomaly, the direction and intensity of the thermohaline circulation and climatic conditions conducive to the transport of fresh water from the Beaufort Gyre to the North Atlantic.

Beaufort Gyre as a flywheel

The origin of the salinity anomaly in the Beaufort Gyre can be inferred by a comparison of the seasonal change in wind and sea ice motion. Figures 129 and 130 show the correlation between wind (NCAR/NCEP 1979–1997 reanalysis data) and ice drift (deduced from the International Arctic Buoy Programme) in the Arctic Ocean averaged for 1979–1997. In winter (September–May), the wind stress drives the ice and ocean anticyclonically (Figures 129–130) and the ocean accumulates potential energy through a deformation of the salinity field (Ekman convergence and subsequent downwelling, see Figure 128a). The strength of the horizontal salinity gradient in Figure 127 (and geostrophic circulation, Figure 128) depends on the intensity and duration of the anticyclonic winds.

In winter the wind-driven and density-driven currents coincide to set up a strong anticyclonic rotation.

In summer (June–August), wind forcing is weaker or it may even drive the ice and ocean cyclonically (Figure 129b), but on average the ice still rotates anticyclonically (Figure 130). An obvious conclusion is that in summer the geostrophic circulation prevails and drives the ice against the wind motion. The salinity anomaly in the Beaufort Gyre must decrease in summer, because without wind support, the ocean loses potential energy, i.e., Ekman pumping is reduced. During the following winter the ocean again accumulates wind energy. Hence, the climatic structure of the salinity and dynamic height distribution remains rather persistent (not shown) although exhibiting some seasonal and interannual variability. Seasonally, the Beaufort Gyre salinity anomaly stabilizes the circulation to remain essentially

anticyclonic throughout the year permitting the Beaufort Gyre circulation cell to serve as a flywheel for the Arctic Ocean circulation. This mechanism can be extended to longer time scales and can explain the interannual and longer variability of the Arctic circulation.

Hypotheses

In order to explain the relationship between the wind-driven and thermohaline circulation and its influence on the accumulation and release of fresh water we examine the interplay between the atmosphere, ice and ocean in terms of the two circulation regimes. The interactions between the thermohaline and wind-driven circulation and the freshwater content of the Arctic Ocean can be described as follow.

Anticyclonic regime

During the ACCR, when high atmospheric pressure prevails in the Arctic, the Arctic Ocean accumulates fresh water through the increase of freshwater volume in the Beaufort Gyre (Ekman convergence and subsequent downwelling, see Figure 128) and through the increase of ice volume and area due to enhanced ice growth during this regime (the Arctic is much colder during an ACCR than during a cyclonic climate state [Proshutinsky et al. 1999]). An ACCR also leads to an increase of ice accumulation and ridging in the Canadian Arctic. Additionally, river runoff is increased and more fresh water accumulates in the surface waters of the Arctic seas. The anticyclonic wind-driven circulation leads to a reduction in flow between the Arctic Ocean and the GIN Sea [P&J; Tremblay and Mysak 1998]. Consequently, the ice and water flux from the Arctic Ocean to the Greenland Sea and transport of Atlantic water into the Arctic Basin are weaker than usual. Deep convection in the Greenland Sea and water exchange between the North Atlantic and GIN Sea are enhanced.

Cyclonic regime

All of the above processes lead (with some time lag) to an increase in the gradient of dynamic height between the Beaufort Gyre and the North Atlantic. The resultant thermohaline circulation increases, as does the outflow of fresh water and ice from the Arctic. During warming of the GIN Sea, the Icelandic Low intensifies and moves to the north. The North Atlantic Oscillation index grows, leading to an intensification of the transport of Atlantic waters into the Arctic Ocean. This increase in warm water flux to higher latitudes enhances the penetration of atmospheric cyclones into the Arctic, and ultimately decreases the atmospheric pressure in the Arctic. These processes also increase ice melting and release of additional fresh water to the central basin. Warming of the Arctic establishes the CCR.

The stronger surface winds of the cyclonic regime [Proshutinsky et al. 1999] increase the transport of thick ice from the Arctic to the Greenland Sea and increase the freshwater transport to the Greenland Sea. The accumulation and storage of fresh water in the Beaufort Gyre is not favored by the CCR (even though the cyclonic regime leads to increased ice melt, the fresh water is not accumulated in the Beaufort Gyre because of Ekman divergence and upwelling causing a decrease of freshwater volume), and hence more fresh water is available for transport to the North Atlantic. At the peak of these processes, when all of them coincide, we observe the low salinity anomalies in the GIN Sea.

Transitional phase

After several years of increased release of ice and fresh water to the GIN Sea, the surface layer becomes cooler and fresher, and the sea ice extent increases in the Greenland Sea. Freshening associated with melting of the increased ice volume and increased flux of fresher surface waters leads to an increase in water stratification and a decrease in the interaction between the deep ocean and the atmosphere; deep water convection is consequently suppressed. After several years the dynamic height gradient between

the Beaufort Gyre and the North Atlantic (and consequently the thermohaline circulation) decreases, the Icelandic Low moves to the south and the interactions between the GIN Sea and the Arctic Ocean become weaker, reestablishing the ACCR.

It is important to note that in this sequence of processes the accumulation and release of fresh water and ice plays a fundamental role in the interaction between the Arctic Basin and GIN Sea. The accumulation and subsequent release of the stored fresh water take time and are regulated by wind-driven and thermohaline forcing through a cascade of oscillations alternating on a decadal cycle.

Supporting evidence

In order to support our hypotheses we have analyzed the variability of the freshwater content in the Beaufort Gyre (shaded box in Figures 127–130) using 1973–1979 (ACCR years) March–May temperature and salinity surveys conducted by the Arctic and Antarctic Research Institute, St. Petersburg, Russia (personal communication). The freshwater content was calculated relative to a salinity of 34.80.

A time series of freshwater content anomaly for this 7-year period is shown in Figure 131a. The dashed line depicts the Arctic Ocean Oscillation (AOO) index (Figures 10 and 19). Note that this is not the Arctic Oscillation index [Thompson and Wallace 1998]. The AOO portrays the intensity of the anticyclonic/cyclonic wind-driven circulation over the Arctic. When the AOO is positive the ACCR prevails and the freshwater volume in the Beaufort Gyre increases and vice versa. This close correlation allows us to reconstruct the freshwater content in the Beaufort Gyre for a longer period (1946–2001) using the AOO index only (Figure 131) and to evaluate its range of variability over several cyclonic and anticyclonic regimes. The difference between freshwater content during anticyclonic and CCRs in the area contained within the light and dark shaded boxes is about 10^4 km^3 which is about three times larger than the annual freshwater input from river runoff estimated by A&C. This suggests that the fresh water released from the Beaufort Gyre during cyclonic regimes can be significantly more important than that from all other freshwater sources.

Another component of freshwater content is the volume of sea ice in the Arctic Ocean. No direct observations are available but we can use some results from modeling studies. Figure 131b shows the anomaly of sea ice volume (solid line) in the Arctic Ocean based on the mean of three separate model studies [Hilmer and Lemke 2000; R. Gerdes, personal communication; A. Makshtas, personal communication]. These simulations reveal a pronounced decadal variability of the sea ice volume which correlates quite well with our AOO index. The correlation between circulation regimes and sea ice volume anomaly is excellent (but with some lag) after 1970. One sees that the sea ice volume increases during ACCRs and decreases during cyclonic climate regimes. The disagreement noted for years prior to 1970 could be explained by model spin-up considerations but this problem has to be investigated more carefully within each of the models.

Another confirmation of different rates of freshwater release from the Arctic Ocean to the GIN Sea is the sea ice condition in the GIN Sea. Figures 132a and 132b show sea ice concentration averaged for the years when cyclonic or anticyclonic regimes were dominant based on satellite data. One sees that much more ice is present in the GIN Sea during cyclonic regimes. This is because of enhanced development of the Odden ice tongue in the region of the Greenland Sea deep ocean convection during cyclonic regimes [Comiso et al. 2001]. This provides indirect confirmation that deep convection is suppressed during cyclonic regimes because of the large volume of fresh water in the surface layer of the Greenland Sea.

One may wonder how the salinity anomaly of the Beaufort Gyre or thermohaline circulation may change in response to global warming and climate change scenarios. Recent observations in the Arctic show that the climatically stable ACCR, dominant during the 1970s and 1980s, has been replaced by a CCR starting

about 1989. As a result, for most of the past decade the intensity of the Arctic High has decreased and the summer cyclonic circulation period (Figure 129b) has commenced earlier and lasted longer than usual. These conditions must necessarily lead to a reduction in the salinity anomaly in the deeper layers in the Beaufort Gyre (upwelling in response to the cyclonic forcing), a reduction in the speed of the thermohaline current and to an increase of fresh water in the upper layers of the Arctic Ocean. This latter is due to increased ice melt and suppression of Ekman pumping reducing the transport of fresh water to the deeper layers. As a result, the fresh water stored in the upper layers of the Beaufort Gyre becomes available for output to the North Atlantic through increased transport by the cyclonic wind-driven circulation (Figure 131b). The data and conclusions of Figure 131b are also supported by recent observations made by McLaughlin et al. [2002] in the Canada Basin. Physical and geochemical data collected between 1989 and 1995 reveal that the freshwater content in the Canada Basin has been significantly reduced, which correlates well with Figure 131b. Since 1997, evidence suggests that a new ACCR may be developing (Figure 131b) and we can expect to observe an increase of freshwater content in the Beaufort Gyre.

A substantial release of the Beaufort Gyre fresh water to the North Atlantic in response to changing climate conditions can be a source for a negative salinity anomaly in the North Atlantic, and consequently, a source for an abrupt global cooling [A&C; Delworth et al. 1997]. These perspectives lead us to the conclusion that it is extremely important to understand the structure of the Beaufort Gyre water properties, its currents, and their variability in space and time. We encourage the creation of an observational and modeling program to test the major hypotheses formulated above.

Anomalous Sea Ice Extent in the Beaufort and Chukchi Seas in 1998–2002

This study was added to the project because the sea ice and weather conditions observed in the Beaufort and Chukchi Seas in 1998 (the first year of the new ACCR) did not correspond to the ACCR conditions described above. Therefore it was important to continue our research and to explain causes of this anomaly and to investigate historical data searching for analogous situations in the past. In this section we analyze sea ice conditions in 1998–2002 in the Beaufort Sea.

Sea ice conditions in 1998

Analyses of Arctic sea ice data suggest an overall negative trend during 1979–2002, and particularly during the past decade, with increased interannual variability in recent years. While most of the loss in ice cover has occurred in the eastern Arctic, the last few years have seen record decreases in summer ice extent in the Beaufort and Chukchi Seas, and an unprecedented persistence in the reduced summer ice extent over five consecutive years. Such large and persistent extremes have important implications for local and regional ecosystems, biology, weather, and climate in northern Alaska and Canada, with possible significance for broader-scale climatic conditions.

The unusual persistence of the ice reductions suggests a possible shift to a new climatic regime, but the recent changes might also result from a localized and essentially chaotic combination of conditions such as the influence of individual synoptic events. Given the local, regional, and global implications of extreme shifts in ice cover, it thus is important to determine what atmospheric and oceanic processes contributed to the recent changes, whether these processes are predictable, whether they have changed and intensified over time, and whether ice conditions are evolving into a new state that is increasingly sensitive to normal interannual variability in atmospheric forcing.

For the western Arctic (Figure 133), no overall trend is apparent in the Walsh data set [Chapman and Walsh 1991, extended], but the large reduction in ice extent in 1998 is clearly shown. Ice cover in the

Beaufort and Chukchi Seas for September 1998 is 25% less than the previous record minimum of 1958, it is 39% below the 1953–1997 average, and more that four standard deviations less than the average minimum extent over the previous nine minimum years from 1953 to 1997. Ice loss began earlier and progressed faster than in previous years in the microwave record.

The ice severity index (the distance northward from Point Barrow, Alaska to the 50% ice concentration limit as measured from National Ice Center (NIC) ice charts for mid-September [see Rogers 1978] reveals that the distance to the ice limit from Point Barrow in September 1998 was 46% greater than for the previous record years of 1954 and 1958 (569 km vs. 390 km). It is important to mention that 1953–1957 are CCR years and 1958 is the first year of ACCR regime. The charts also show that complete freeze-over did not occur until the second week of November—considerably later than in other years. In addition, the least ice cover ever observed in the channels of the Canadian Arctic Archipelago occurred in September 1998 [Canadian Ice Service of Environment Canada, personal communication].

As evident in Figure 133 and noted by McPhee et al. [1998] in their description of conditions during deployment of the SHEBA field camp, the Beaufort Sea ice extent in autumn 1997 was also well below normal, with an unusual lack of thick, old ice. Recognizing that thin first-year ice will melt out earlier than old ice, McPhee et al. [1998] predicted a negative ice anomaly in summer/autumn 1998. Observations bear out this prediction, but as indicated in Figure 133, persistence of a substantially reduced ice extent in this region over two or more years is rare. Indeed, 1997 and 1998 are the only successive years in the Walsh record with summer ice extent at least one standard deviation below the mean. As we discuss below, atmospheric conditions through autumn 1997 and summer 1998 were unusual, favoring ice retreat through enhanced melt and transport.

Atmospheric conditions

Rogers [1978] examined ice conditions in the Beaufort Sea in terms of composite differences in summer-averaged sea level pressure (SLP) for light- minus heavy-ice years (defined in terms of below- or above-normal ice extent). Light-ice years were associated with positive pressure differences over the northern Canadian Archipelago and north-central Siberia, and negative differences over the East Siberian Sea. This strengthens the mean easterly and southerly winds over the Beaufort Sea and favors positive temperature anomalies, promoting melt and advection of ice to the west and north. Summer-month (June–August) composites of SLP and anomalies for the ten years with the least ice cover in the western Arctic (as noted in the Figure 133 caption) show that with respect to long-term mean (1953–1998) conditions, the more dominant feature is above-average pressure centered over the northeastern Beaufort Sea (Figure 134). However, when examined in relation to the corresponding NCAR/NCEP surface air temperature (Figure 135) and wind anomalies (not shown), Rogers' [1978] general conclusions are supported. There is a positive air temperature anomaly up to 1 °C along the Beaufort Sea coastline (Figure 135) and we assume that the source of this anomaly is a direct solar radiation heating of the surface in the condition of absence of sea ice in the area.

The SLP anomaly pattern for June–August 1998 (Figure 136) is similar to that in Figure 134 for the northeastern Beaufort Sea, but this feature is coupled with negative anomalies over the northern Bering and Chukchi Seas and extensive positive anomalies over the eastern Arctic. Regional pressure gradients are consequently larger, favoring stronger ice advection to the west and north as compared to most light-ice years. Temperature anomalies in summer 1998 (Figure 137) are also substantially greater over the southern Beaufort Sea than in typical light-ice years. When considered in conjunction with preconditioning by antecedent (autumn 1997) ice conditions (Figure 133) in the western Arctic [see also McPhee et al. 1998], the summer circulation/temperature patterns are consistent with the large size of the 1998 anomaly.

Figures 138 and 139 show a very similar condition in 1958, the first year of ACCR after the 1953–1957 CCR. SLP and air temperature anomalies in 1958 were even larger than in 1998 but sea ice area reduction was not as large as in 1998, which could be explained by a general trend of warming and reduction in the sea ice area in the Arctic during last 30 years.

However, the magnitude and early development of the 1998 ice reductions require us to consider other aspects of preconditioning during the intervening autumn and spring. In 1997–1998, mean temperatures in the eastern Beaufort Sea and Canadian Archipelago were well above normal from November to April (Figure 140), with a continuation of easterly winds that may have advected warmer air into the region, or perhaps affected surface temperatures through changes in net radiation. But it is more likely that these air temperature anomalies result from local conditions. In Figure 140, most of the large anomalies are located around Arctic islands where in the summer of 1998 sea ice was absent. It means that during the summer, the ocean accumulated significantly more heat (especially in the coastal polynyas) than in the typical years and released this heat during autumn and winter of 1998, warming the atmosphere.

The autumn/winter temperature anomalies suggest that ice growth in the southern and eastern Beaufort Sea may have been below normal. However, relatively small mean winter/spring temperature anomalies (albeit with large month-to-month variability) were observed along the SHEBA drift track in the central and northern Beaufort and Chukchi Seas in 1997–1998 [R. Lindsay, personal communication]. Unusually thin ice in autumn 1998 observed at the SHEBA camp is argued instead to mainly reflect greater summer melt rather than a deficit of ice growth [D. Perovich, personal communication]

Composites of November–April SLP ((Figures 141–143), November–April SAT (Figures 144–145), and geostrophic wind anomalies (not shown) for the minimum extent years in Figure 133 suggest that the cold months preceding light-ice summers are characterized by a below-normal Aleutian Low pressure system, extending northward and below normal atmospheric pressure over eastern Siberia, with above-normal pressure over North America and the central Arctic Basin. A common feature for all light-ice years is a decrease in northerly winds in the Canadian Basin and Chukchi Sea, either through a weakening of the mean high-pressure area, or a northward displacement of the high pressure system.

In addition to modifying heat and moisture transport, this decrease in northerly winds affects the Beaufort Gyre, reducing the southward advection of thick, old ice into the Beaufort and Chukchi Seas. As noted earlier, the extent of old ice was much reduced in autumn 1997. Decreased southward ice transport through autumn 1997–spring 1998 thus allowed a large expanse of thinner first-year ice to remain in the area, likely contributing to the large loss of ice extent in summer 1998. It is important to note though that while each of the lightest ice years fits the pattern of modified Beaufort Gyre circulation, this winter pattern alone does not necessary coincide with a subsequent light-ice summer. Instead, the winter pattern may precondition the ice pack to favor the reductions in ice extent that may then occur in response to the summer circulation regime described here and by Rogers [1978].

A possible relationship between general modes of atmospheric circulation and the summer and winter patterns described above remains to be determined. In general, the below normal SLP in the Arctic is typical of the positive modes of the North Atlantic Oscillation and Arctic Oscillation (AO), and for the CCR. However, the light-ice years in Figure 133 are almost equally divided between positive and negative NAO, and AO winters (see Figure 146). Modifications in western Arctic circulation in the 1997 and 1957 winters appear driven more by below-normal SLP in the north Pacific than by central Arctic SLP anomalies, and thus are reflected in the North Pacific and Pacific North American indices. The reduction in the North Pacific SLP in 1998 corresponds to the strong ENSO (El Niño/Southern Oscillation) event in 1997–1998, but as with the other indices, no clear correlation of light-ice years with ENSO is readily apparent. This is consistent with the analyses of SLP patterns for individual years, which suggests that the western Arctic winds and ice drift that favor reduced ice cover are associated with

relatively fine-scale, regional variations in SLP that lie within the larger patterns reflected in existing indices.

Sea ice conditions in 1999–2002

For 1999–2002, Walsh data [Chapman and Walsh 1991, extended], are not available at this time and in order to characterize the sea ice conditions in the Beaufort and Chukchi Seas we calculated sea ice area and sea ice extent for a region, shown in Figure 147 and covering the Beaufort and Chukchi Sea area, using National Snow and Ice Data Center SSM/I data processed with the bootstrap algorithm. This information is shown in Figure 148. One sees that these data correlate very well with Walsh's data for 1979–1998 (Figure 133) but our data set is extended to cover 1999–2002. During 1999–2001 the sea ice conditions gradually returned to their climatologic norm and more or less corresponded to the conditions of a typical ACCR regime. But in 2002 the second historic minimum in sea ice area and sea ice extent was recorded in the Arctic Ocean and reported by Serreze et al. [2003]. They concluded that the 2002 anomaly is the most recent manifestation of a general downward trend in the Arctic sea ice during the passive microwave era. From 1978 through 1996 a trend of $-2.8 \pm 0.3\%$ per decade is reported [Cavalieri et al. 1997; Parkinson et al. 1999].

For the Beaufort and Chukchi Seas the September 2002 ice extent is the second minimum ice extent after the 1998 absolute minimum for the last 23 years of microwave observations and it is 20% greater then the previous minimum in 1998. Figure 149 shows the September sea ice concentration in the Arctic Ocean for 1997–2002 in order to illustrate interannual variability and to evaluate the rate of sea ice loss during the summer period relative to entire Arctic ice conditions.

Causes of the 2002 anomaly

Serreze et al. [2003] propose at least three possible causes of the sea ice anomaly in the Arctic Ocean in 2002. They include:

1. Early formation of leads and polynyas along the Beaufort and Chukchi Sea coastline during March–May driven by large positive pressure anomalies over this region: Development of such features favors summer ice loss through enhanced absorption of solar radiation [Maslanik et al. 1996; Polyakov et al. 1999]. High air temperatures may have contributed by inhibiting ice growth and promoting early melt.

2. Anomalous low sea level pressure in the central Arctic Ocean from June through August (Figure 150): Low mean pressure prevailed for the three months individually. This is highly unusual, and consistent with the widespread development of low ice concentration.

3. This SLP pattern accompanied by relatively high surface air temperatures (Figure 151): By itself, a divergent ice pack will lead to greater ice extent. However, enhanced absorption of solar radiation in open water likely fostered melting. A contributing factor was continued warmth during summer, except near the center of mean low pressure (Figure 151). On the other hand, in the Beaufort Sea the air temperature anomaly is close to zero or even negative, which contradicts the above conclusion. This is probably because the surface air temperature from reanalysis data is strongly influenced by the modeled surface energy budget and can have substantial error in the areas where observations are lacking.

Our analysis shows that 2002 was the year with the cyclonic circulation regime and that 2002 summer sea ice conditions confirm our general conclusion that CCR years are characterized by lower ice extent and

area than ACCR years. Table 1 (p. 2) presents major characteristics of the cyclonic (CCR) and anticyclonic circulation regimes (ACCR) in the Arctic Ocean and in the Beaufort and Chukchi Seas.

Final Conclusions

1. Analysis of observational data and results of numerical experiments reveal significant differences in atmospheric, ice, and oceanic parameters during two Arctic climate states for the entire Arctic Ocean and particularly for the Beaufort and Chukchi Seas (Table 1). During the anticyclonic circulation regime, "winter" conditions with a cold and dry atmosphere, increased ice thickness and ice concentration, and a saltier and colder upper ocean, prevail in the seasonal cycle. During the cyclonic circulation regime, "summer" conditions dominate, with a relatively warm and wet atmosphere, reduced ice thickness and ice concentration, and a fresher and warmer upper ocean.

2. In ACCR years both winter and summer ice drift is anticyclonic, whereas in CCR years, summer ice drift is cyclonic. This is crucial for the distribution of summer leads and other openings in the ice cover. Both observations and modeling results demonstrate that about 50% of the summer ice-free area in the Arctic is due to leads in the pack ice; the rest is due to ice melt in the marginal ice zone. Satellite images and numerical experiments showed numerous openings in the ice cover in 1992 (CCR), reaching up to 40–45% of the total area in the center of the cyclonic rotation to the north of the Laptev Sea. In the year of the anticyclonic regime (1987) summer openings were mainly grouped along the ice edge.

3. Both winds and water density gradients maintained summer anticyclonic surface oceanic circulation in 1987 (ACCR); in 1992 (CCR) these two factors acted in opposition, resulting in weaker summer surface currents and ice drift than in summer of the ACCR year (1987), even though winds were stronger in 1992 than in 1987.

4. Ice concentration directly controls the surface temperature via warming/cooling of the upper ocean in leads and indirectly controls the surface salinity via ice melt/freezing processes. In ice-covered areas the typical ranges of seasonal variability of the SST and salinity are 0.1–0.3 °C and 0.5–1.0 ppt, respectively. In ice-free regions, seasonal temperature fluctuations reach up to several degrees, whereas salinity fluctuations are small. The SST reaches its maximum in August. In winter the Arctic SST is near the freezing point. The seasonal cycle of water salinity in the central Arctic is mainly determined by the annual variability of the ice mass, with a summer minimum in September and a winter maximum in May. The seasonal signal is weaker when the ice is more compact. Both summer and winter processes are responsible for the stronger seasonal signal in 1992 than in 1987 to the north of the Laptev Sea where ice concentration was reduced by summer cyclonic winds.

5. The different sea ice distributions due to ACCR or CCR atmospheric forcing are essential to the continued development of the ice and ocean responses that are observed over the longer term. Differences due to the seasonal cycle in ACCR (1987) and CCR (1992) years seem to accumulate, leading to significant interannual variations. For example, summer openings in the pack ice due to cyclonic winds during the CCR are replaced with first year ice by the end of the following winter. Domination of CCR during several years results in thinner ice in the central Arctic. This result is supported by observations in the Beaufort Sea in 1997–98 by McPhee et al. [1998] who reported that unridged ice rarely exceeded 1.8 m; i.e., the thickness of first year ice. The increased ice export from the Arctic Ocean

into the Kara, Barents, and Greenland Seas and an accumulation of ice off the Canadian Archipelago are also due to the summer ice drift pattern during CCR.

Wide ice-free summer areas in the Arctic marginal seas and central Arctic lead to warming of the upper ocean, resulting in a longer period of ice melt and thinner ice under the CCR. This modeling result agrees well with the recent findings of Smith [1998]. Our experiments show that extra ice melting in 1992 leads to freshening of the upper ocean in the Arctic. Observations by McPhee et al. [1998] and analysis of data from oceanographic expeditions in the 1990s [Steele and Boyd 1998] do show warming and freshening of the upper ocean in the Canadian Basin. However, Steele and Boyd found a remarkable salinification of the surface layer in the Nansen and Amundsen Basins. They hypothesized that these changes were due to intrusion of the Icelandic Low SLP cell into the Arctic Basin during the 1990s and mixing, additionally, the upper ocean.

6. The simulations suggest that ice and freshwater export from the Arctic Ocean may be an effective regulator of stratification in the Greenland Sea. According to Häkkinen [1993], this anomalous ice and freshwater transport from the Arctic into the GIN Sea caused the Great Salinity Anomaly. Our numerical experiments show that a CCR year is associated with significant freshening in the Greenland Sea and adjacent areas. Thus, one may speculate that establishment of strong stratification in the GIN Sea due to excess freshwater supply from the Arctic follows a cyclic pattern with periods coinciding with the change of Arctic Ocean circulation regimes.

7. Analysis of remotely-sensed fields indicates that the anticyclonic and cyclonic modes differ substantially in their effects on total ice concentration, multi-year ice concentration, ice motion, deformation, and ice extent. These results have a variety of implications for regional and long-term ice prediction, assessment of the sea ice record as an indicator of climatic change, and estimation of the role of sea ice on climate variability under different atmospheric circulation regimes.

Abbreviations

A&C	Aagaard and Carmack 1989
ACCR	anticyclonic circulation regime
AO	Arctic Oscillation
AOO	Arctic Ocean Oscillation
AIDJEX	Arctic Ice Dynamics Joint Experiment
ARLIS	Arctic Research Laboratory Ice Station
AVHRR	Advanced Very High Resolution Radiometer
CCR	cyclonic circulation regime
CIRES	Cooperative Institute for Research in Environmental Sciences
EASE-Grid	equal area scalable earth grid
ENSO	El Niño/Southern Oscillation
EOF	empirical orthogonal function
EWG	Environmental Working Group
GIN Sea	Greenland, Iceland, and Norwegian Seas
IABP	International Arctic Buoy Programme
IOEB	Ice–Ocean Environmental Buoy
NAO	North Atlantic Oscillation
NCAR	National Center for Atmospheric Research
NCEP	National Centers for Environmental Predictions
NIC	National Ice Center
NMC	National Meteorological Center
NOAA	National Oceanic and Atmospheric Administration
NSIDC	National Snow and Ice Data Center
P&J	Proshutinsky and Johnson 1997
SALARGOS	Argos-located buoy equipped with temperature and conductivity sensors
SAT	surface air temperature
SCICEX	Scientific Ice Expeditions
SEVER	systematic high latitude airborne expeditions
SHEBA	Surface Heat Budget of the Arctic Ocean
SLP	sea level atmospheric pressure
SMMR	scanning multichannel microwave radiometer
SSH	simulated sea surface height
SSM/I	special sensor microwave/imager
SST	sea surface temperature

Study Products

Publications

Peer reviewed

Drobot, S.D. and J.A. Maslanik. 2002. A practical method for long-range forecasting in the Beaufort Sea. Geophys. Res. Lett. 29:10.1029/2001GL014173.

Polyakov, I.V., A.Y. Proshutinsky and M. Johnson. 1999. Seasonal cycles in two regimes of Arctic climate. J. Geophys. Res. 104:25761–25788.

Proshutinsky, A.Y., R.H. Bourke and F.A. McLaughlin. 2002. The role of the Beaufort Gyre in Arctic climate variability: Seasonal to decadal climate scales. Geophys. Res. Lett. 29(23), 1110, doi:10.1029/2002GL015847.

Proshutinsky, A.Y., and M. Johnson. 2001. Two regimes of the Arctic's circulation from ocean models with ice and contaminants. Mar. Pollut. Bull. 43:61–70.

Proshutinsky, A., M. Johnson and T. Proshutinsky. 2001. Understanding climatic controls on sea-ice transport pathways in the Arctic Ocean. Ann. Glaciol. 33:551–554.

Proshutinsky, A., V. Pavlov and R.H. Bourke. 2001. Sea level rise in the Arctic Ocean, Geophys. Res. Lett. 28:2237–2240.

Proshutinsky A.Y., I.V. Polyakov and M.A. Johnson. 1999. Climate states and variability of Arctic ice and water dynamics during 1946–1997, Polar Res. 18:135–142.

Peer-reviewed (submitted or in preparation):

Drobot, S.D., and J.A. Maslanik. Interannual variability in summer Beaufort Sea ice conditions: Relationship to spring and summer surface and atmospheric variability. J. Geophys. Res. (in review)

Proshutinsky, A.Y., and R.H. Bourke. The role of the Beaufort Gyre in Arctic climate variability: Seasonal to decadal climate scales, Geophys. Res. Lett. (resubmitted)

Proshutinsky, A.Y., J.A. Maslanik, T.O. Proshutinsky and M.A. Johnson. Seasonal variability of the Beaufort and Chukchi Sea for two arctic climate states. (in preparation)

Proshutinsky, A.Y., J.A. Maslanik and S. Solomon. Arctic storms in the Beaufort and Chukchi Seas from observations and model results. (in preparation)

Non-refereed

Proshutinsky A. 2001. Arctic climate variability in the 20th century, p. 125–128. *In* Extended abstracts of the Second Wadati Conference, 7–9 March 2001, Tsukuba, Japan.

Proshutinsky, A. 2001. Arctic climate variability in the 20th Century, p. 28–29. *In* Woods Hole Oceanographic Institution 2001 Annual Report.

Proshutinsky, A. 2002. Investigation of sea level change in the Arctic Ocean, p. 52–53. *In* V. Rachold, J. Brown, and S. Solomon [eds.], Arctic Coastal Dynamics, Report of an International Workshop, Potsdam (Germany) 26–30 November 2001. Alfred Wegener Institute for Polar and Marine Research.

Proshutinsky, A.Y., M.A. Johnson, J.A. Maslanik and T.O. Proshutinsky. 2000. Beaufort and Chukchi Sea seasonal variability for two arctic climate states, p. 59–68. *In* University of Alaska Coastal Marine Institute Annual Report No. 7. OCS Study MMS 2000-070, University of Alaska Fairbanks and USDOI, MMS, Alaska OCS Region.

Proshutinsky, A.Y., M.A. Johnson, T.O. Proshutinsky and J.A. Maslanik. 2003. Beaufort and Chukchi Sea seasonal variability for two arctic climate states. Final Report. OCS Study MMS 2003-024,

University of Alaska Coastal Marine Institute, University of Alaska Fairbanks and USDOI, MMS, Alaska OCS Region, 197 p.

Proshutinsky, A.Y., J.A. Maslanik, M.A. Johnson and T.O. Proshutinsky. 2002. Beaufort and Chukchi Sea seasonal variability for two arctic climate states, p. 52–64. *In* University of Alaska Coastal Marine Institute Annual Report No. 8. OCS Study MMS 2002-001, University of Alaska Fairbanks and USDOI, MMS, Alaska OCS Region.

Proshutinsky, A., and T. Proshutinsky. 1999. Arctic atmosphere and ocean oscillations. Arctic Oscillation Section A42C-01, Supplement to EOS, Transactions, AGU 80:F212.

Presentations

(A.Y. Proshutinsky except where noted)

International

Arctic climate variability during 20th century. WOCE/CLIVAR Representativeness and Variability Workshop, 17–20 October 2000, Fukuoka, Japan.

Arctic atmosphere and ocean oscillations. NOAA/IPRC/CLIVAR Decadal Climate Variability Meeting, 8–12 January 2001, Honolulu, Hawaii.

Arctic climate variability during 20th century. The Second Wadati Conference on Global Change and the Polar Climate, 7–9 March 2001, Tsukuba, Japan. (organizer and chairman)

The Bering and Barents Seas data bases. Trajectories of Marine Ecosystem Workshop, 7–9 April 2001. Fairbanks, Alaska.

A.Y. Proshutinsky, R.H. Bourke and T. Proshutinsky. Variability of freshwater storage and thermohaline circulation of the Arctic Ocean. IAPSO Meeting, October 2001, Mar Del Plata, Argentina.

Beaufort Gyre as a flywheel of the Arctic Ocean Circulation: Seasonal, interannual and decadal time scales. 22 March 2002, McGill University.

Once again: Two circulation regimes of the Arctic Ocean circulation. Beaufort Gyre case study. Workshop on Measurement/Modelling of the Arctic Ocean Circulation, 17–20 June 2002, Lamont-Doherty Observatory.

National

Seasonal Variability of the Beaufort and Chukchi Seas in two arctic climate states. University of Alaska Coastal Marine Institute Annual Research Review, 9 March 2000, Fairbanks, Alaska.

Beaufort and Chukchi Seas seasonal variability for two arctic climate states. MMS seminar presentation, 1 June 2000, Anchorage, Alaska.

Seasonal Variability of the Beaufort and Chukchi Seas in two arctic climate states. MMS, February 2001, Anchorage, Alaska.

Seasonal Variability of the Beaufort and Chukchi Seas in two arctic climate states. University of Alaska Coastal Marine Institute Annual Research Review, 23 February 2001, Fairbanks, Alaska.

Arctic storms. Eighth MMS Information Transfer Meeting, 3–5 April 2001, Anchorage Alaska.

Beaufort and Chukchi Sea seasonal variability for two arctic climate states. Eighth MMS Information Transfer Meeting, 3–5 April 2001, Anchorage Alaska.

Investigation of the Beaufort Sea Seasonal Variability. NOAA Arctic Exploratory Expedition Planning Workshop, 25–26 July 2001, Washington, D.C.

Sea ice assimilation in the storm surge models: A case study for the Arctic seas. NASA Sea Ice Data Assimilation Workshop, 23–24 July 2002, Annapolis, Maryland.

References

Aagaard, K., and E.C. Carmack. 1989. The role of sea ice and other fresh water in the Arctic circulation. J. Geophys. Res. 94:14485–14498.

Barnes, P.W., D.M. Schell and E. Reimnitz [eds.]. 1984. The Alaskan Beaufort Sea: Ecosystems and Environment. Academic Press. 466 p.

Barnett, D.G. 1980. A long-range ice forecasting method for the north coast of Alaska, p. 402–409. *In* R. Pritchard [ed.], Sea Ice Processes and Models. University of Washington Press, Seattle.

Berg, L.S. 1947. Climate and Life. Gosgeografizdat, Moscow. 356 p. (in Russian)

Bourke, R.H., and R.P. Garrett. 1987. Sea ice thickness distribution in the Arctic Ocean. Cold Regions Sci. Technol. 13:259–280.

Brower, W.A., Jr., H.W. Searby, J.L. Wise, H.F. Diaz and A.S. Prechtel. 1977. Climatic Atlas of the Outer Continental Shelf Waters and Coastal Regions of Alaska. Arctic Environmental Information and Data Center Publ. B-770, University of Alaska Anchorage. 43 p.

Buinitskii, V.Kh. 1951. Formation and drift of ice cover in the Arctic Basin, p. 12–40. *In* Trudy Dreifuyushechei Ekspeditsii Glavsevmorputi ns l/p G. Sedov, 4, Moskva-Leningrad. (in Russian)

Buinitskii, V.Kh. 1958. Perennial flow of surface water and the general pattern of sea ice drift in the Arctic Basin, p. 17–31. *In* Nauchnye Doklady Vyshei Shkoly. Geologichecko-Geograficheskie Nauki, 1. (in Russian)

Campbell, W.J. 1965. Wind-driven circulation of ice and water in a Polar Ocean. J. Geophys. Res. 70:3279–3303.

Carmack, E.C. 1990. Large-scale physical oceanography of polar oceans, p. 171–222. *In* W.O. Smith, Jr. [ed.], Polar Oceanography, Part A, Physical Science. Academic Press, San Diego.

Carmack, E.C., R.W. Macdonald, R.G. Perkin, F.A. McLaughlin and R.J. Pearson. 1995. Evidence for warming of Atlantic Water in the Southern Canadian Basin of the Arctic Ocean: Results from the Larsen-93 Expedition. Geophys. Res. Lett. 22:1061–1064.

Cavalieri, D., P. Gloersen, C.L. Parkinson, J.C. Comiso and H.J. Zwally. 1997. Observed hemispheric asymmetry in global sea ice changes. Science 278:1104–1106.

Chapman, W.L., and J.E. Walsh. 1991. Long-range prediction of regional sea ice anomalies in the Arctic. Weather Forecast 6:271–288.

Coachman, L.K., and K. Aagaard. 1988. Transports through Bering Strait: Annual and interannual variability. J. Geophys. Res. 93:15535–15539.

Coachman, L.K., K. Aagaard and R.B. Tripp. 1975. Bering Strait: The Regional Physical Oceanography, University of Washington Press, Seattle. 172 p.

Comiso, J.C., and R. Kwok. 1996. Surface and radiative characteristics of the summer Arctic sea ice cover from multisensor satellite observations. J. Geophys. Res. 101:28397–28416.

Comiso, J.C., P. Wadhams, L.T. Pederson and R.A. Gersten. 2001. Seasonal and interannual variability of the Odden ice tongue and a study of environmental effects. J. Geophys. Res. 106:9093–9116.

Curry, J.A., W.B. Rossow, D. Randall and J.L. Schramm. 1996. Overview of Arctic cloud and radiation characteristics. J. Climate 9:1731–1764.

Davydov, I.V. 1989. Characteristics of development of atmospheric circulation in the northern Pacific Ocean and their role in determining long-term changes in the abundance of certain fishes, p. 181–194. *In* R.J. Beamish and G.A. McFarlane [eds.], Effects of Ocean Variability on Recruitment and Evaluation of Parameters Used in Stock Assessment Models. Can. Spec. Publ. Fish. Aquat. Sci. 108.

Delworth, T.L., S. Manabe and R.J. Stouffer. 1997. Multidecadal climate variability in the Greenland Sea and surrounding regions: A coupled model simulation. Geophys. Res. Lett. 24:257–260.

Doronin, N.Yu., and A.Yu. Proshutinsky. 1991. Mathematical modeling in studies of Arctic Ocean circulation, p. 310–316. *In* Proc. Int. Conf. on the Role of the Polar Regions in Global Change, vol. 1. University of Alaska Press, Fairbanks.

Drobot, S., and M. Anderson. 2001. Snow melt onset over Arctic sea ice from SMMR and SSM/I brightness temperatures. National Snow and Ice Data Center, Boulder, Colorado. Digital media.

Englebretson, R.E., and J.E. Walsh. 1989. Fram Strait ice flux calculations and associated Arctic sea ice conditions. Geojournal 18:61–67.

Environmental Working Group (EWG), Gore–Chernomyrdin Commission. 1997. Joint U.S.–Russian Atlas of the Arctic Ocean. National Snow and Ice Data Center, Boulder, Colorado. CD-ROM.

Felzenbaum, A.I. 1958. Theory of steady-state ice drift and calculation of multi-year averaged ice drift in the Central Arctic Basin. Problemy Severa 2:16–47. (in Russian)

Fleming, G.H., and A.J. Semtner, Jr. 1991. A numerical study of interannual ocean forcing on Arctic ice. J. Geophys. Res. 96:4589–4603.

Galt, J.A. 1973. A numerical investigation of Arctic Ocean dynamics. J. Phys. Oceanogr. 3:379–396.

Gazova, L.A., and V.I. Ponomarev. 1983. Simulation of the Atlantic Water propagation in the Arctic Basin. Meteorologia and Gidrologia 1:17–25. (in Russian)

Gloersen, P., W.J. Campbell, D.J. Cavalieri, J.C. Comiso, C.L. Parkinson and H.J. Zwally. 1992. Arctic and Antarctic Sea Ice, 1978–1987: Satellite Passive-Microwave Observations and Analysis. Scientific and Technical Information Program, NASA SP511, National Aeronautics and Space Administration, Washington, D.C. 290 p.

Gordienko, P.A. 1958. Arctic ice drift, p. 210–220. *In* Proc. Int. Conf. on the Study of Sea Ice. National Academy of Sciences and National Research Council, Washington, D.C.

Gordienko, P.A., and D.B. Karelin. 1945. Problems of the motion and distribution of ice in the Arctic Basin. Problemy Arktiki 3:25–38. (in Russian)

Gorshkov, S.G. 1980. Atlas of Oceans: Arctic Ocean. Ministry of Defense, USSR, Moscow. 199 p. (in Russian).

Guay, C.K., K.K. Falkner, R.D. Muench and R. Bayer. 1998. Ocean transport pathways for Eurasian arctic river discharge. 1998 Fall Meet. Suppl., EOS, Trans., AGU 79:F440.

Gudkovich, Z.M. 1961a. Relation of the ice drift in the Arctic Basin to ice conditions in Soviet Arctic seas. Trudy Okeanographicheskoi Komissii 11:14–21. (in Russian)

Gudkovich, Z.M. 1961b. On the nature of Pacific currents in the Bering Strait and the causes of seasonal variations in their intensity. Okeanologiya 1:608–612. (in Russian)

Gudkovich, Z.M. 1966. Anticyclonic circulation of ice and water in the Arctic Basin and drift of the station NP-8. Problemy Arktiki and Antarktiki 23:5–10.

Gudkovich, Z.M., and E.G. Nikiforov. 1965. Investigation of water circulation in the Arctic Basin using a model. Okeanologiya 5:75–83. (in Russian)

Häkkinen, S. 1990. Models and their applications to polar oceanography, p. 335–384. *In* W.O. Smith, Jr. [ed.], Polar Oceanography, Part A, Physical Science. Academic Press.

Häkkinen, S. 1993. An arctic source for the Great Salinity Anomaly: A simulation of the Arctic ice–ocean system for 1955–1975. J. Geophys. Res. 98:16397–16410.

Häkkinen, S. 1995. Simulated interannual variability of the Greenland Sea deep water formation and its connection to surface forcing. J. Geophys. Res. 100:4761–4770.

Häkkinen, S., and G.L. Mellor. 1992. Modeling the seasonal variability of a coupled Arctic ice–ocean system. J. Geophys. Res. 97:20285–20304.

Hansen, D.V., and H.F. Bezdek. 1996. On the nature of decadal anomalies in North Atlantic sea surface temperature. J. Geophys. Res. 101:8749–8758.

Hart, J.E. 1975. The flow of two layer fluid over topography in a Polar Ocean. J. Phys. Oceanogr. 5:678–685.

Hibler, W.D. III. 1989. Arctic ice–ocean dynamics, p. 47–91. *In* Y. Herman [ed.], The Arctic Seas: Climatology, Oceanography, Geology, and Biology. VanNostrand Reinhold, New York.

Hibler, W.D. III, and K. Bryan. 1987. A diagnostic ice–ocean model. J. Phys. Oceanogr. 17:987–1015.

Hilmer, M., and P. Lemke. 2000. On the decrease of Arctic sea ice volume. Geophys. Res. Lett. 27:3751–3754.

Holland, D.M., L.A. Mysak and J.M. Oberhuber. 1996. Simulation of the mixed-layer circulation in the Arctic Ocean. J. Geophys. Res. 101:1111–1128.

Holloway, G., and T. Sou. 2001. Is Arctic sea ice rapidly thinning? Ice and Climate News 1:2. http://acsys.npolar.no/news/2001/No1_p2.htm

Hudak, D.R., and J.M.C. Young. 2002. Storm climatology of the Southern Beaufort Sea. Atmosphere–Ocean 40:145–158.

Johnson, M.A., A.Y. Proshutinsky and I.V. Polyakov. 1999. Atmospheric patterns forcing two regimes of arctic circulation: A return to anticyclonic conditions? Geophys. Res. Lett. 26:1621–1624.

Karklin, V.P. 1977. State and future of using of geliogeophysical factors for ice forecasts. Problemy Arctiki i Antarktiki 50:45–48. (in Russian)

Kowalik, Z. 1981. A study of the M2 tide in the ice-covered Arctic Ocean, Model. Ident. Control 2:201–223.

Kowalik, Z., and T.S. Murty. 1993. Numerical Modeling of Ocean Dynamics. World Scientific, Singapore. 481 p.

Kowalik, Z., and A.Yu. Proshutinsky. 1994. The Arctic Ocean tides, p. 137–158. *In* O. Johannessen, R.D. Muench, and J.E. Overland [eds.], The Polar Oceans and Their Role in Shaping the Global Environment: The Nansen Centennial Volume, Geophys. Monogr. Ser., vol. 85. AGU, Washington, D.C.

Kutzbach, J.E. 1970. Large-scale features of monthly mean Northern Hemisphere anomaly maps of sea level pressure. Mon. Weather Rev. 98:708–716.

Lemke, P. [ed.]. 1997. World Climate Research Programme, Arctic Climate System Study (ACSYS). Report of the Second ACSYS Sea-Ice/Ocean Modelling Workshop, Bremerhaven, Germany. WCRP Informal Report No. 1. 36 p.

Levitus, S. 1982. Climatological Atlas of the World Ocean. NOAA Professional Paper 13, U.S. Department of Commerce, Washington, D.C. 173 p.

Lewis, E.L., E.P. Jones, P. Lemke, T.D. Prowse and P. Wadhams [eds.]. 2000. The freshwater budget of the Arctic Ocean. Proceedings of the NATO Advanced Research Workshop, Tallinn, Estonia, 27 April–1 May 1998. NATO Science Series IV, vol. 70, Kluwer Academic Publishers. 623 p.

Lorenz, E.N. 1951. Seasonal and irregular variations of the northern hemisphere sea level pressure profile. J. Meteorol. 8:52–59.

Martin, S., and E.A. Munoz. 1997. Properties of the Arctic 2-meter air temperature field for 1979 to the present derived from a new gridded dataset. J. Climate 10:1428–1440.

Maslanik, J.A., M.C. Serreze and R.G. Barry. 1996. Recent decreases in arctic summer ice cover and linkages to atmospheric circulation anomalies. Geophys. Res. Lett. 23:1677–1680.

Maykut, G.A., and M.G. McPhee. 1995. Solar heating of the Arctic mixed layer. J. Geophys. Res. 100:24691–24703.

Maykut, G.A., and N. Untersteiner. 1971. Some results from a time-dependent thermodynamic model of sea ice. J. Geophys. Res. 76:1550–1575.

McLaughlin, F., E. Carmack, R.W. Macdonald, A.J. Weaver and J. Smith. 2002. The Canada Basin 1989–1995: Upstream events and far-field effects of the Barents Sea. J. Geophys. Res. 107(C7), 10.1029/2001JC000904.

McPhee, M.G. 1986. Analysis and prediction of short-term ice drift, p. 385–393. *In* Proc. Fifth Int. Offshore Mechanics and Arctic Engineering Symposium, vol. 4, ASME.

McPhee, M.G. 1999. The SHEBA upper ocean physics program, p. 368–371. *In* Preprints, Fifth Conf. on Polar Meteorology and Oceanography, 10–15 January 1999, Dallas, Texas. American Meteorological Society.

McPhee, M.G., T.P. Stanton, J.H. Morison and D.G. Martinson. 1998. Freshening of the upper ocean in the Arctic: Is perennial sea ice disappearing? Geophys. Res. Lett. 25:1729–1732.

Melnikov, I.A. 2000. The Arctic sea ice ecosystem and global warming, p. 72–82. *In* H.P. Huntington [ed.], Impacts of Changes in Sea Ice and Other Environmental Parameters in the Arctic: Report of the Marine Mammal Commission Workshop, Girdwood, Alaska, 15–17 February 2000. Marine Mammal Commission, Bethesda, Maryland.

Mysak, L.A. 1995. Interdecadal variability in the Arctic and northern North Atlantic: Observations and models, p. 49. *In* The Abstracts, IAPSO, XX1 General Assembly, Honolulu.

Mysak, L.A., D.K. Manak and R.F. Marsden. 1990. Sea ice anomalies observed in the Greenland and Labrador seas during 1901–1984 and their relation to an interdecadal Arctic climate cycle. Climate Dynamics 5:111–133.

Mysak, A.M., and S.A. Venegas. 1998. Decadal climate oscillations in the Arctic: A new feedback loop for atmosphere–ice–ocean interactions. Geophys. Res. Lett. 25:3607–3610.

Nansen, F. [ed.]. 1902. The Oceanography of the North Polar Basin. The Norwegian North Polar Expedition, 1893–1896, Scientific Results, vol. 3., Longmans, Green and Co. 427 p.

National Center for Atmospheric Research (NCAR). 1990. National Meteorological Center Grid Point Data Set: Version II. General Information and User's Guide. CD-ROM. NCAR, Boulder, Colorado. 9 p.

National Snow and Ice Data Center (NSIDC). 1989. DMSP SSM/I brightness, temperatures, and sea ice concentrations grids for the Polar Regions, 1987. Digital data available from nsidc@kryos.colorado.edu. NSIDC Distributed Active Archive Center, University of Colorado, Boulder.

Niebauer, H.J. 1988. Effects of El Niño–Southern Oscillation and North Pacific weather patterns on interannual variability in the subarctic Bering Sea. J. Geophys. Res. 93:5051–5068.

Nikiforov, Ye.G., and A.O. Shpaikher. 1980. Features of the formation of hydrological regime large-scale variations in the Arctic Ocean. Gydrometeoizdat, Leningrad. 269 p. (in Russian)

Oberhuber, J.M. 1993. Simulation of the Atlantic circulation with a coupled sea ice–mixed layer–isopycnal general circulation model. Part II: Model experiment. J. Phys. Oceanogr. 23:830–845.

Osterkamp, T.E., T. Zhang and V.E. Romanovsky. 1994. Evidence for a cyclic variation of permafrost temperatures in northern Alaska. Permafrost Periglac. 5:137–144.

Parkinson, C.L. 1978. A numerical simulation of the annual cycle of sea ice in the Arctic and Antarctic. NCAR Cooperative Thesis No. 46, The Ohio State University and National Center for Atmospheric Research, NTIS #PB 279789/AS. 191 p.

Parkinson, C.L., D. Cavalieri, P. Gloersen, J.C. Comiso and H.J. Zwally. 1999. Arctic sea ice extents, areas, and trends, 1978–1996. J. Geophys. Res. 104:20837–20856.

Pavlov, V.K., L.A. Timokhov, G.A. Baskakov, M.Yu. Kulakov, V.K. Kurazhov, P.V. Pavlov, S.V. Pivovarov and V.V. Stanovoy. 1994. Hydrometeorological regime of the Kara, Laptev and East-Siberian seas. Part

1 of the research subcontract “Processes of transfer and transformation of contaminants inflowing by continental discharge into the Kara, Laptev and East Siberian seas”. Arctic and Antarctic Research Institute, St. Petersburg, Russia. 179 p.

Piacsek, S., R. Allard and A. Warn-Varnas. 1991. Studies of the arctic ice cover and upper ocean with a coupled ice–ocean model. J. Geophys. Res. 96:4631–4650.

Polyakov, I.V., I.Yu. Kulakov, S.A. Kolesov, N.Eu. Dmitriev, R.S. Pritchard, D. Driver and A.K. Naumov. 1998. Coupled sea ice–ocean model of the Arctic Ocean. J. Offshore Mech. Arctic Eng. 120:77–84.

Polyakov, I., A.Y. Proshutinsky and M.A. Johnson. 1999. The seasonal cycles in two regimes of Arctic climate. J. Geophys. Res. 104:25761–25788.

Polyakov, I.V., and L.A. Timokhov. 1994. Mean fields of temperature and salinity of the Arctic Ocean. Russian Meteorol. Hydrol. 7:33–38.

Polyakov, I.V., and L.A. Timokhov. 1995. Thermohaline circulation of the Arctic Ocean. Doklady Akademii Nauk, Okeanologia 342:254–258. (in Russian)

Ponomarev, V.I. 1977. Calculations of large-scale water circulation in the Arctic Basin using diagnostic models. Problemy Arctiki i Antarktiki 51:65–75. (in Russian)

Ponomarev, V.I. and A.I. Felzenbaum. 1975. 2-D non-stationary model of wind driven circulation in the Arctic Basin. Okealologia 15:17–23. (in Russian)

Proshutinsky, A.Y. 1978. On the problem of numerical simulation of storm surges in the shelf zone of the Arctic seas, p. 72–79. *In* Soviet Meteorology and Hydrology, vol. 1. (Transl. from Russian by Allerton Press, Inc.)

Proshutinsky, A.Y. 1986. On the problem of calculating the storm surge fluctuations of sea level and water circulation in the Chukchi Sea, p. 54–61. *In* Soviet Meteorology and Hydrology, vol. 1. (Transl. from Russian by Allerton Press, Inc.)

Proshutinsky, A.Y. 1988. Modeling seasonal fluctuations of the level of the Arctic Ocean, p. 57–65. *In* Soviet Meteorology and Hydrology, vol. 2. (Transl. from Russian by Allerton Press, Inc.)

Proshutinsky, A.Y. 1993. The Arctic Ocean level oscillations, Gydrometeoizdat. 216 p. (in Russian)

Proshutinsky, A.Y., and M.A. Johnson. 1997. Two circulation regimes of the wind-driven Arctic Ocean. J. Geophys. Res. 102:12493–12514.

Proshutinsky, A., I.V. Polyakov and M. Johnson. 1999. Climate states and variability of Arctic ice and water dynamics during 1946–1997. Polar Res. 18:135–142.

Reed, J.C., and J.E. Sater [eds.]. 1974. The Coast and Shelf of the Beaufort Sea, Proceedings of a Symposium on Beaufort Sea Coast and Shelf Research. Arctic Institute of North America. Arlington, Virginia.

Riedlinger, S. H., and R. H. Preller. 1991. The development of a coupled ice–ocean model for forecasting ice conditions in the Arctic. J. Geophys. Res. 96:16955–16977.

Roach, A.T., K. Aagaard, C.H. Pease, S.A. Salo, T. Weingartner, V. Pavlov and M. Kulakov. 1995. Direct measurements of transport and water properties through the Bering Strait. J. Geophys. Res. 100:18443–18457.

Rogers, J.C. 1978. Meteorological factors affecting interannual variability of summertime ice extent in the Beaufort Sea. Mon. Weather Rev. 196:890–897.

Romanov, I.P. 1992. The Ice Cover of the Arctic Basin. Arctic and Antarctic Research Institute, St. Petersburg, Russia. 211 p. (in Russian)

Rothrock, D.A. 1975. Mechanical behavior of pack ice. Ann. Rev. Earth Pl. Sci. 3:317–342.

Rothrock, D.A., Y. Yu and G.A. Maykut. 1999. Thinning of the Arctic sea ice cover. Geophys. Res. Lett. 26:3469–3472.

Royer, T.C. 1996. Interdecadal hydrographic variability in the Gulf of Alaska, 1970–1995. 1996 Fall Meet. Suppl., EOS, Trans., AGU 77:F368.

Rudels, B., E.P. Jones, L.G. Anderson, and G. Kattner. 1994. On the intermediate depth waters of the Arctic ocean, p. 33–46. *In* O. Johannessen, R.D. Muench, and J.E. Overland [eds.], The Polar Oceans and Their Role in Shaping the Global Environment: The Nansen Centennial Volume, Geophys. Monogr. Ser., vol., 85. AGU, Washington, D.C.

Semtner, A.J., Jr. 1976. Numerical simulation of the Arctic Ocean circulation. J. Phys. Oceanogr. 6:409–429.

Semtner, A.J., Jr. 1987. A numerical study of sea-ice and ocean circulation in the Arctic. J. Phys. Oceanogr. 17:1077–1099.

Serreze, M.C., R.G. Barry and A.S. McLaren. 1989. Seasonal variations in sea ice motion and effects on sea ice concentration in the Canada Basin. J. Geophys. Res. 94:10955–10970.

Serreze, M.C., F. Carse, R.G. Barry and J.C. Rogers. 1997. Icelandic Low cyclone activity: Climatological features, linkages with the NAO, and relationships with recent changes in the Northern Hemisphere circulation. J. Climate 10:453–464.

Serreze, M.C., J.A. Maslanik, R.G. Barry and T.L. Demaria. 1992. Winter atmospheric circulation in the Arctic Basin and possible relationships to the Great Salinity Anomaly in the northern North Atlantic. Geophys. Res. Lett. 19:293–296.

Serreze, M.C., J.A. Maslanik, R. Preller and R.G. Barry. 1990. Sea ice concentration in the Canada Basin during 1988: Comparisons with other years and evidence of multiple forcing mechanisms. J. Geophys. Res. 95:22253–22267.

Serreze, M.C., J.A. Maslanik, T.A. Scambos, F. Fetterer, J. Stroeve, K. Knowles, C. Fowler, S. Drobot, R.G. Barry and T.M. Haran. 2003. A record minimum arctic sea ice extent and area in 2002. Geophys. Res. Lett. 30(3), 1110, doi:10.1029/2002GL016406.

Shirshov, P.P. 1944. Scientific results of the drift of the Severnyi Polyus station. Report delivered at the General Assembly of the USSR Academy of Sciences on 14–17 February 1944, Moscow, p. 110–140. *In* Izdatel'stvo Akademii Nauk SSSR. (in Russian)

Shokalskii, Yu.M. 1940. The G. Sedov, its drift, and the geography of the Arctic Basin. Problemy Arktiki, 2:34–38. (in Russian)

Shuleikin, V.V. 1941. Analysis of the drift of Severnyi Polyus station, DAN SSSR 31:886–892. (in Russian)

Smith, D.M. 1998. Recent increase in the length of the melt season of perennial arctic sea ice. Geophys. Res. Lett. 25:655–658.

Steele, M., and T. Boyd. 1998. Retreat of the cold halocline layer in the Arctic Ocean. J. Geophys. Res. 103:10419–10435.

Steele, M., D. Thomas, D. Rothrock and S. Martin. 1996. A simple model study of the Arctic Ocean freshwater balance, 1979–1985. J. Geophys. Res. 101:20833–20848.

Steele, M., J. Zhang, D. Rothrock and H. Stern. 1997. The force balance of sea ice in a numerical model of the Arctic Ocean. J. Geophys. Res. 102:21061–21079.

Swift, J.H., E.P. Jones, K. Aagaard, E.C. Carmack, M. Hingston, R.W. Macdonald, F.A. McLaughlin and R.G. Perkin. 1997. Waters of the Makarov and Canada basins. Deep-Sea Res. 44:1503–1529.

Thompson, D.W.J., and M. Wallace. 1998. The Arctic Oscillation signature in the wintertime geopotential height and temperature fields. Geophys. Res. Lett. 25:1297–1300.

Thorndike, A.S., and R. Colony. 1982. Sea ice motion in response to geostrophic winds. J. Geophys. Res. 87:5845–5852.

Thorndike, A.S., R. Colony and E.A. Munoz. 1982. Arctic Ocean Buoy Program. Data report, 1 January 1982–31 December 1982. Polar Science Center, University of Washington, Seattle. 132 p.

Tremblay, L.-B., and L.A. Mysak. 1998. On the origin and evolution of sea-ice anomalies in the Beaufort–Chukchi Sea. Climate Dynamics 14:451–460.

Trenberth, K.E. 1992. Global analysis from ECMWF and atlas of 1000 to 10 mb circulation statistics, NCAR Tech. note, NCAR/TN-373+STR, National Center for Atmospheric Research, Boulder, Colorado, 191 p.

Trenberth, K.E., and D.A. Paolino. 1981. Characteristic patterns of variability of sea level pressure in the Northern Hemisphere. Mon. Weather Rev. 109:1169–1189.

Treshnikov, A.F. 1959. Surface water in the Arctic Basin. Problemy Arktiki 7:5–14. (in Russian)

Treshnikov, A.F. [ed.]. 1985. Atlas of the Arctic. Main Admin. Geod. and Cartogr., Moscow. 204 p. (in Russian).

Treshnikov, A.F., and G.I. Baranov. 1972. Water circulation in the Arctic Basin. Gidrometeoizdat, Leningrad. 145 p. (Transl. from Russian, Israel Program for Scientific Translations, Jerusalem 1973).

Vinje, T., and O. Finnekåsa. 1986. The Ice Transport Through the Fram Strait, Rep. no. 186. Norsk Polarinstitutt, Oslo. 39 p.

Vitels, L.A. 1948. Multi-year changes of the pressure-circulation regime and their effect on climate fluctuations, p. 51–109. *In* Proc. Main Geophysical Observatory, vol. 8. Gidrometeoizdat, Leningrad. (in Russian)

Vize, V.Yu. 1944. The foundations of long-term sea ice predictions for the arctic seas. Glavsevmorput, Moscow. 274 p. (in Russian)

Wallace, J.M., and D.S. Gutzler. 1981. Teleconnections in the geopotential height field during the Northern Hemisphere winter. Mon. Weather Rev. 109:784–812.

Walsh, J.E., and W.L. Chapman. 1990. Arctic contribution to upper ocean variability in the North Atlantic. J. Climate 3:1462–1473.

Walsh, J.E., and W.L. Chapman. 1998. Arctic cloud-radiation–temperature associations in observational data and atmospheric reanalyses, J. Climate 11:3030–3045.

Walsh, J.E., W.D. Hibler III and B. Ross. 1985. Numerical simulation of Northern Hemisphere sea ice variability, 1951–1980. J. Geophys. Res. 90:4847–4865.

Walsh, J.E., and C.M. Johnson. 1979. An analysis of Arctic sea ice fluctuations, 1953–1977. J. Phys. Oceanogr. 9:580–591.

Weingartner, T.J., D.J. Cavalieri, K. Aagaard and Y. Sasaki. 1998. Circulation, dense water formation, and outflow on the northeast Chukchi Sea shelf. J. Geophys. Res. 103:7647–7661.

Weingartner, T.J., and T. Proshutinsky. 1998. Modeling the Circulation on the Chukchi Sea Shelf. Final Report. OCS Study MMS 98-0017, University of Alaska Coastal Marine Institute, University of Alaska Fairbanks and USDOI, MMS, Alaska OCS Region, 75 p.

Worthington, L.V. 1953. Oceanographic results of Project Skijump I and Skijump II in the Polar Sea, 1951–1952. Trans. Amer. Geophys. Un. 34:543–551.

Zhang, J., A.D. Rothrock and M. Steele. 1998. Warming of the Arctic Ocean by a strengthened Atlantic inflow: Model results. Geophys. Res. Lett. 25:1745–1748.

Zubov, N.N., and M.M. Somov. 1940. Ice drift in the northern Arctic Basin. Problemy Arktiki 2:51–68. (in Russian)

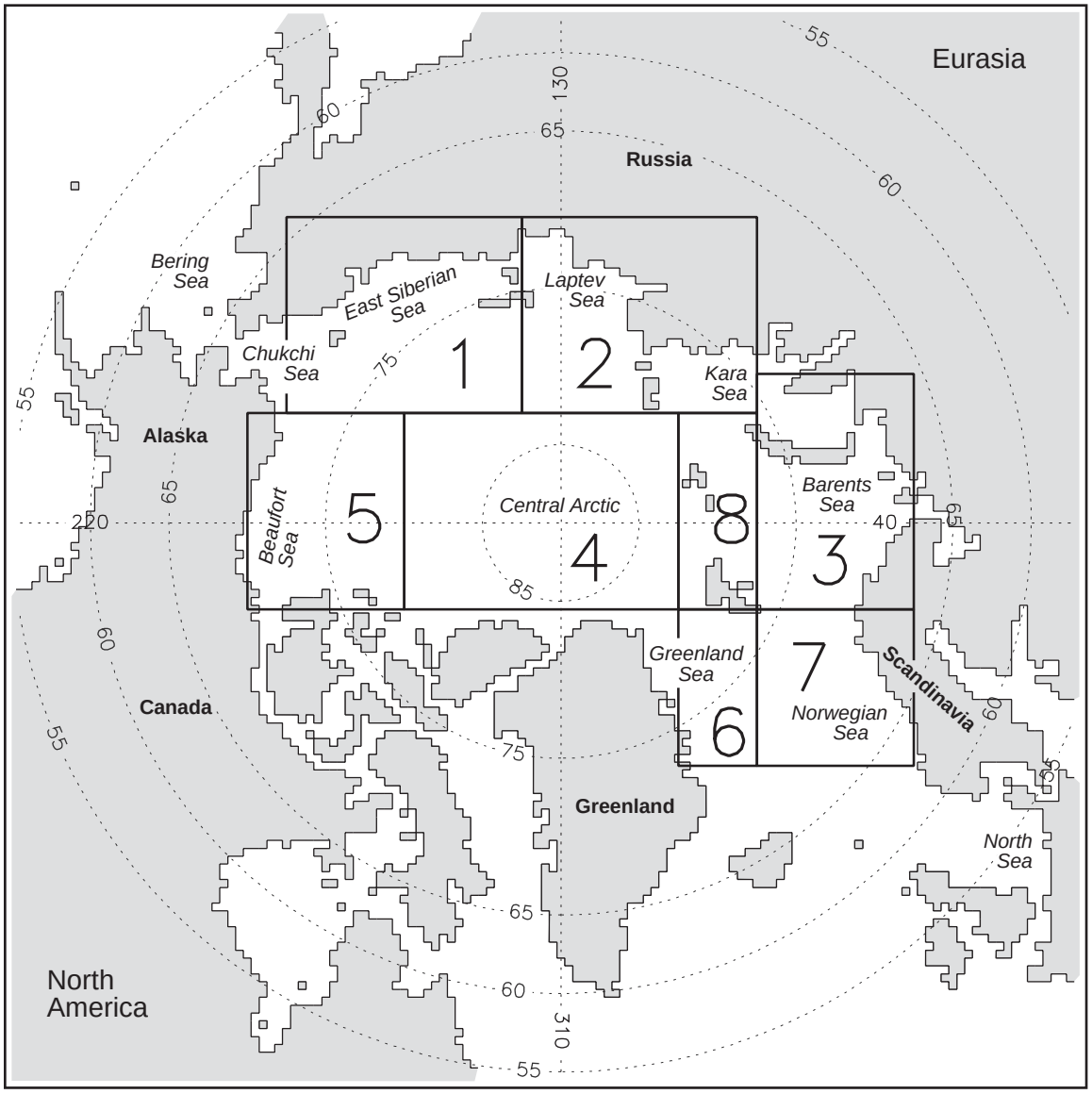

Figure 1. Arctic Ocean model domain. Labeled boxes denote regions for observational data analysis. 1 – Pacific region; 2 – Siberian region; 3 – Western region; 4 – Central Arctic region; 5 – Beaufort Sea region; 6 – Greenland Sea region; 7 – Norwegian Sea region; 8 – Franz Josef Land region.

Figure 2a. Summer (June–October) surface thermohaline circulation in the Arctic Ocean from the 3-D diagnostic model of Polyakov and Timokhov [1995]. The 3-D temperature and salinity fields were obtained from observations and were the only force generating motions.

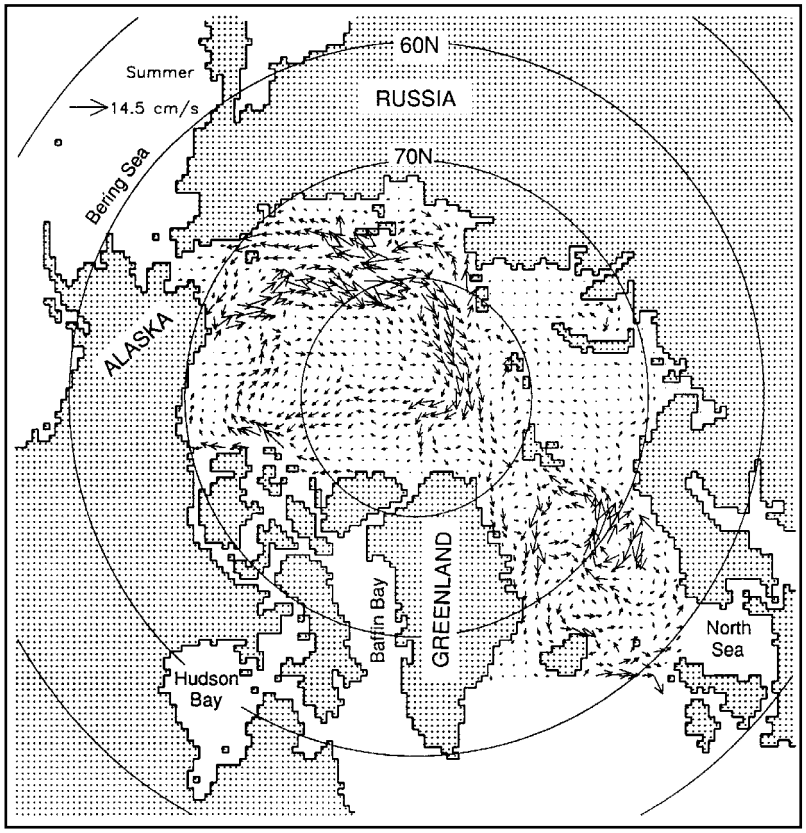

Figure 2b. Winter (November–May) surface thermohaline circulation in the Arctic Ocean from the 3-D diagnostic model of Polyakov and Timokhov [1995]. The 3-D temperature and salinity fields were obtained from observations and were the only force generating motions.

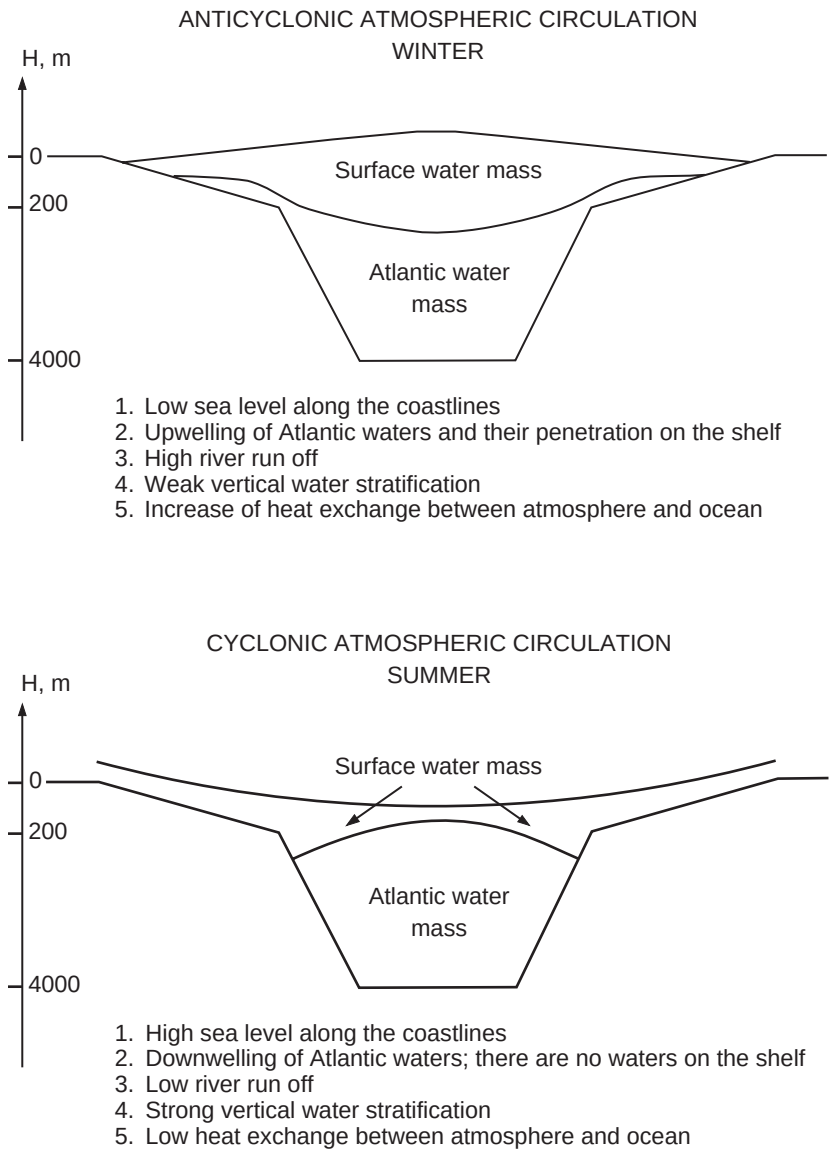

Figure 3. Schematic water mass structure and prevailing processes during winter and summer in the Arctic Basin. Pacific and deep waters are not shown.

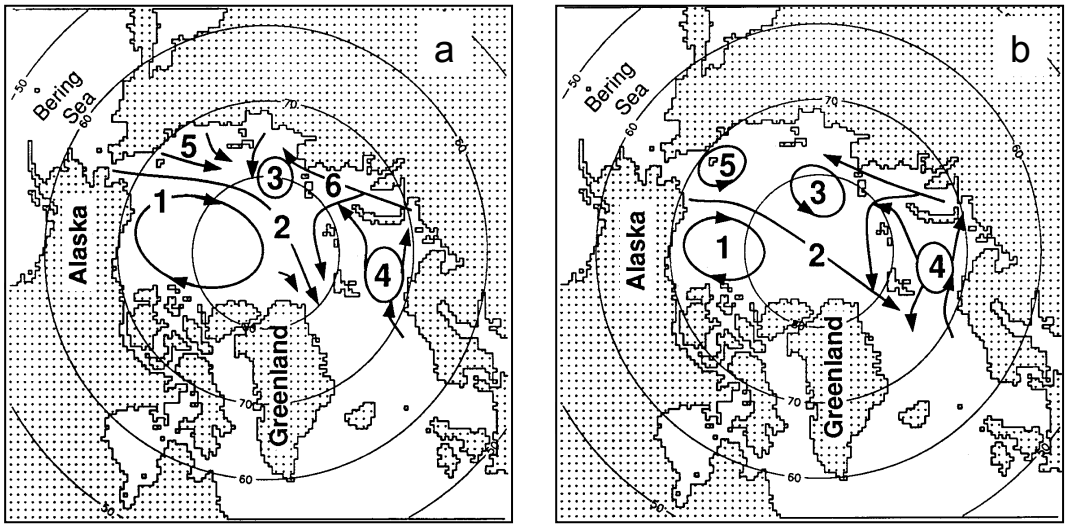

Figure 4. Regimes of surface currents and ice drift in the Arctic Ocean redrawn from Gudkovich [1961a]. a) Type A circulation, corresponding to prevailing Arctic High atmospheric pressure; b) Type B circulation, corresponding to prevailing Icelandic Low atmospheric pressure. Numbered features include: 1–Beaufort Gyre, 2–Transarctic Drift Current, 3–Laptev Sea cyclonic circulation, 4–Barents Sea cyclonic circulation, 5–circulation in the East Siberian Sea, and 6–Kara Sea coastal flow.

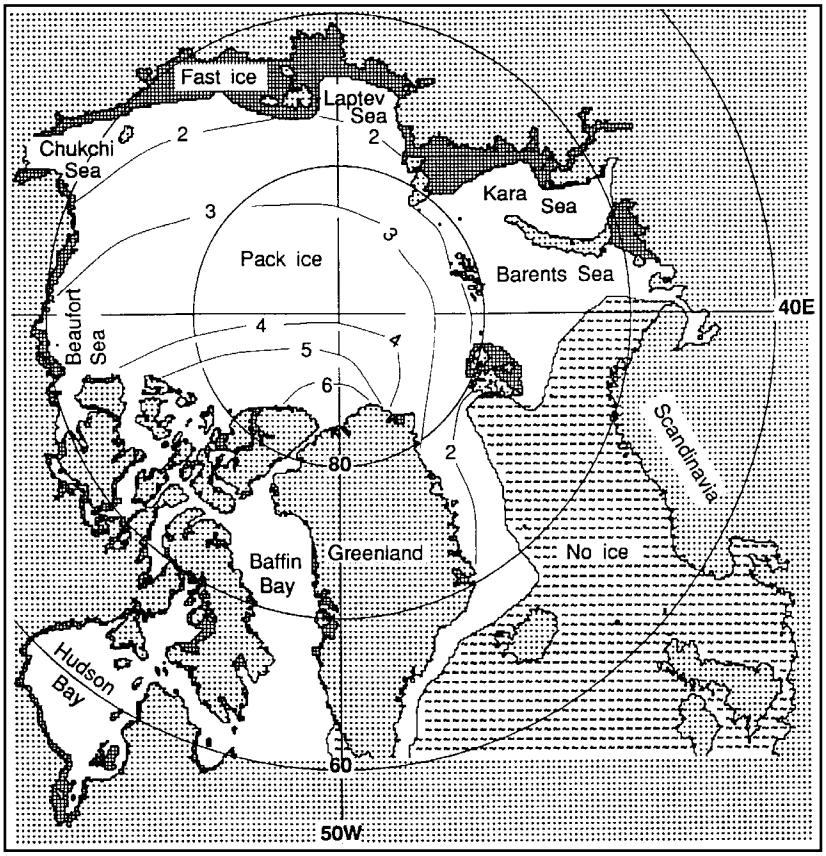

Figure 5. Contours of ice thickness in meters in the Arctic for average winter conditions. The model ice thickness is explicitly prescribed and does not change in the simulations presented here. Data are combined from Bourke and Garret [1980], Hibler [1989], and Romanov [1993].

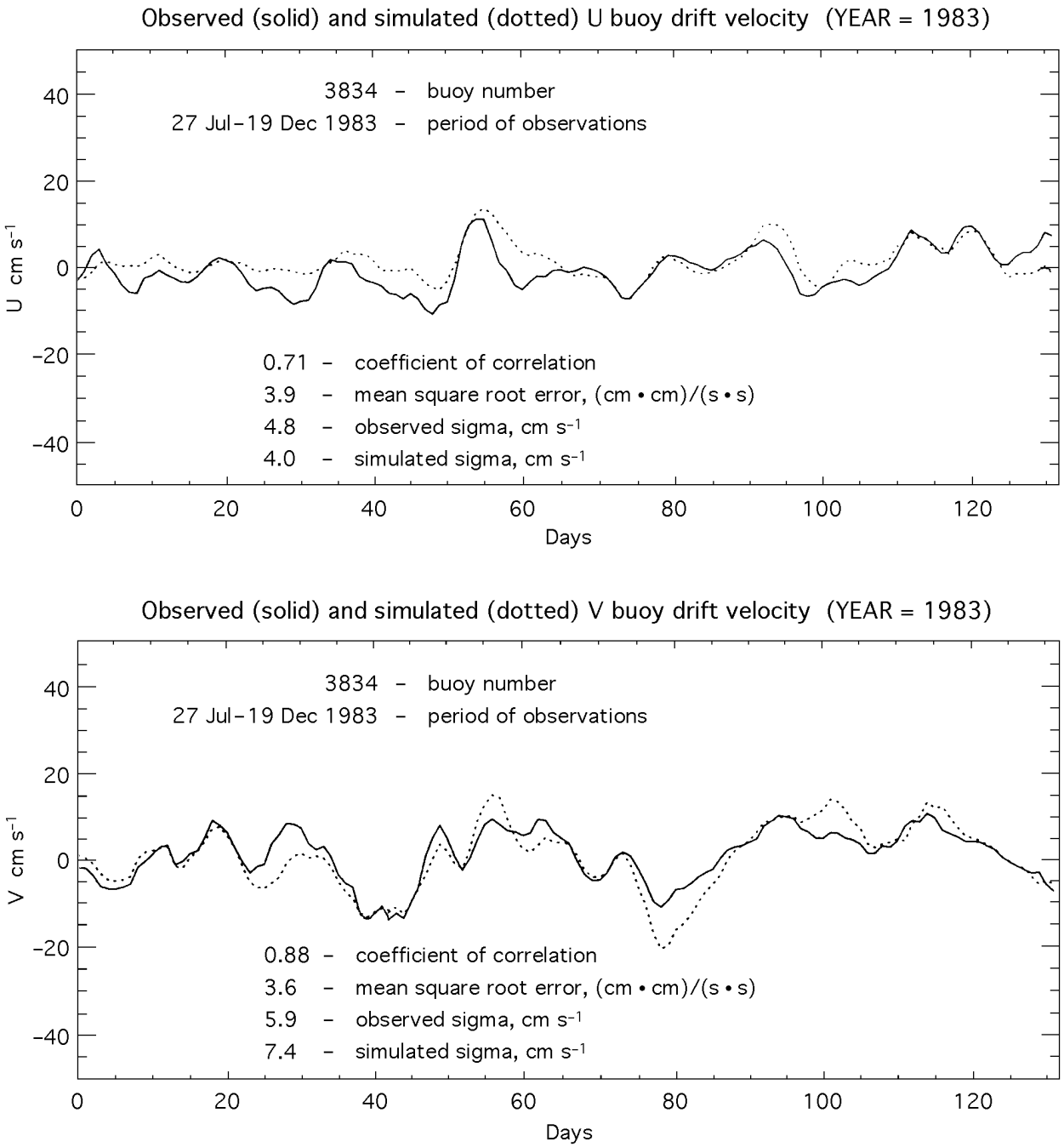

Figure 6. U and V velocities from observed buoy drift (solid lines) and computed by the model (dotted lines) for 1983 in the central Arctic Basin.

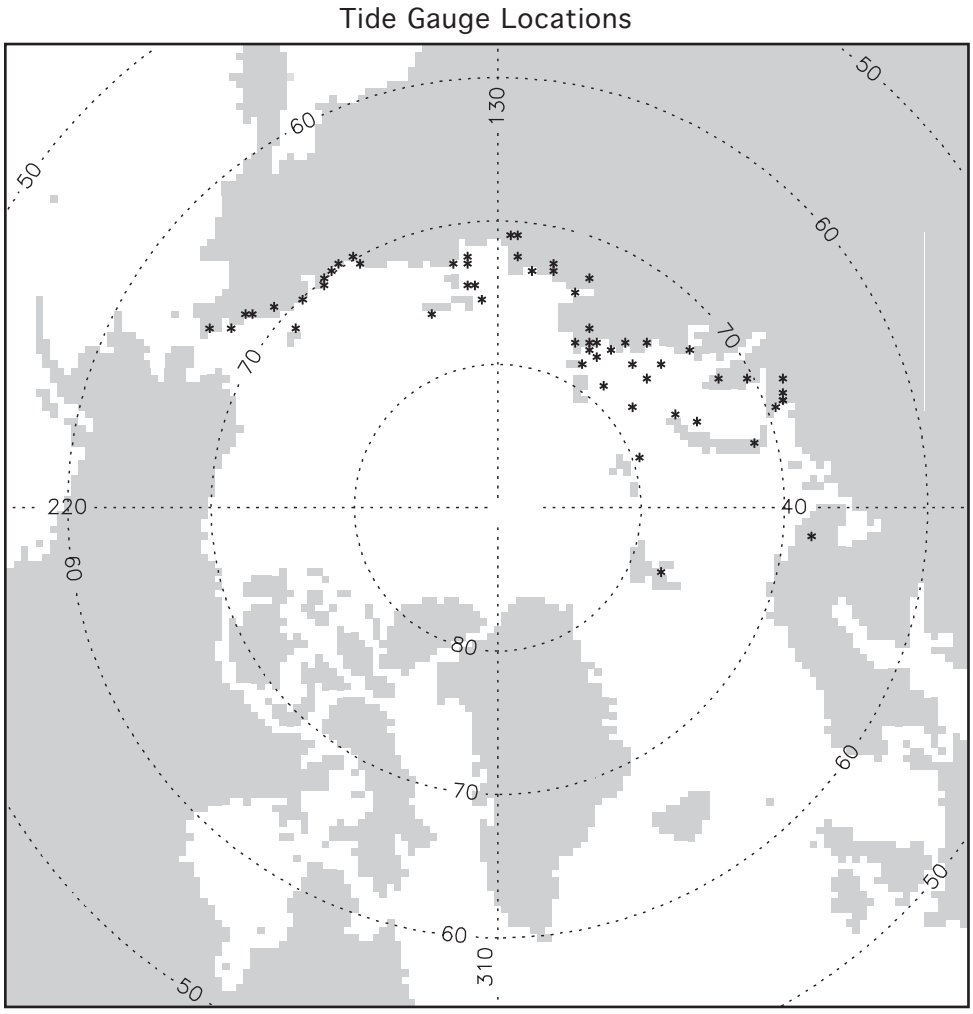

Figure 7. Tide gauge locations (stars) where observed and simulated sea level data were analyzed.

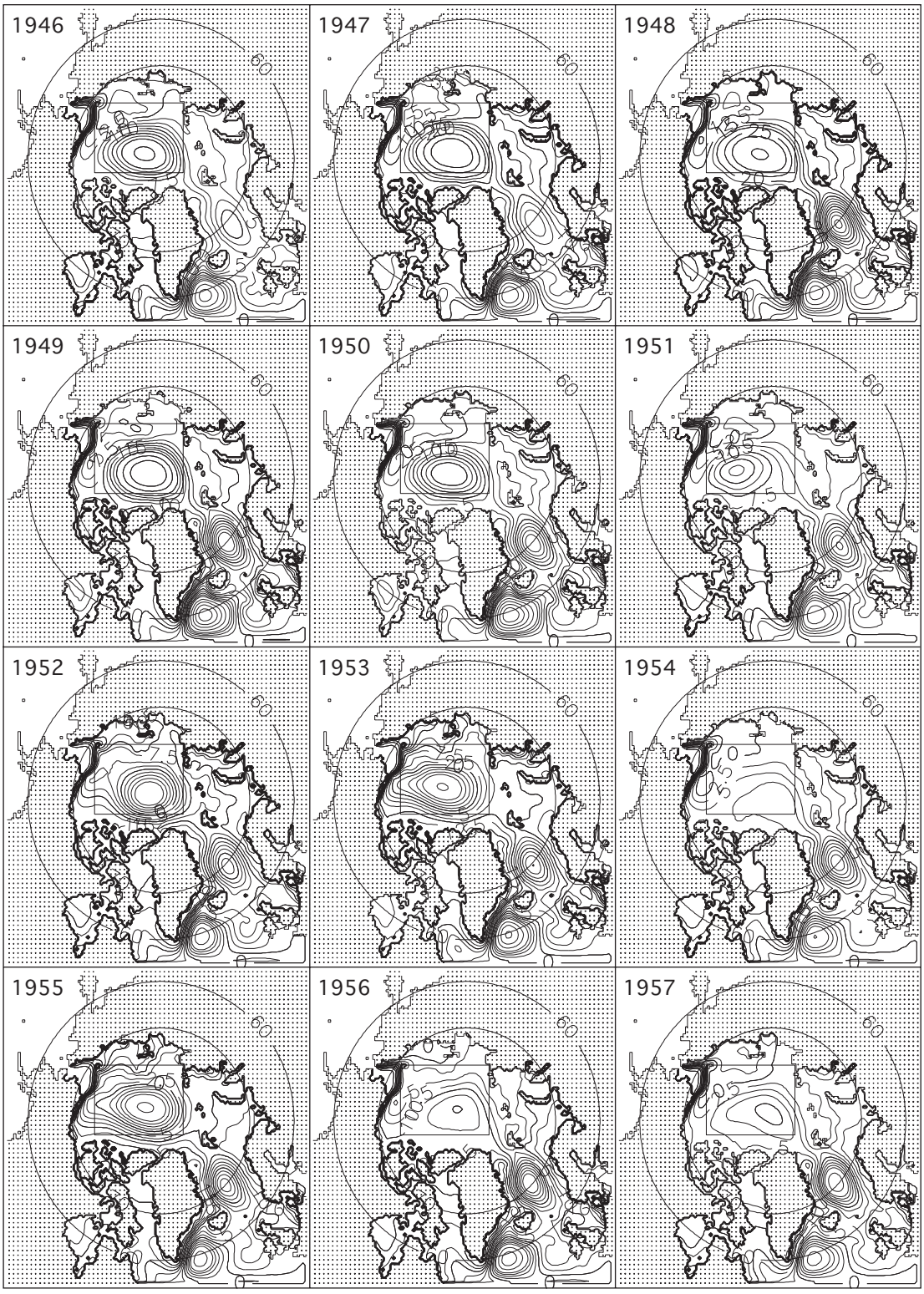

Figure 8a. Mean annual simulated surface heights (cm) for 1946–1957. Boxes show the central Arctic Ocean, where maximum or minimum sea level were located and sea level gradients were calculated.

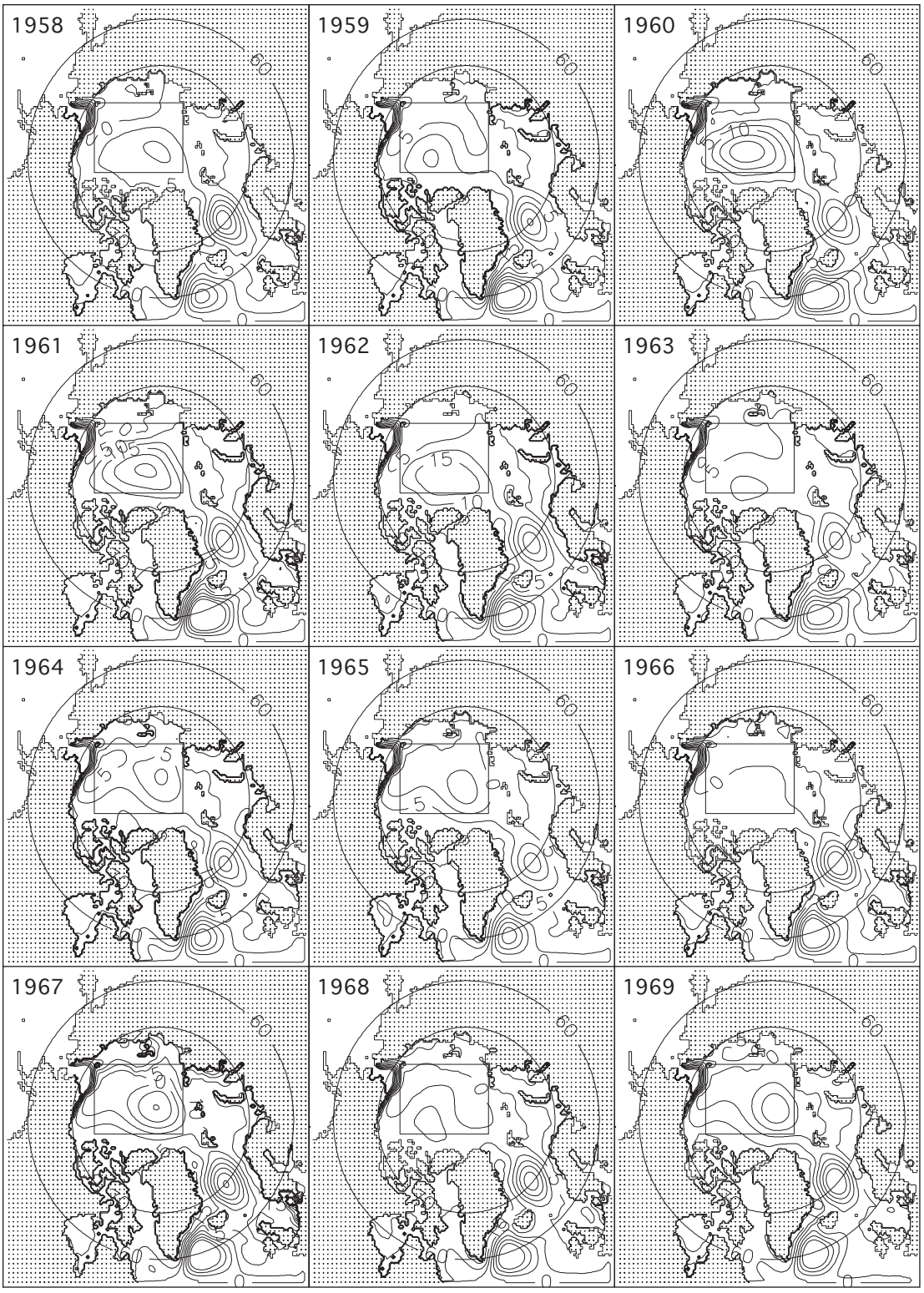

Figure 8b. Mean annual simulated surface heights (cm) for 1958–1969. Boxes show the central Arctic Ocean, where maximum or minimum sea level were located and sea level gradients were calculated.

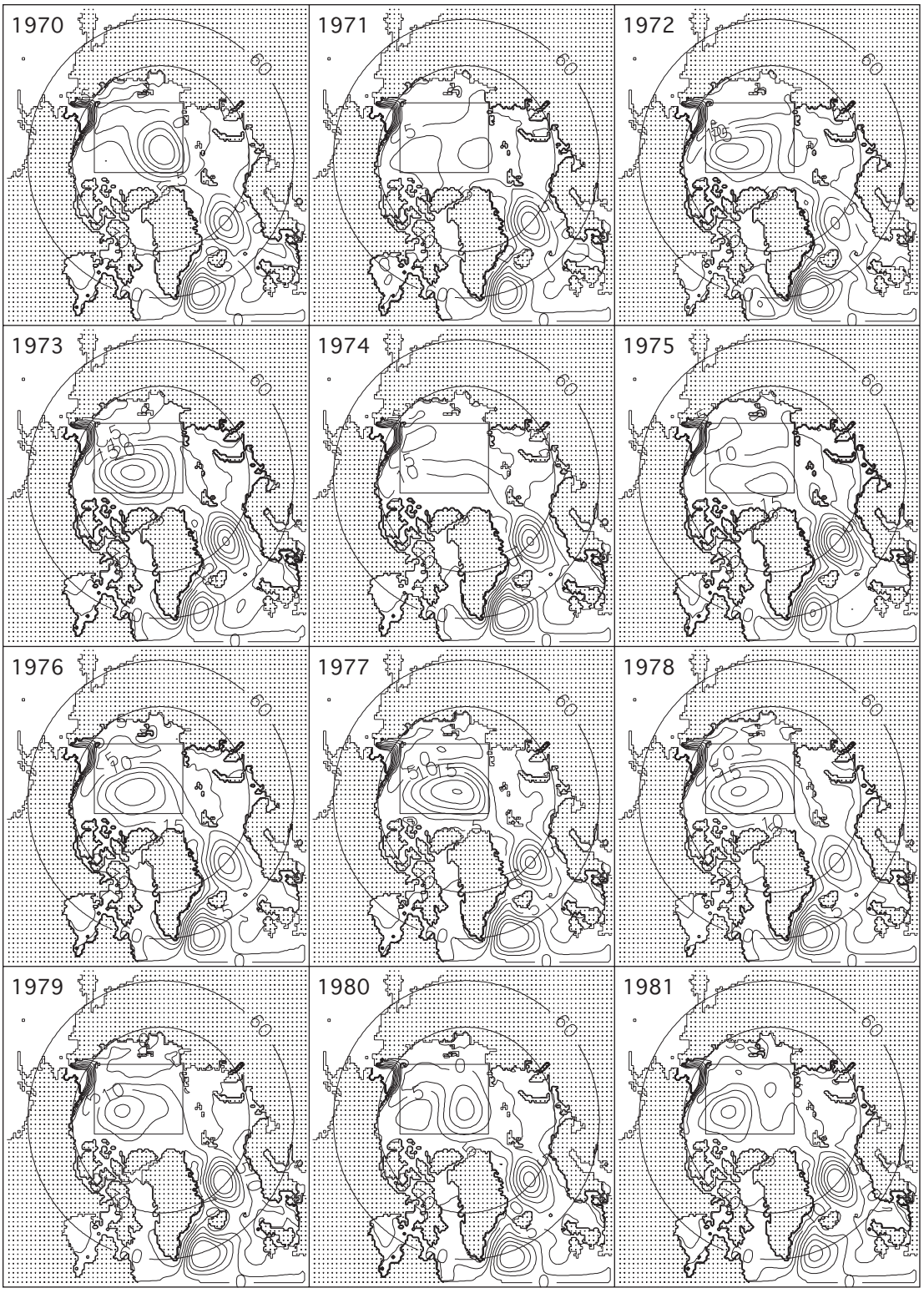

Figure 8c. Mean annual simulated surface heights (cm) for 1970–1981. Boxes show the central Arctic Ocean, where maximum or minimum sea level were located and sea level gradients were calculated.

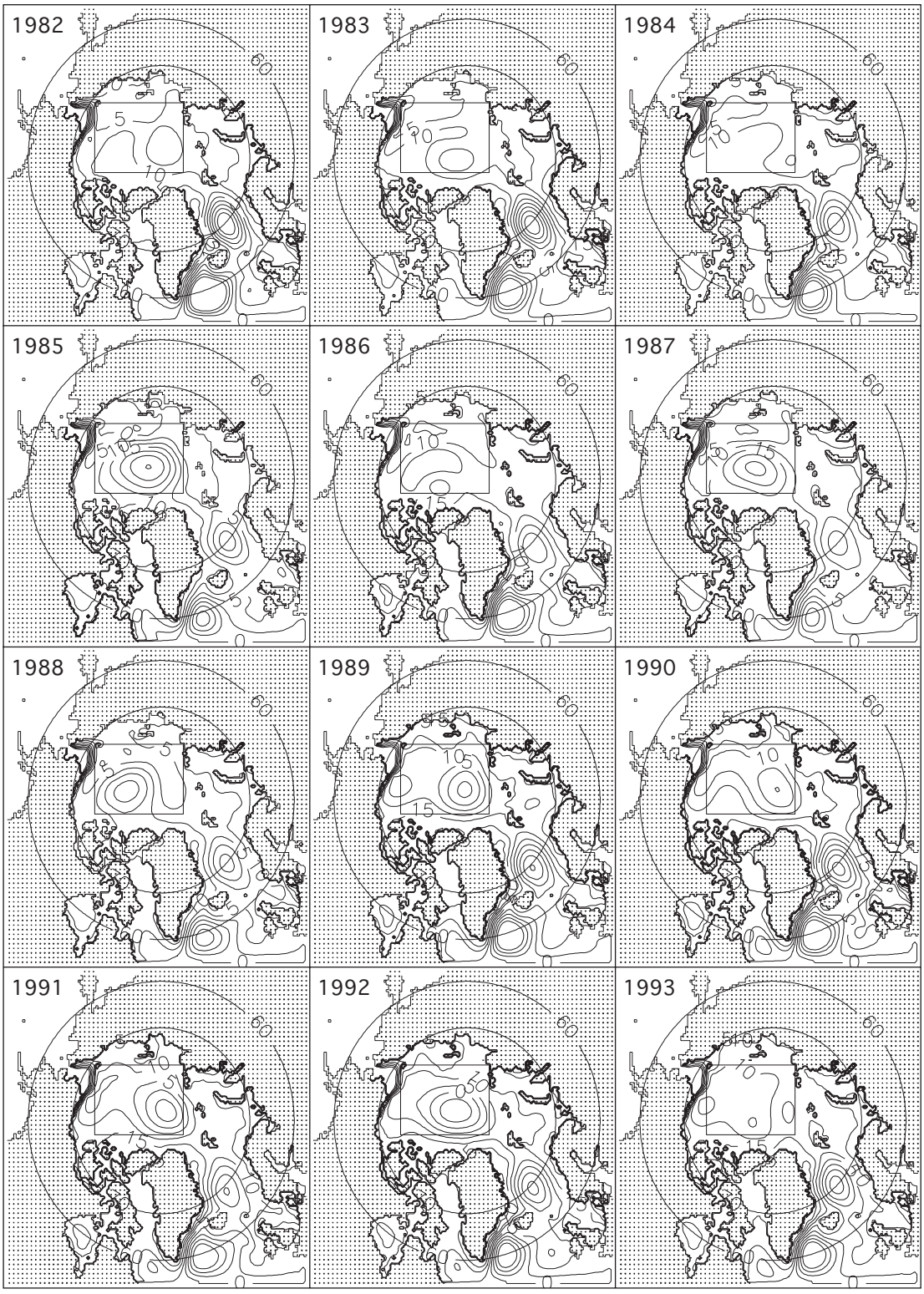

Figure 8d. Mean annual simulated surface heights (cm) for 1982–1993. Boxes show the central Arctic Ocean, where maximum or minimum sea level were located and sea level gradients were calculated.

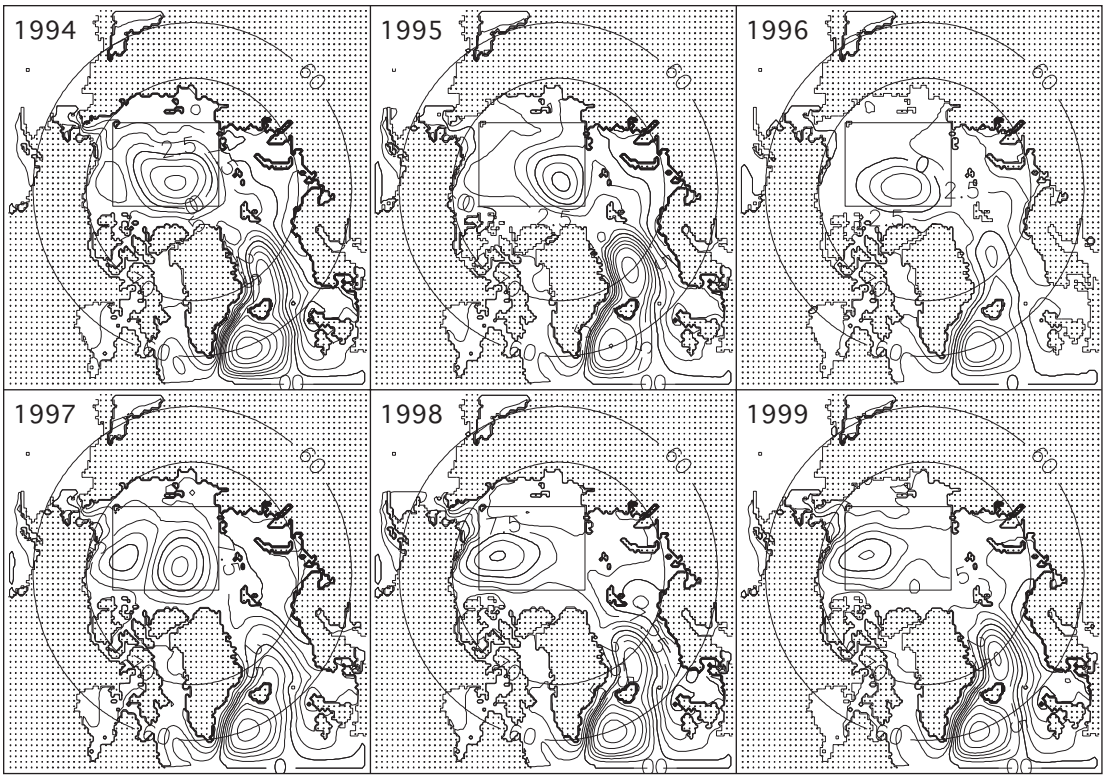

Figure 8e. Mean annual simulated surface heights (cm) for 1994–1999. Boxes show the central Arctic Ocean, where maximum or minimum sea level were located and sea level gradients were calculated.

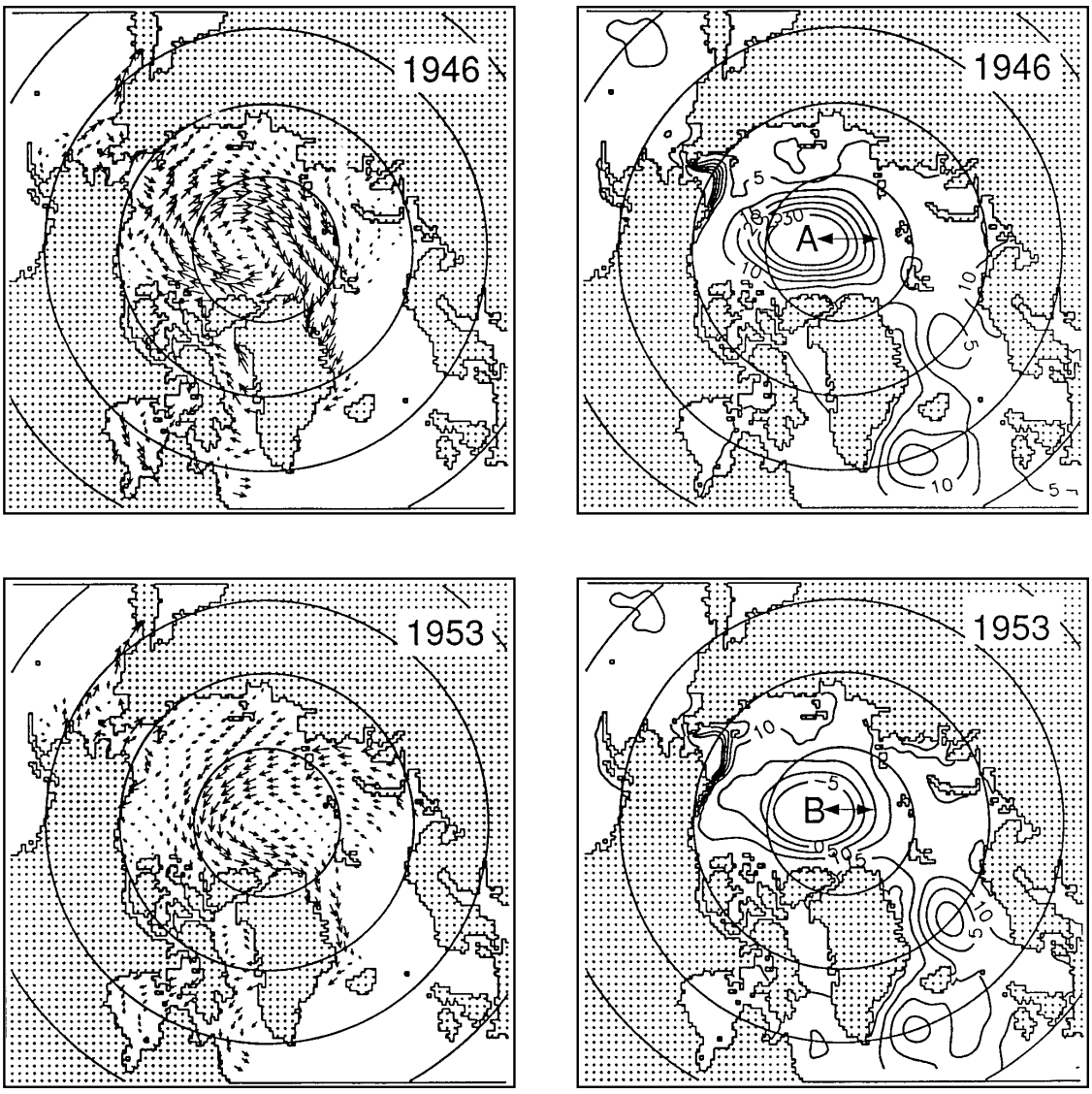

Figure 9. Simulated mean annual ice circulation (left) and surface heights in centimeters (right) in 1946 and 1953 for the anticyclonic and cyclonic regimes, respectively. A and B denote the centers of circulation. The arrows (right figures) show the approximate radius of the closed circulation cells used to calculate the sea level gradients.

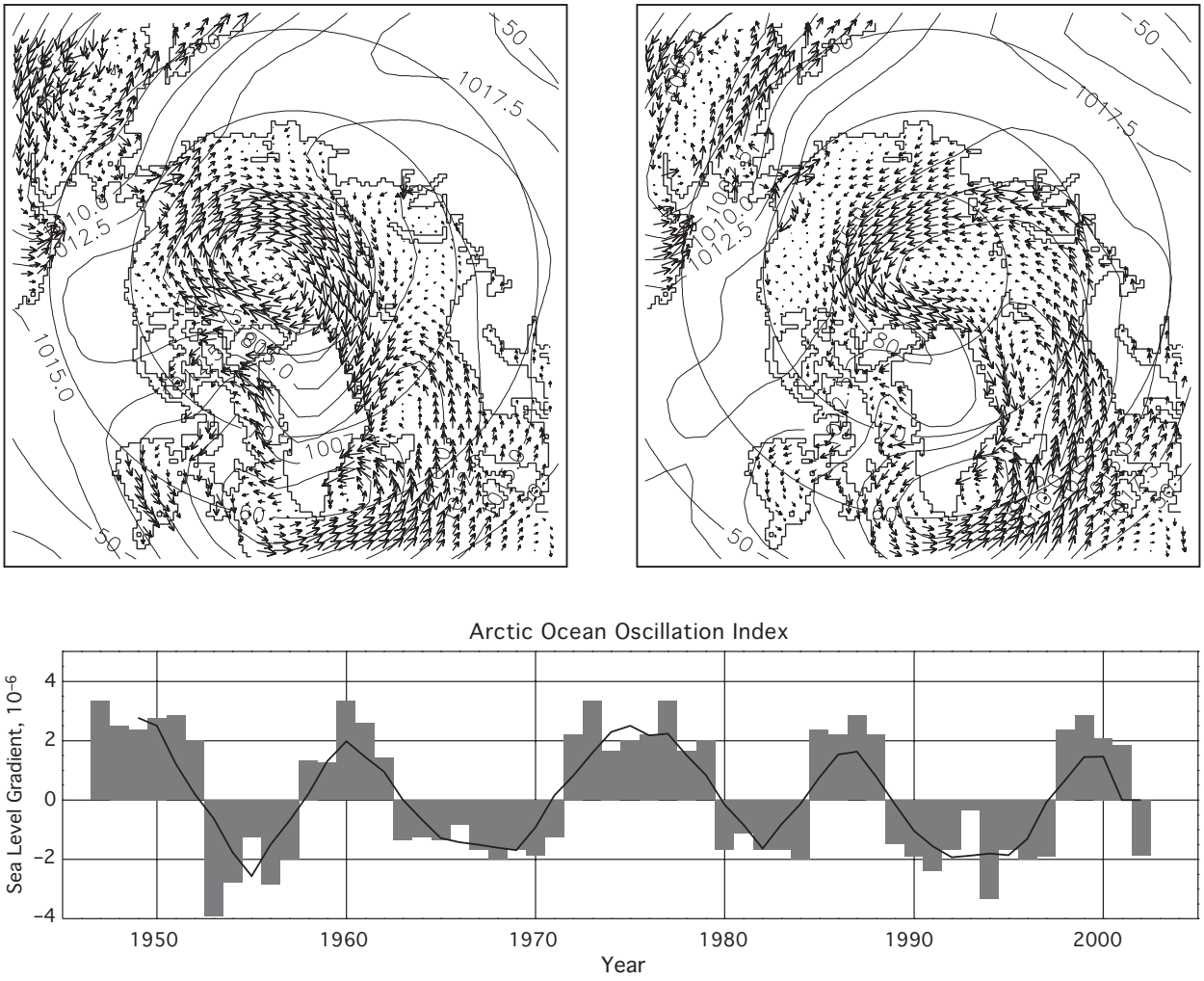

Figure 10. Upper panels: Typical annual wind-driven sea ice and surface water circulation (arrows) and sea level atmospheric pressure distribution (hPa) during anticyclonic (left) and cyclonic (right) circulation regimes. The bottom panel shows the time series of the sea level gradients (Arctic Ocean Oscillation index) simulated using a 2-D coupled ice–ocean model.

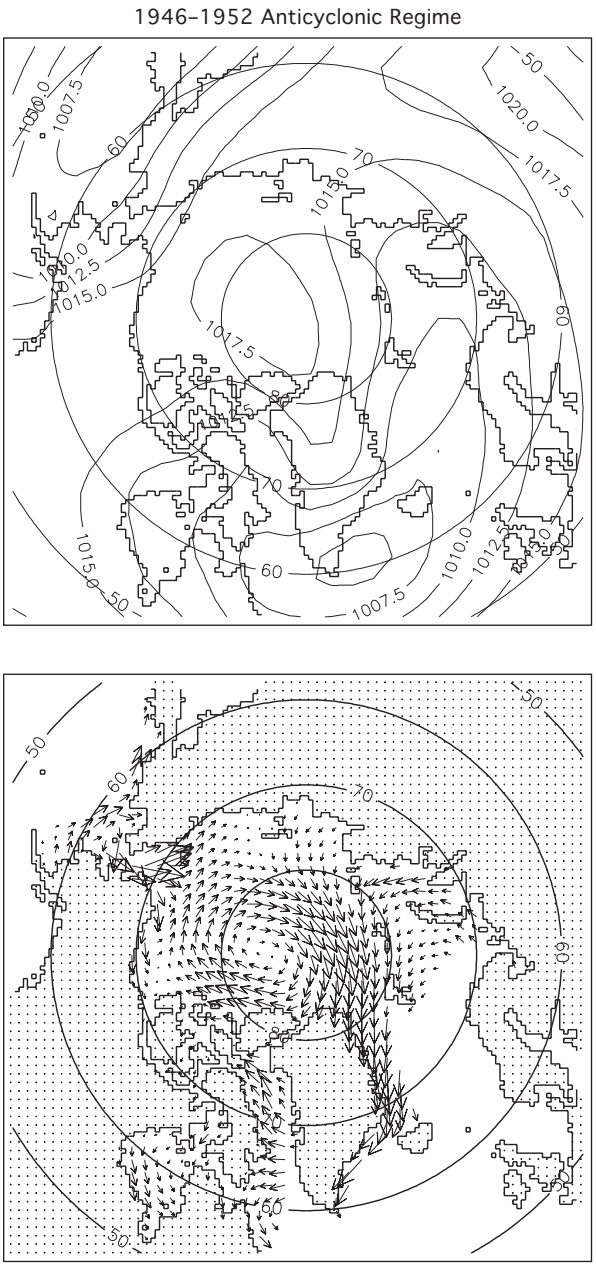

Figure 11a. Observed SLP (top) and simulated ice motion (bottom) for 1946–1952.

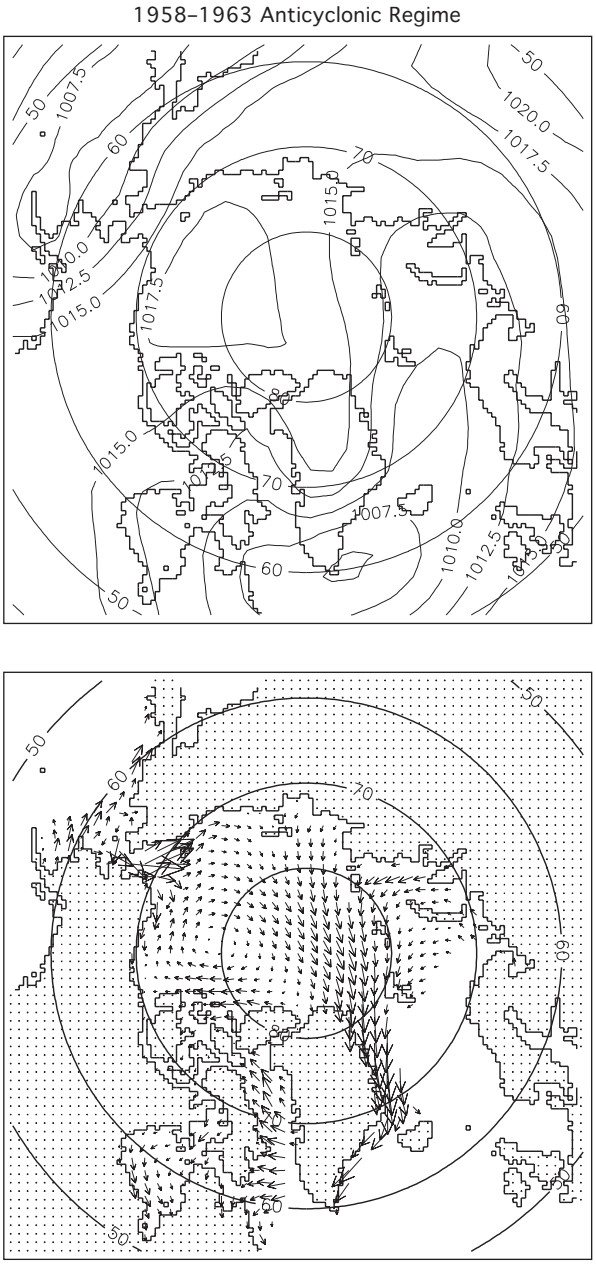

Figure 11b. Observed SLP (top) and simulated ice motion (bottom) for 1958–1963.

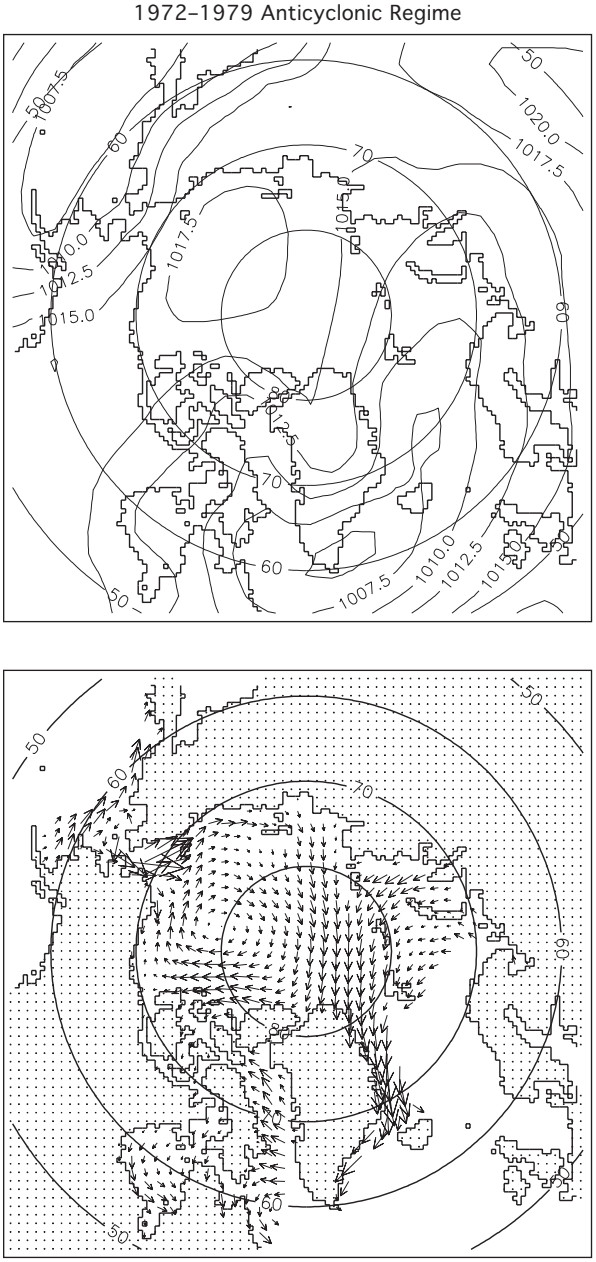

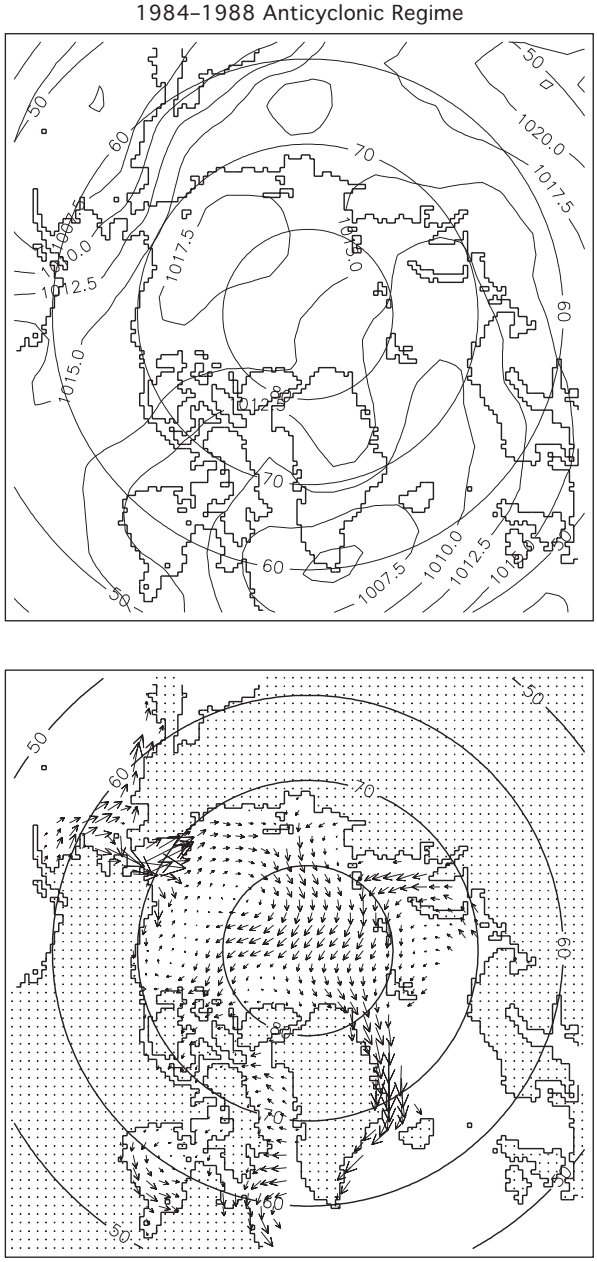

Figure 11c. Observed SLP (top) and simulated ice motion (bottom) for 1972–1979.

Figure 11d. Observed SLP (top) and simulated ice motion (bottom) for 1984–1988.

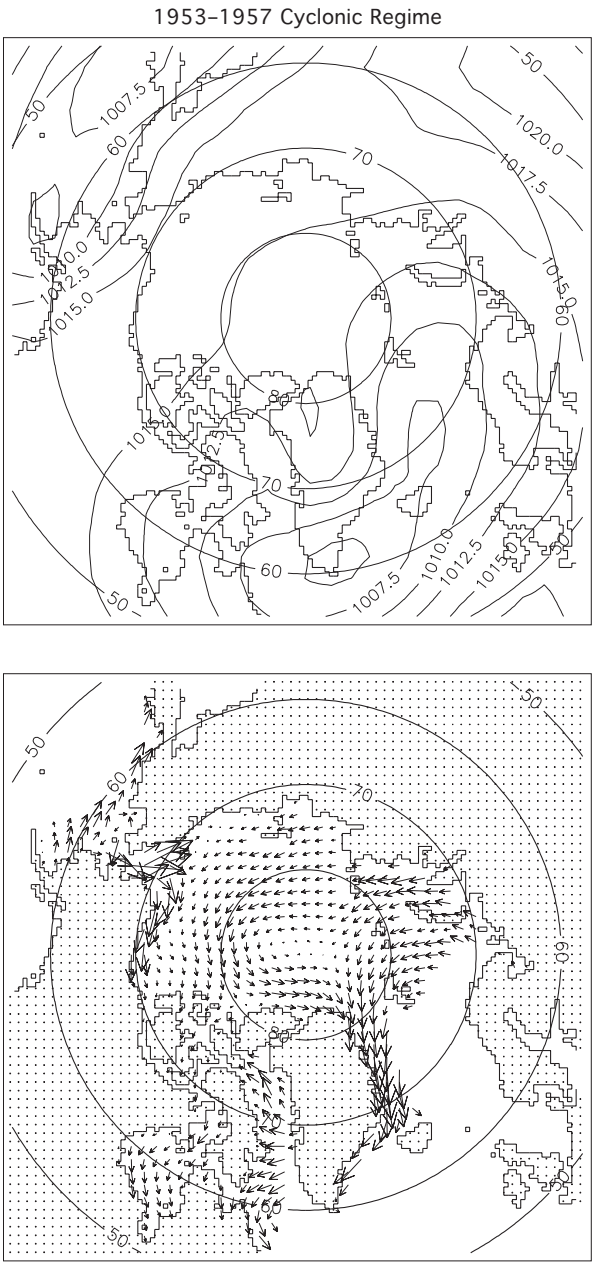

Figure 12a. Observed SLP (top) and simulated ice motion (bottom) for 1953–1957.

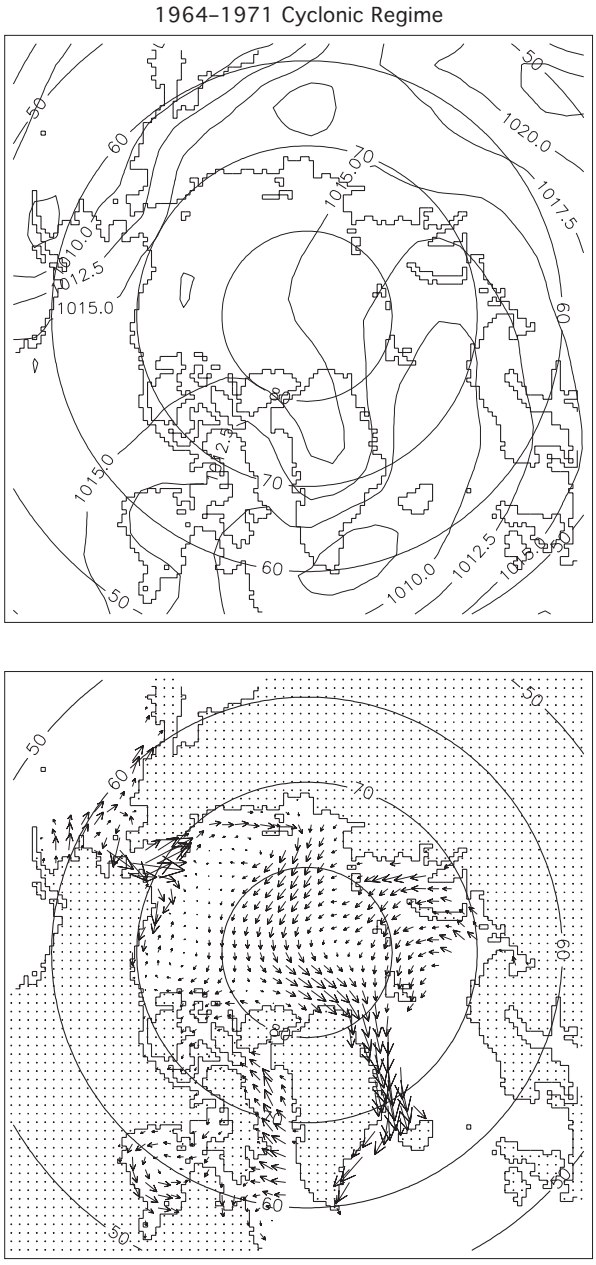

Figure 12b. Observed SLP (top) and simulated ice motion (bottom) for 1964–1971.

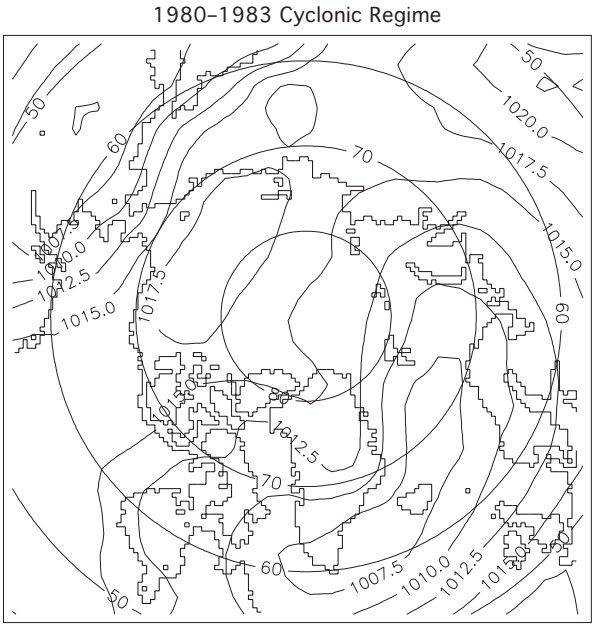

Figure 12c. Observed SLP (top) and simulated ice motion (bottom) for 1980–1983.

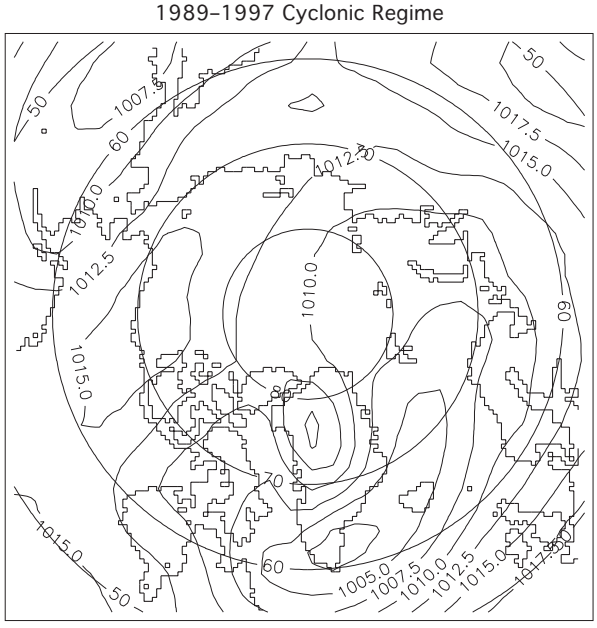

Figure 12d. Observed SLP (top) and simulated ice motion (bottom) for 1989–1993.

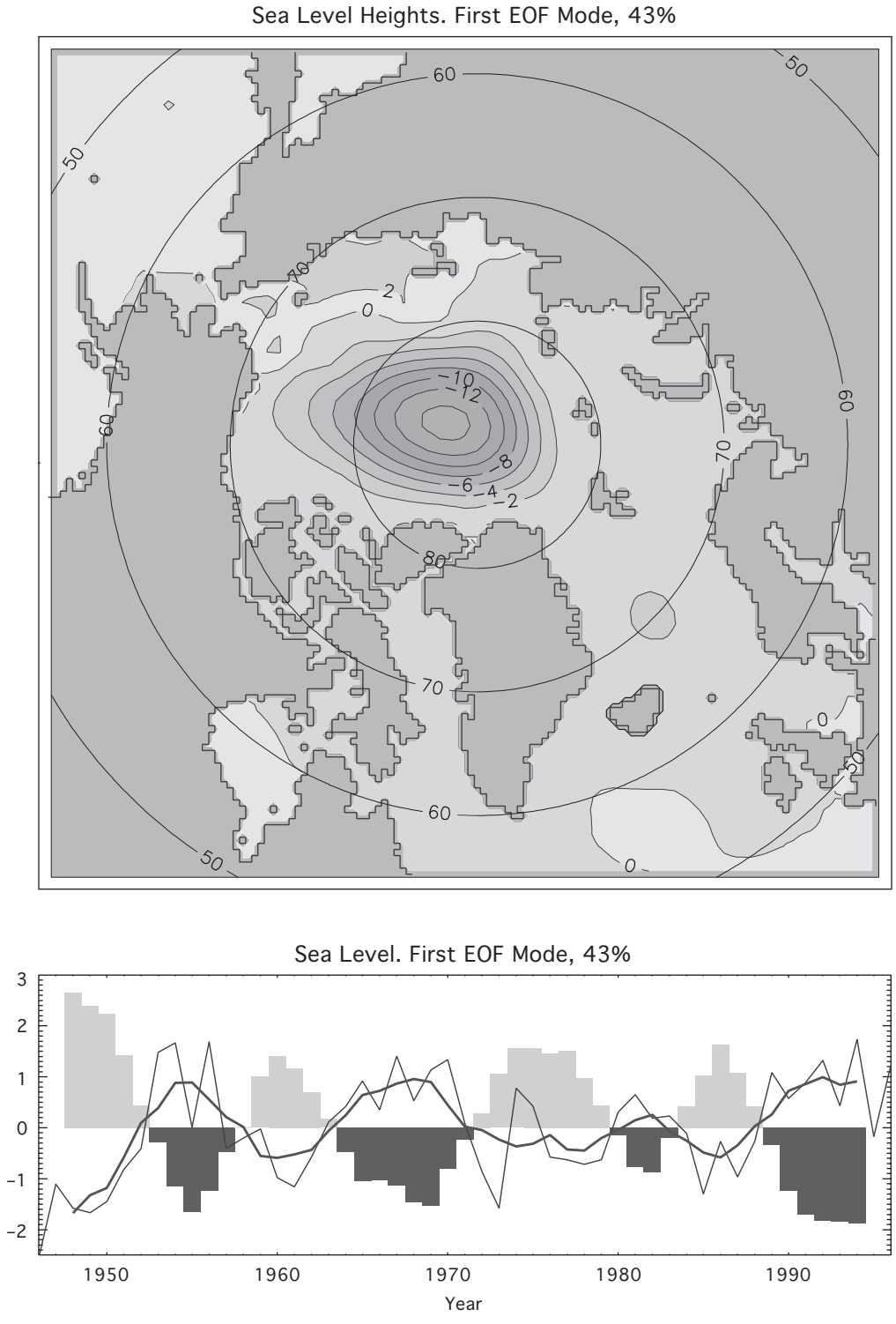

Figure 13. EOF analysis of SSHs.

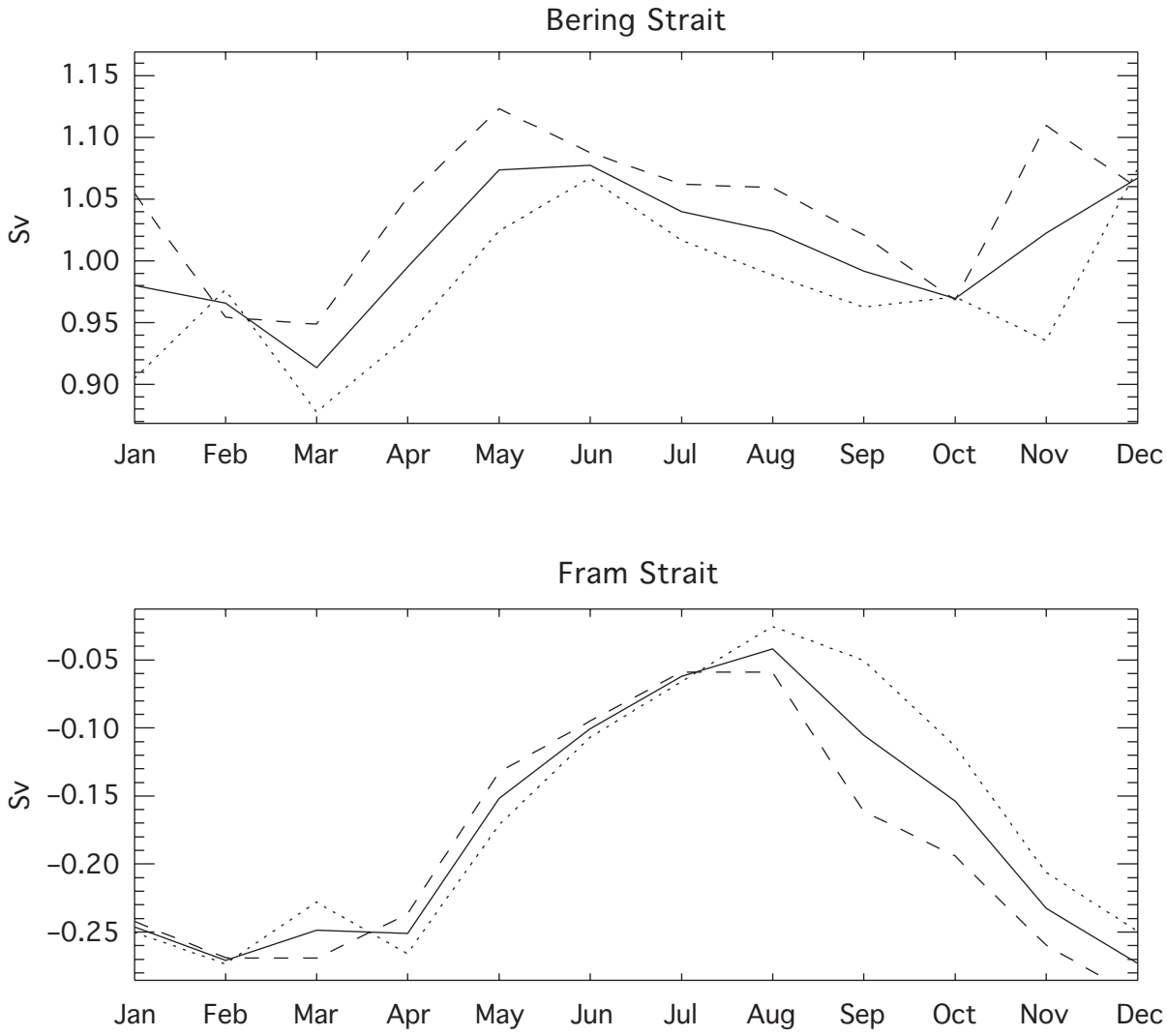

Figure 14. Seasonal variability of water transport through Bering Strait (top) and sea ice transport through Fram Strait (bottom) in Sverdrups (Sv; 1 Sv = 10^6 m^3 s^{-1}). The solid line depicts the 1946–2002 average; the dashed line shows transport for the cyclonic and the dotted line for the anticyclonic circulation regime.

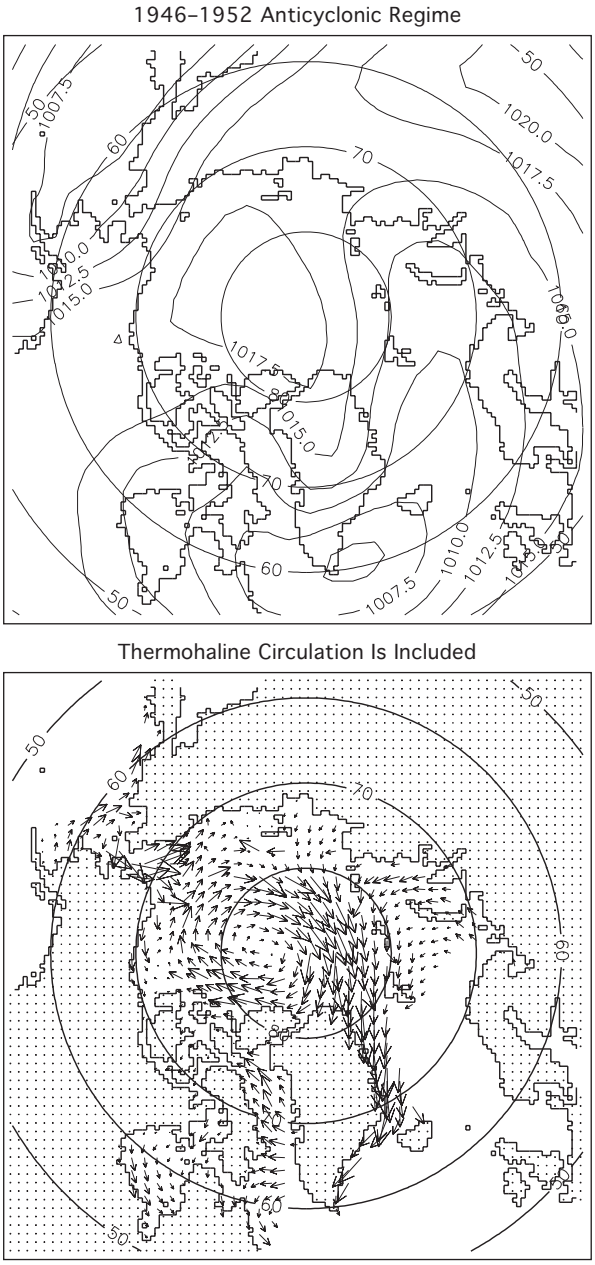

Figure 15. Observed SLP (top) and simulated ice drift (bottom) for 1946–1952 with thermohaline currents.

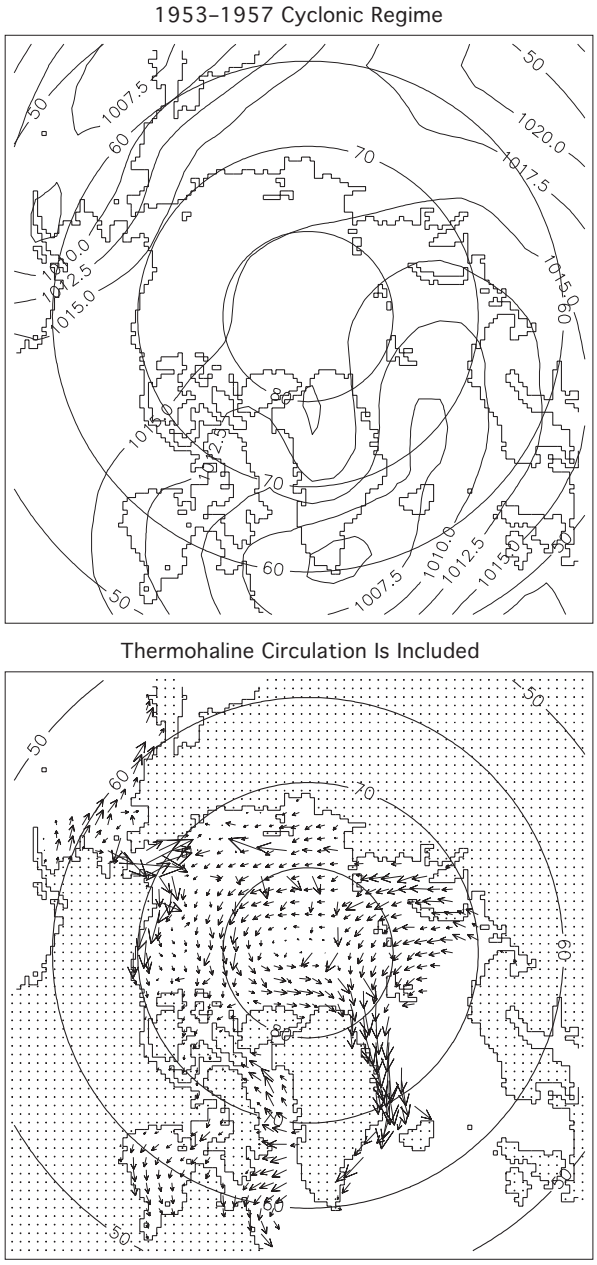

Figure 16. Observed SLP (top) and simulated ice drift for 1953–1957 with thermohaline currents.

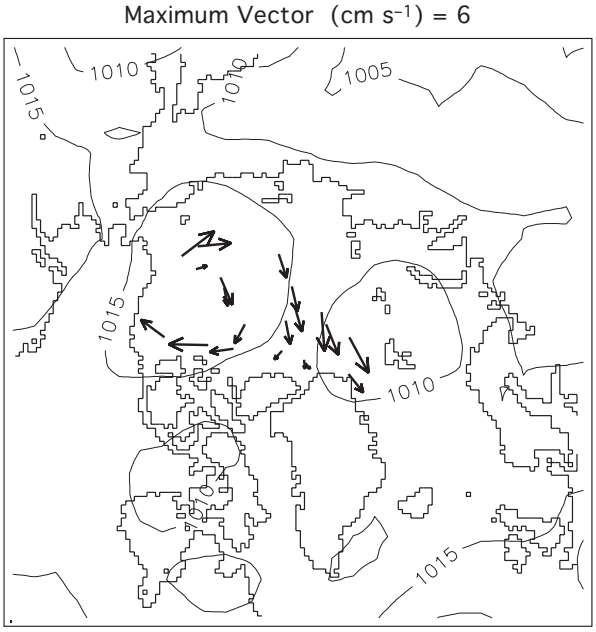

Figure 17a. Buoy drift and SLP from observations (top) and simulations (bottom) for July 1987.

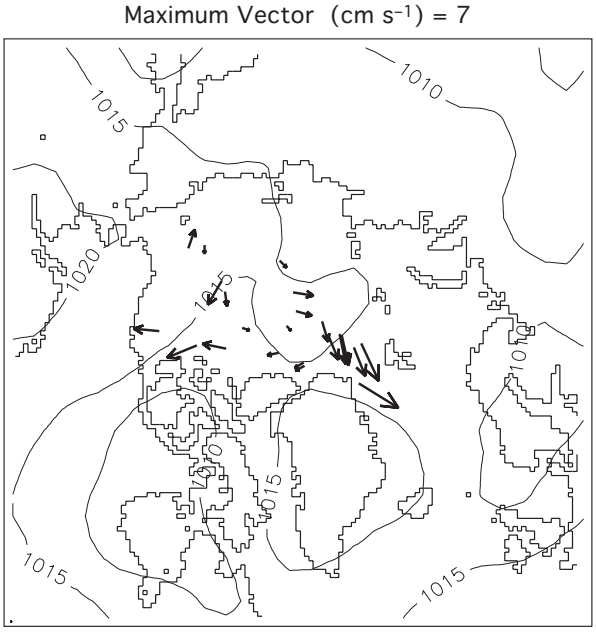

Figure 17b. Buoy drift and SLP from observations (top) and simulations (bottom) for August 1987.

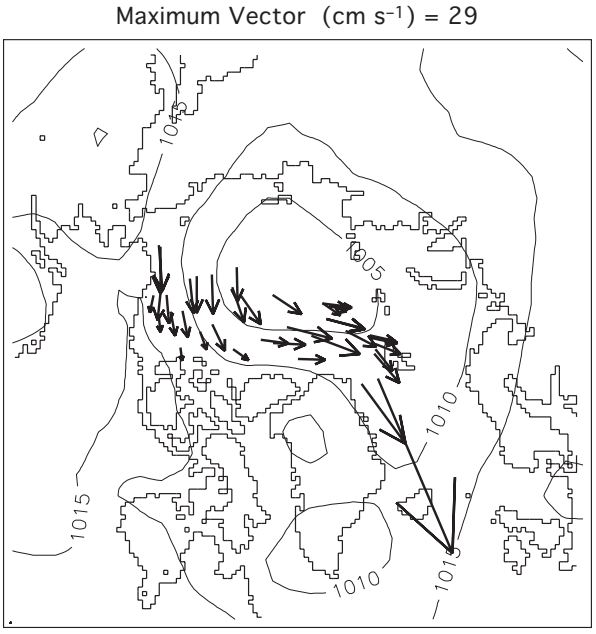

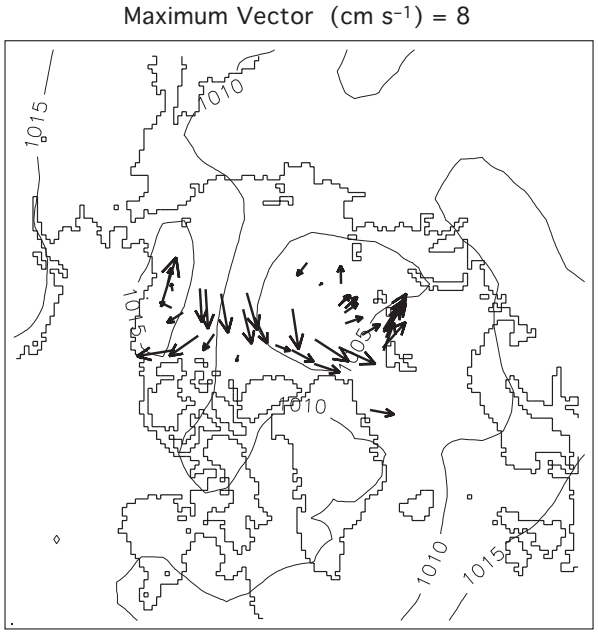

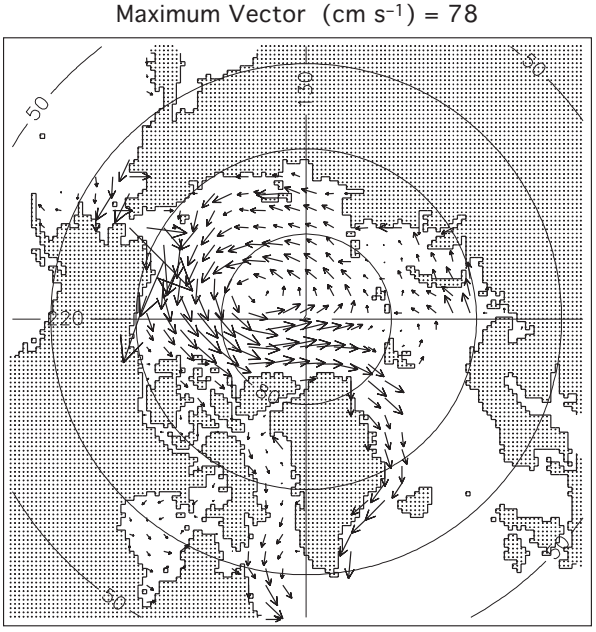

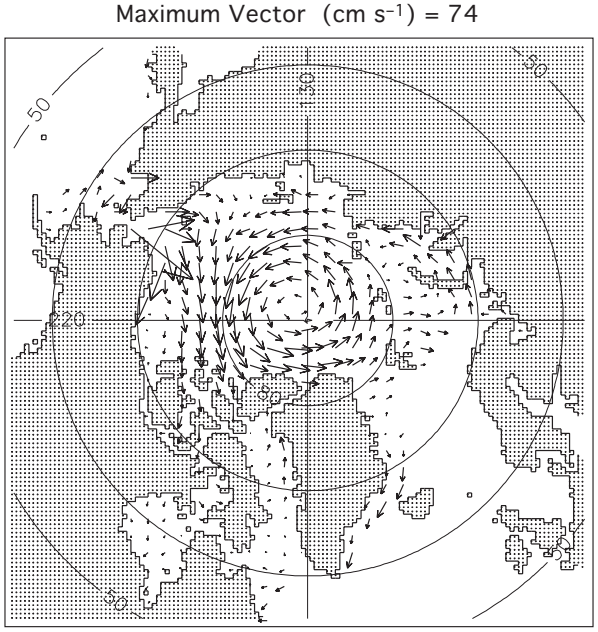

Figure 18a. Buoy drift and SLP from observations (top) and simulations (bottom) for May 1992.

Figure 18b. Buoy drift and SLP from observations (top) and simulations (bottom) for July 1992.

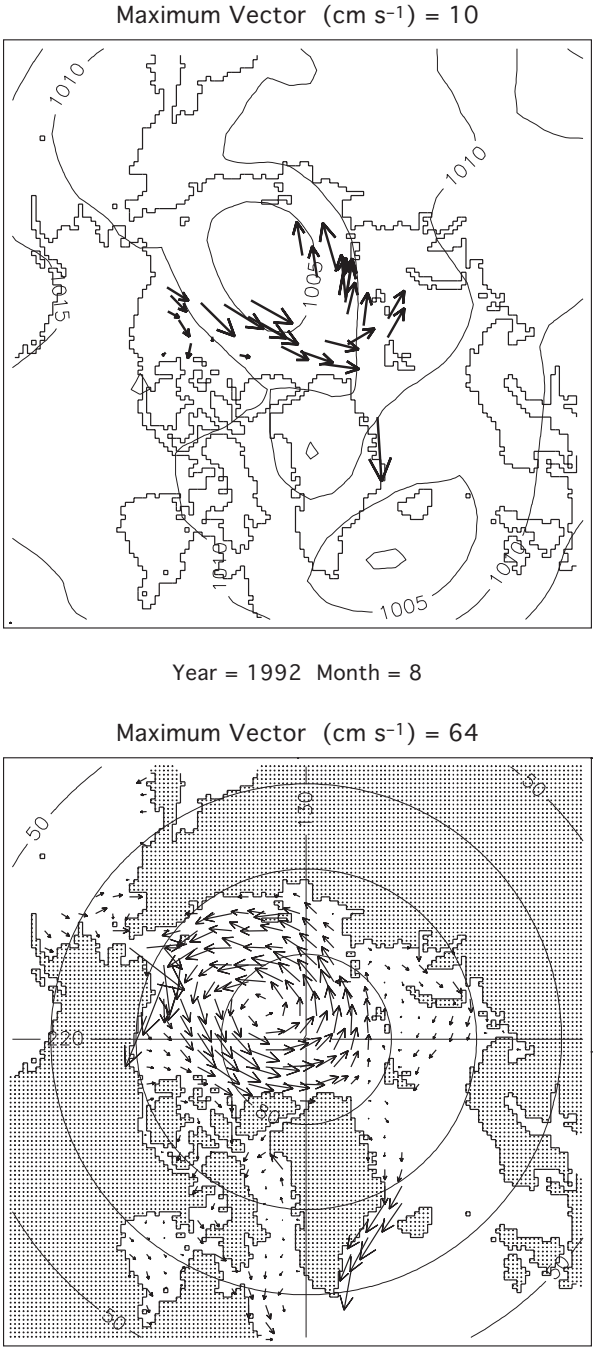

Figure 18c. Buoy drift and SLP from observations (top) and simulations (bottom) for August 1992.

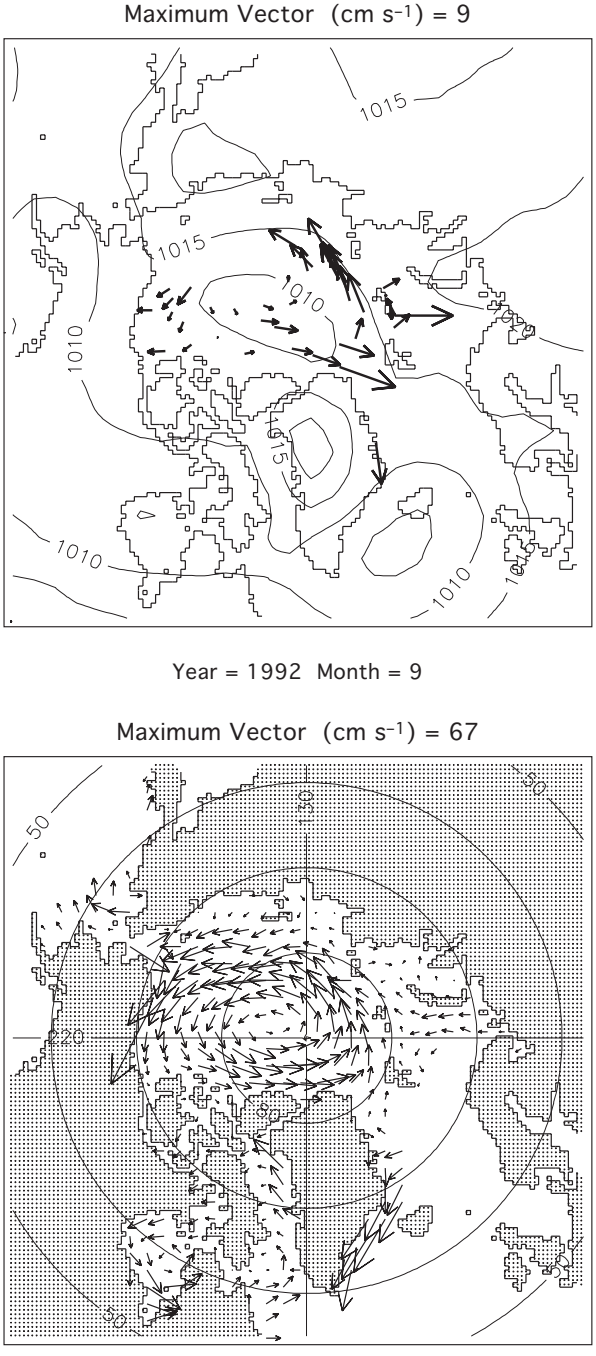

Figure 18d. Buoy drift and SLP from observations (top) and simulations (bottom) for September 1992.

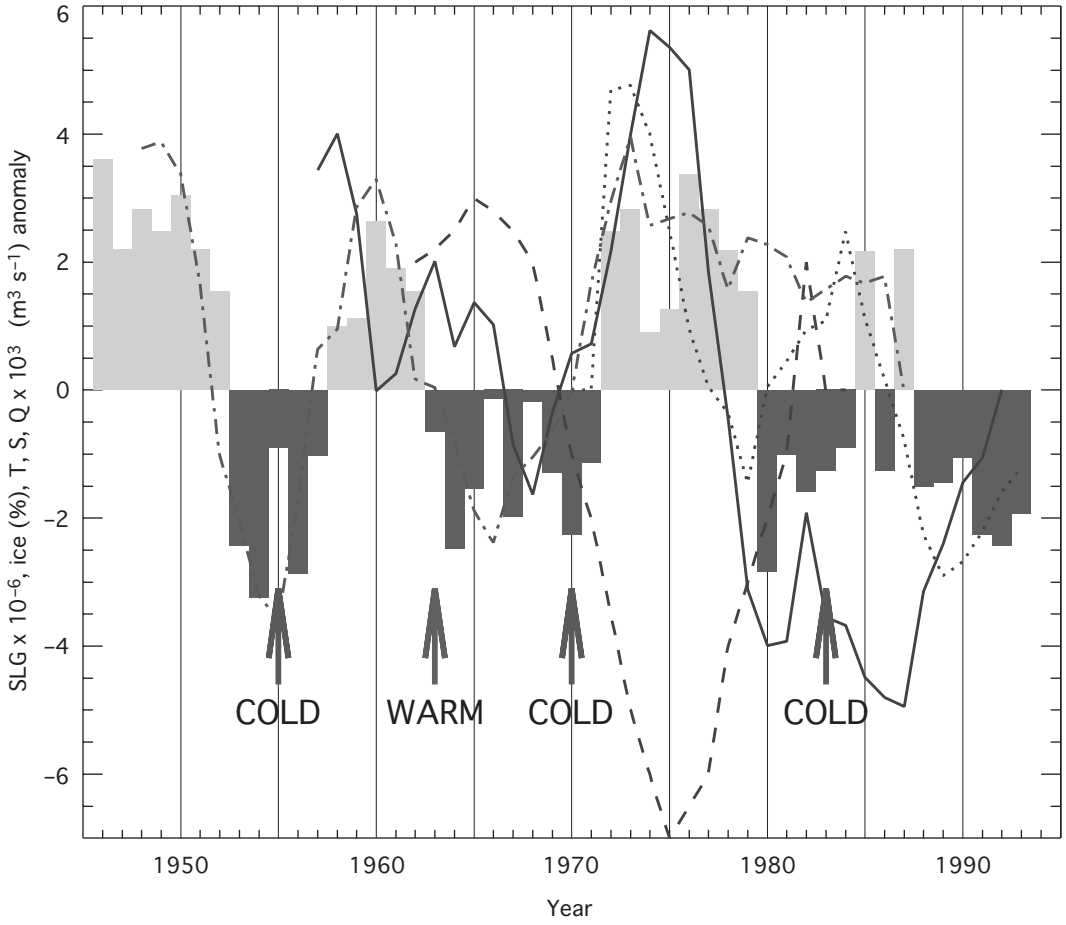

Figure 19. Time series of sea level gradients (SLG) in the central Arctic Basin (vertical bars). Positive gradients correspond to an anticyclonic regime of circulation and negative gradients correspond to a cyclonic regime of circulation The solid line shows change in percent of sea ice in the Bering Sea [Niebauer 1988]. The dashed line shows variations in water temperature anomaly (°C) in the cold intermediate layer southeast of Kamchatka [Davydov 1989], the dotted line shows variations in the salinity anomaly in the Gulf of Alaska [Royer 1996], and the mixed dash/dot line shows anomalies in annual river runoff to the Arctic Ocean. Arrows depict beginning of cold or warm SST events in the far North Atlantic [Hansen and Bezdek 1996].

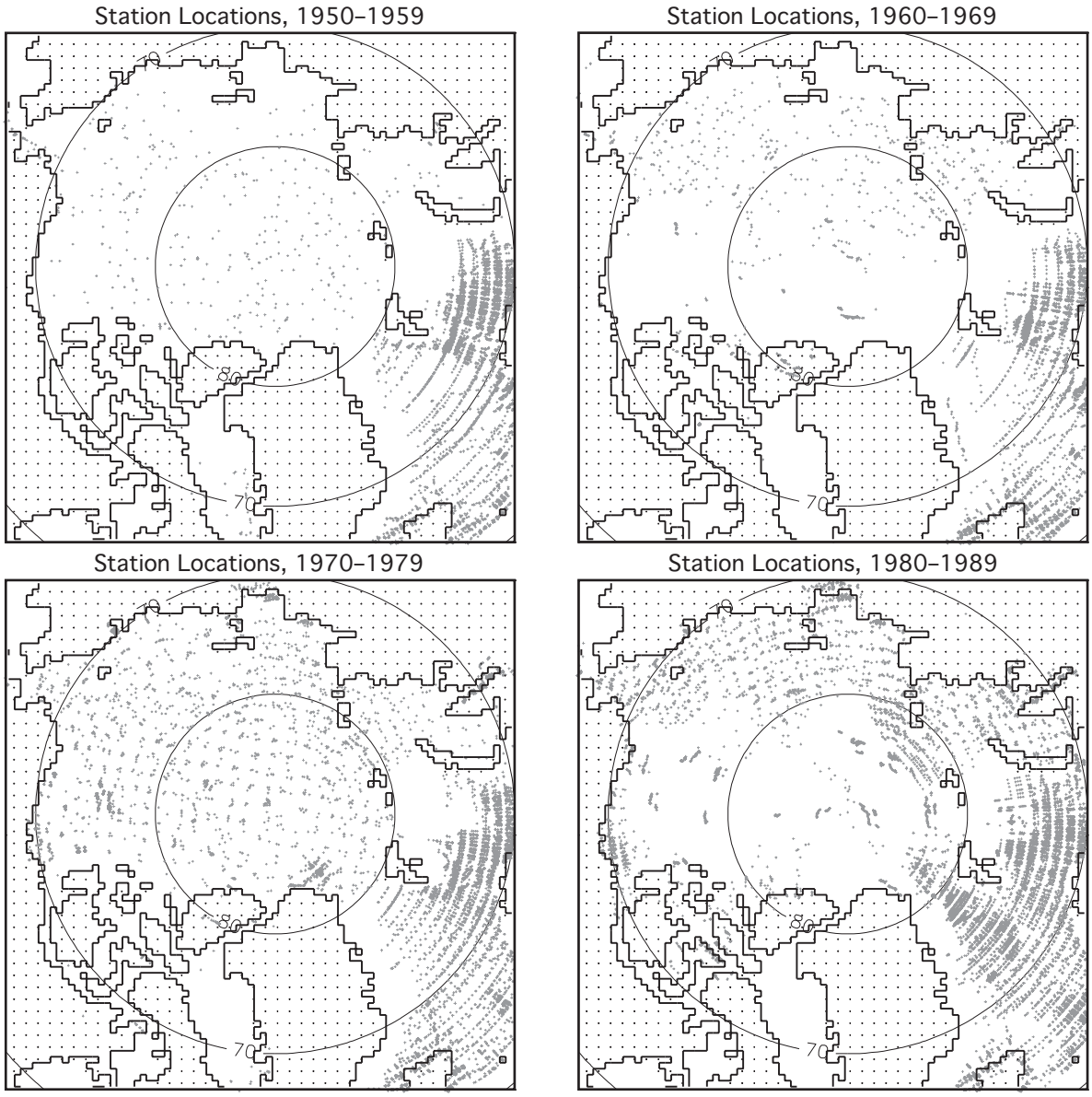

Figure 20. Location of hydrographic stations in the Arctic Ocean for 1950–1959, 1960–1969, 1970–1979, and 1980–1989 based on the EWG [1997] atlas data.

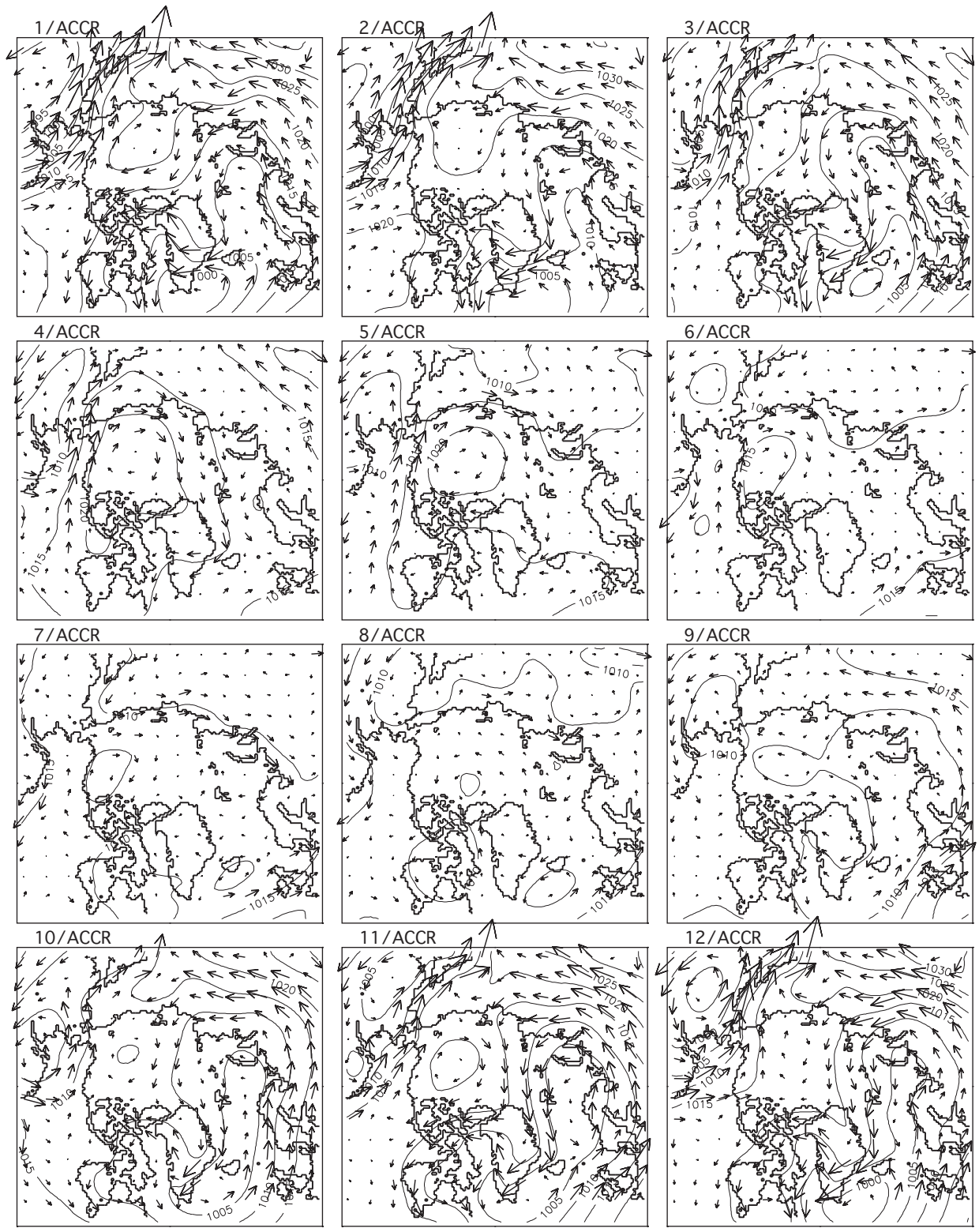

Figure 21. Monthly mean SLP for ACCR years.

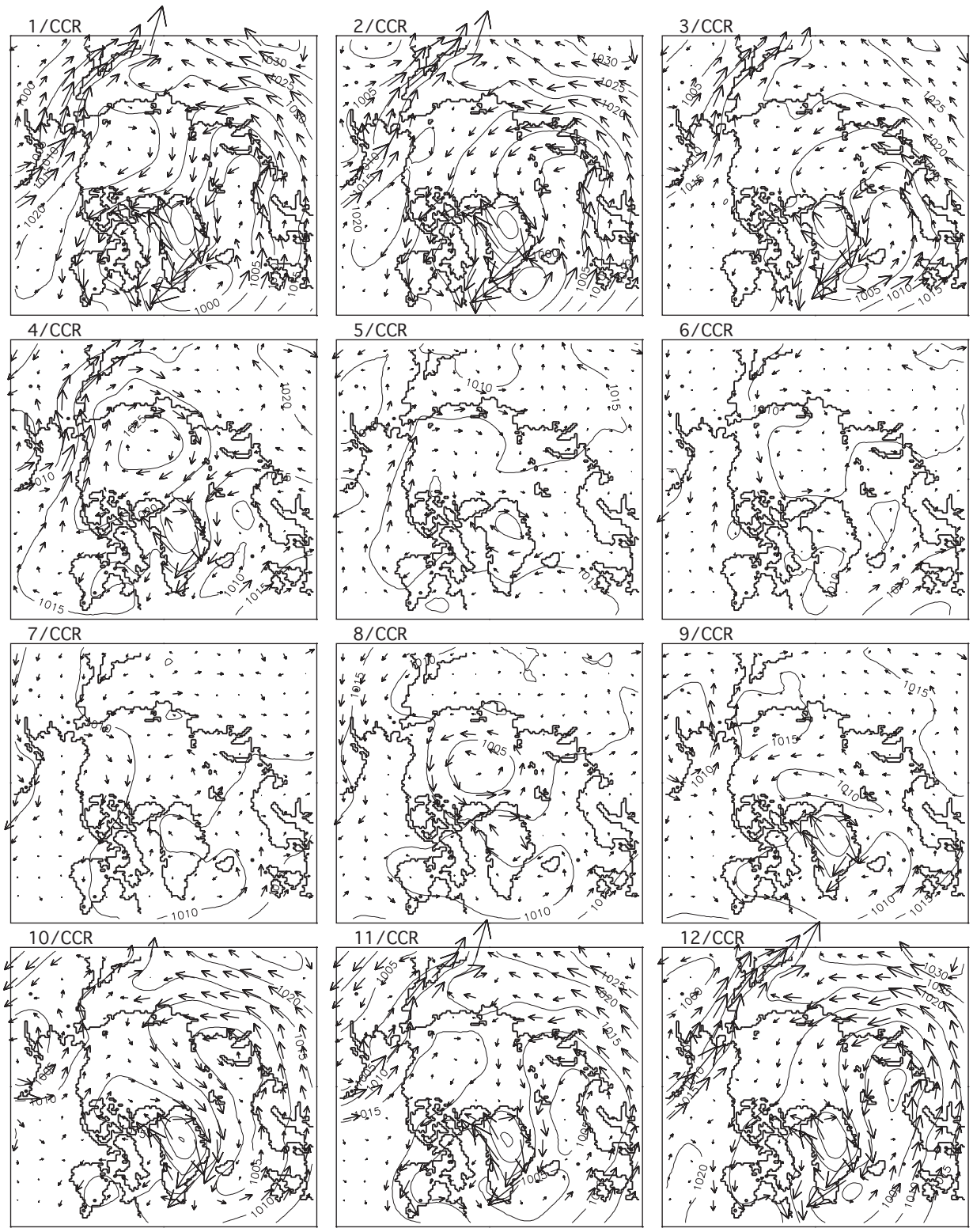

Figure 22. Monthly mean SLP for CCR years.

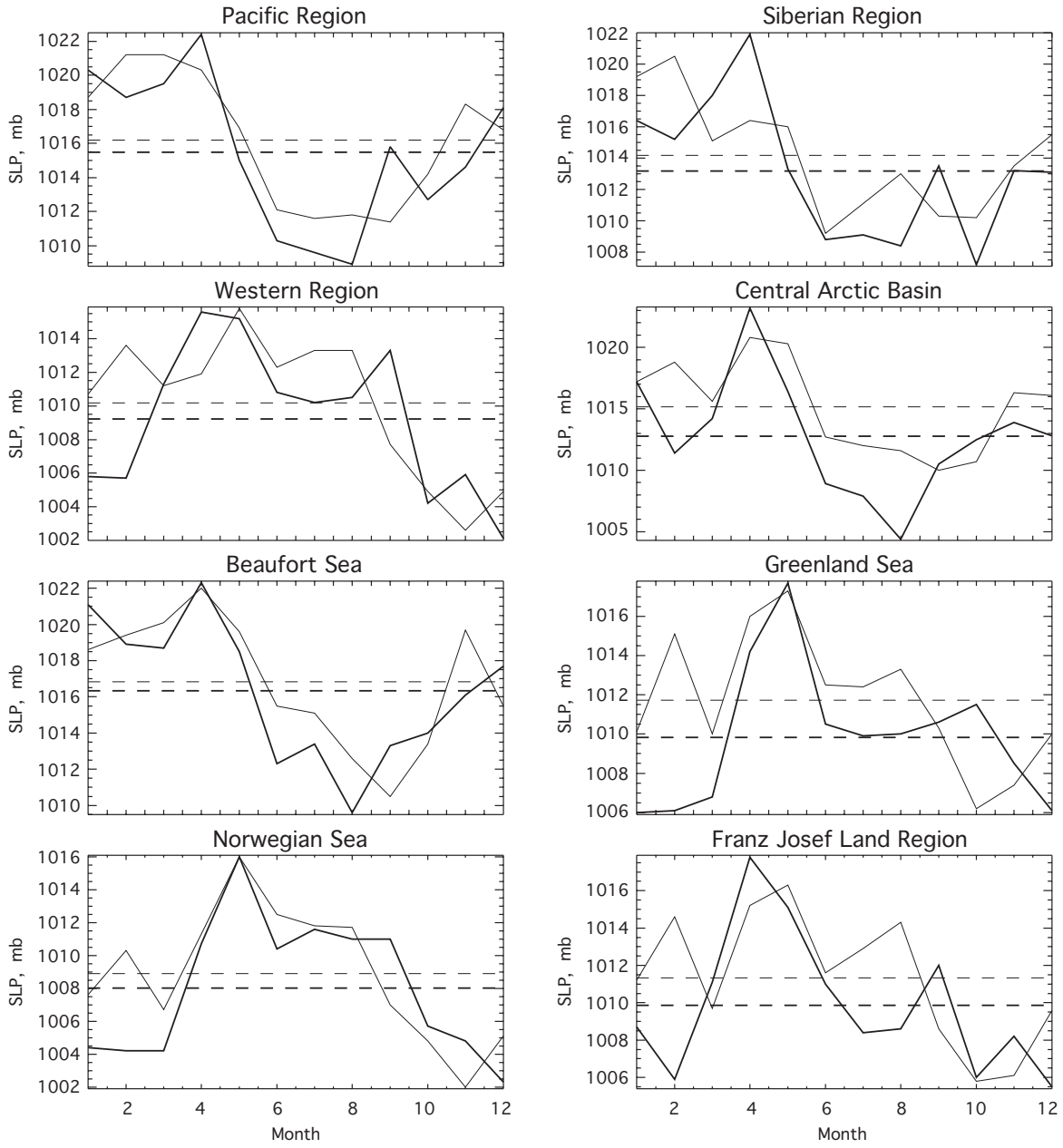

Figure 23. Monthly mean (solid lines) and annual mean (straight horizontal dashed lines) SLP averaged over all ACCR (thin lines) and CCR (thick lines) years. Note that the SLP scale is different among regions.

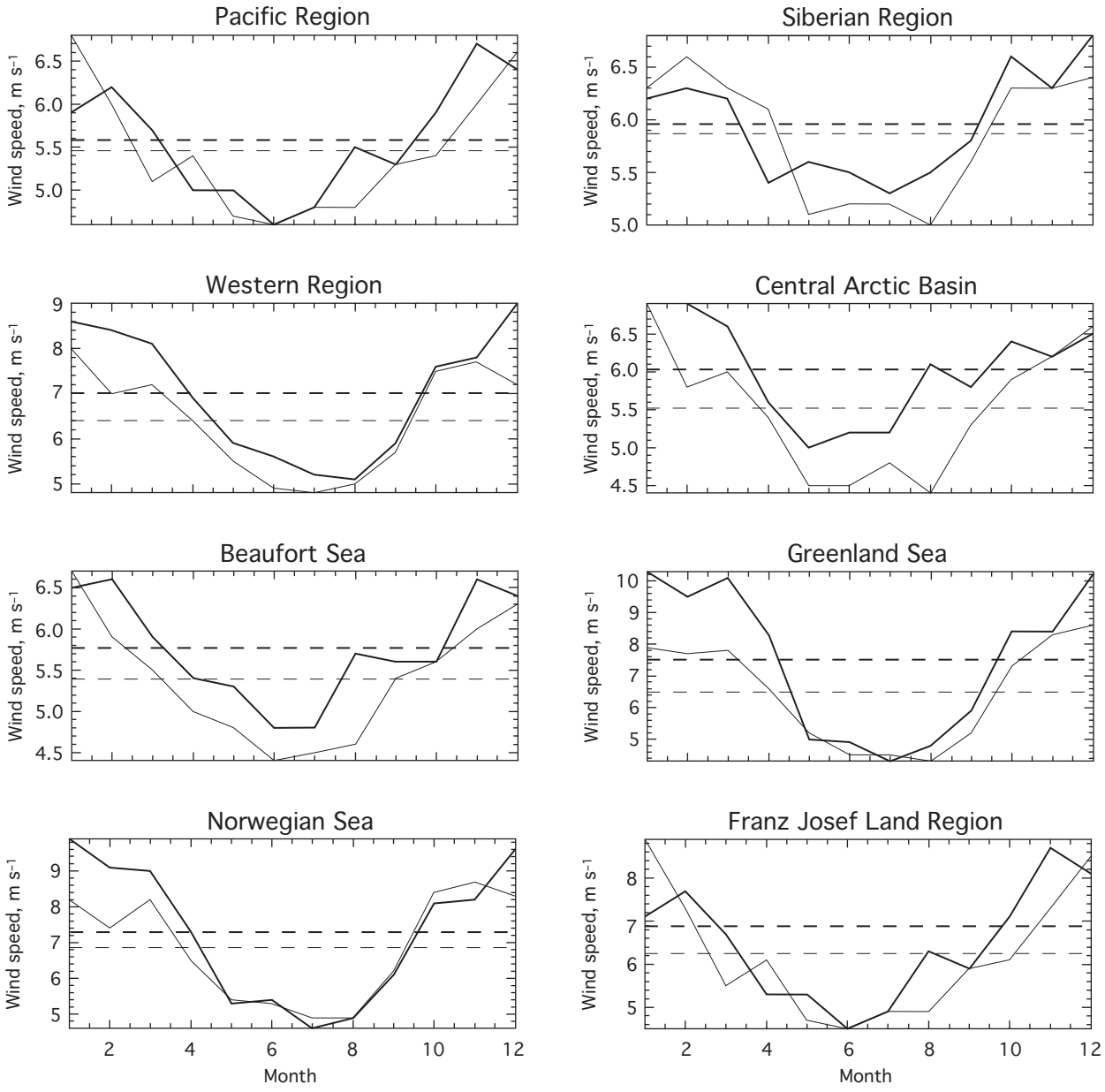

Figure 24. Monthly mean (solid lines) and annual mean (straight horizontal dashed lines) wind speed averaged over all ACCR (thin lines) and CCR (thick lines) years. Note that the wind speed scale is different among regions.

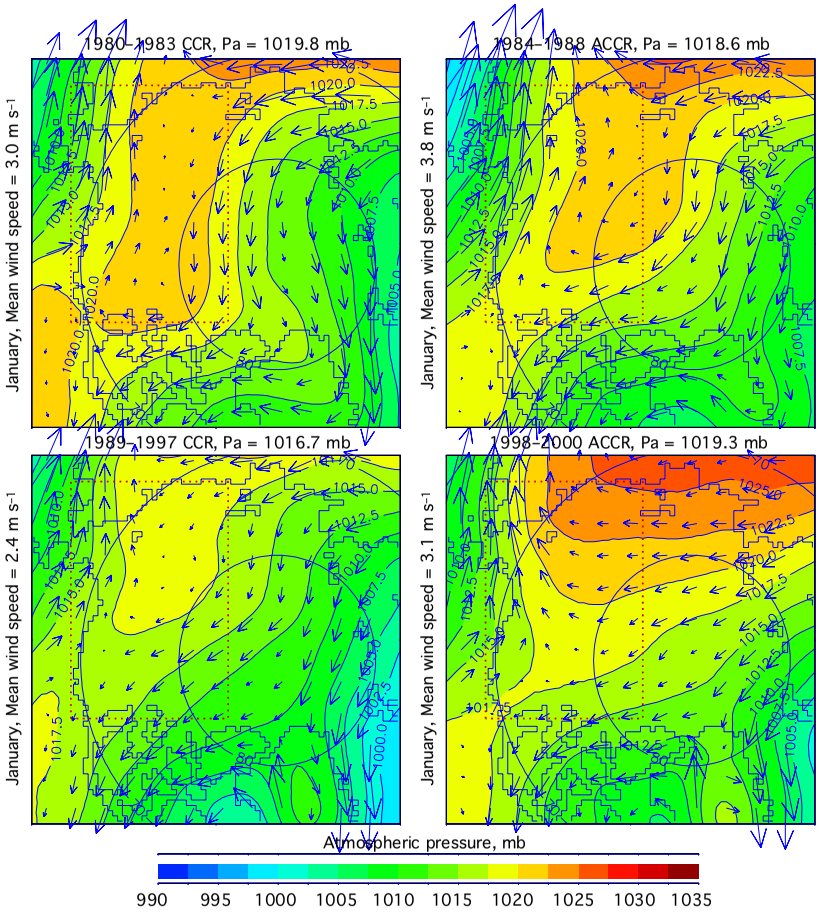

Figure 25. Observed SLP and calculated geostrophic wind in January for years with cyclonic (CCR) and anticyclonic (ACCR) circulation regimes. “Pa” and “Mean wind speed” show SLP and wind speed averaged over the box limited by the dotted line.

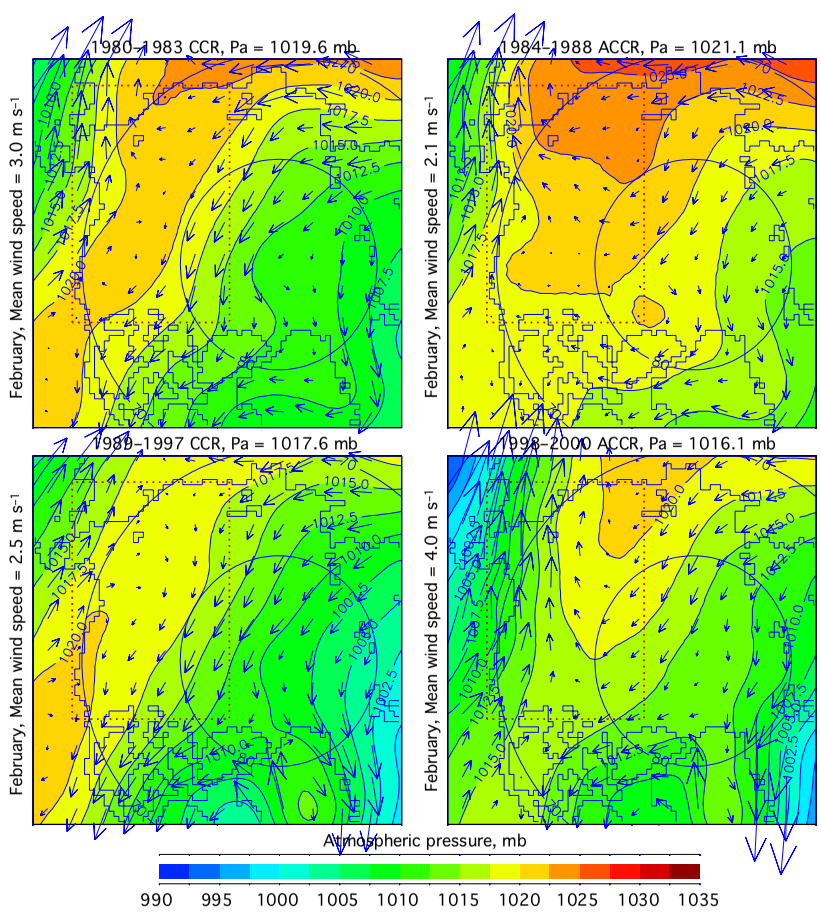

Figure 26. Observed SLP and calculated geostrophic wind in February for years with cyclonic (CCR) and anticyclonic (ACCR) circulation regimes. “Pa” and “Mean wind speed” show SLP and wind speed averaged over the box limited by the dotted line.

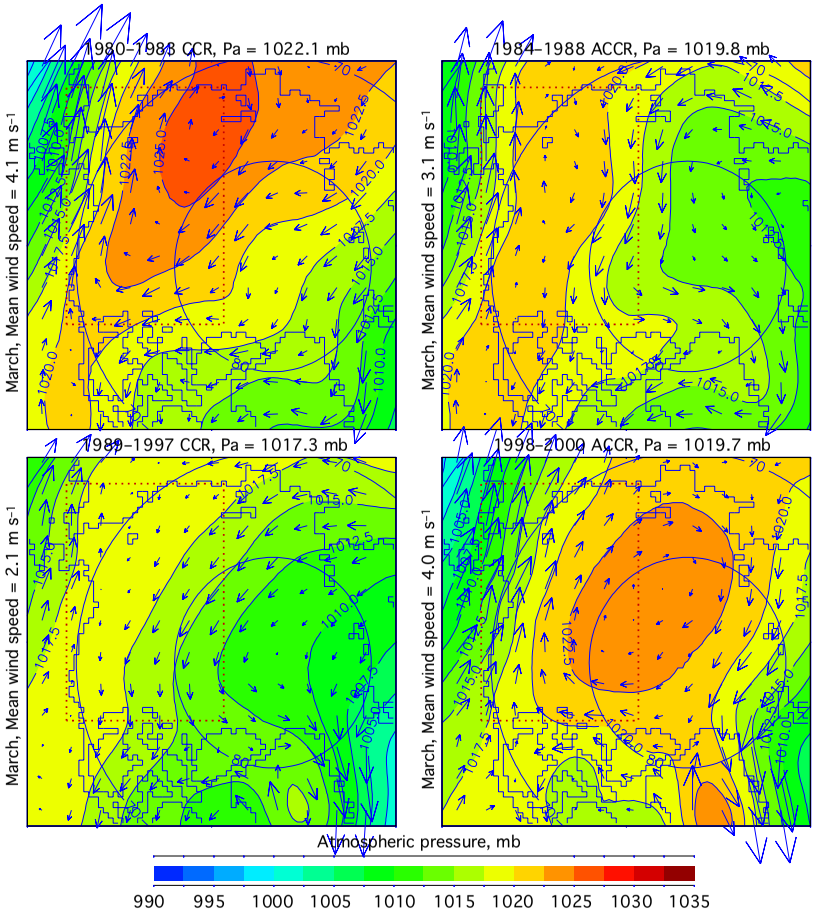

Figure 27. Observed SLP and calculated geostrophic wind in March for years with cyclonic (CCR) and anticyclonic (ACCR) circulation regimes. “Pa” and “Mean wind speed” show SLP and wind speed averaged over the box limited by the dotted line.

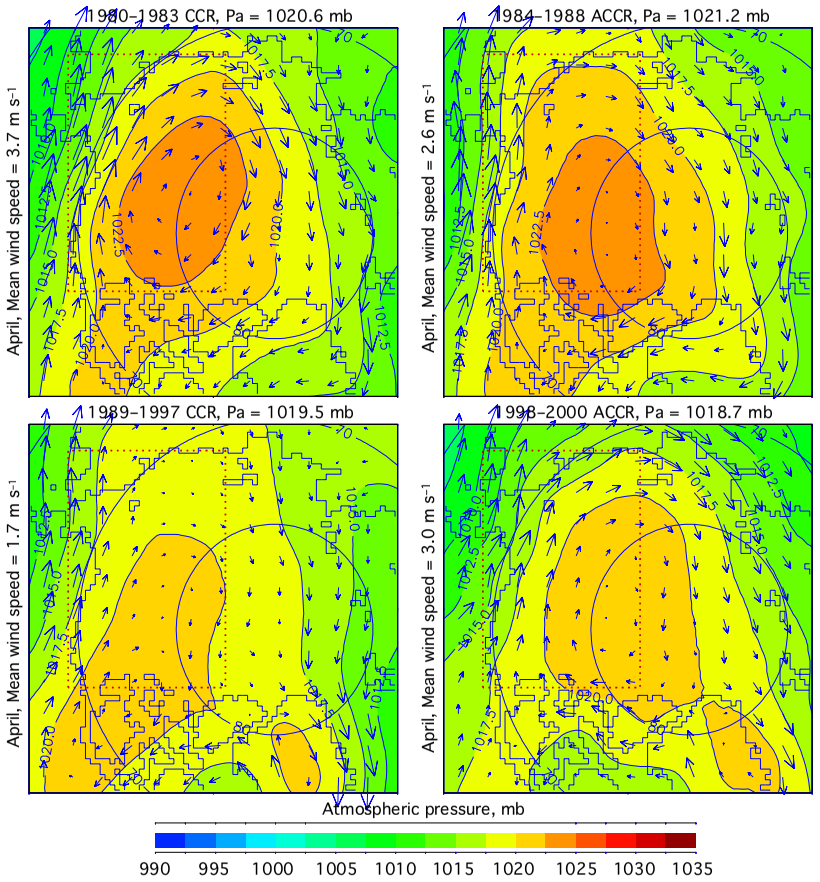

Figure 28. Observed SLP and calculated geostrophic wind in April for years with cyclonic (CCR) and anticyclonic (ACCR) circulation regimes. “Pa” and “Mean wind speed” show SLP and wind speed averaged over the box limited by the dotted line.

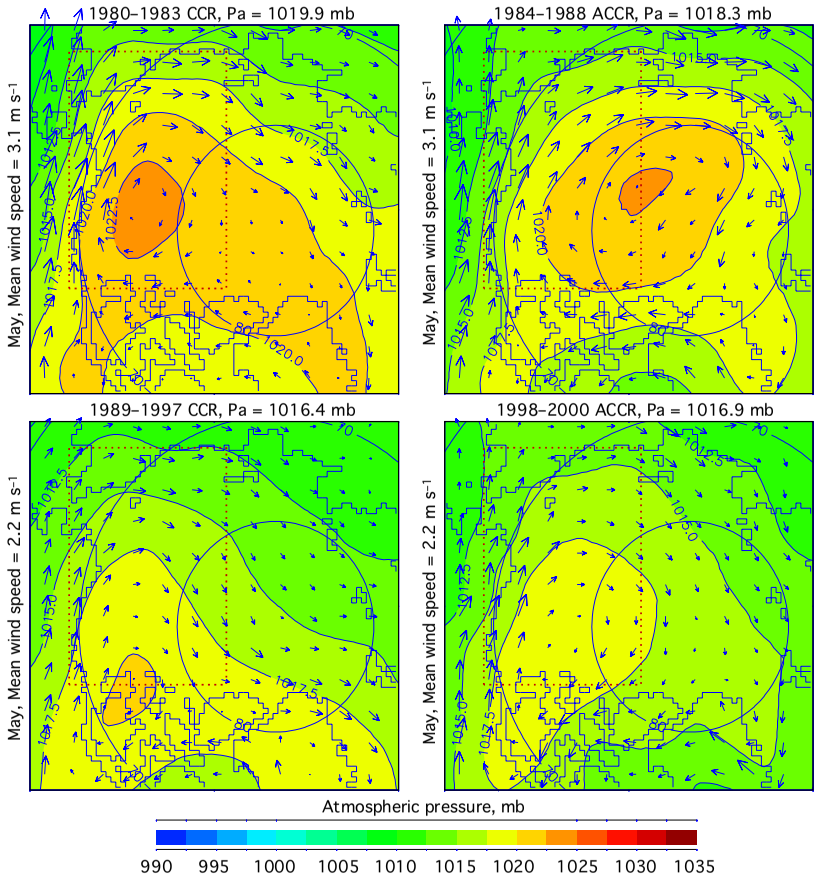

Figure 29. Observed SLP and calculated geostrophic wind in May for years with cyclonic (CCR) and anticyclonic (ACCR) circulation regimes. “Pa” and “Mean wind speed” show SLP and wind speed averaged over the box limited by the dotted line.

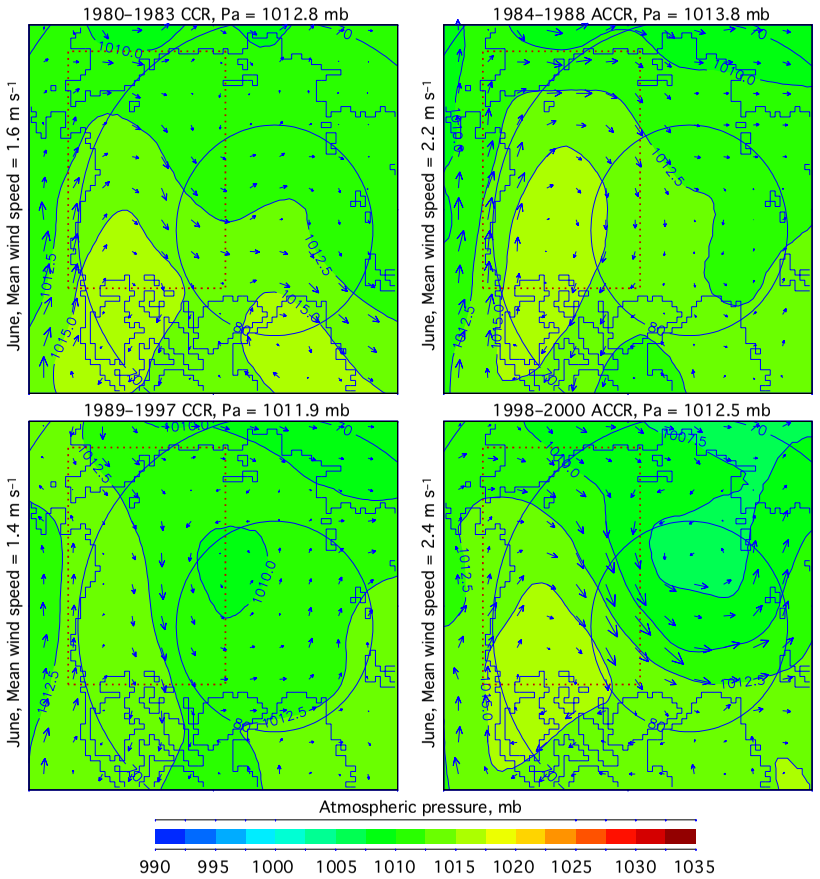

Figure 30. Observed SLP and calculated geostrophic wind in June for years with cyclonic (CCR) and anticyclonic (ACCR) circulation regimes. “Pa” and “Mean wind speed” show SLP and wind speed averaged over the box limited by the dotted line.

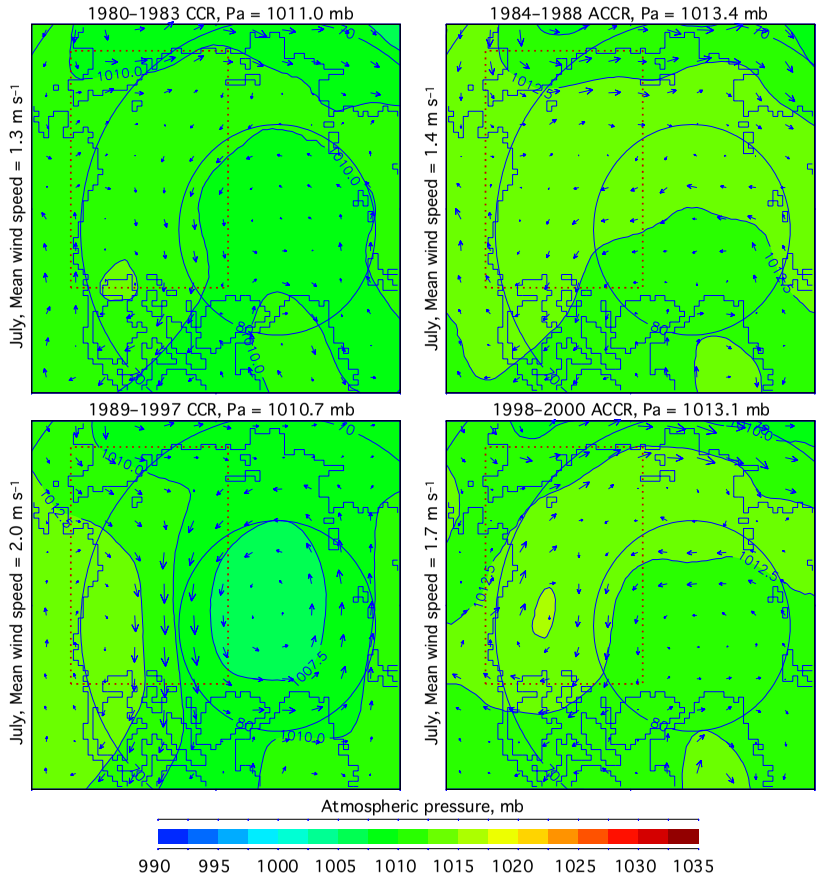

Figure 31. Observed SLP and calculated geostrophic wind in July for years with cyclonic (CCR) and anticyclonic (ACCR) circulation regimes. “Pa” and “Mean wind speed” show SLP and wind speed averaged over the box limited by the dotted line.

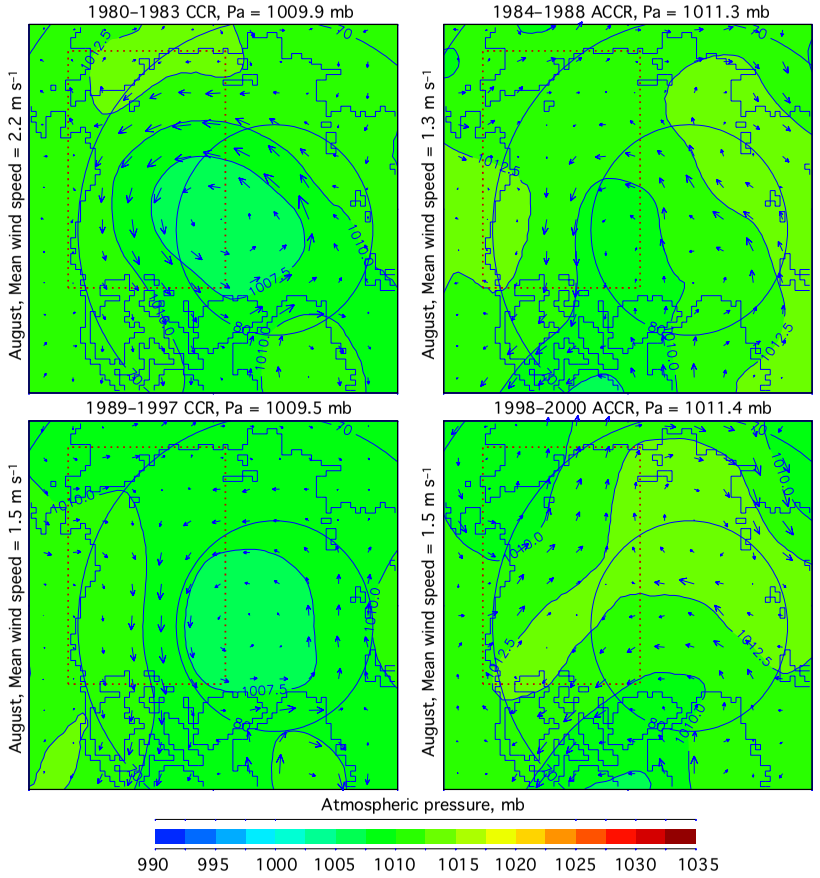

Figure 32. Observed SLP and calculated geostrophic wind in August for years with cyclonic (CCR) and anticyclonic (ACCR) circulation regimes. “Pa” and “Mean wind speed” show SLP and wind speed averaged over the box limited by the dotted line.

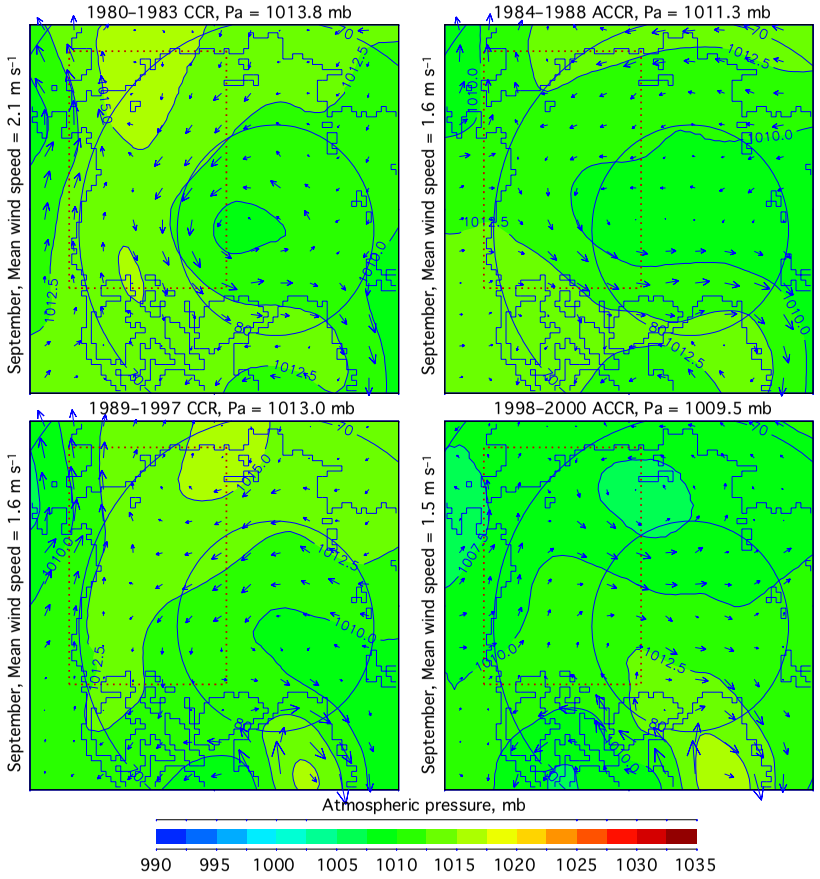

Figure 33. Observed SLP and calculated geostrophic wind in September for years with cyclonic (CCR) and anticyclonic (ACCR) circulation regimes. “Pa” and “Mean wind speed” show SLP and wind speed averaged over the box limited by the dotted line.

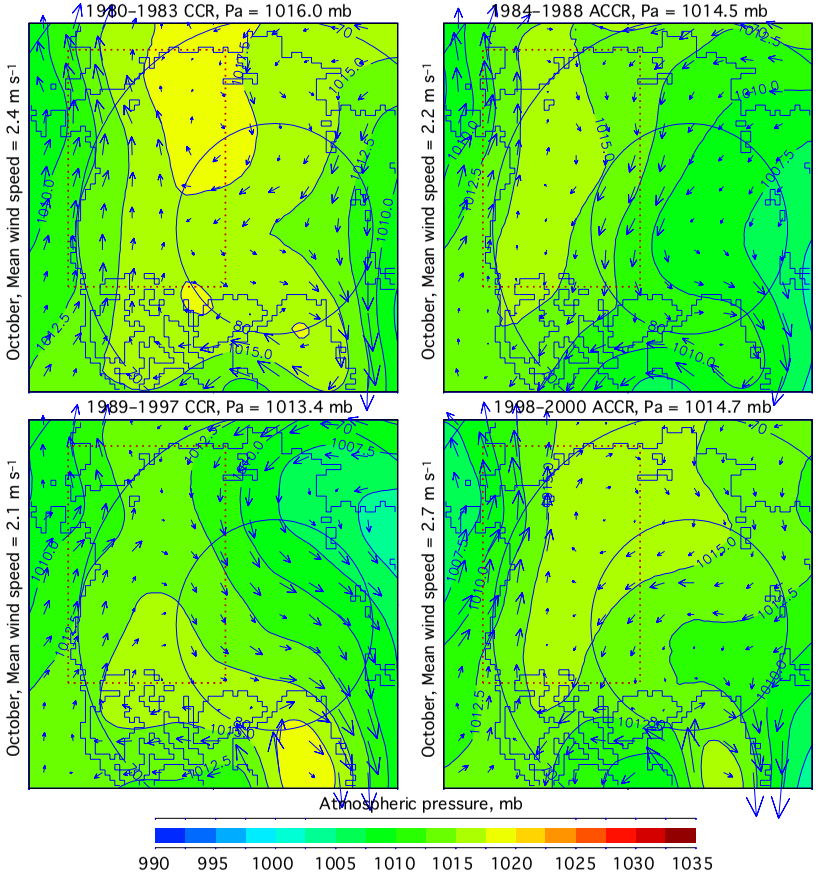

Figure 34. Observed SLP and calculated geostrophic wind in October for years with cyclonic (CCR) and anticyclonic (ACCR) circulation regimes. “Pa” and “Mean wind speed” show SLP and wind speed averaged over the box limited by the dotted line.

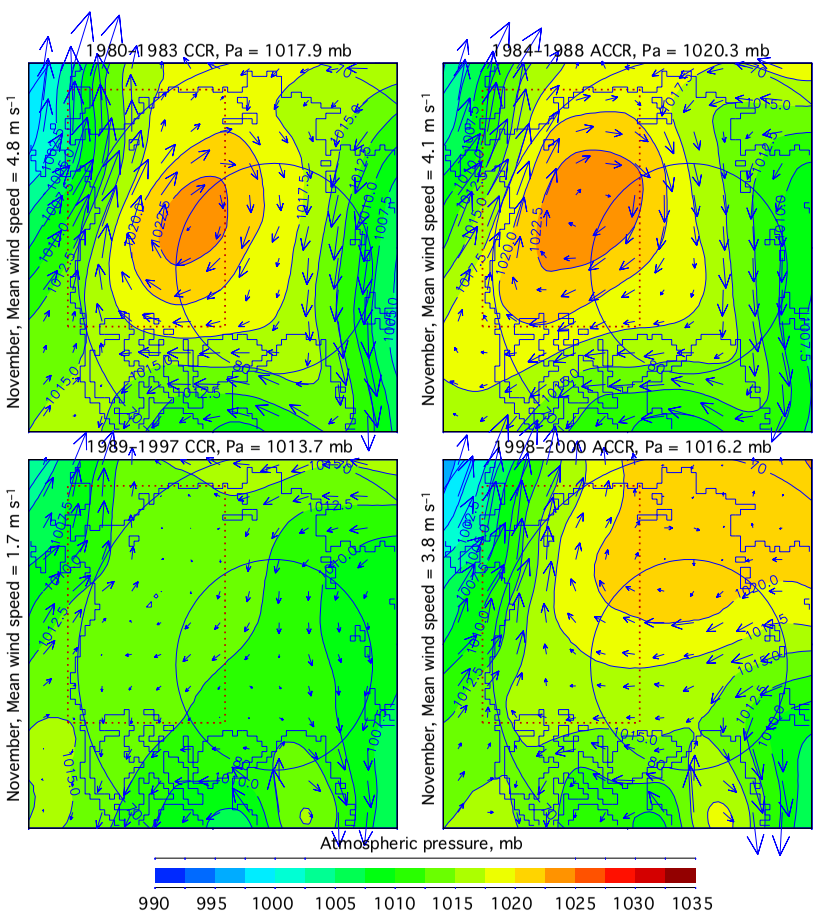

Figure 35. Observed SLP and calculated geostrophic wind in November for years with cyclonic (CCR) and anticyclonic (ACCR) circulation regimes. “Pa” and “Mean wind speed” show SLP and wind speed averaged over the box limited by the dotted line.

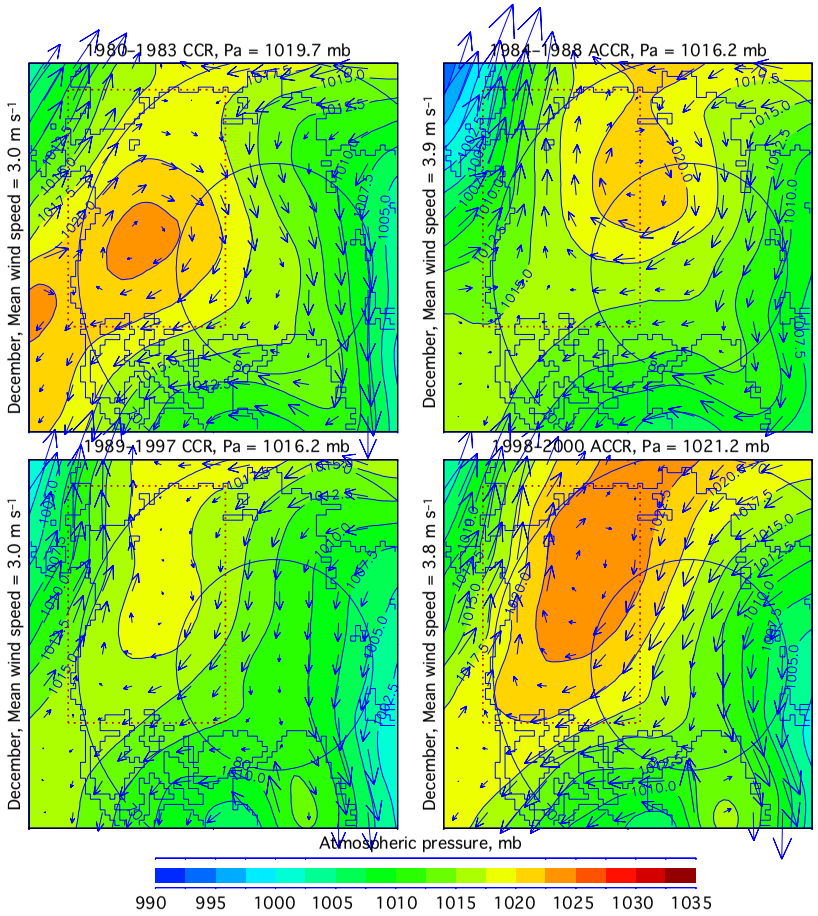

Figure 36. Observed SLP and calculated geostrophic wind in December for years with cyclonic (CCR) and anticyclonic (ACCR) circulation regimes. “Pa” and “Mean wind speed” show SLP and wind speed averaged over the box limited by the dotted line.

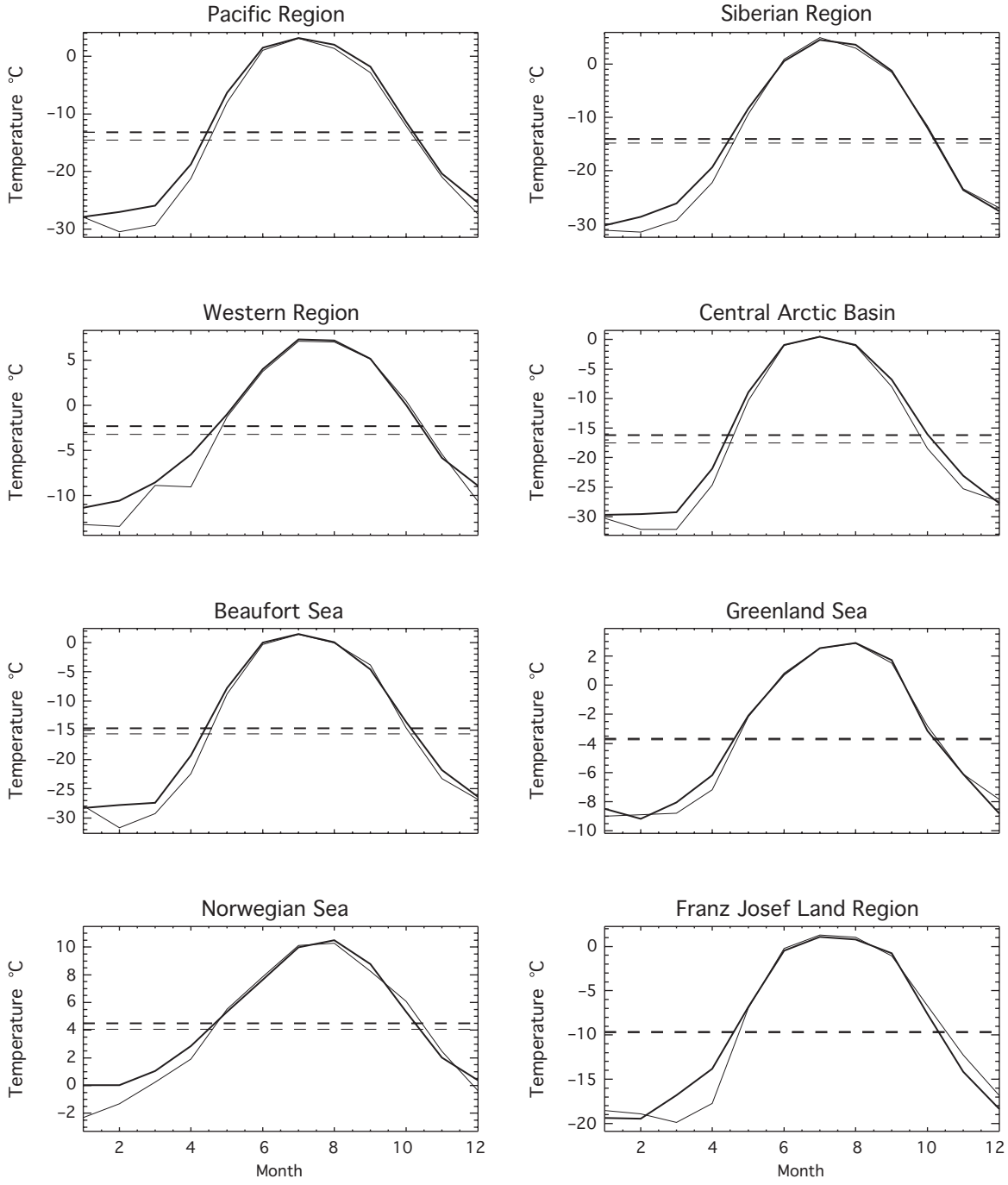

Figure 37. Monthly mean (solid lines) and annual mean (straight horizontal dashed lines) SAT averaged over all ACCR (thin lines) and CCR (thick lines) years. Note that the temperature scale is different among regions.

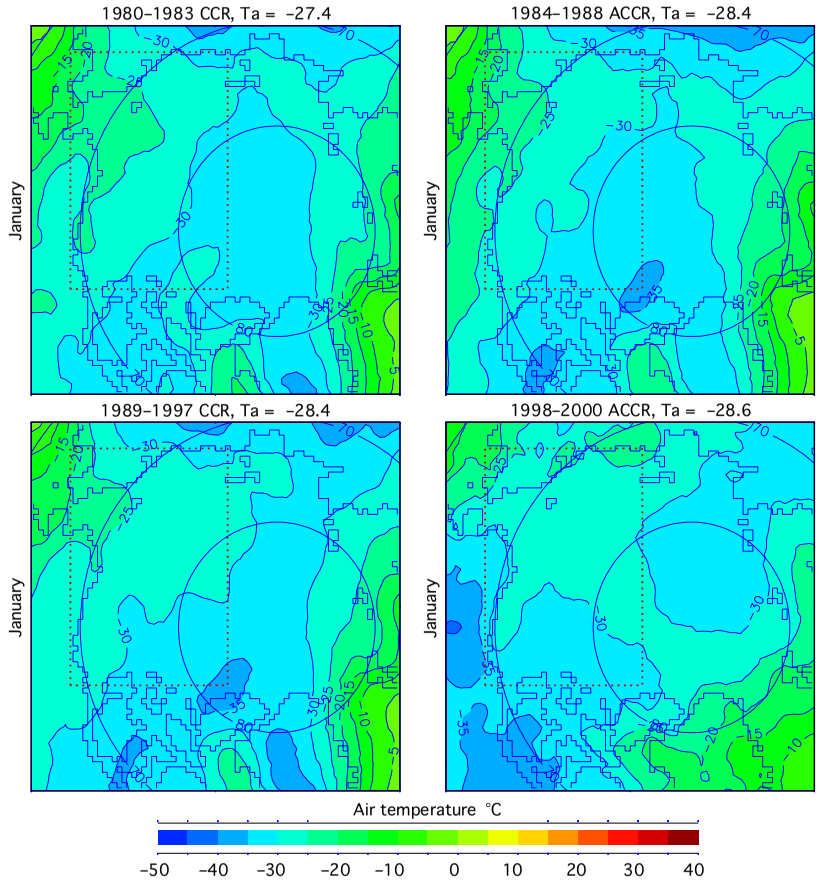

Figure 38. SAT in January for years with cyclonic (CCR) and anticyclonic (ACCR) circulation regimes. “Ta” shows SAT averaged over the box limited by the dotted line.

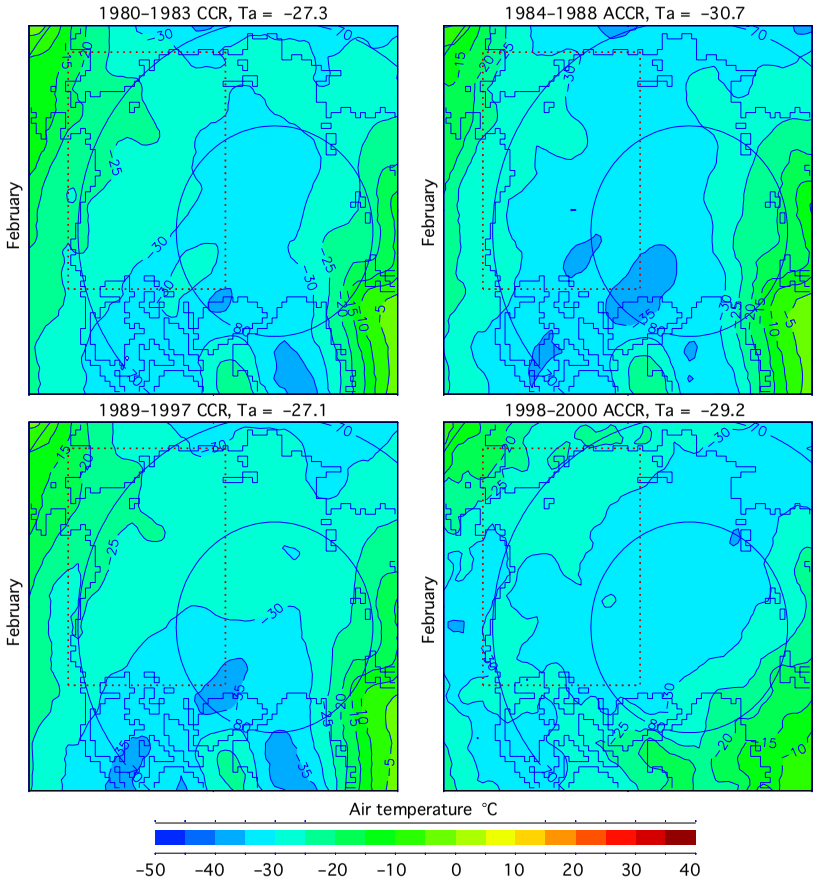

Figure 39. SAT in February for years with cyclonic (CCR) and anticyclonic (ACCR) circulation regimes. “Ta” shows SAT averaged over the box limited by the dotted line.

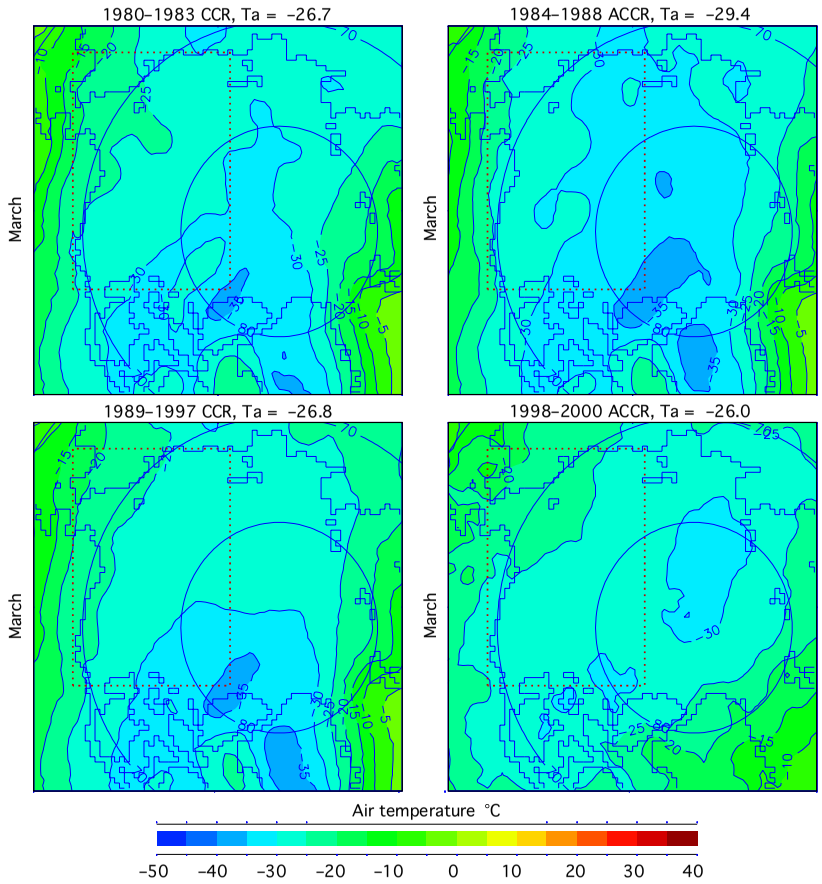

Figure 40. SAT in March for years with cyclonic (CCR) and anticyclonic (ACCR) circulation regimes. “Ta” shows SAT averaged over the box limited by the dotted line.

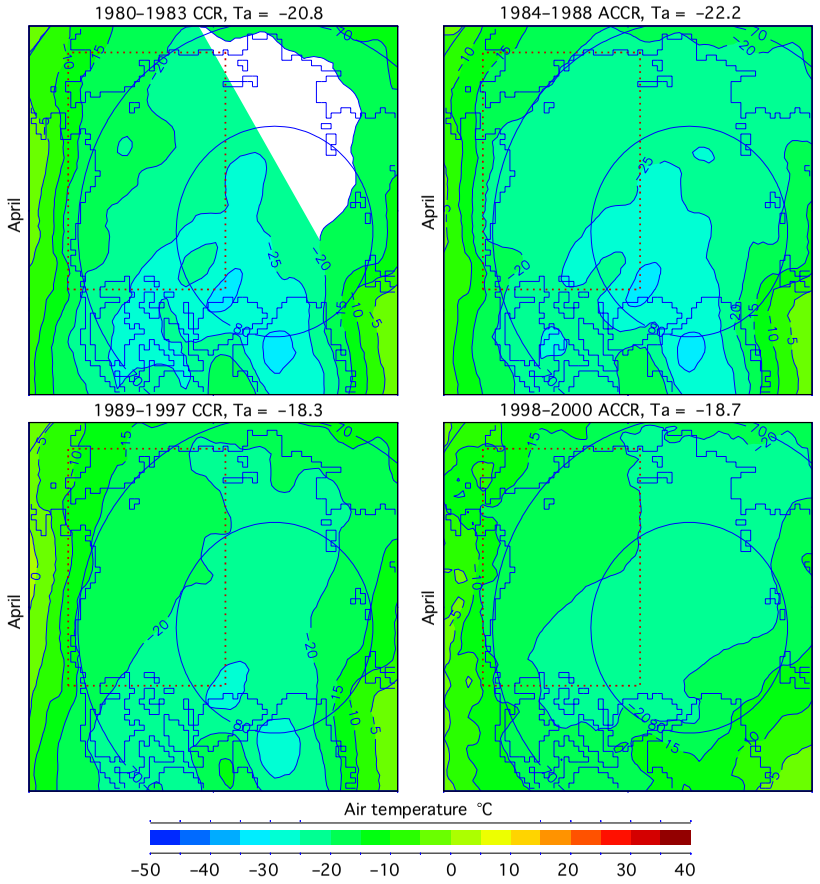

Figure 41. SAT in April for years with cyclonic (CCR) and anticyclonic (ACCR) circulation regimes. “Ta” shows SAT averaged over the box limited by the dotted line.

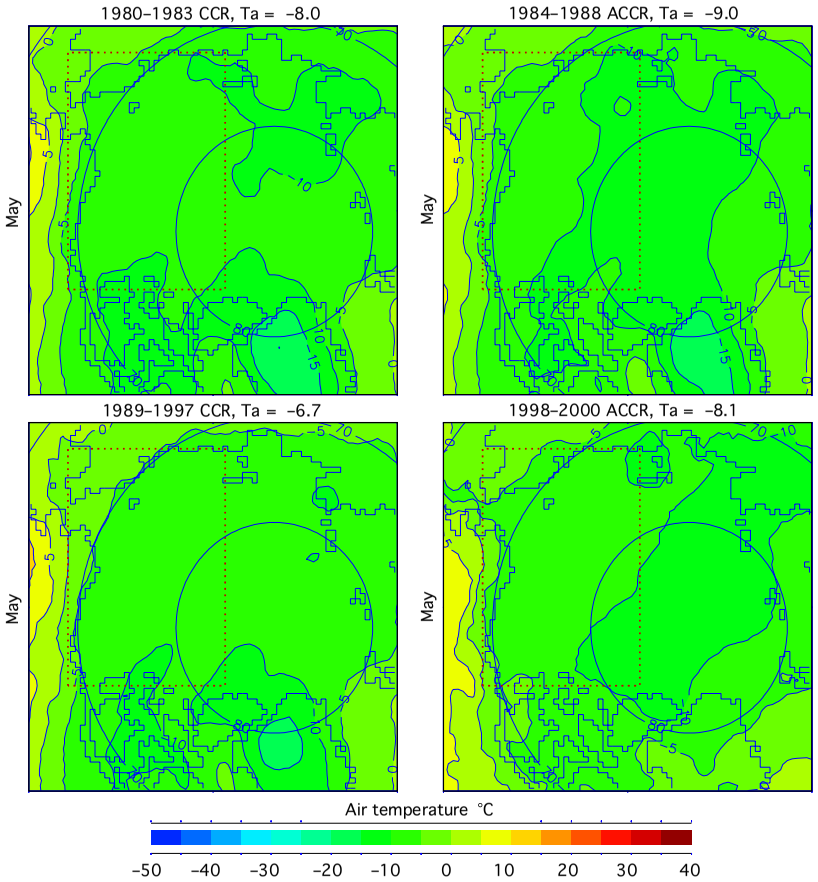

Figure 42. SAT in May for years with cyclonic (CCR) and anticyclonic (ACCR) circulation regimes. “Ta” shows SAT averaged over the box limited by the dotted line.

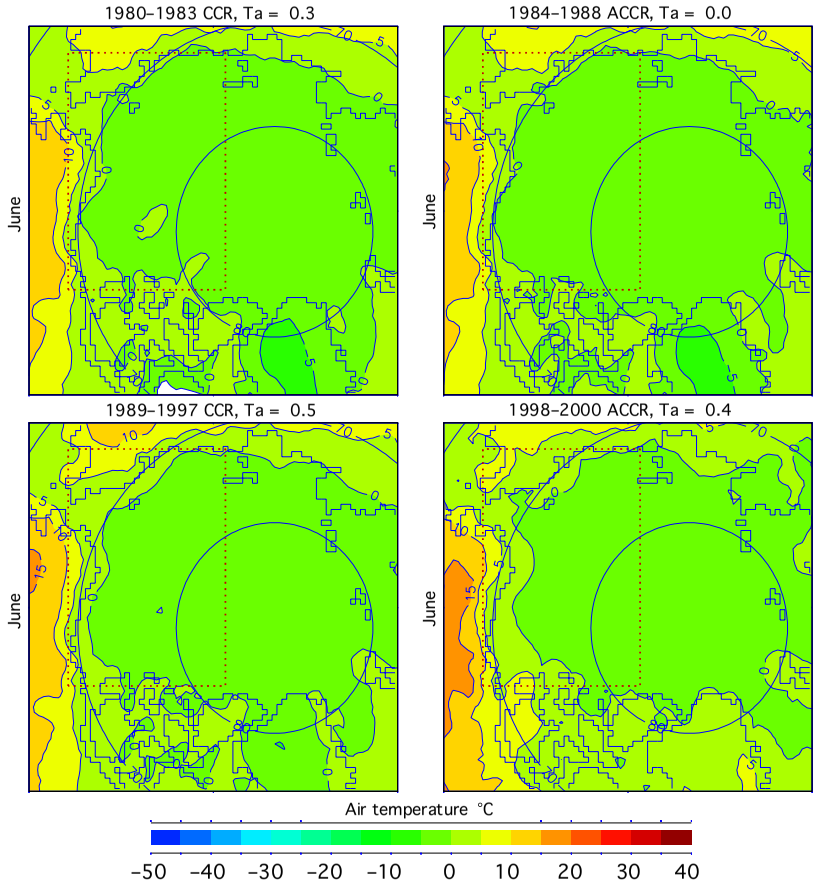

Figure 43. SAT in June for years with cyclonic (CCR) and anticyclonic (ACCR) circulation regimes. “Ta” shows SAT averaged over the box limited by the dotted line.

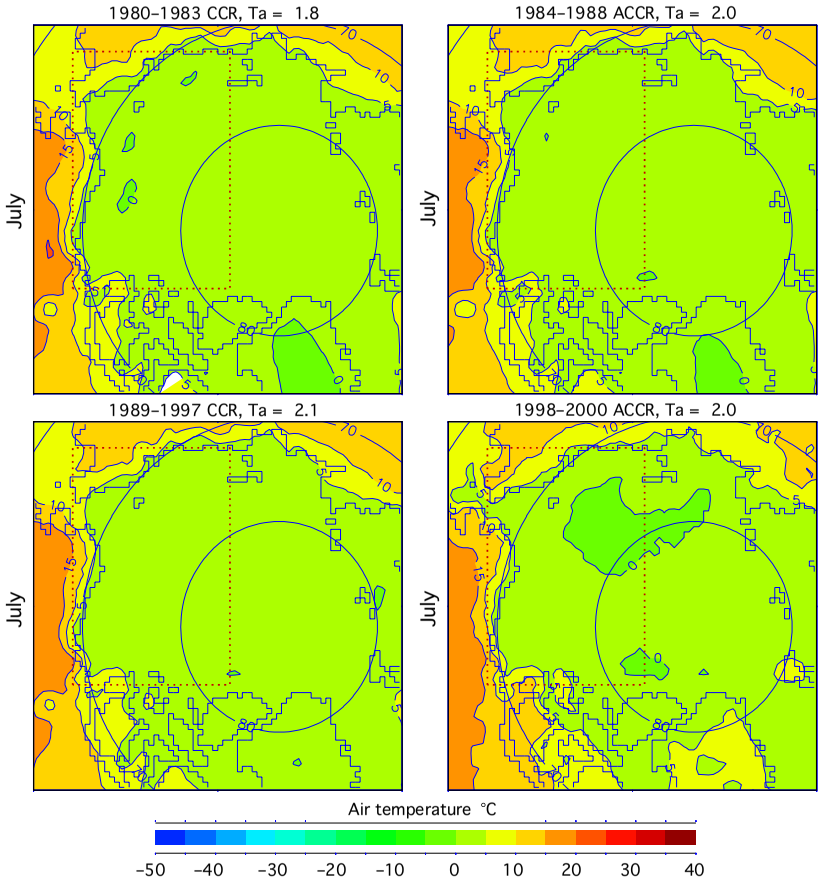

Figure 44. SAT in July for years with cyclonic (CCR) and anticyclonic (ACCR) circulation regimes. “Ta” shows SAT averaged over the box limited by the dotted line.

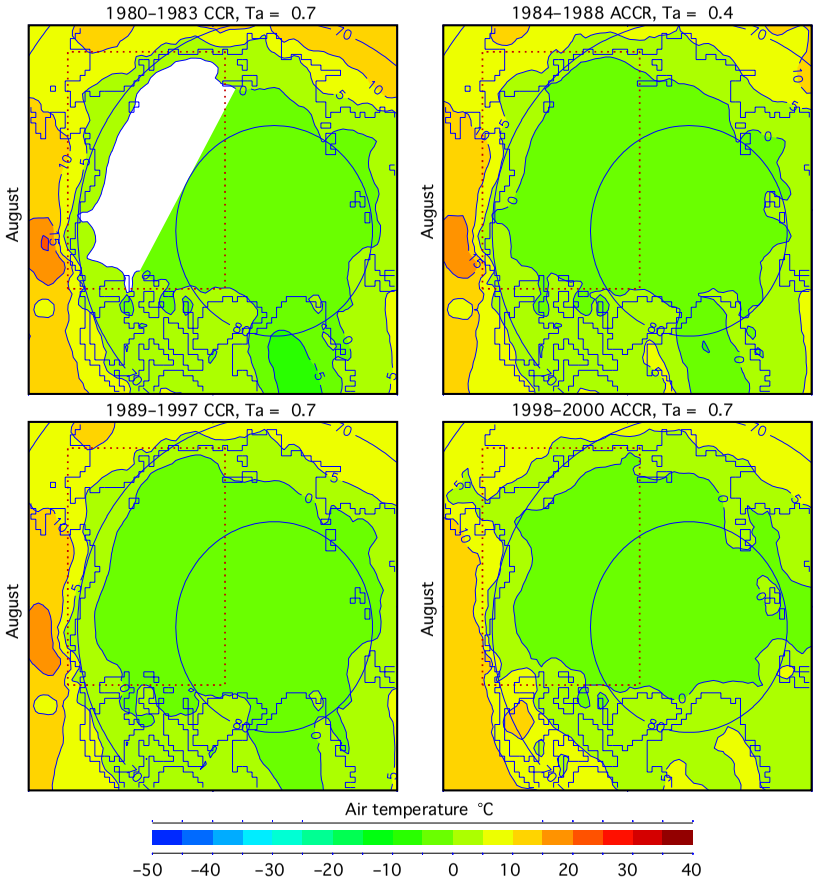

Figure 45. SAT in August for years with cyclonic (CCR) and anticyclonic (ACCR) circulation regimes. “Ta” shows SAT averaged over the box limited by the dotted line.

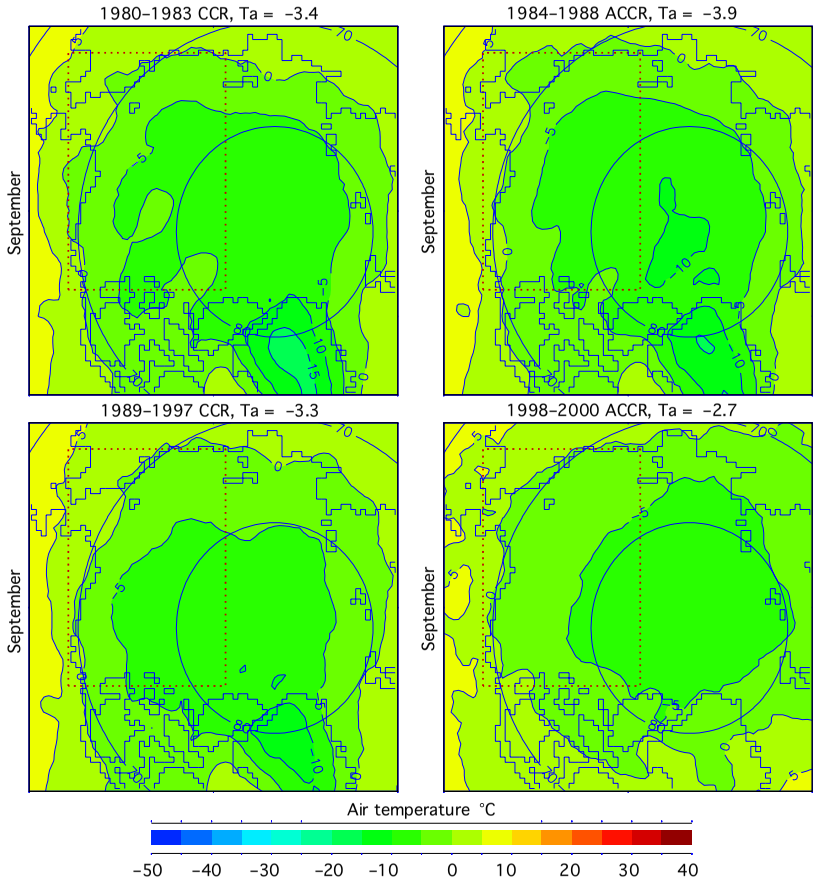

Figure 46. SAT in September for years with cyclonic (CCR) and anticyclonic (ACCR) circulation regimes. “Ta” shows SAT averaged over the box limited by the dotted line.

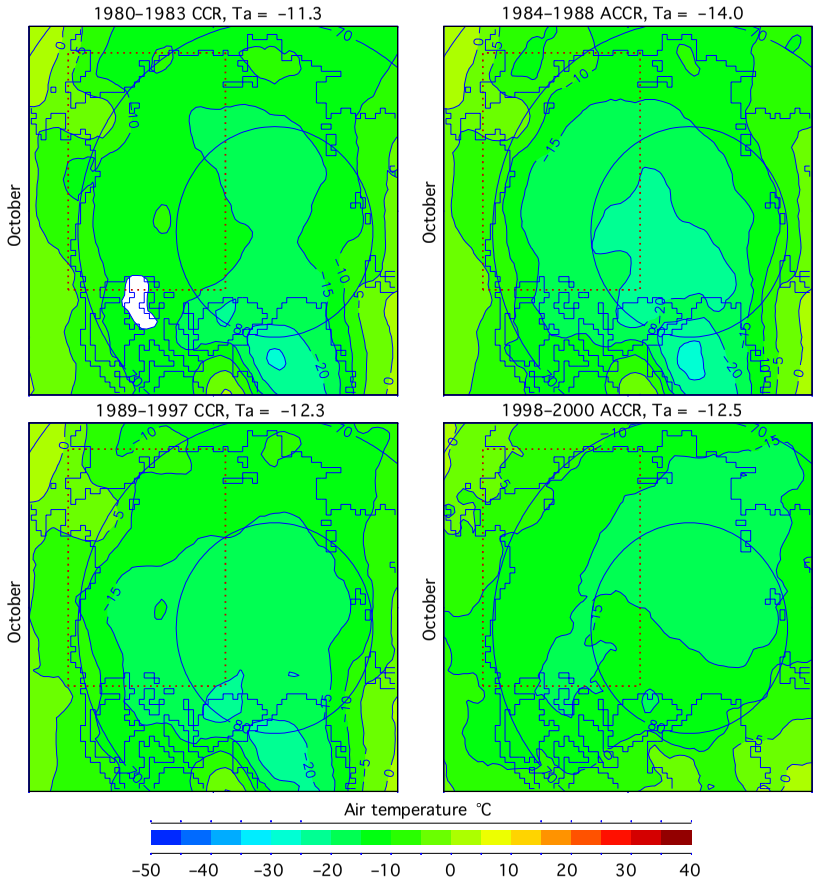

Figure 47. SAT in October for years with cyclonic (CCR) and anticyclonic (ACCR) circulation regimes. “Ta” shows SAT averaged over the box limited by the dotted line.

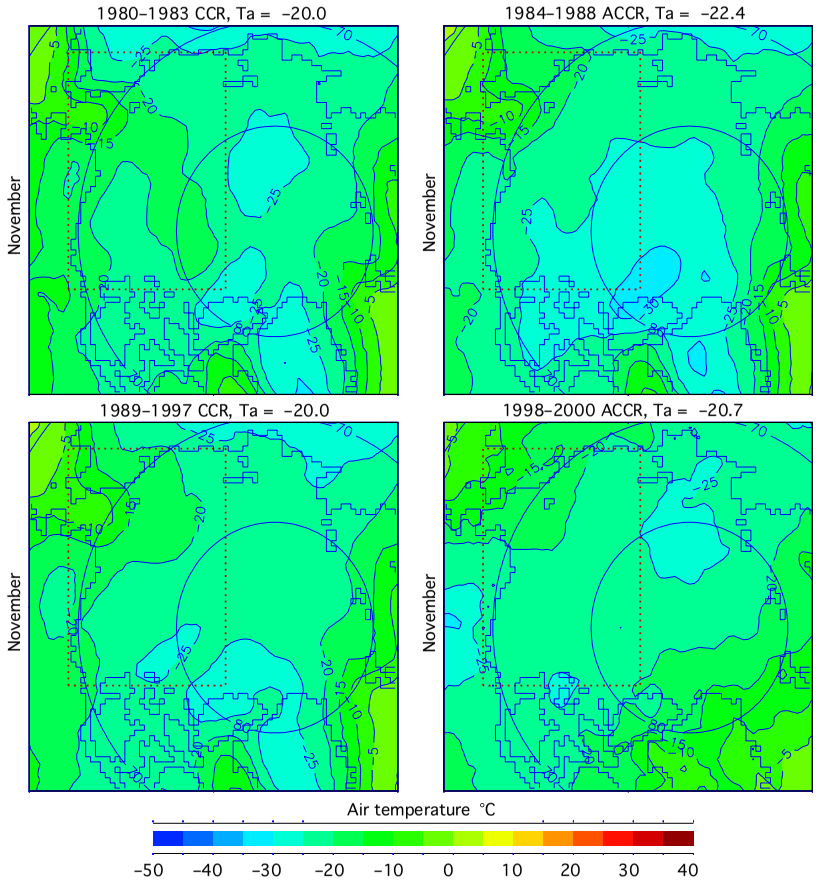

Figure 48. SAT in November for years with cyclonic (CCR) and anticyclonic (ACCR) circulation regimes. “Ta” shows SAT averaged over the box limited by the dotted line.

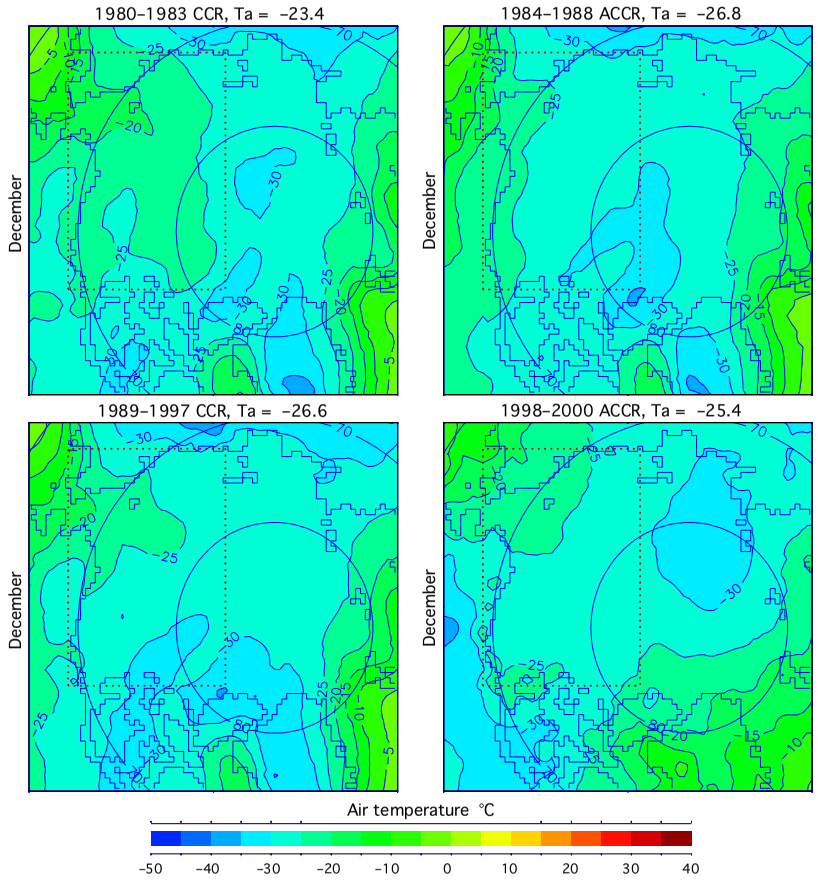

Figure 49. SAT in December for years with cyclonic (CCR) and anticyclonic (ACCR) circulation regimes. “Ta” shows SAT averaged over the box limited by the dotted line.

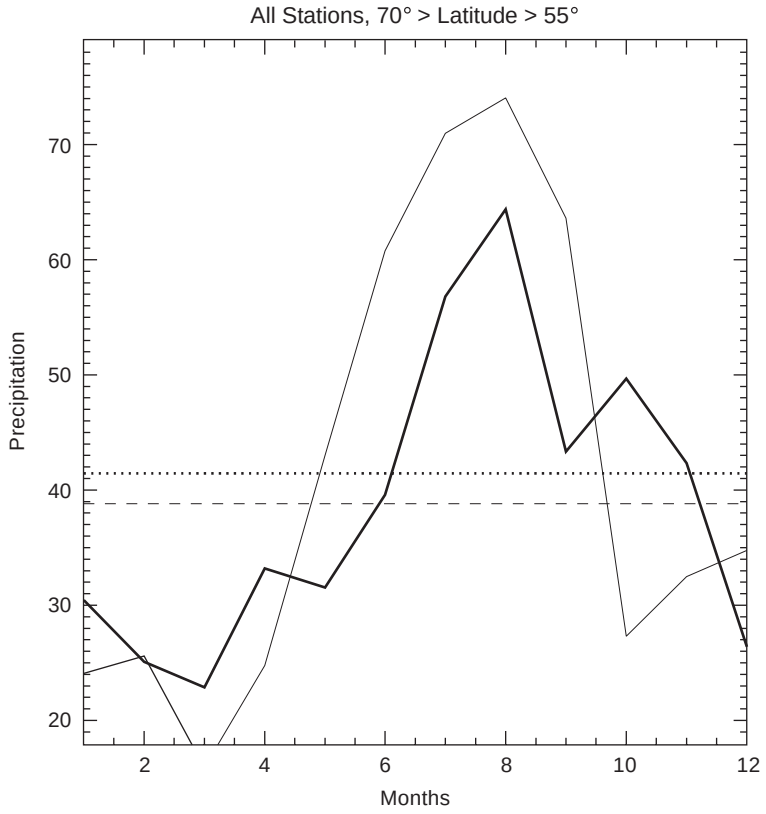

Figure 50. Monthly mean (solid lines) and annual mean (dashed lines) precipitation averaged over all ACCR (thin line) and CCR (thick line) years for the region dominated by land (latitude is less than 70°N and greater than 55°N).

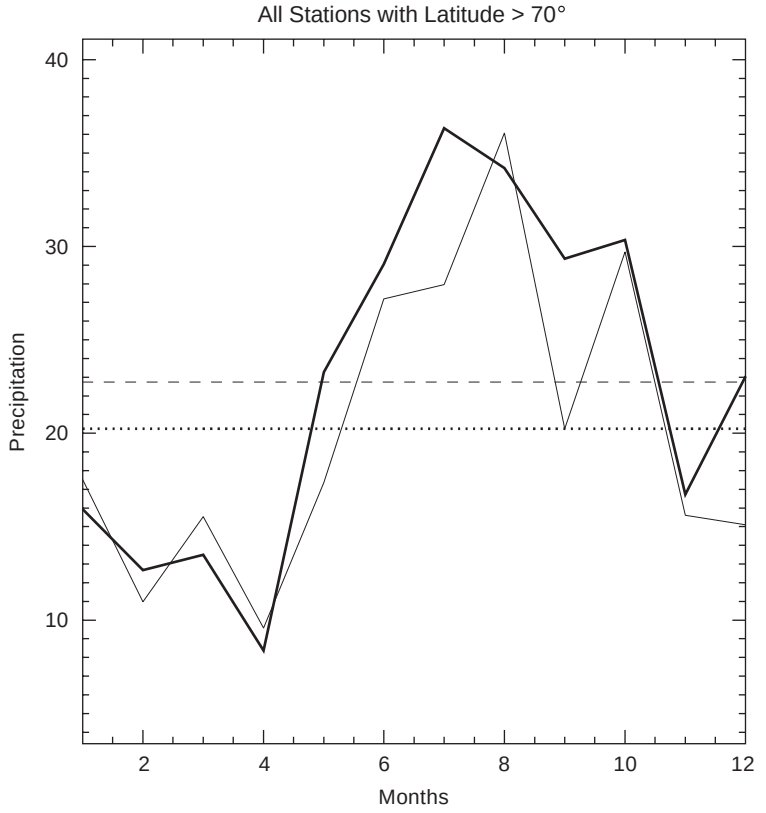

Figure 51. Monthly mean (solid lines) and annual mean (dashed lines) precipitation averaged over all ACCR (thin line) and CCR (thick line) years for the region dominated by the Arctic Ocean (latitude is greater than 70°N).

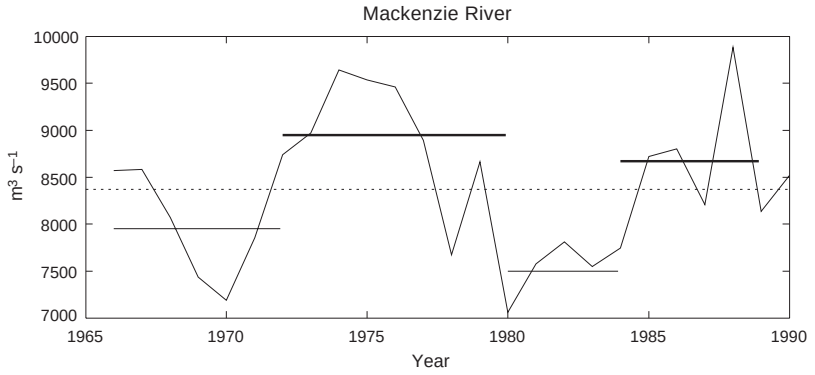

Figure 52. The 3-year smoothed Mackenzie River discharge time series. The regime mean river discharges for the cyclonic regimes are shown by thin lines and the regime mean discharges for anticyclonic regimes are shown by thick lines.

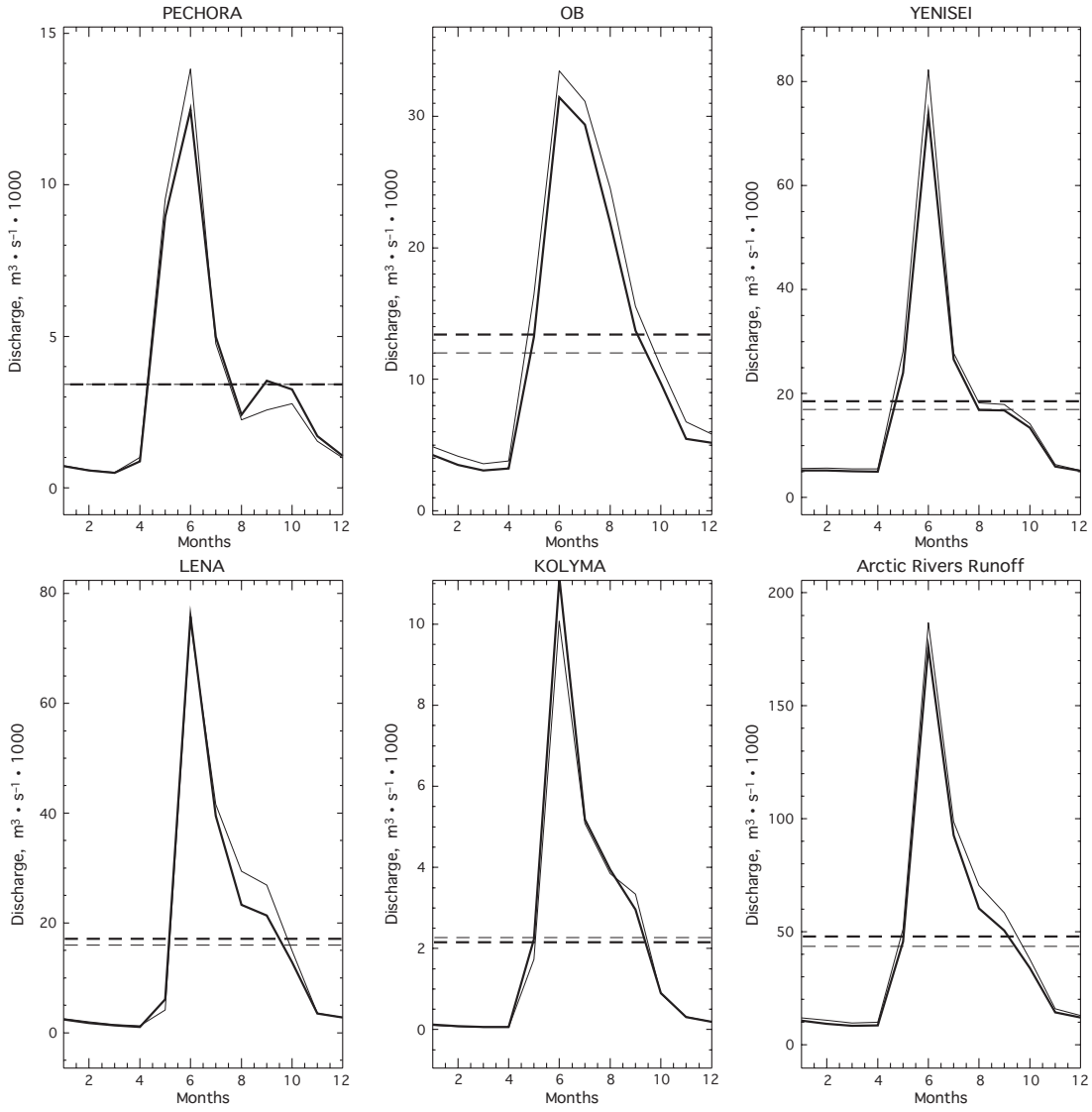

Figure 53. Monthly (solid lines) and annual (dashed lines) mean Siberian River discharges averaged over all ACCR (thin line) and CCR (thick line) years.

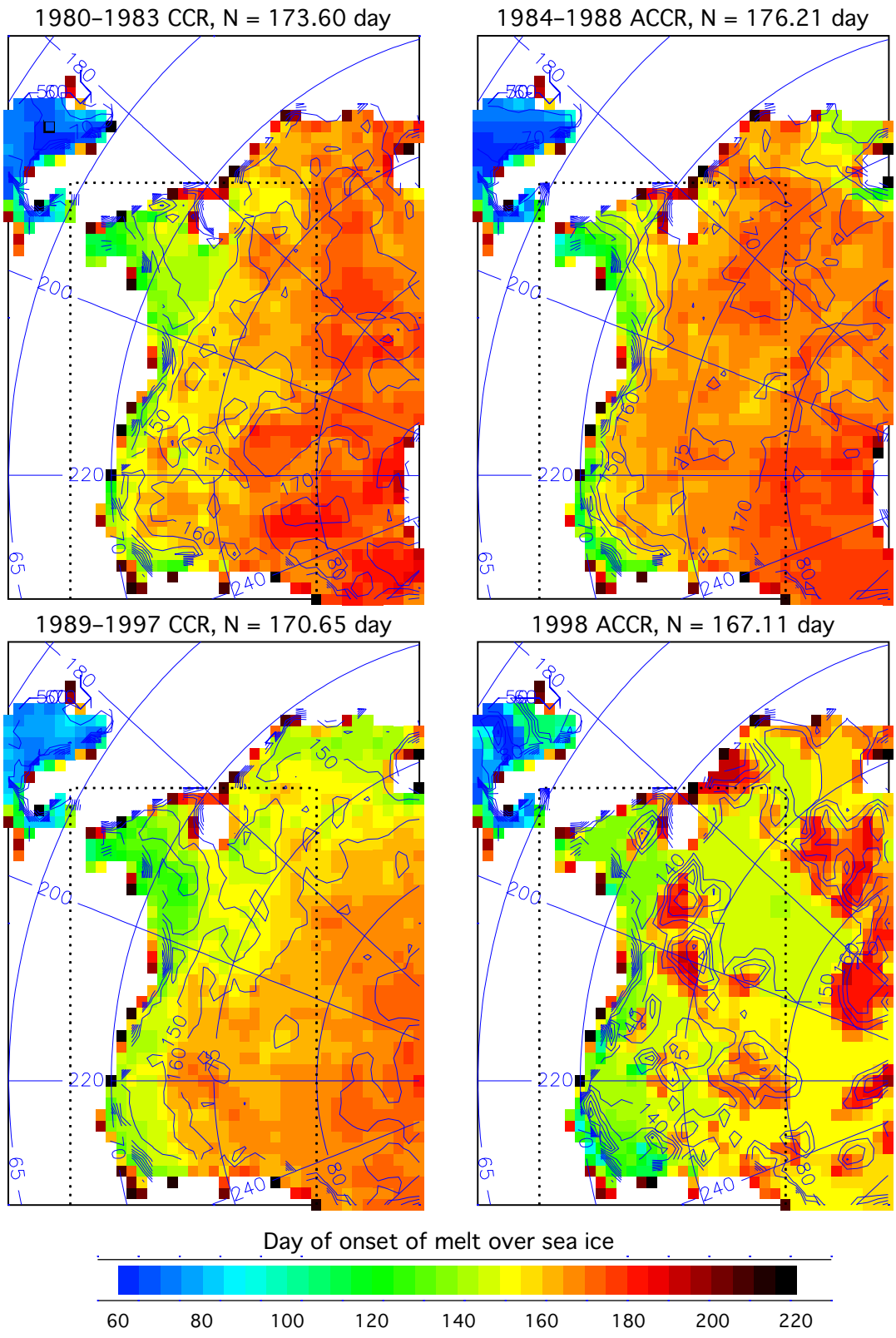

Figure 54. Regime mean day of onset of melt over sea ice. "N" shows the mean day of onset of melt over sea ice averaged over the region limited by the dotted line.

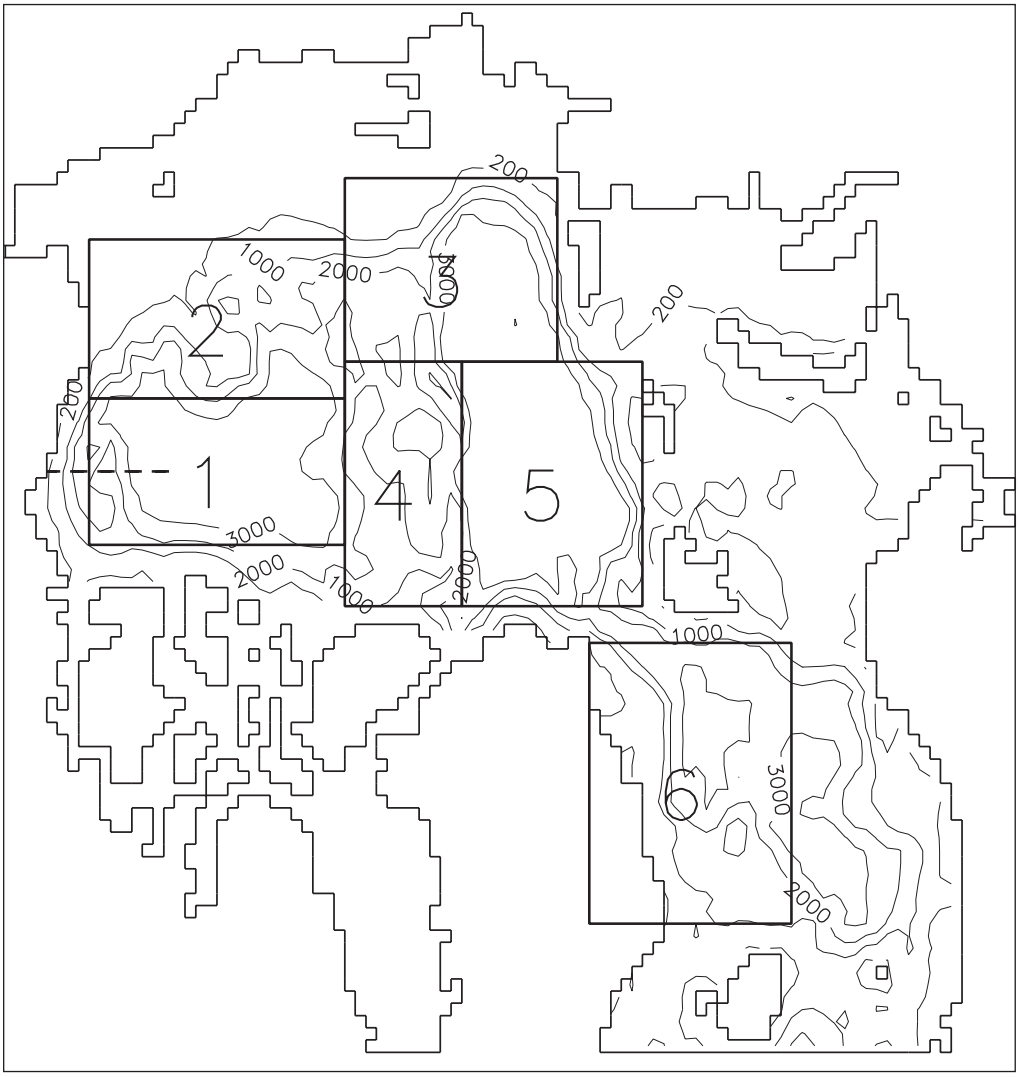

Figure 55. 3-D Arctic Ocean model domain.

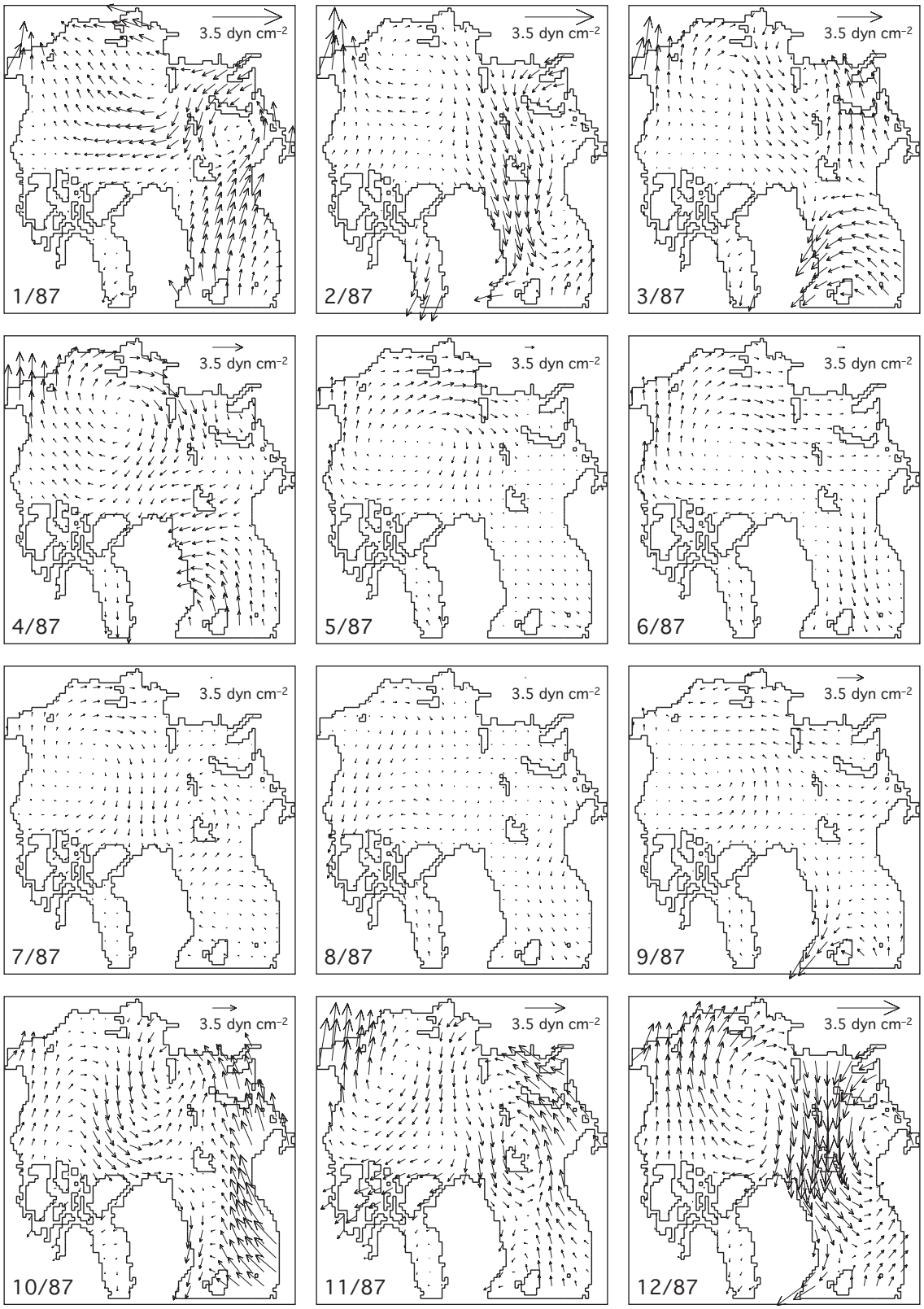

Figure 56. Wind stresses for 1987 (ACCR).

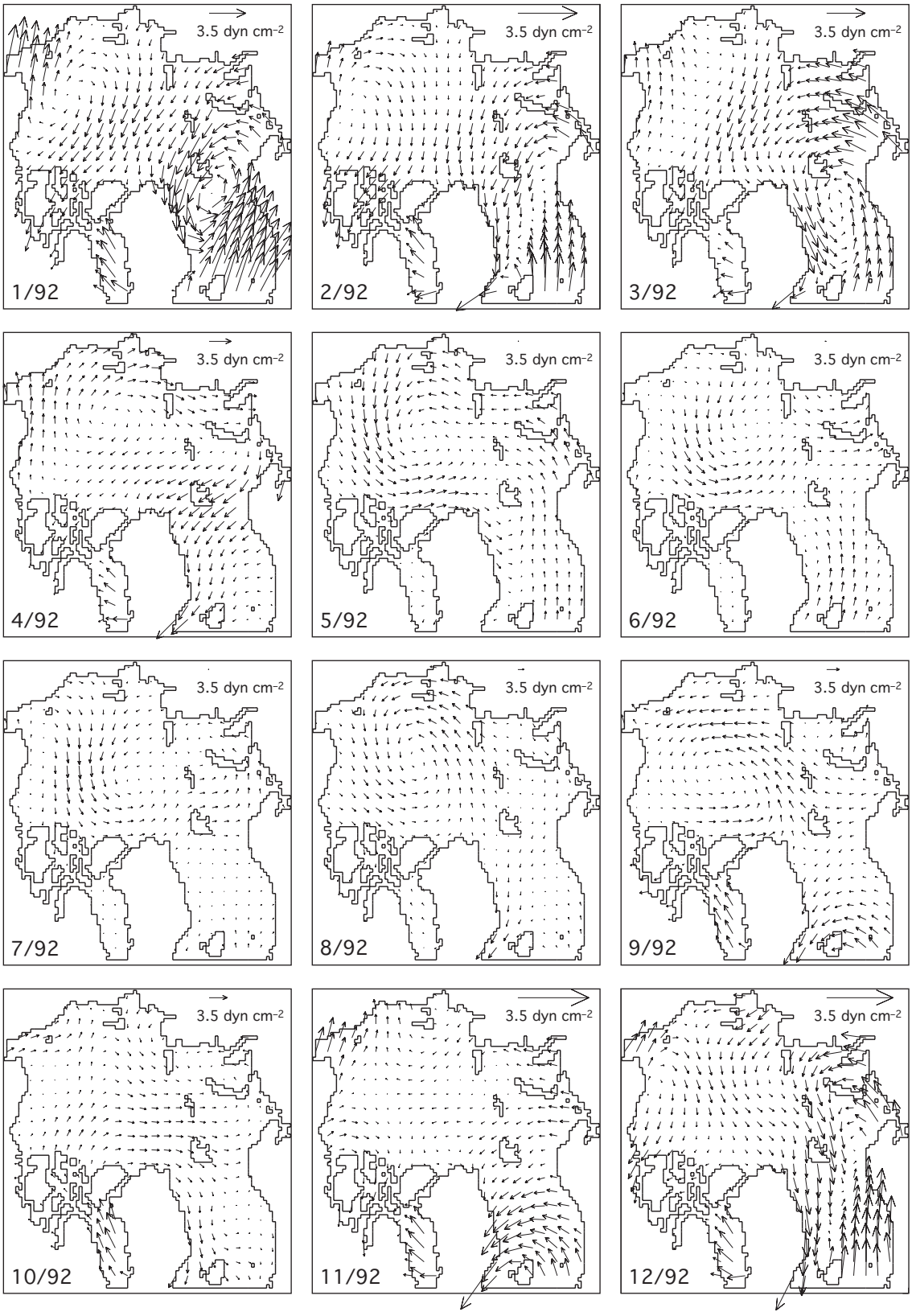

Figure 57. Wind stresses for 1992 (CCR).

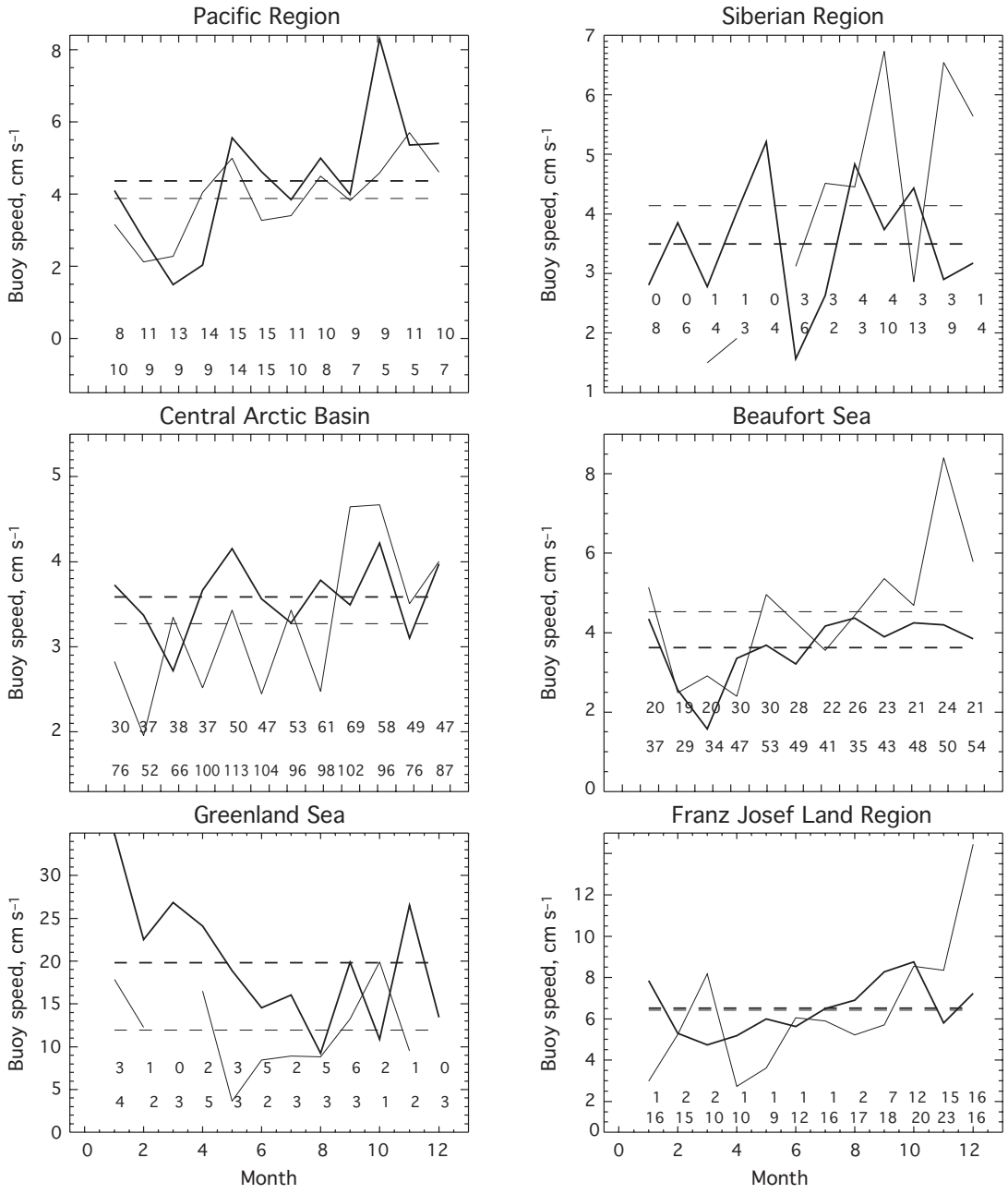

Figure 58. Monthly mean (solid lines) and annual mean (straight horizontal dashed lines) buoy drift speed averaged over all ACCR years (thin lines) and CCR years (thick lines). Numbers in the lower part of the panels show the number of buoys used for averaging (upper row is for ACCR, lower row is for CCR). Note that the buoy speed scale is different among regions.

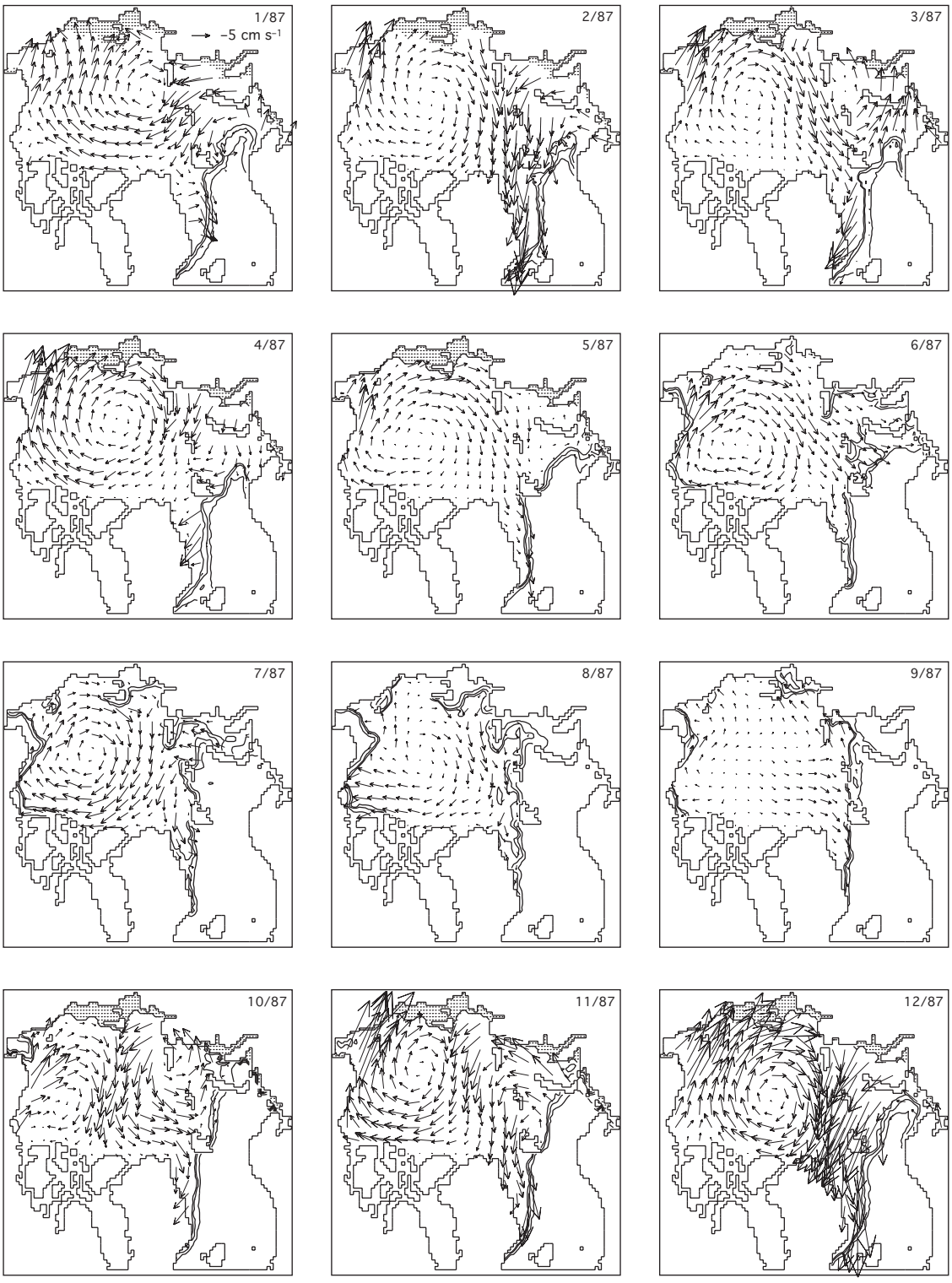

Figure 59. Computed monthly ice drift for 1987 (ACCR).

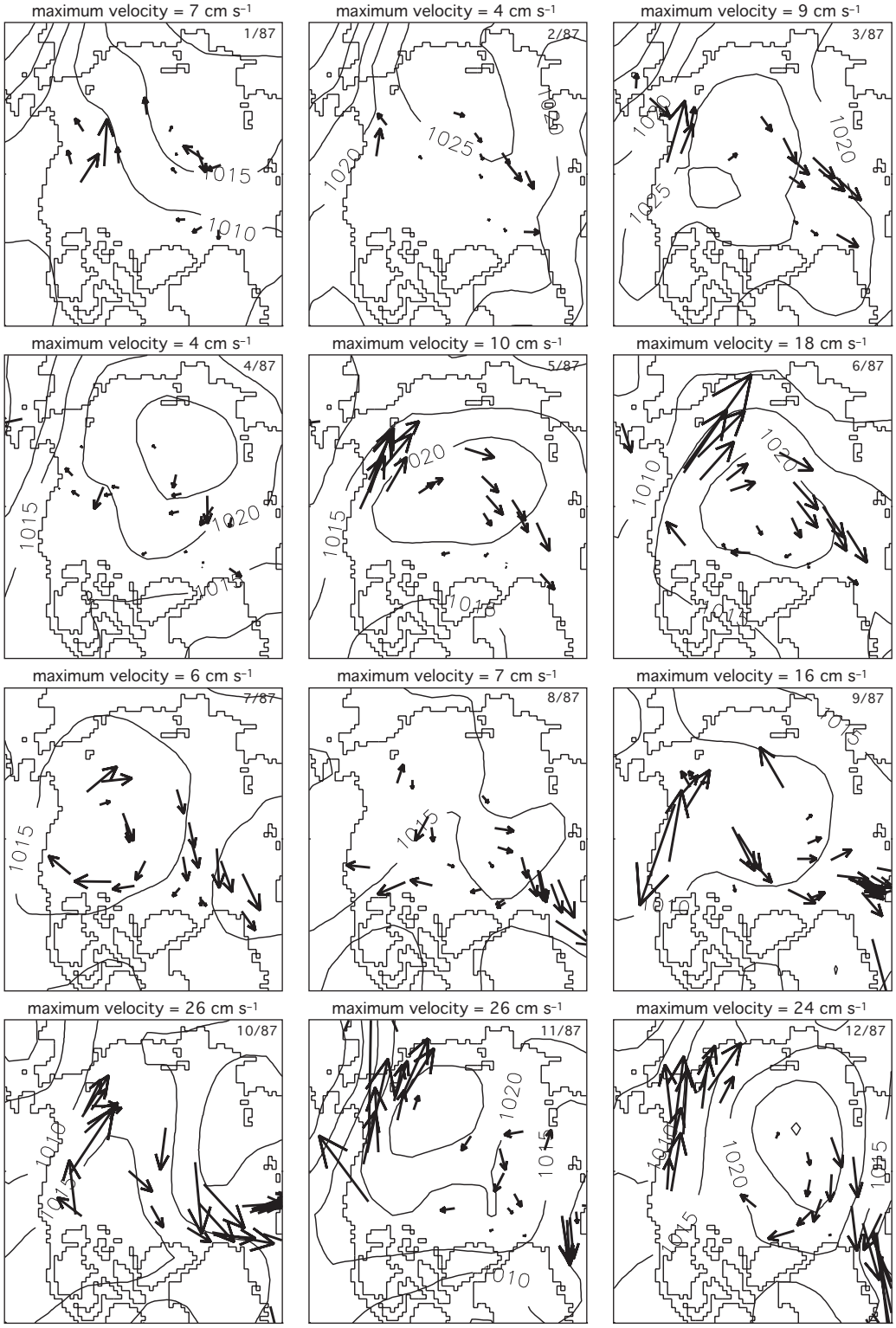

Figure 60. Monthly mean buoy drift and SLP distribution (hPa) in 1987 (ACCR).

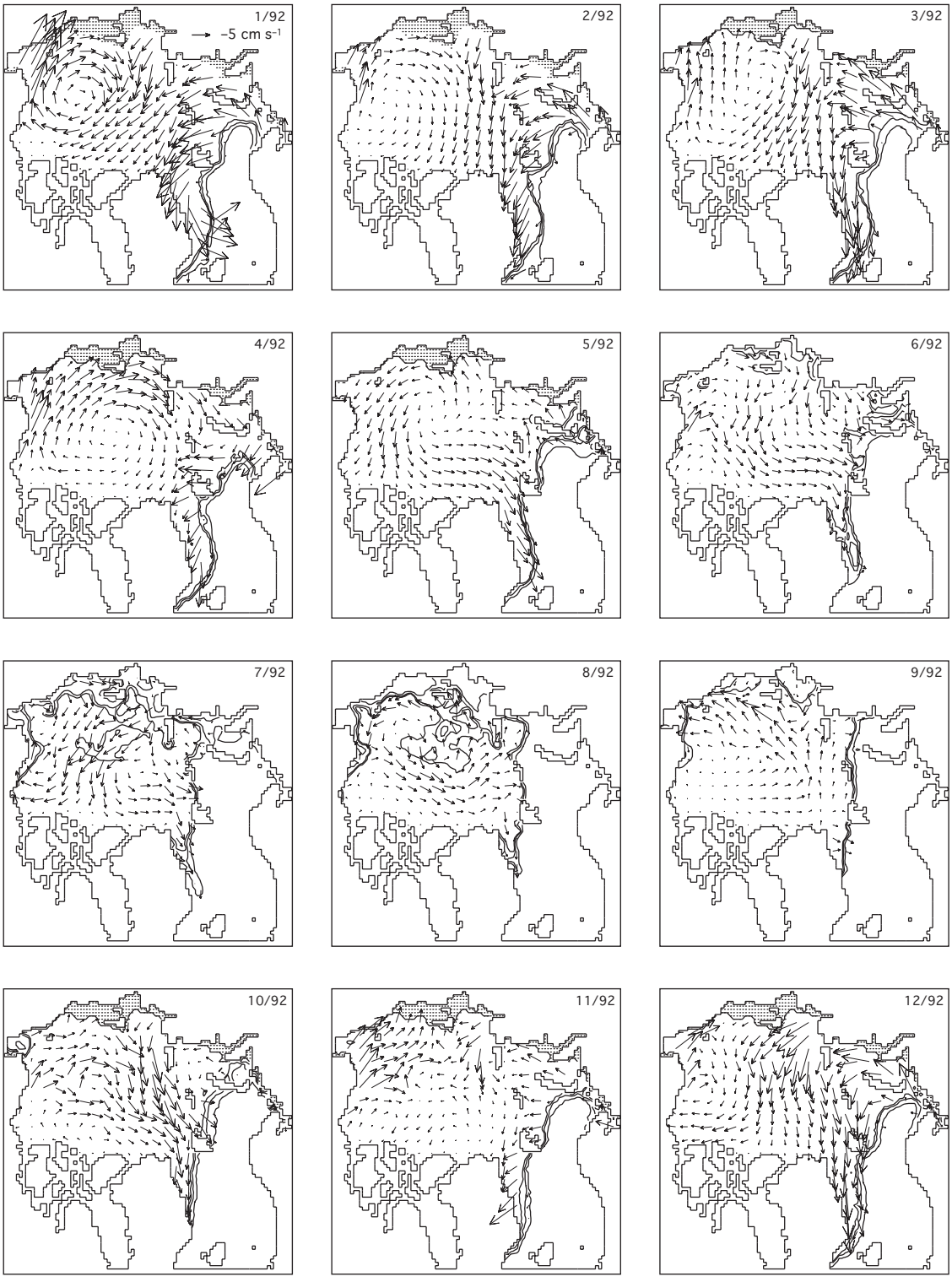

Figure 61. Computed monthly ice drift for 1992 (CCR).

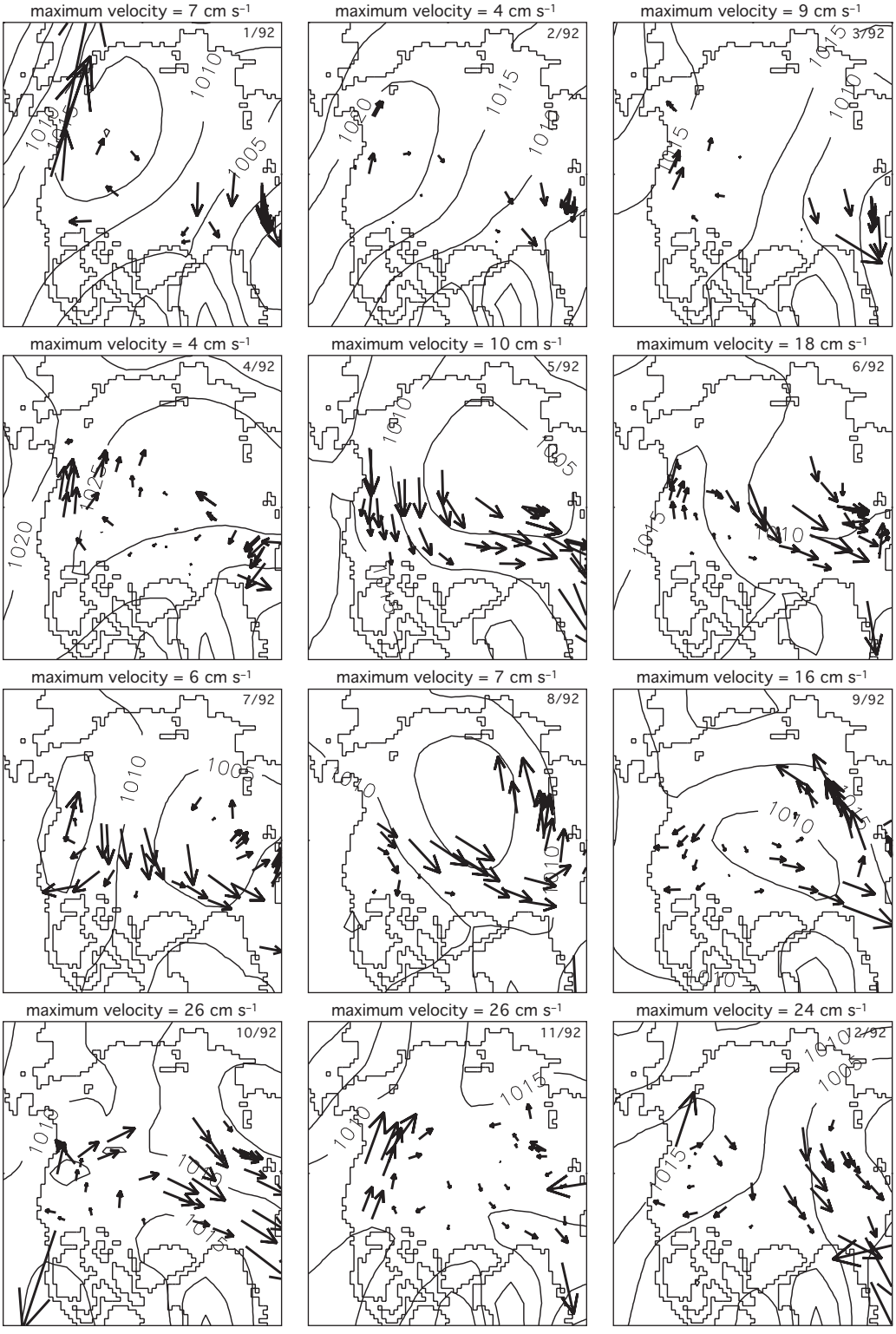

Figure 62. Monthly mean buoy drift and SLP distribution (hPa) in 1992 (CCR).

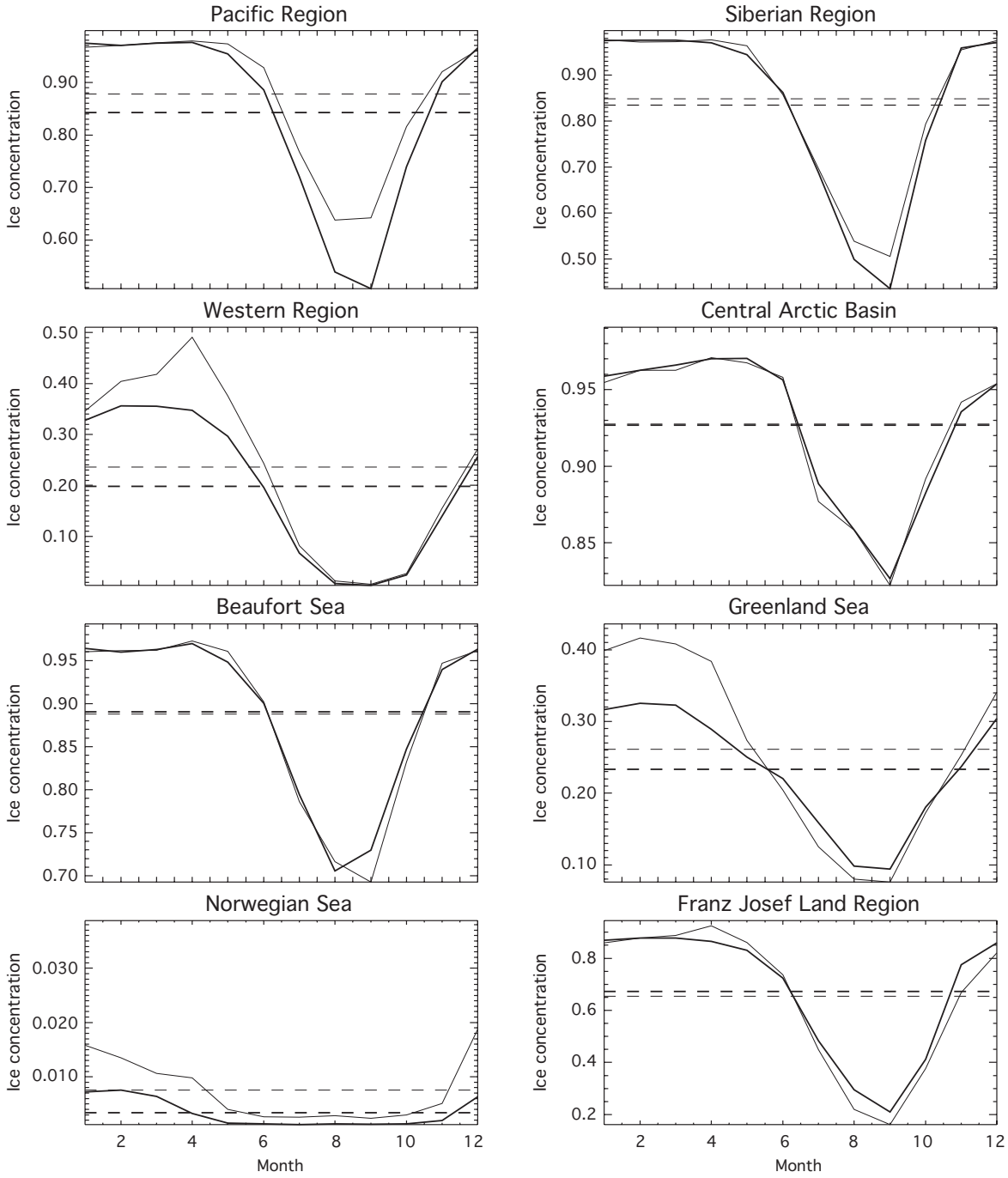

Figure 63. Monthly mean (solid lines) and annual mean (straight horizontal dashed lines) ice concentration (National Snow and Ice Data Center [1989] updated) averaged over all ACCR (thin lines) and CCR (thick lines) years. Note that the ice concentration scale is different among regions.

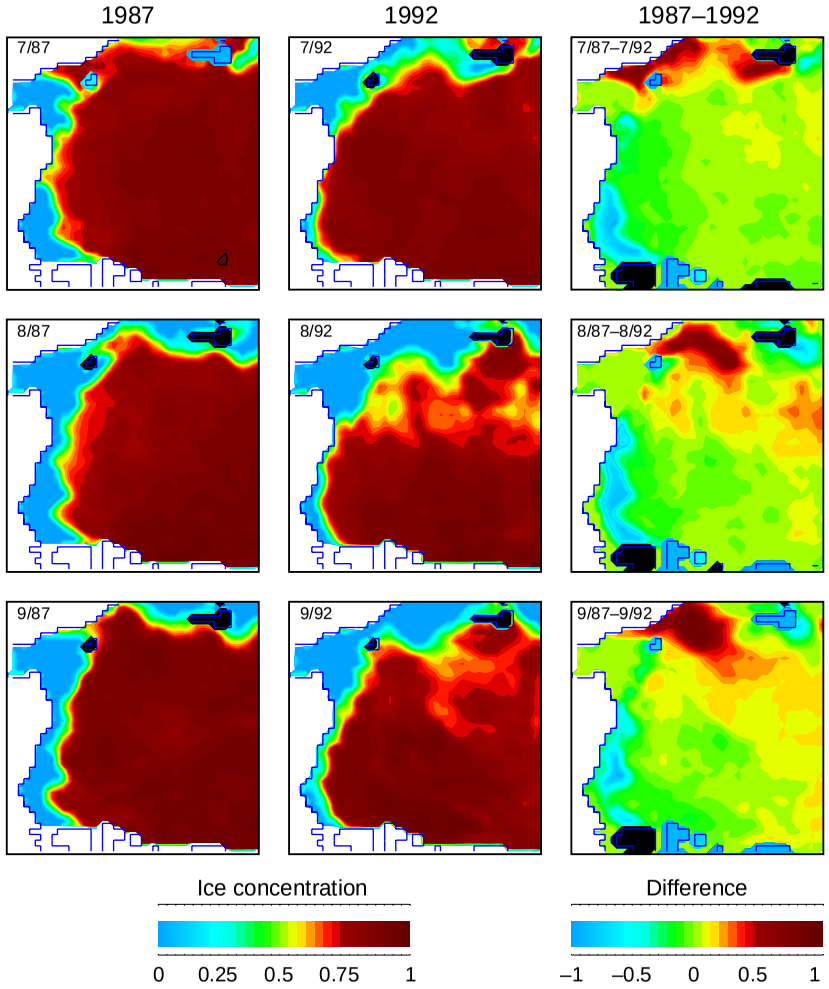

Figure 64. Summer observed sea ice concentration.

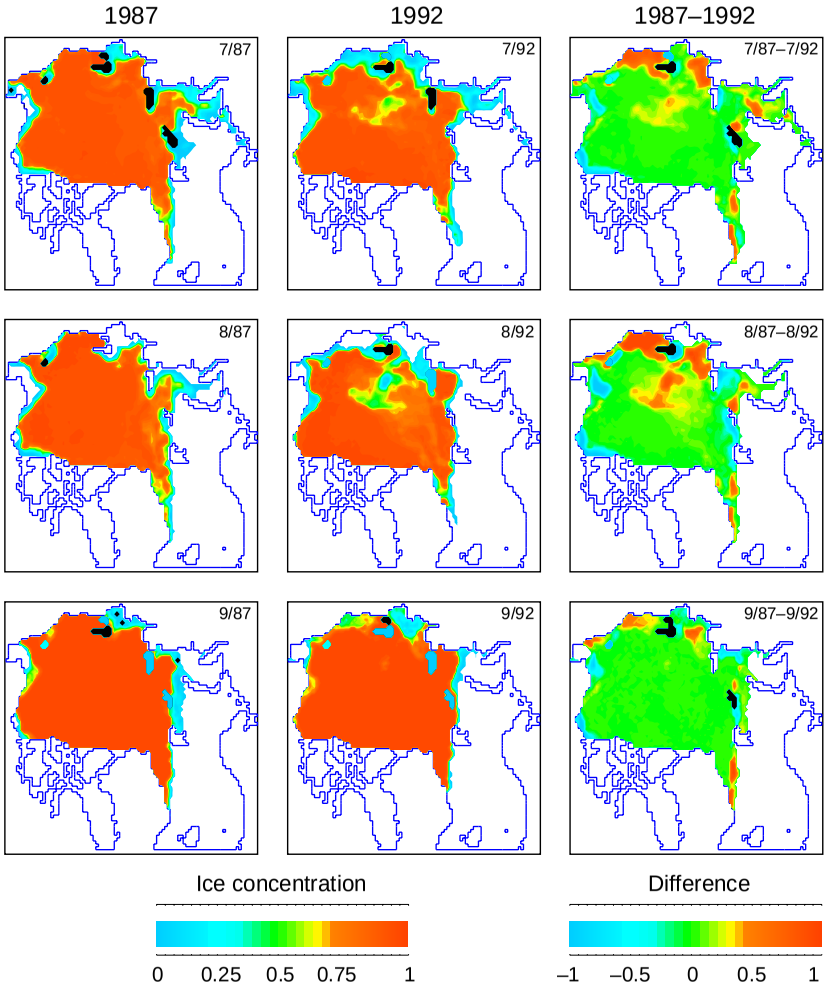

Figure 65. Summer simulated sea ice concentration.

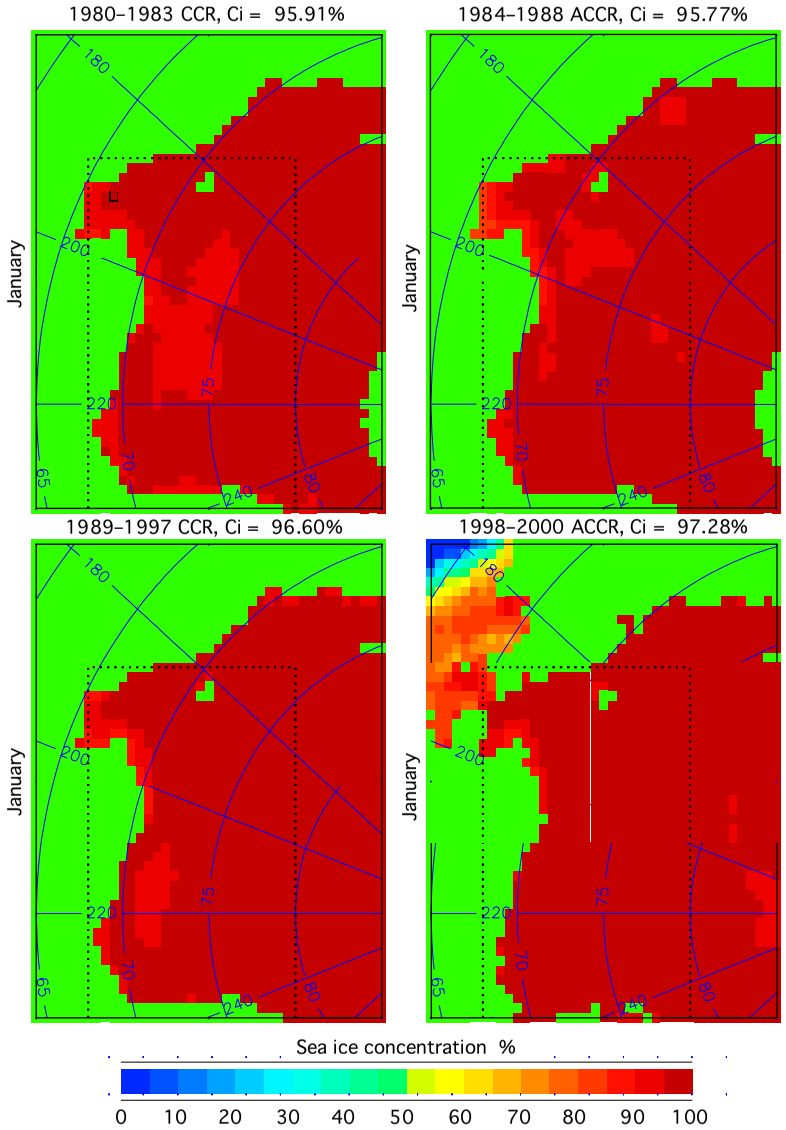

Figure 66. Observed sea ice concentration in January. "Ci" shows sea ice concentration averaged for the box limited by the dotted line.

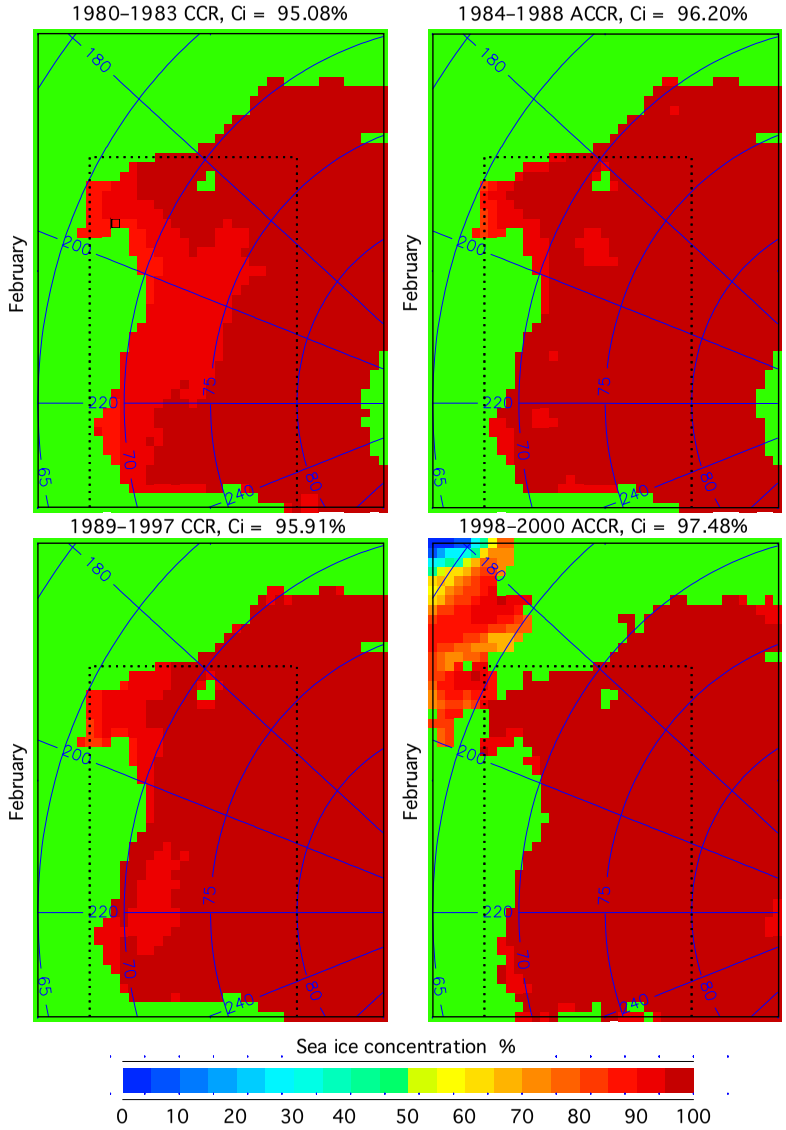

Figure 67. Observed sea ice concentration in February. "Ci" shows sea ice concentration averaged for the box limited by the dotted line.

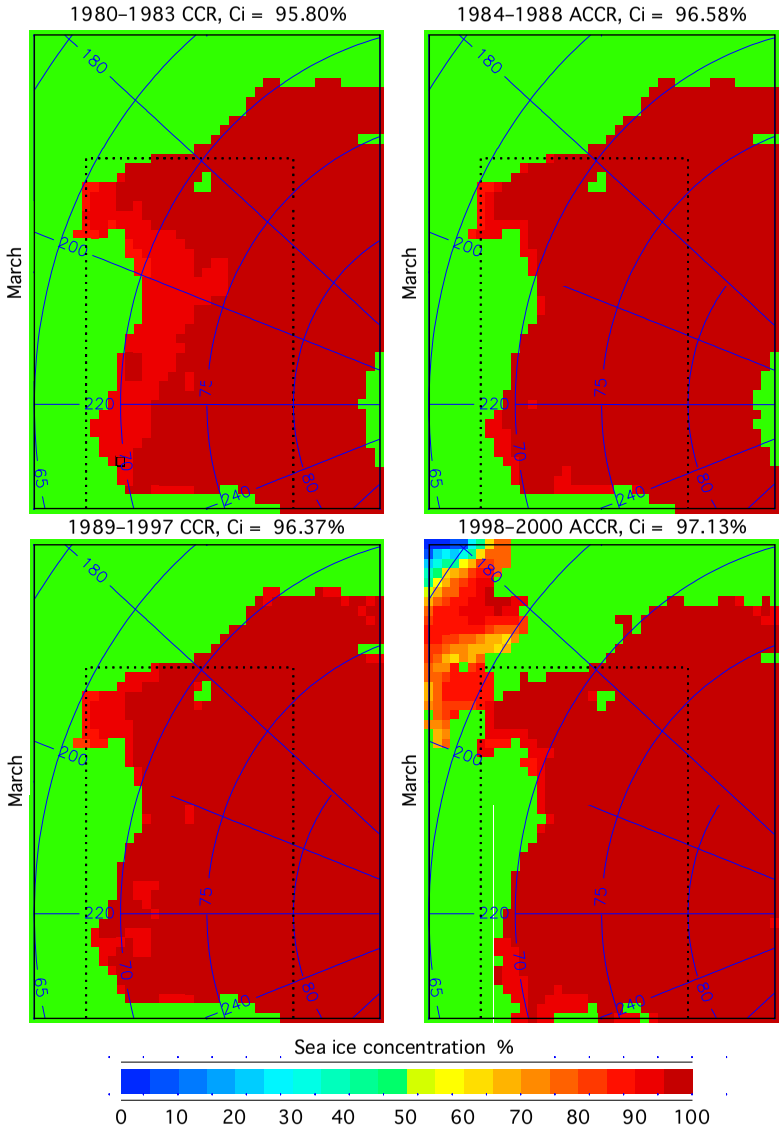

Figure 68. Observed sea ice concentration in March. "Ci" shows sea ice concentration averaged for the box limited by the dotted line.

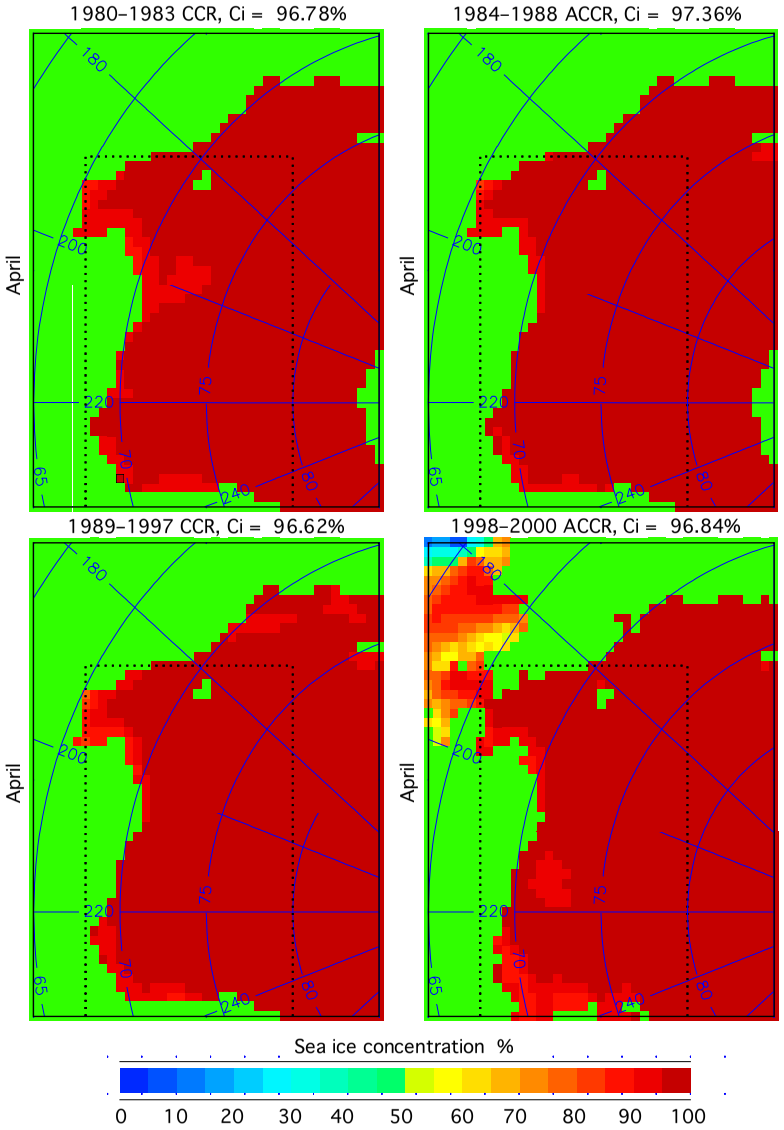

Figure 69. Observed sea ice concentration in April. "Ci" shows sea ice concentration averaged for the box limited by the dotted line.

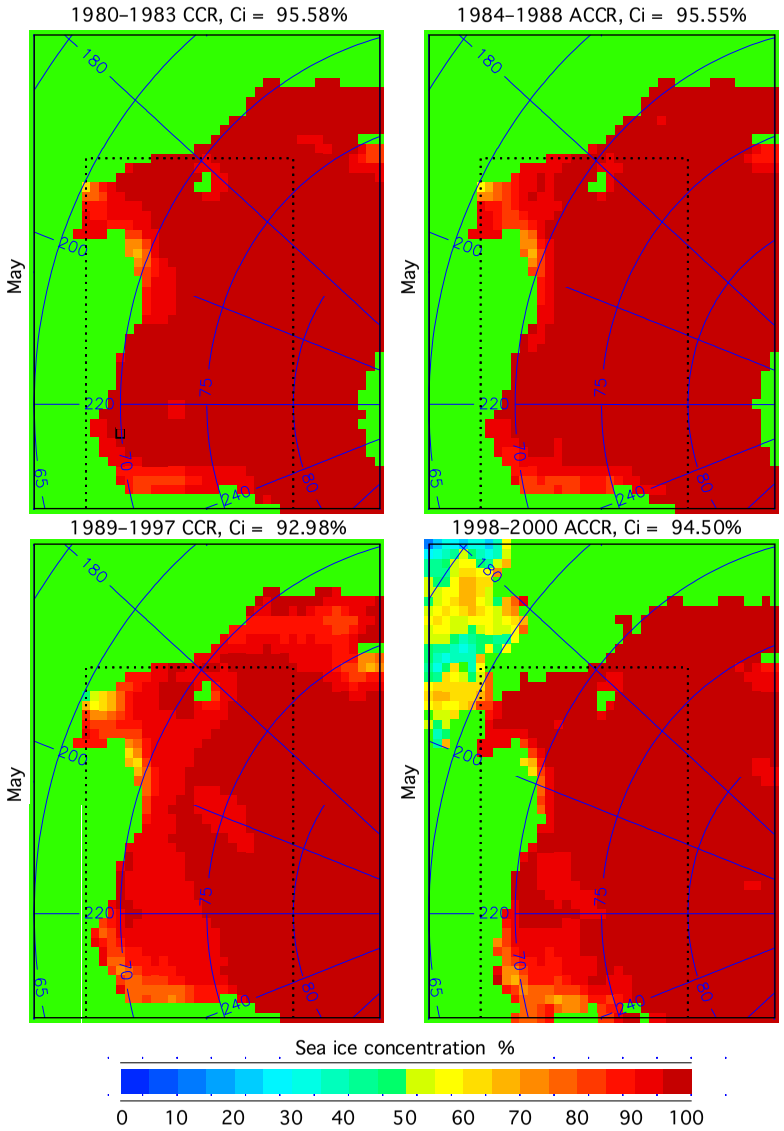

Figure 70. Observed sea ice concentration in May. "Ci" shows sea ice concentration averaged for the box limited by the dotted line.

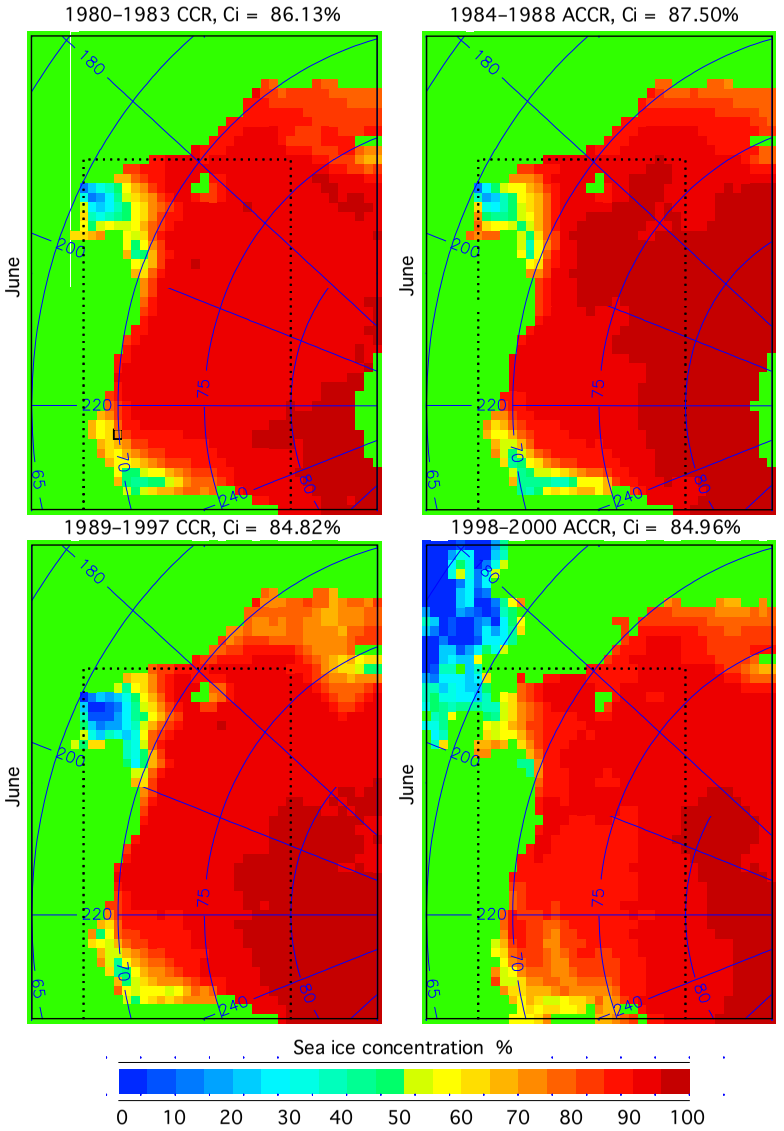

Figure 71. Observed sea ice concentration in June. "Ci" shows sea ice concentration averaged for the box limited by the dotted line.

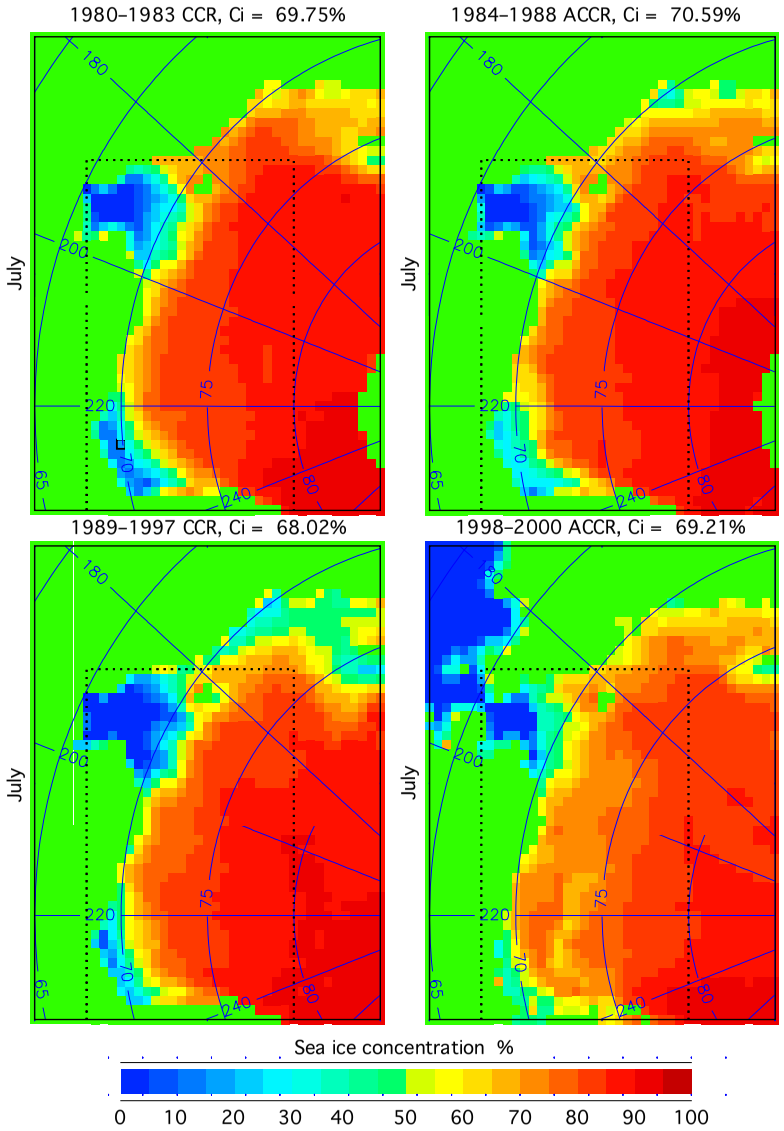

Figure 72. Observed sea ice concentration in July. "Ci" shows sea ice concentration averaged for the box limited by the dotted line.

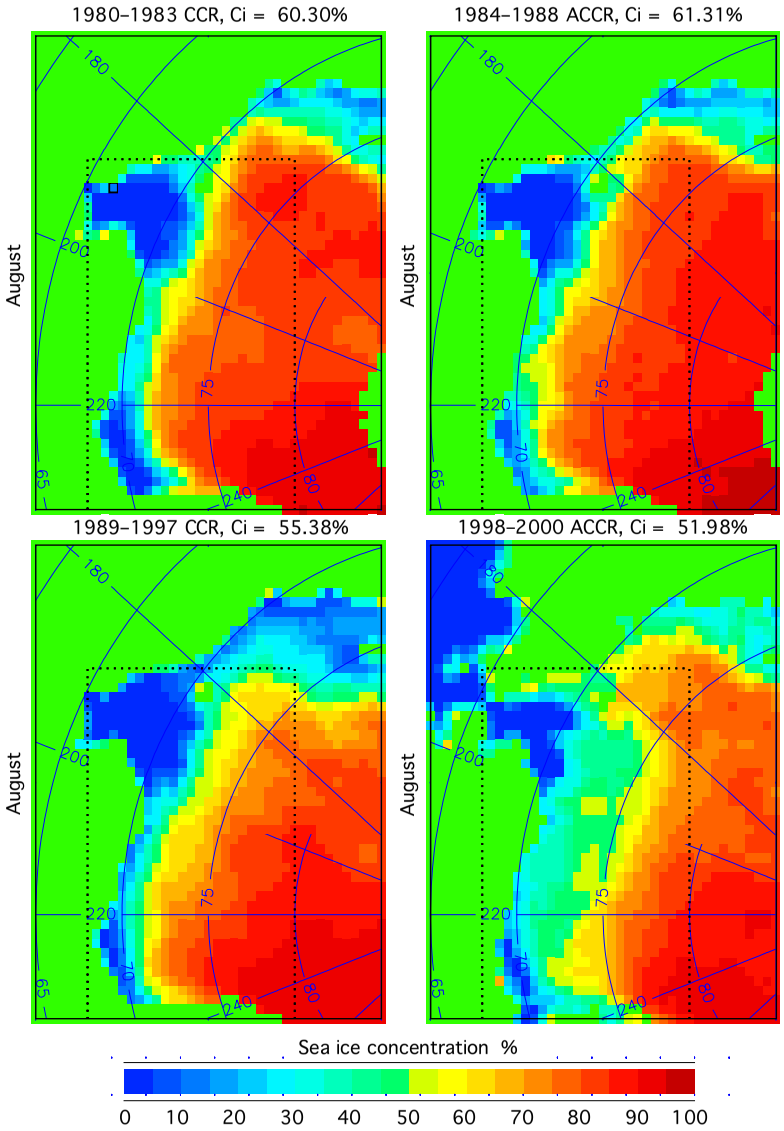

Figure 73. Observed sea ice concentration in August. "Ci" shows sea ice concentration averaged for the box limited by the dotted line.

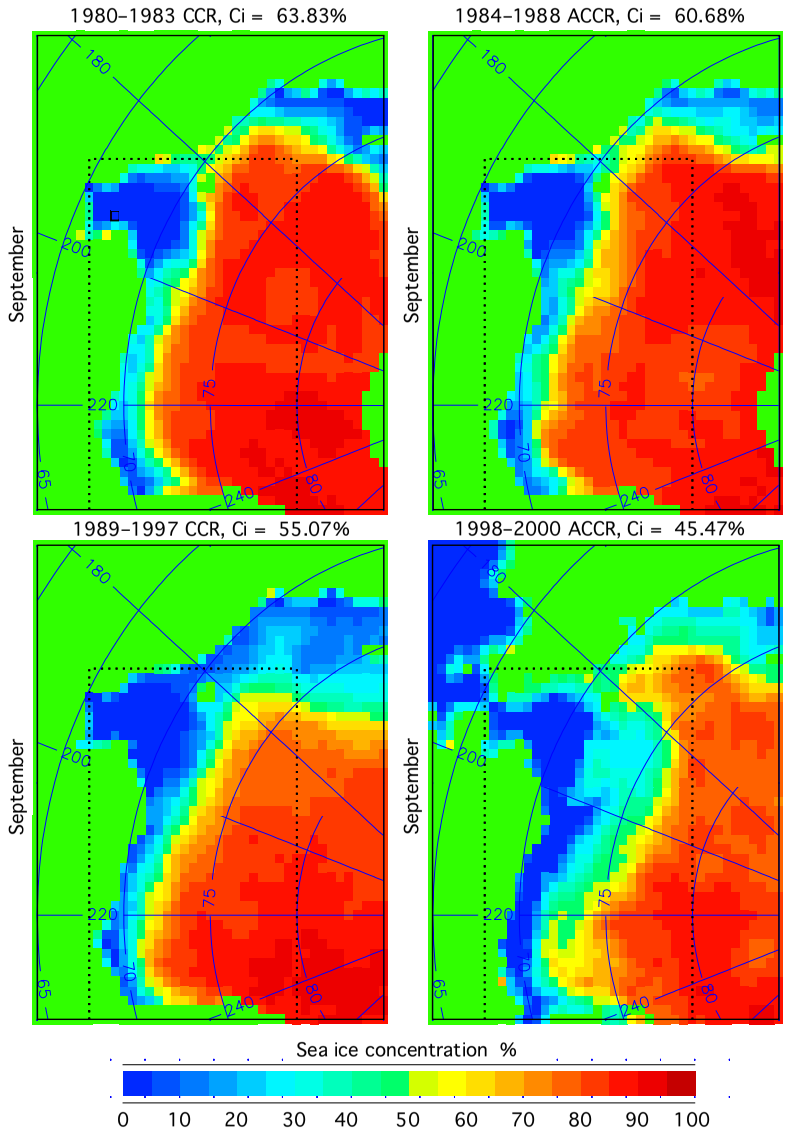

Figure 74. Observed sea ice concentration in September. "Ci" shows sea ice concentration averaged for the box limited by the dotted line.

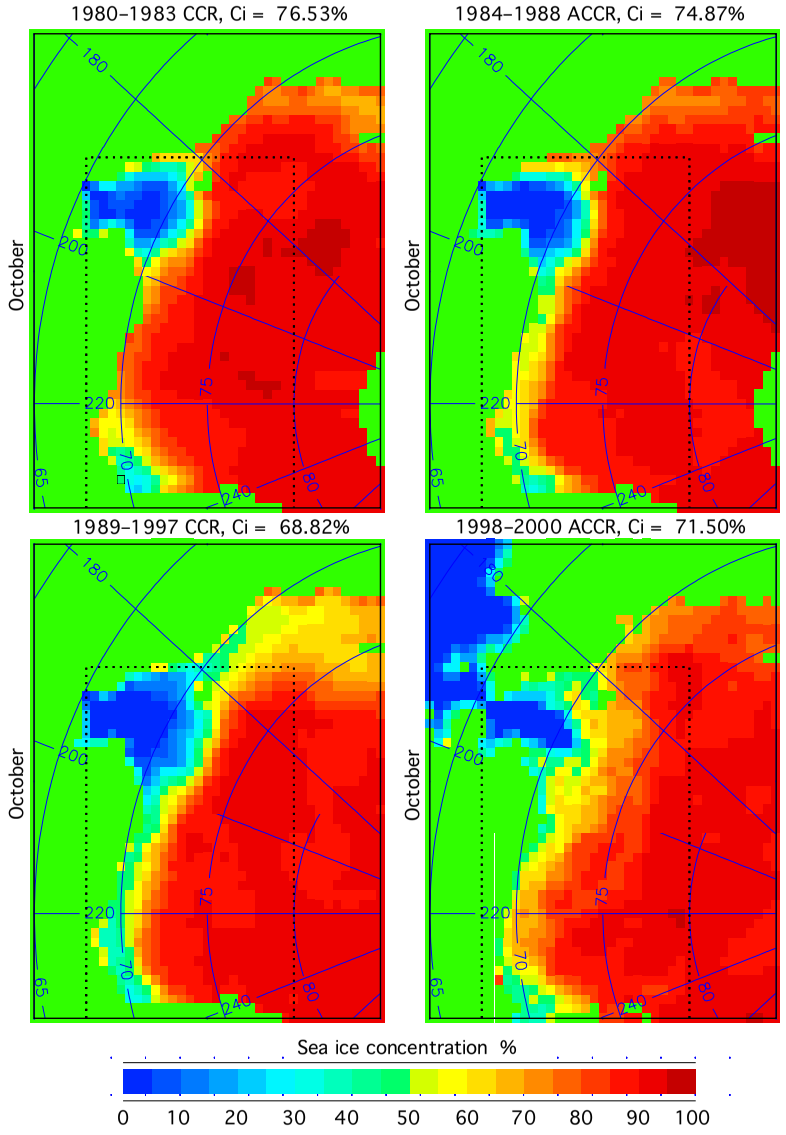

Figure 75. Observed sea ice concentration in October. "Ci" shows sea ice concentration averaged for the box limited by the dotted line.

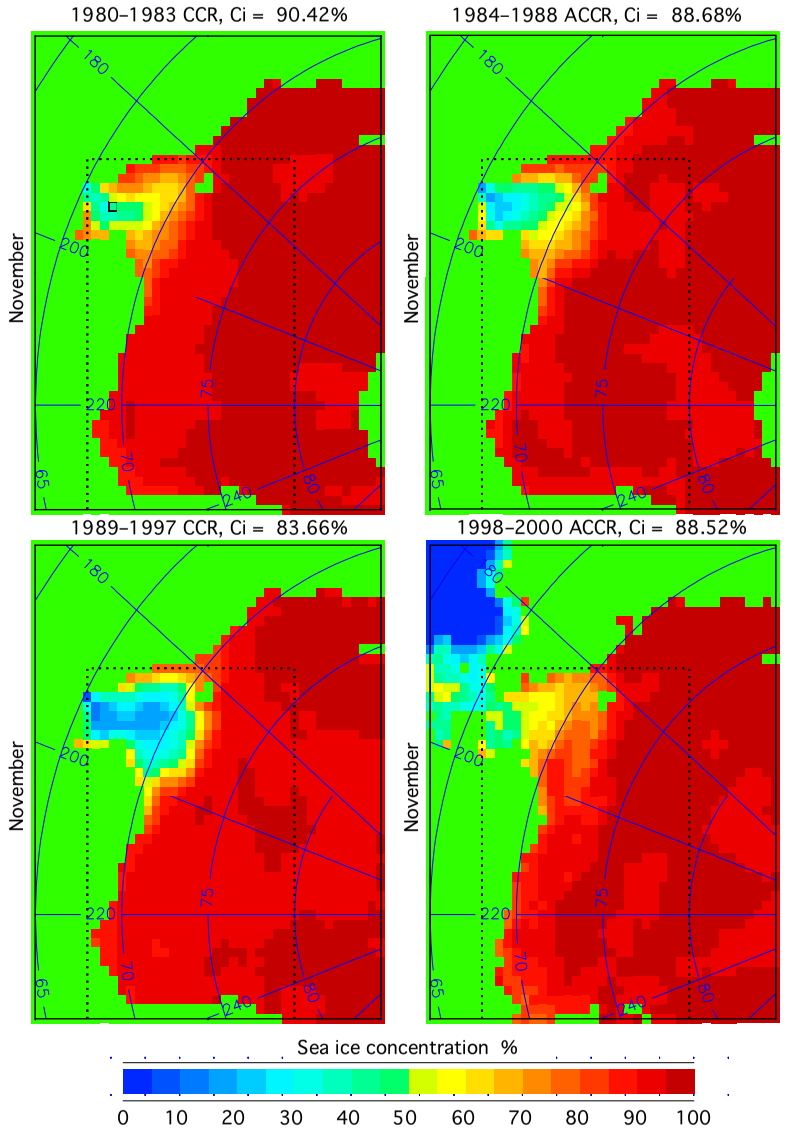

Figure 76. Observed sea ice concentration in November. "Ci" shows sea ice concentration averaged for the box limited by the dotted line.

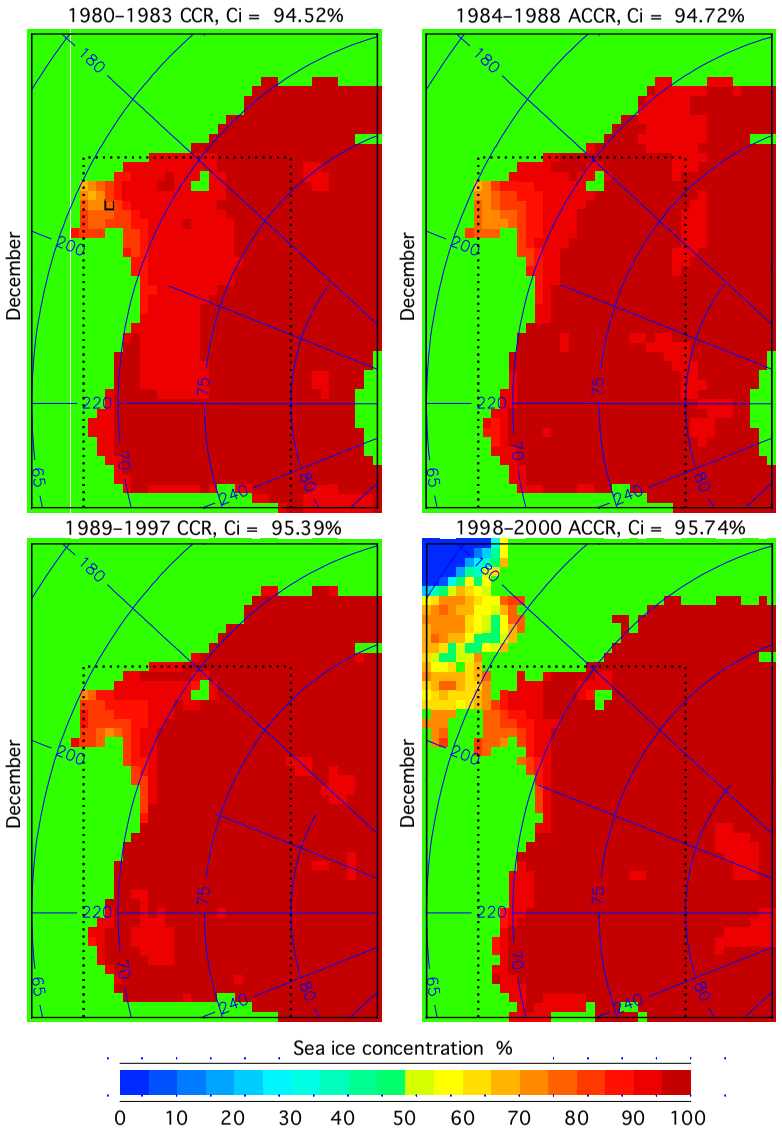

Figure 77. Observed sea ice concentration in December. "Ci" shows sea ice concentration averaged for the box limited by the dotted line.

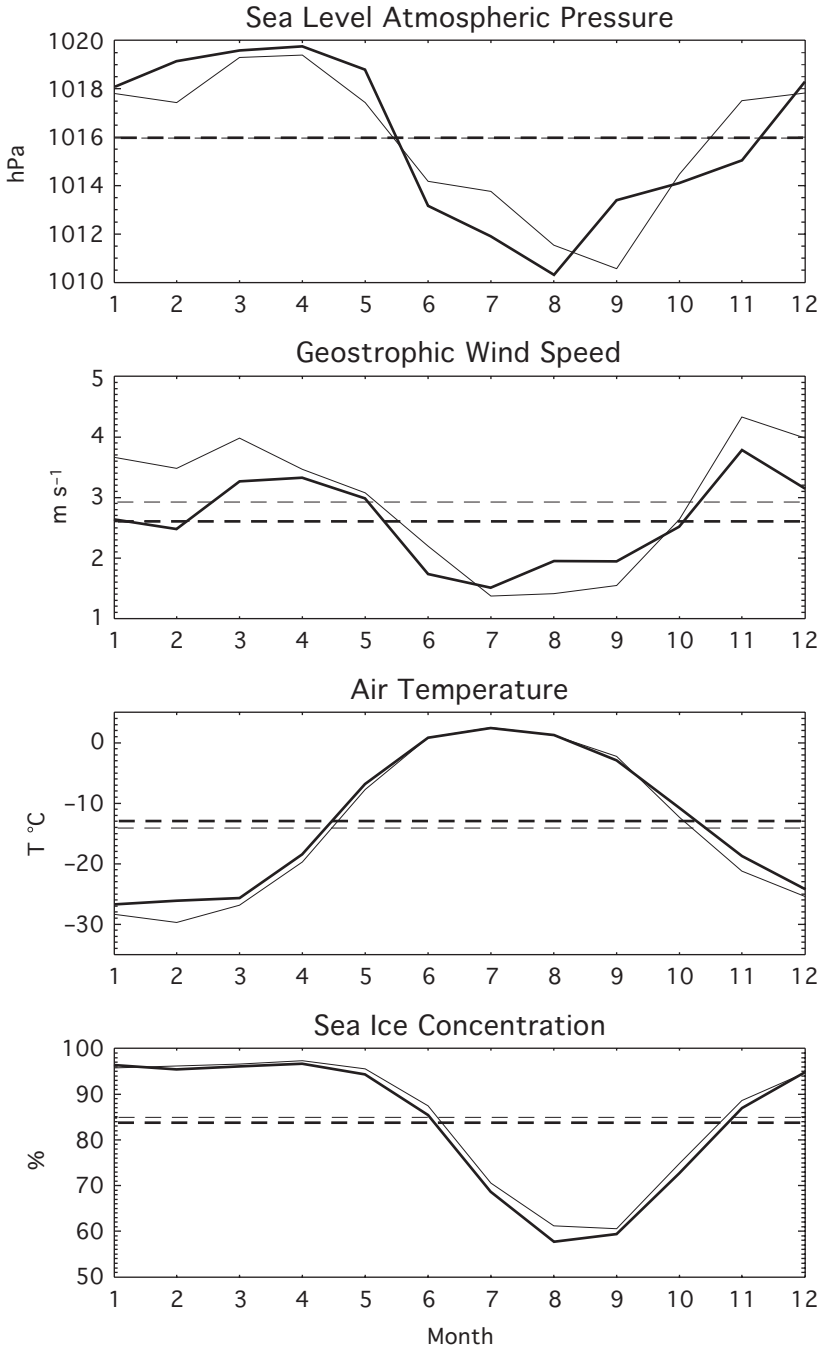

Figure 78. Environmental parameters for ACCR and CCR. Thin solid lines depict monthly mean parameters averaged for ACCR years; thick solid lines show monthly mean parameters for CCR years. Straight thin and thick dashed lines show annual mean parameters for ACCR and CCR years, respectively.

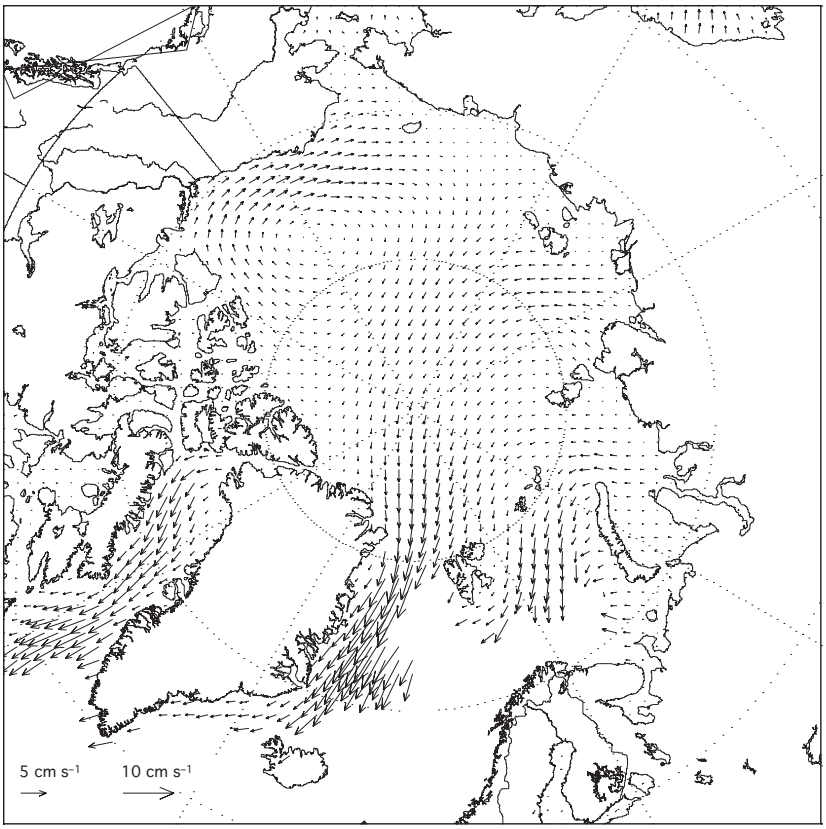

Figure 79. Sea ice drift for CCR.

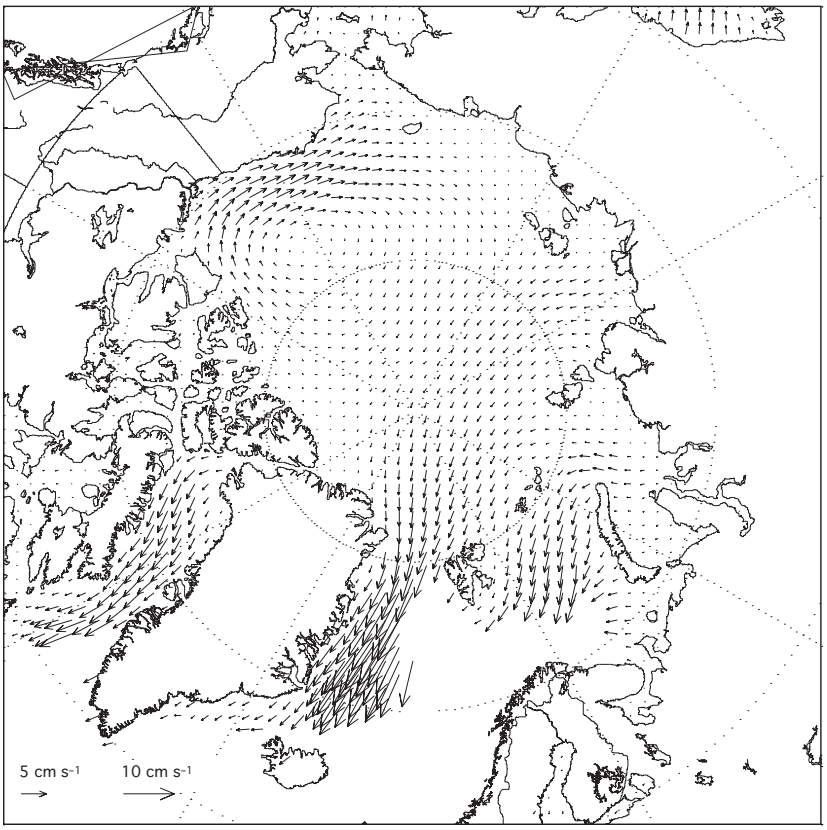

Figure 80. Sea ice drift for ACCR.

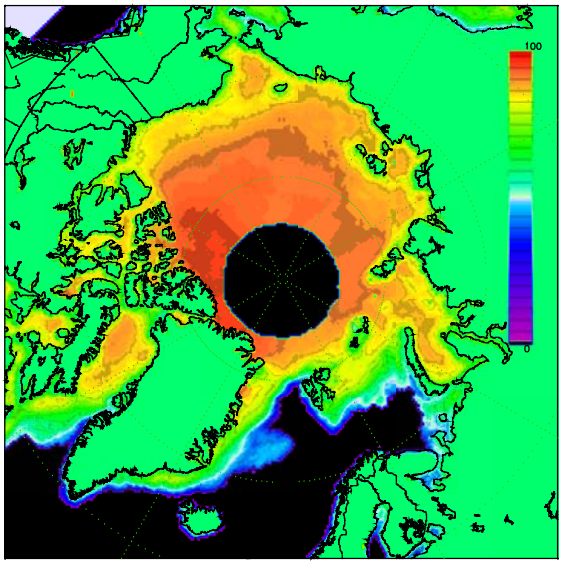

Figure 81. Total sea ice concentration for CCR.

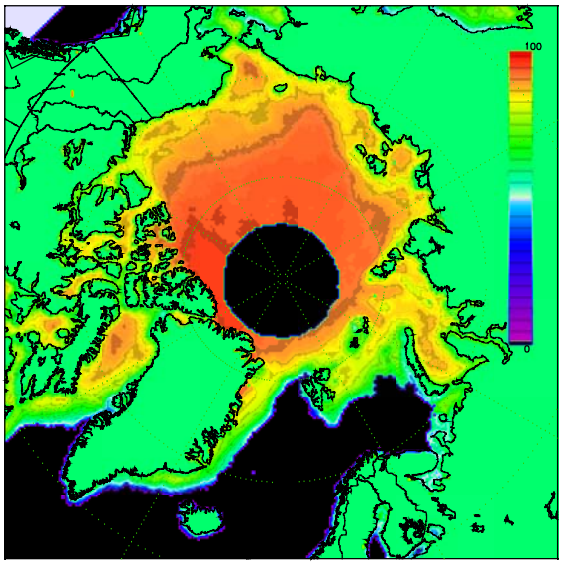

Figure 82. Total sea ice concentration for ACCR.

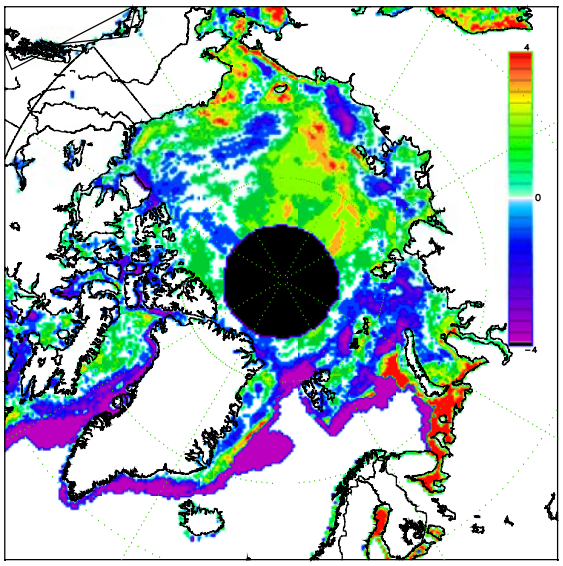

Figure 83. Differences in total sea ice concentration.

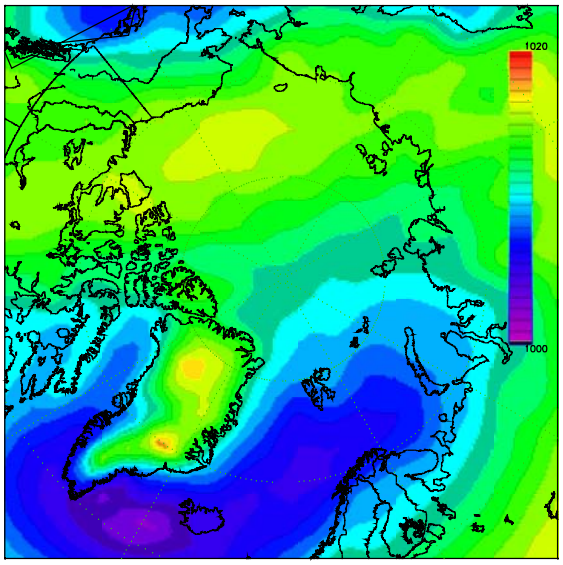

Figure 84. SLP (hPa) for CCR from NCAR/NCEP.

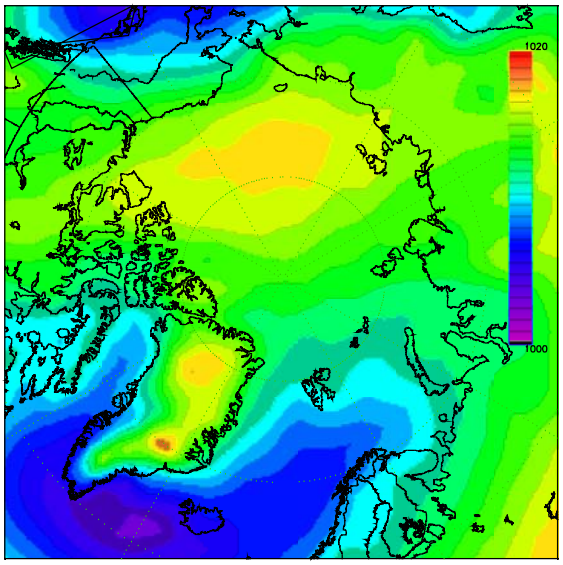

Figure 85. SLP (hPa) for ACCR from NCAR/NCEP.

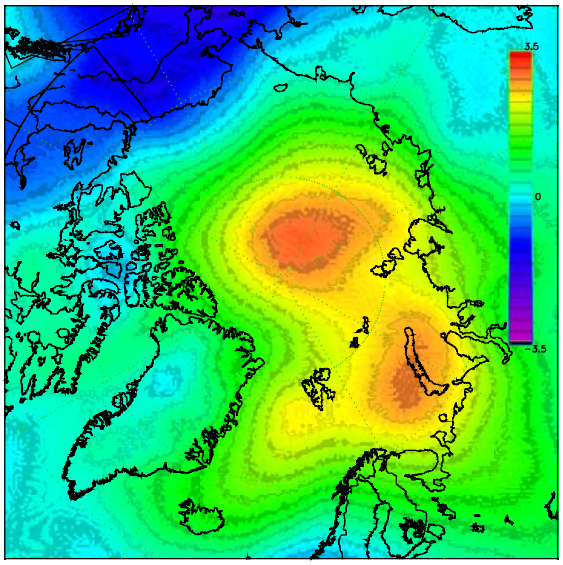

Figure 86. SLP (hPa) differences between ACCR and CCR.

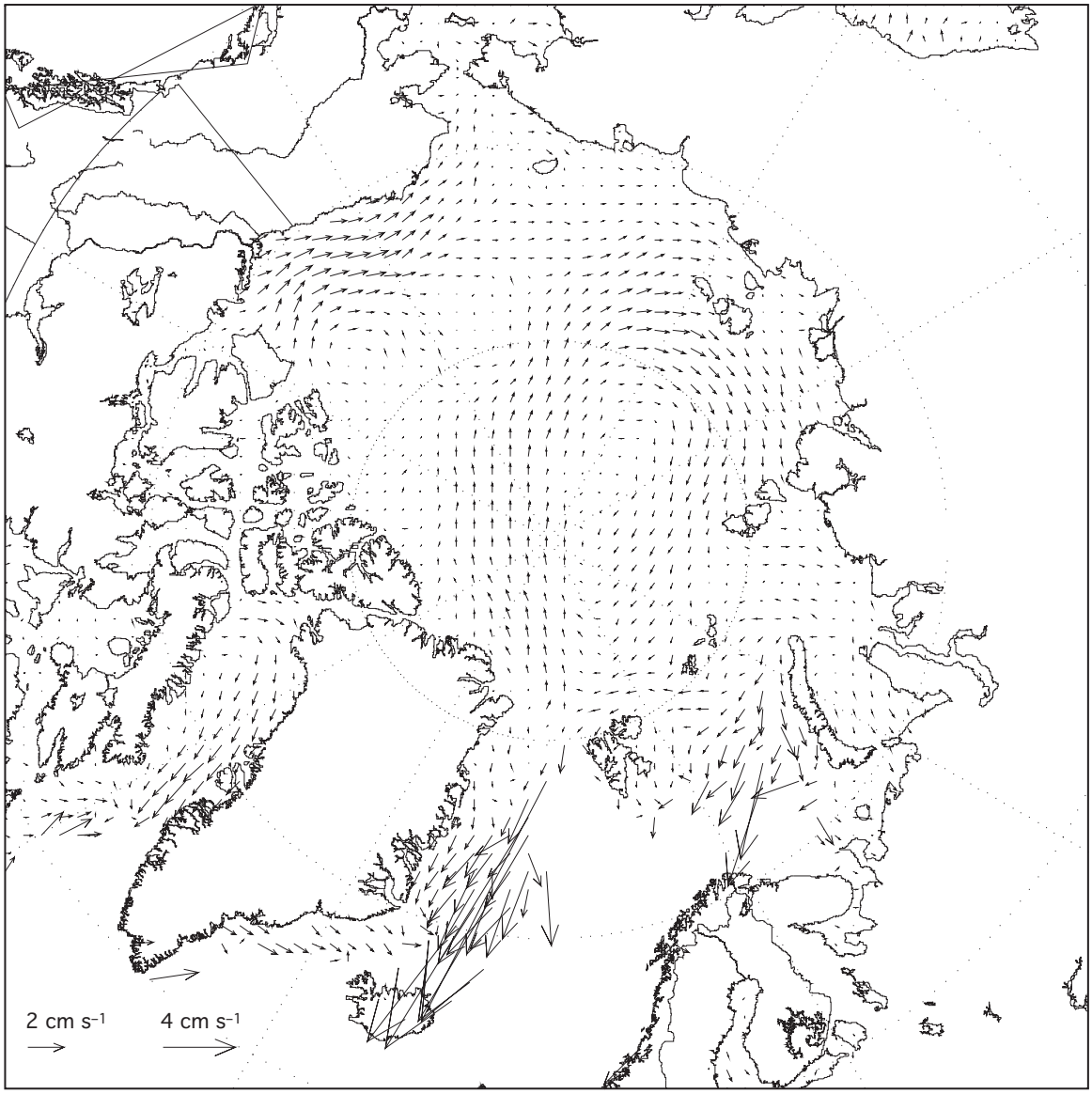

Figure 87. Sea ice drift differences between ACCR and CCR.

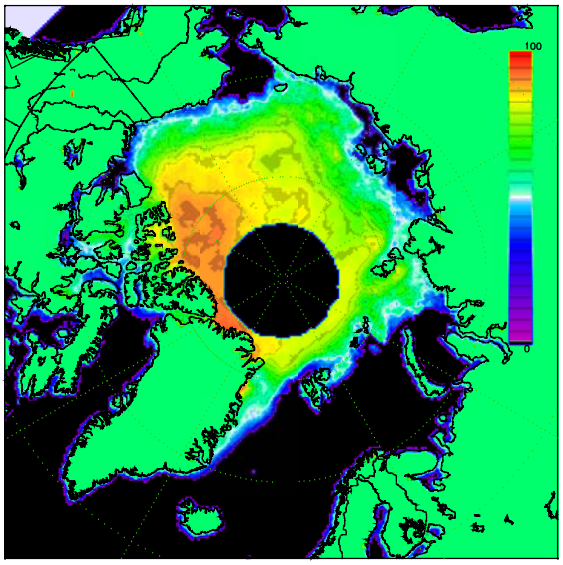

Figure 88. September total sea ice concentration for CCR.

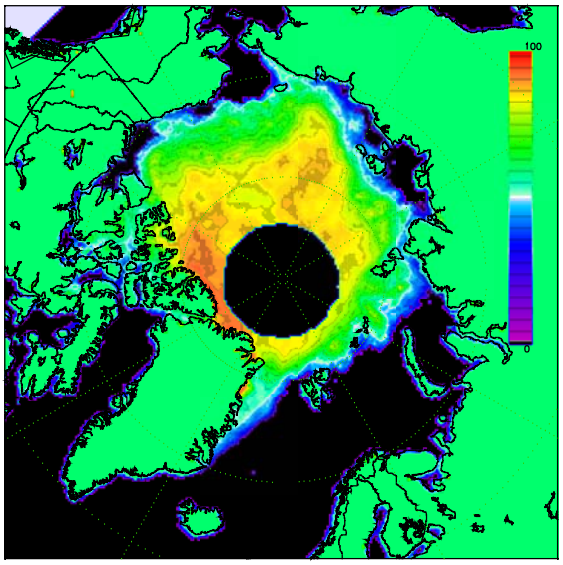

Figure 89. September total sea ice concentration for ACCR.

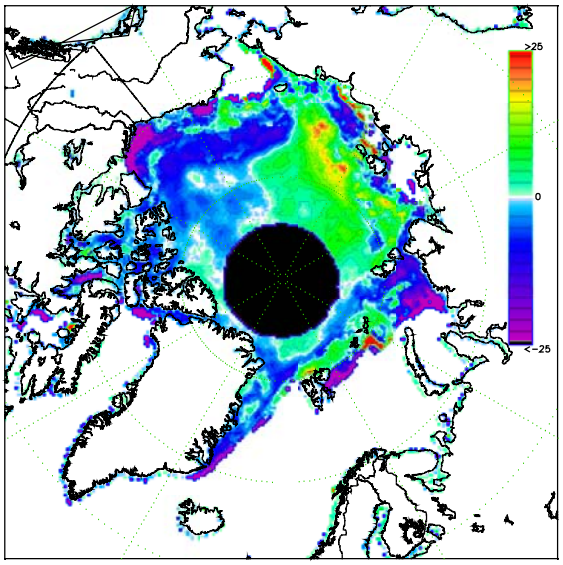

Figure 90. Differences in September total sea ice concentration.

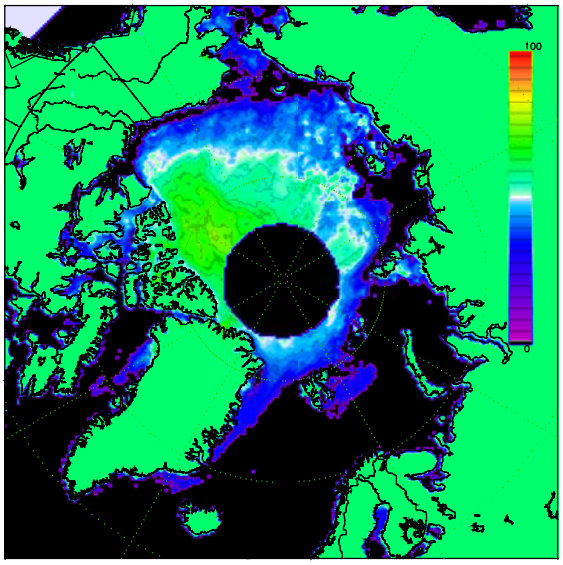

Figure 91. March multi-year sea ice concentration for CCR.

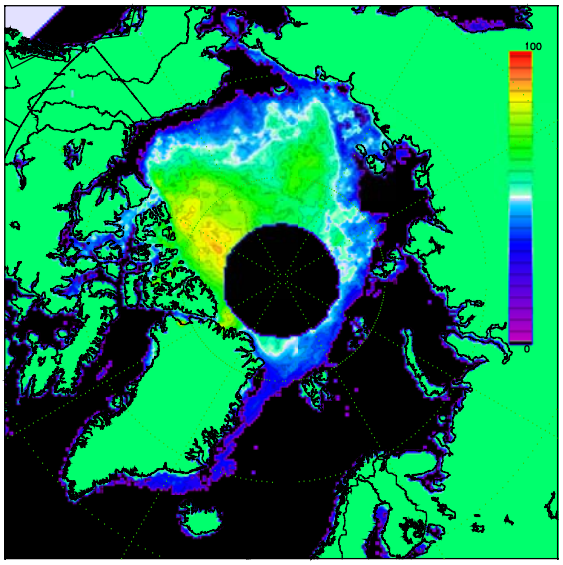

Figure 92. March multi-year sea ice concentration for ACCR.

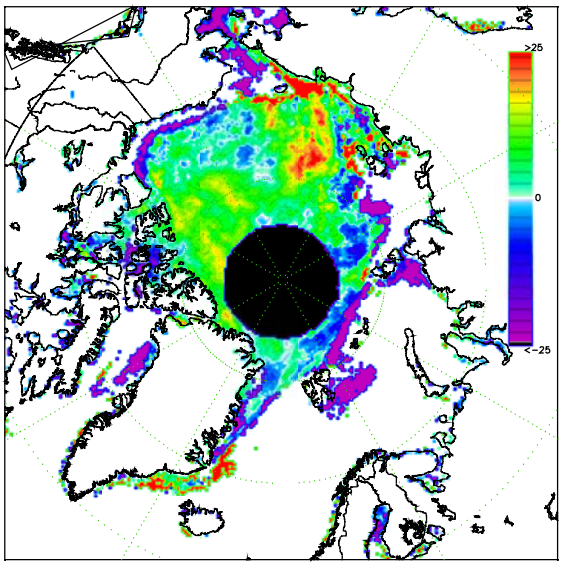

Figure 93. Differences in March multi-year sea ice concentration.

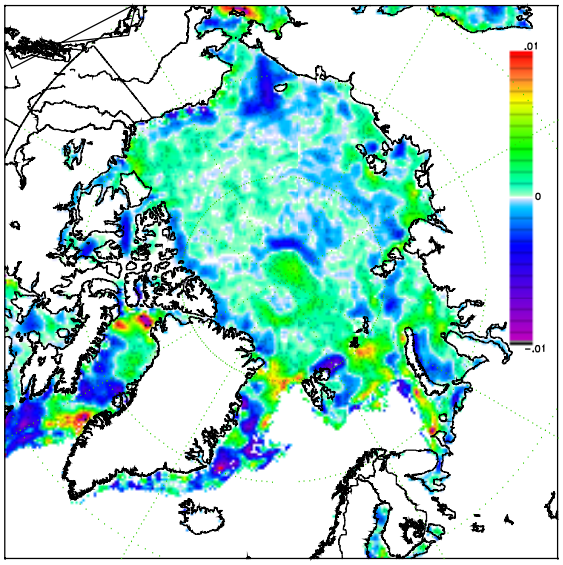

Figure 94. Divergence of sea ice drift for CCR.

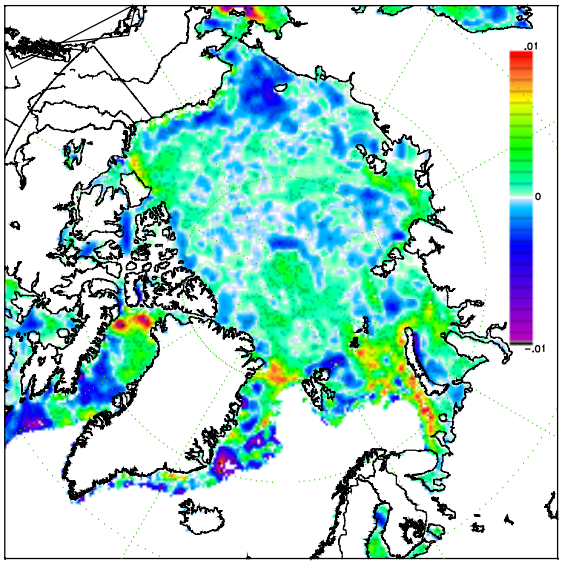

Figure 95. Divergence of sea ice drift for ACCR.

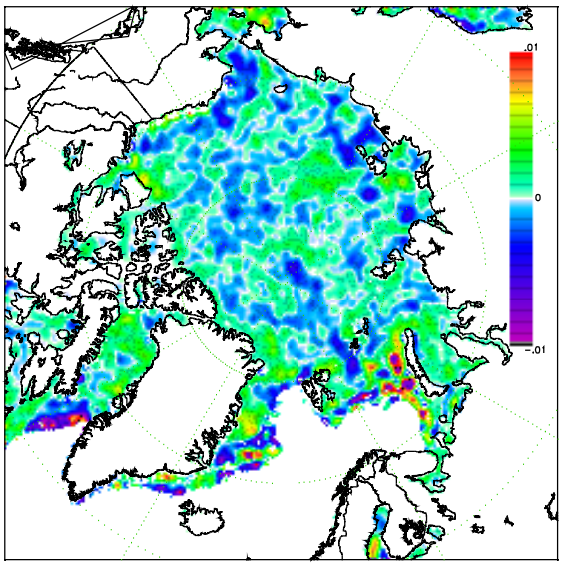

Figure 96. Differences in the divergence of sea ice drift.

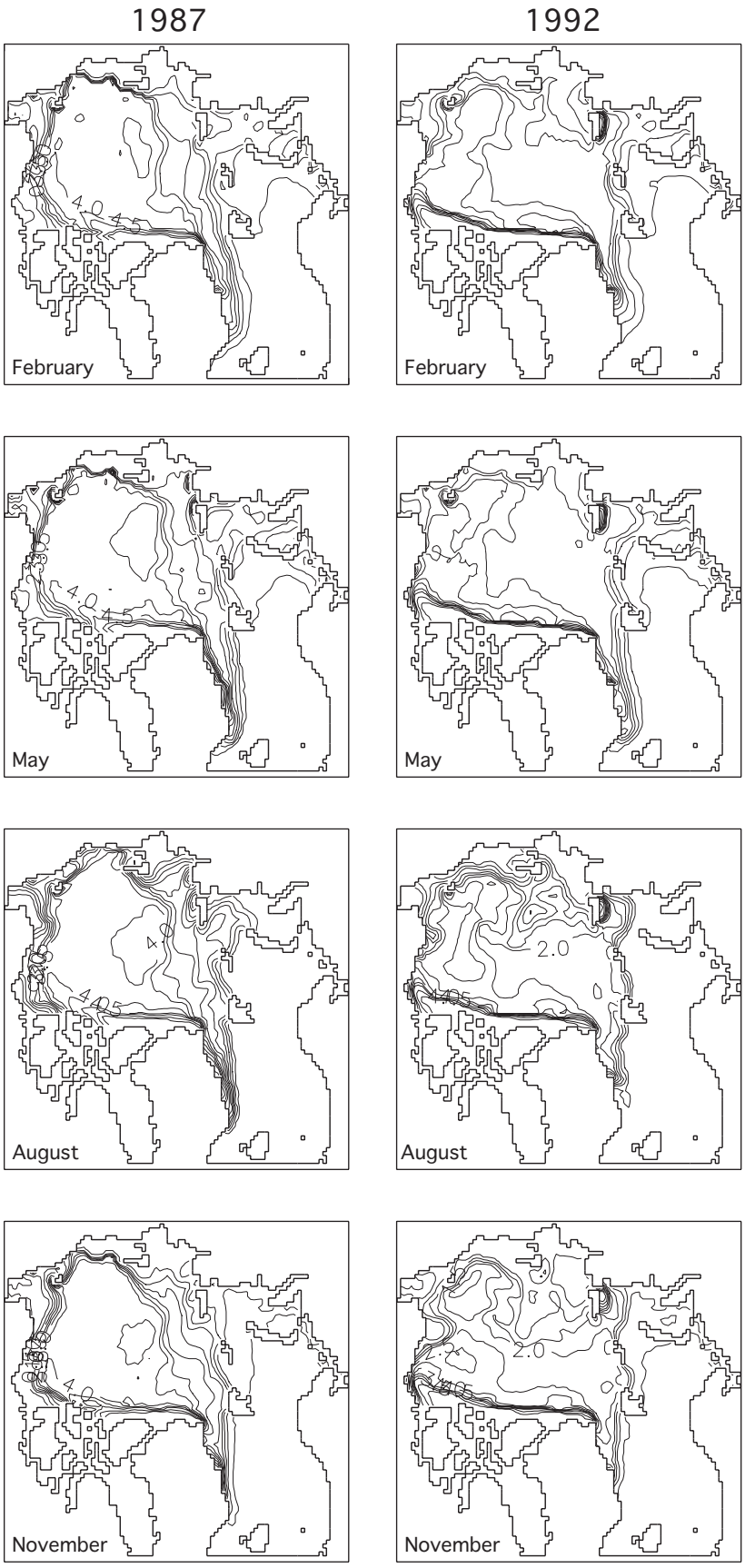

Figure 97. Simulated sea ice thickness (m) in 1987 (ACCR) and 1992 (CCR).

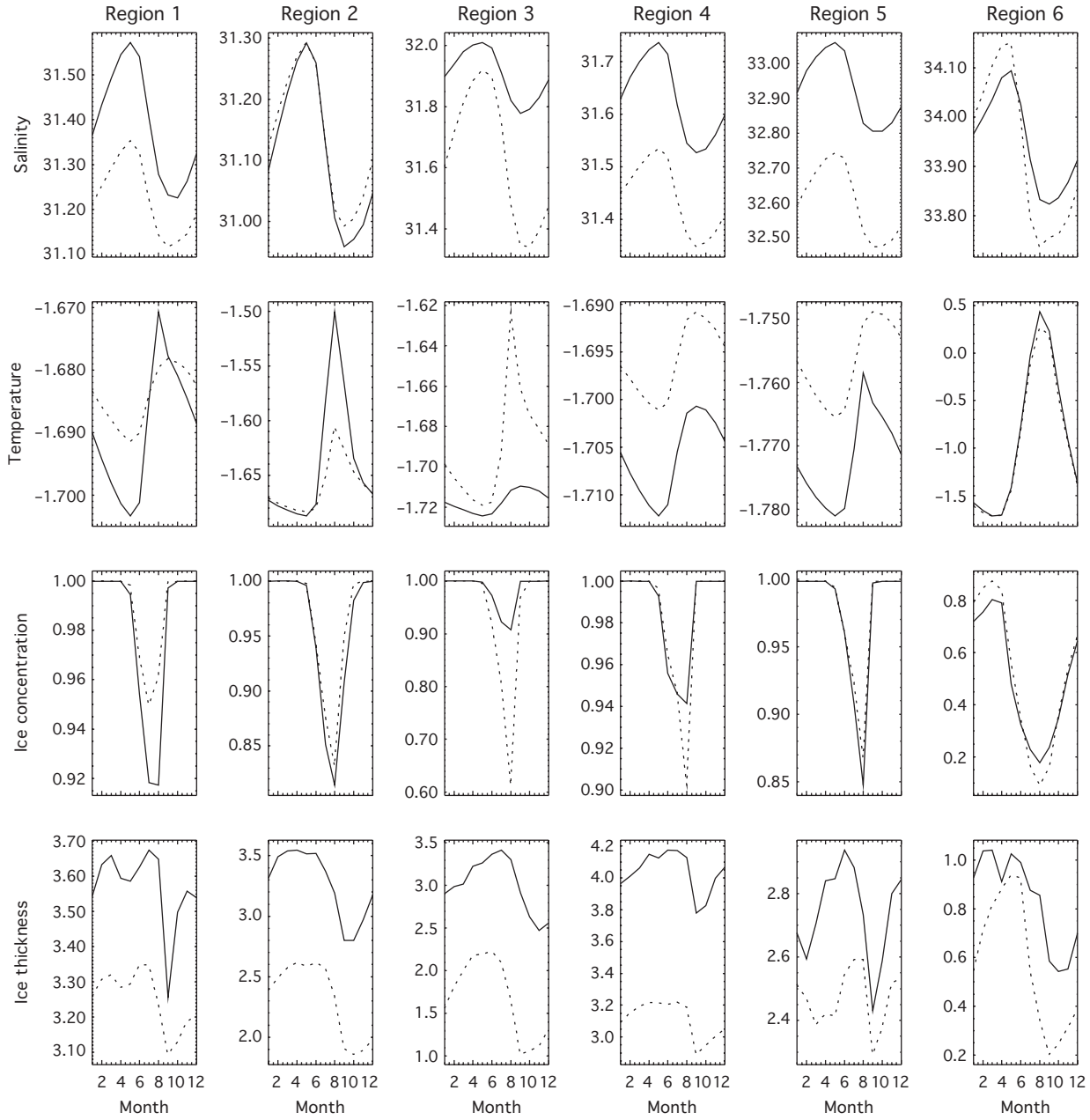

Figure 98. Seasonal variability of simulated water salinity and temperature (°C) in the upper 50-m layer, ice thickness (m), and ice concentration for Regions 1–6 (see Figure 55) in 1987 (ACCR, solid lines) and 1992 (CCR, dotted lines). Note that the vertical scales are different among regions.

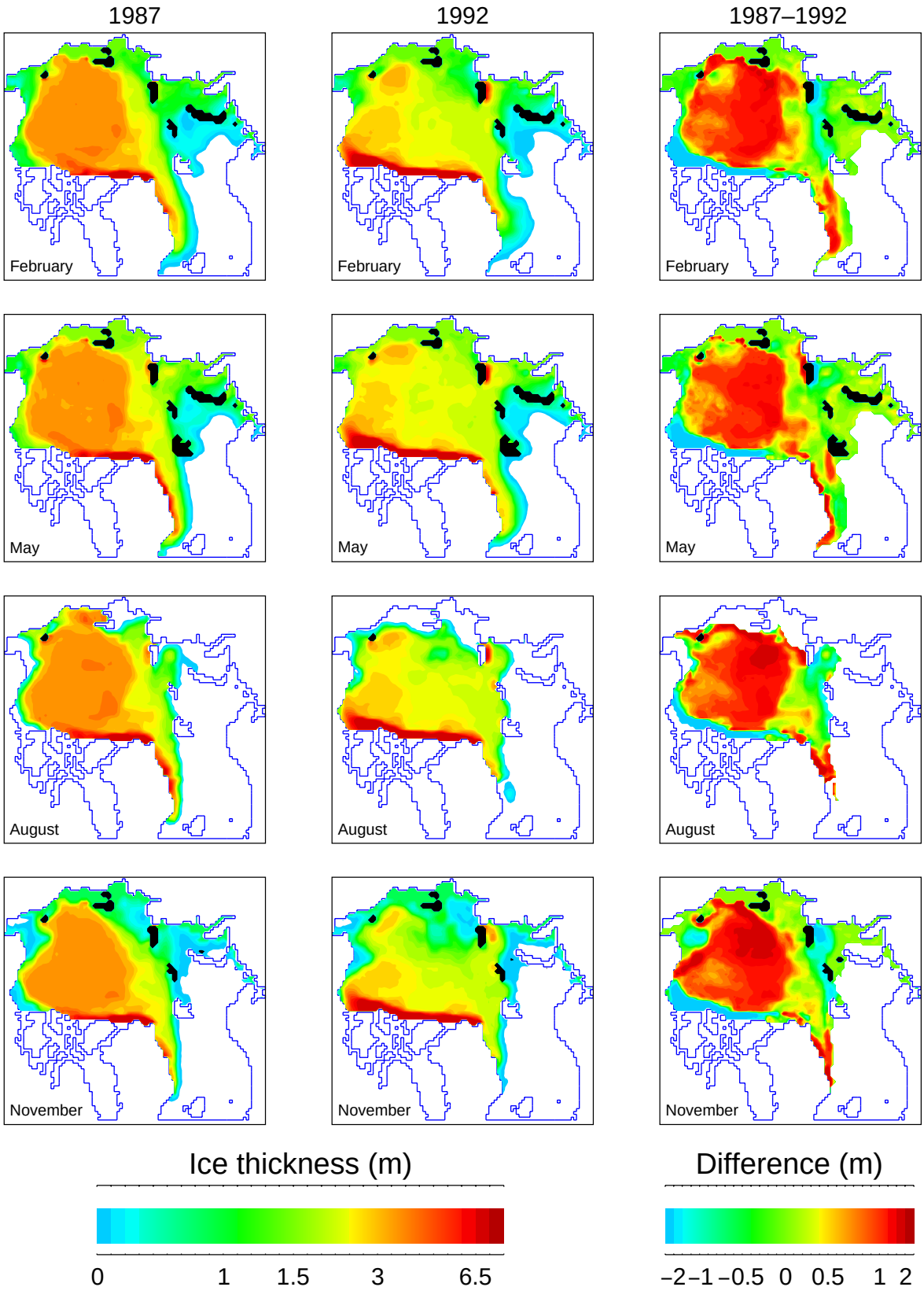

Figure 99. Seasonal variability of the simulated sea ice thickness in 1987 (left) and 1992 (middle), and their difference (right).

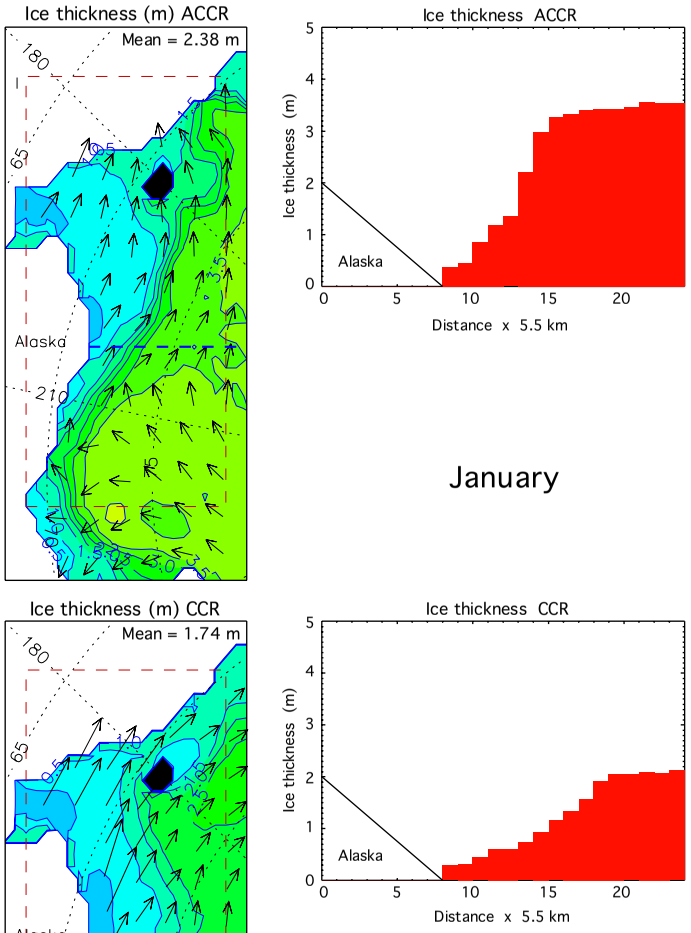

Figure 100. Simulated sea ice thickness in the Beaufort and Chukchi Seas in January for the ACCR and CCR years. Isolines (left) show sea ice thickness (m) and bars (right) show sea ice thickness along the section denoted by a thick dashed line. Mean sea ice thickness in the area is shown in the left top corner of the figure. Arrows show prevailing ice drift.

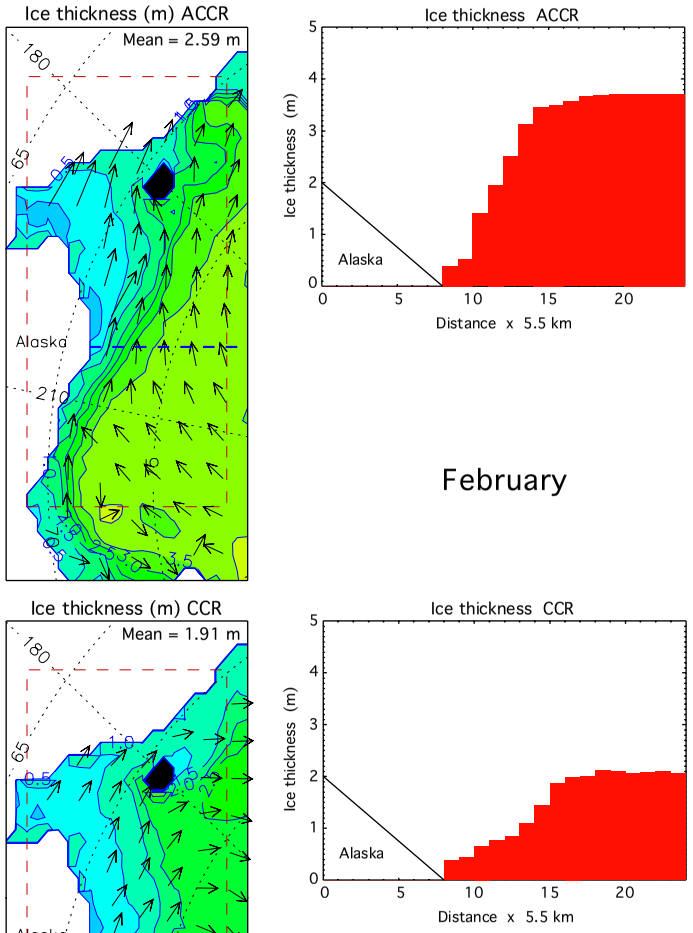

Figure 101. Simulated sea ice thickness in the Beaufort and Chukchi Seas in February for the ACCR and CCR years. Isolines (left) show sea ice thickness (m) and bars (right) show sea ice thickness along the section denoted by a thick dashed line. Mean sea ice thickness in the area is shown in the left top corner of the figure. Arrows show prevailing ice drift.

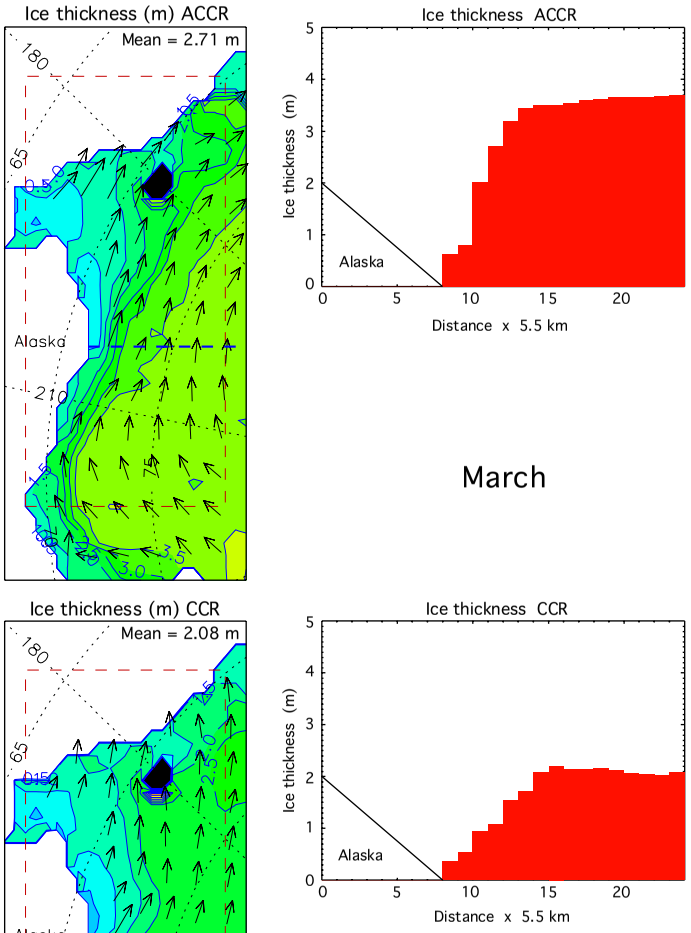

Figure 102. Simulated sea ice thickness in the Beaufort and Chukchi Seas in March for the ACCR and CCR years. Isolines (left) show sea ice thickness (m) and bars (right) show sea ice thickness along the section denoted by a thick dashed line. Mean sea ice thickness in the area is shown in the left top corner of the figure. Arrows show prevailing ice drift.

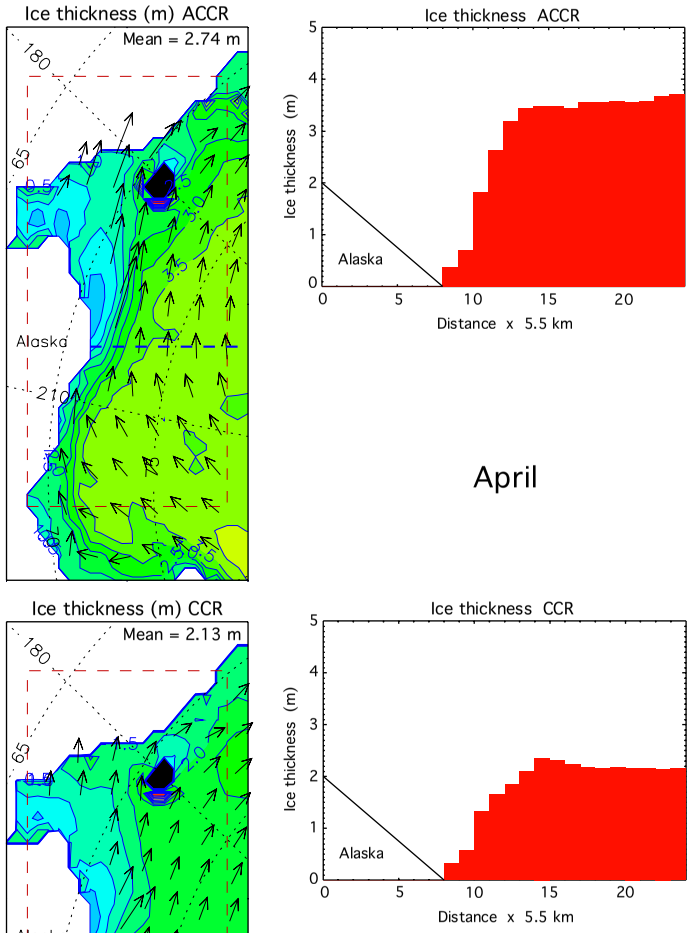

Figure 103. Simulated sea ice thickness in the Beaufort and Chukchi Seas in April for the ACCR and CCR years. Isolines (left) show sea ice thickness (m) and bars (right) show sea ice thickness along the section denoted by a thick dashed line. Mean sea ice thickness in the area is shown in the left top corner of the figure. Arrows show prevailing ice drift.

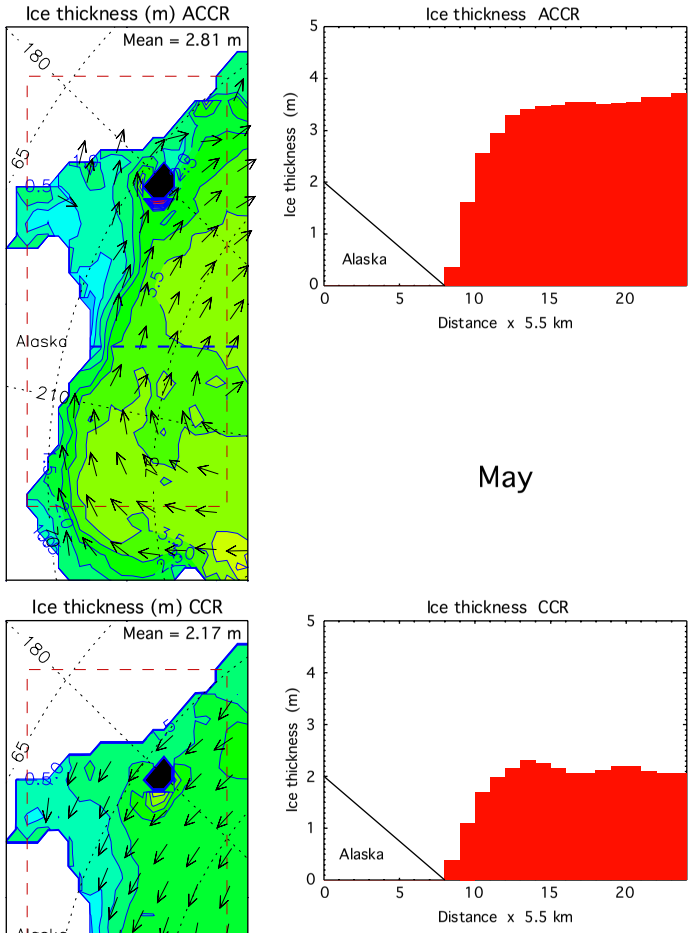

Figure 104. Simulated sea ice thickness in the Beaufort and Chukchi Seas in May for the ACCR and CCR years. Isolines (left) show sea ice thickness (m) and bars (right) show sea ice thickness along the section denoted by a thick dashed line. Mean sea ice thickness in the area is shown in the left top corner of the figure. Arrows show prevailing ice drift.

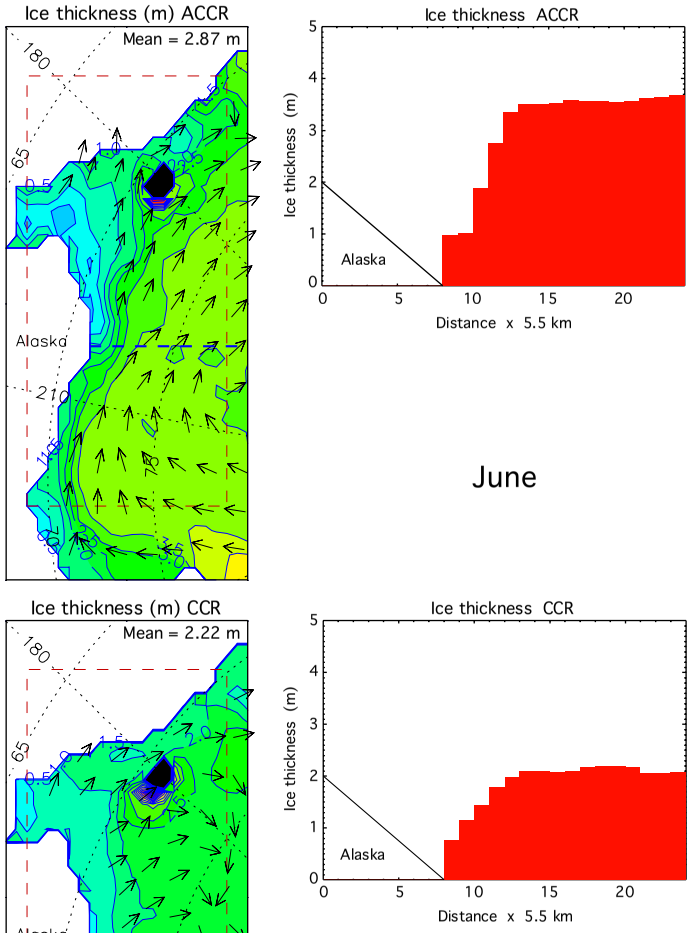

Figure 105. Simulated sea ice thickness in the Beaufort and Chukchi Seas in June for the ACCR and CCR years. Isolines (left) show sea ice thickness (m) and bars (right) show sea ice thickness along the section denoted by a thick dashed line. Mean sea ice thickness in the area is shown in the left top corner of the figure. Arrows show prevailing ice drift.

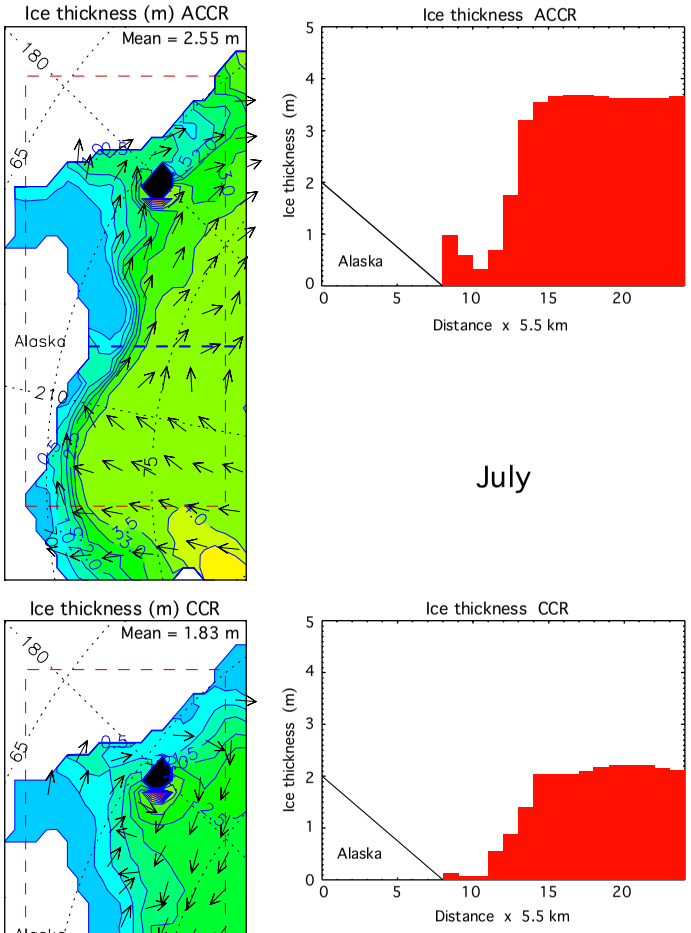

Figure 106. Simulated sea ice thickness in the Beaufort and Chukchi Seas in July for the ACCR and CCR years. Isolines (left) show sea ice thickness (m) and bars (right) show sea ice thickness along the section denoted by a thick dashed line. Mean sea ice thickness in the area is shown in the left top corner of the figure. Arrows show prevailing ice drift.

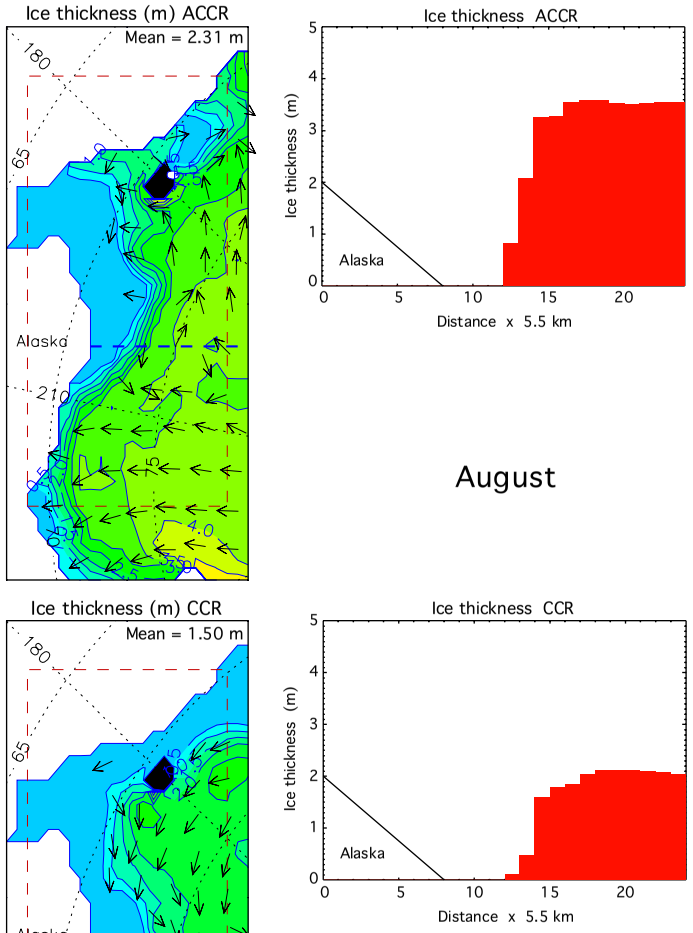

Figure 107. Simulated sea ice thickness in the Beaufort and Chukchi Seas in August for the ACCR and CCR years. Isolines (left) show sea ice thickness (m) and bars (right) show sea ice thickness along the section denoted by a thick dashed line. Mean sea ice thickness in the area is shown in the left top corner of the figure. Arrows show prevailing ice drift.

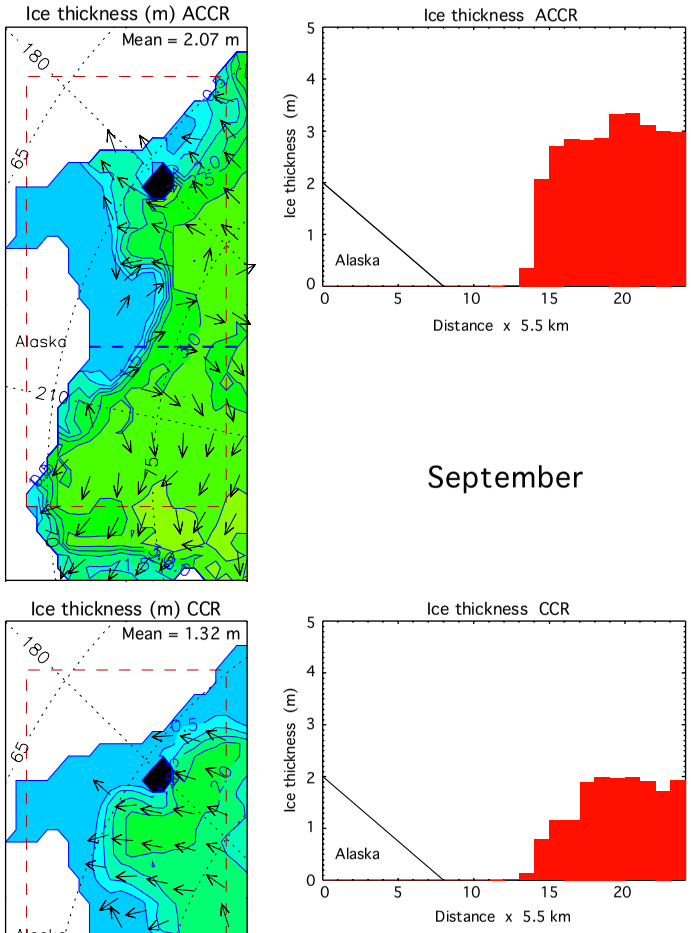

Figure 108. Simulated sea ice thickness in the Beaufort and Chukchi Seas in September for the ACCR and CCR years. Isolines (left) show sea ice thickness (m) and bars (right) show sea ice thickness along the section denoted by a thick dashed line. Mean sea ice thickness in the area is shown in the left top corner of the figure. Arrows show prevailing ice drift.

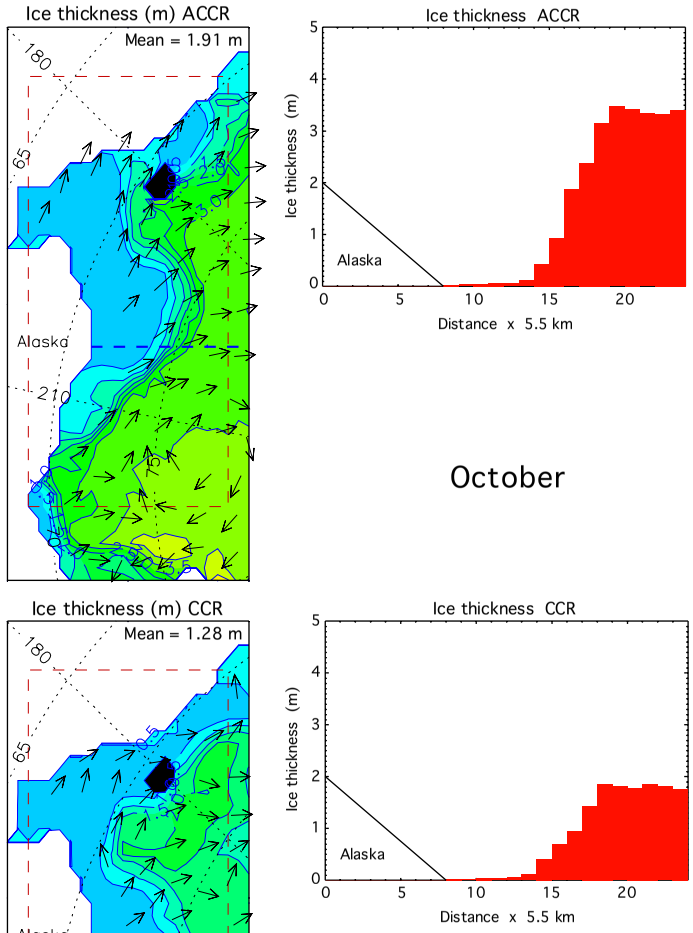

Figure 109. Simulated sea ice thickness in the Beaufort and Chukchi Seas in October for the ACCR and CCR years. Isolines (left) show sea ice thickness (m) and bars (right) show sea ice thickness along the section denoted by a thick dashed line. Mean sea ice thickness in the area is shown in the left top corner of the figure. Arrows show prevailing ice drift.

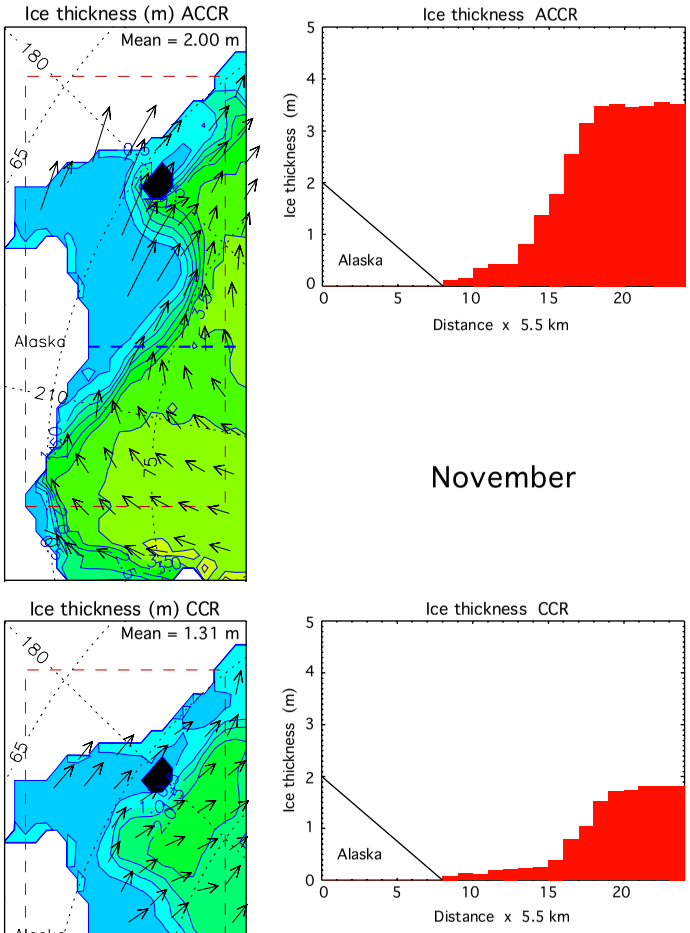

Figure 110. Simulated sea ice thickness in the Beaufort and Chukchi Seas in November for the ACCR and CCR years. Isolines (left) show sea ice thickness (m) and bars (right) show sea ice thickness along the section denoted by a thick dashed line. Mean sea ice thickness in the area is shown in the left top corner of the figure. Arrows show prevailing ice drift.

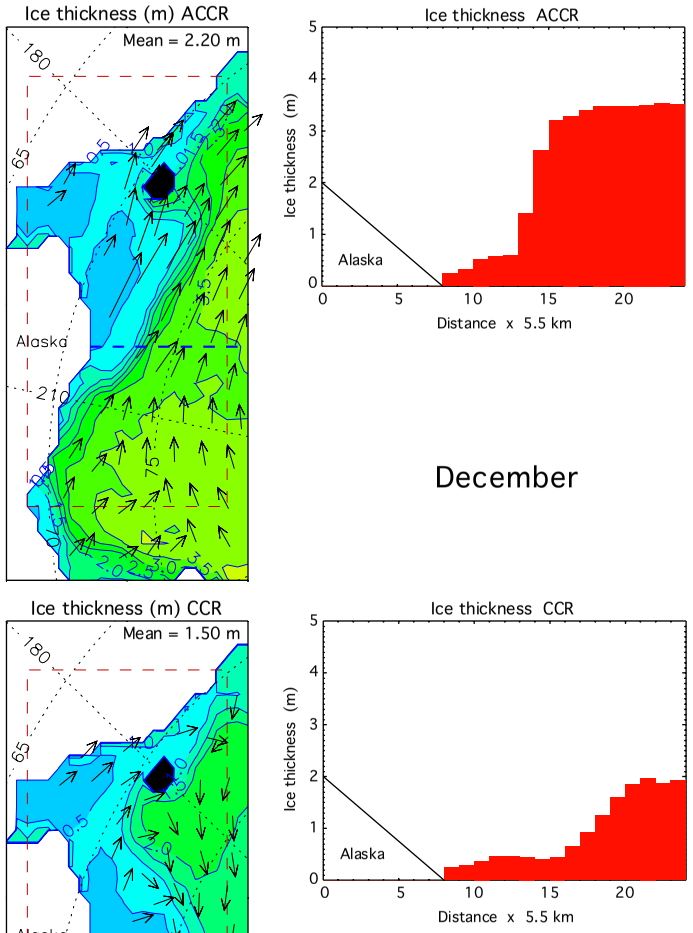

Figure 111. Simulated sea ice thickness in the Beaufort and Chukchi Seas in December for the ACCR and CCR years. Isolines (left) show sea ice thickness (m) and bars (right) show sea ice thickness along the section denoted by a thick dashed line. Mean sea ice thickness in the area is shown in the left top corner of the figure. Arrows show prevailing ice drift.

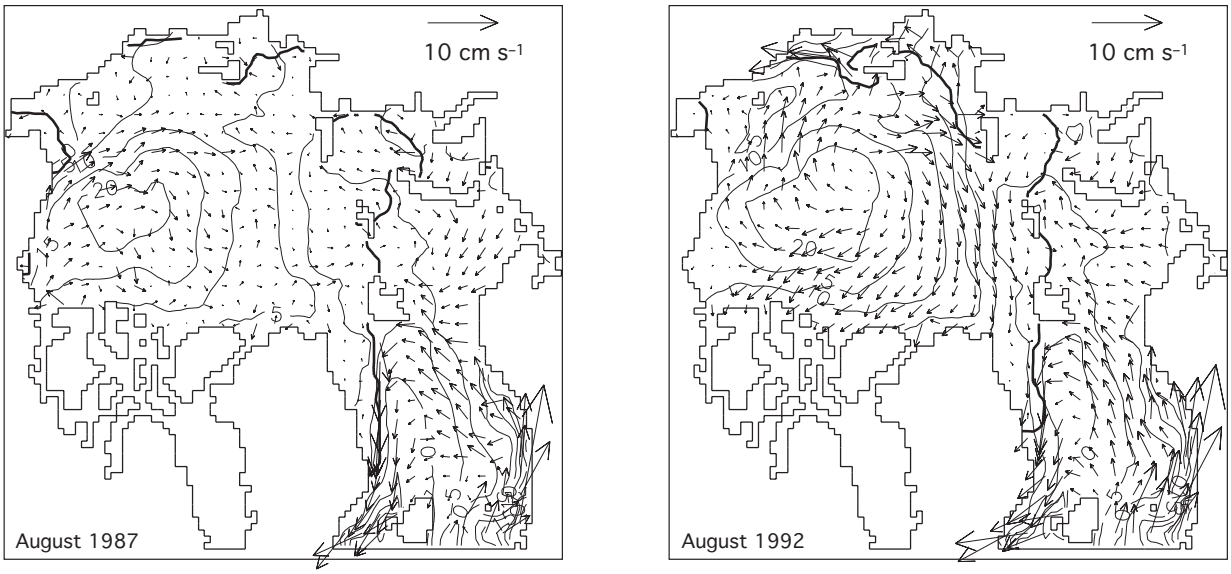

Figure 112. Differences between surface current and sea ice drift during ACCR (left) and CCR (right). Contour lines show sea surface heights (cm).

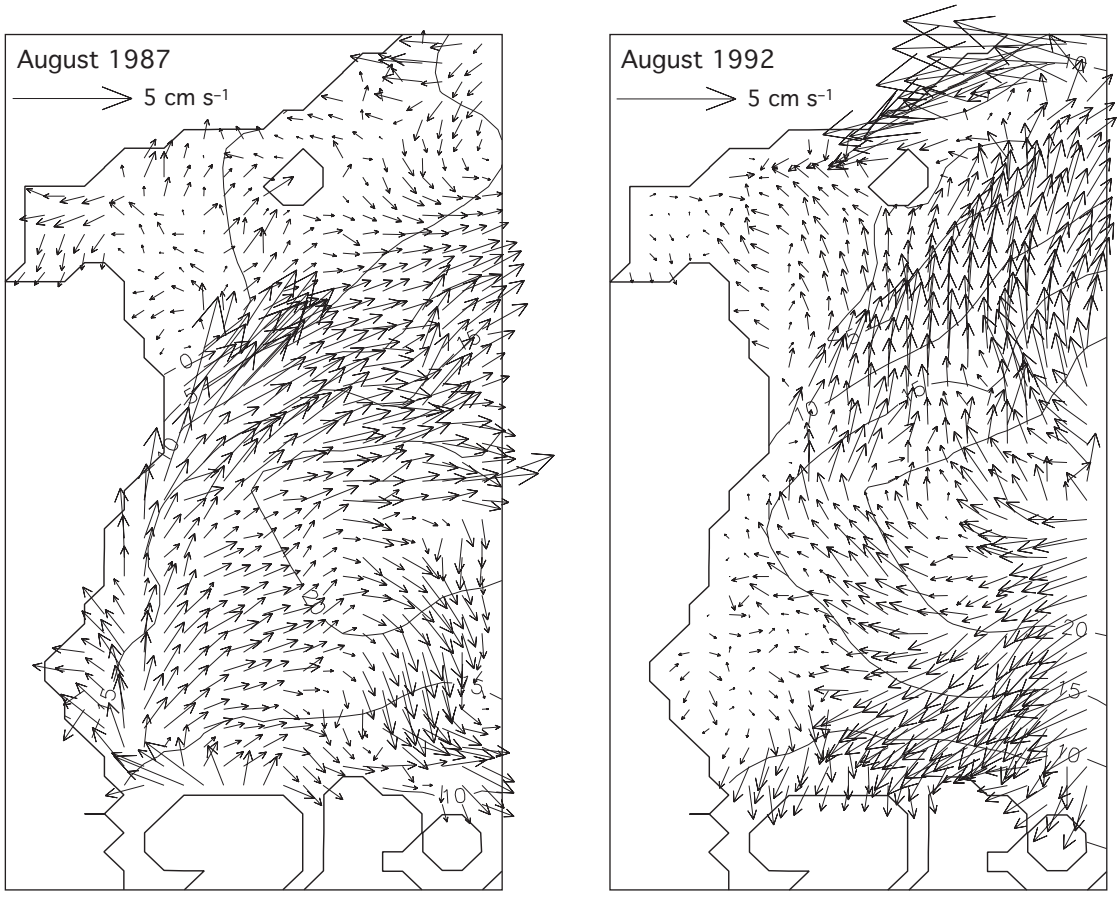

Figure 113. Differences between surface current and sea ice drift during ACCR (left) and CCR (right) in the Beaufort and Chukchi Seas. Contour lines show sea surface heights (cm).

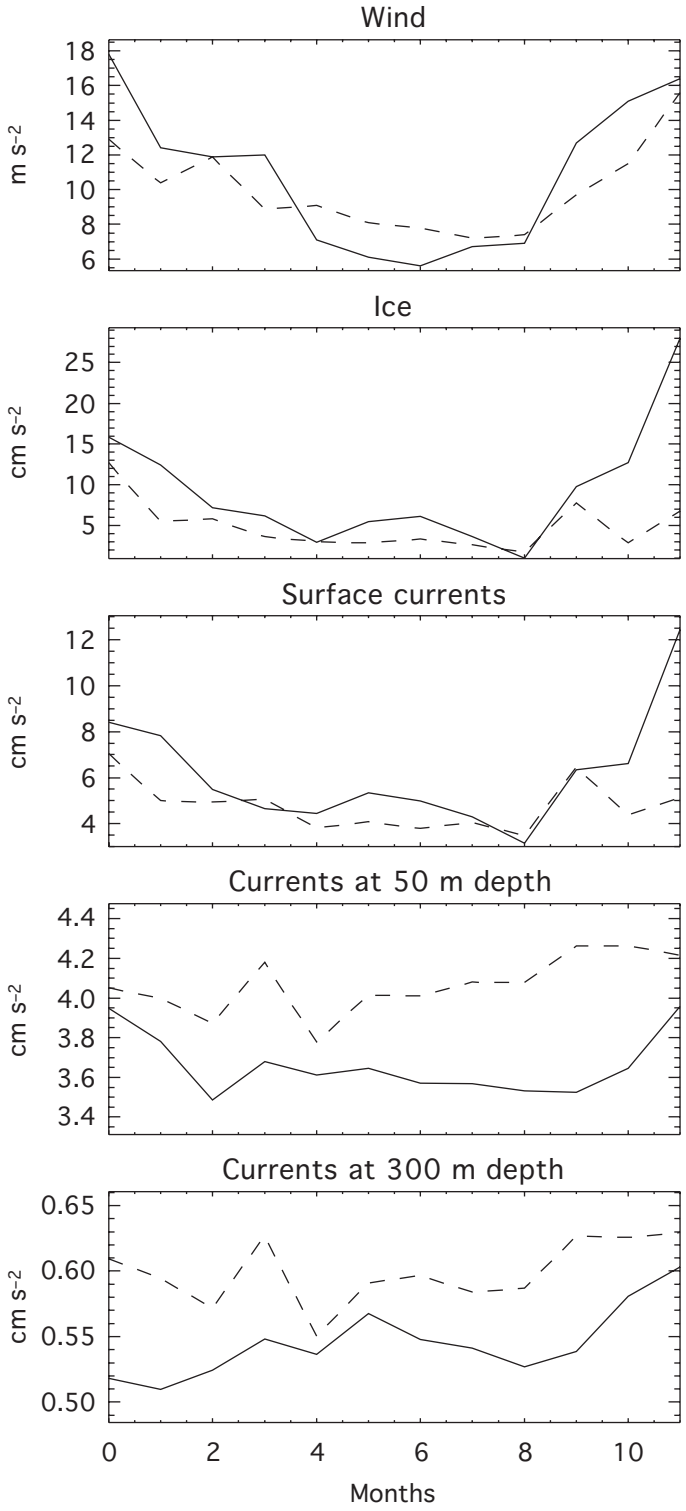

Figure 114. Kinetic energy of wind, ice drift, and oceanic currents in 1987 (ACCR, solid lines) and 1992 (CCR, dashed lines). The data are averaged over the deep (depth is greater than 200 m) Arctic Ocean.

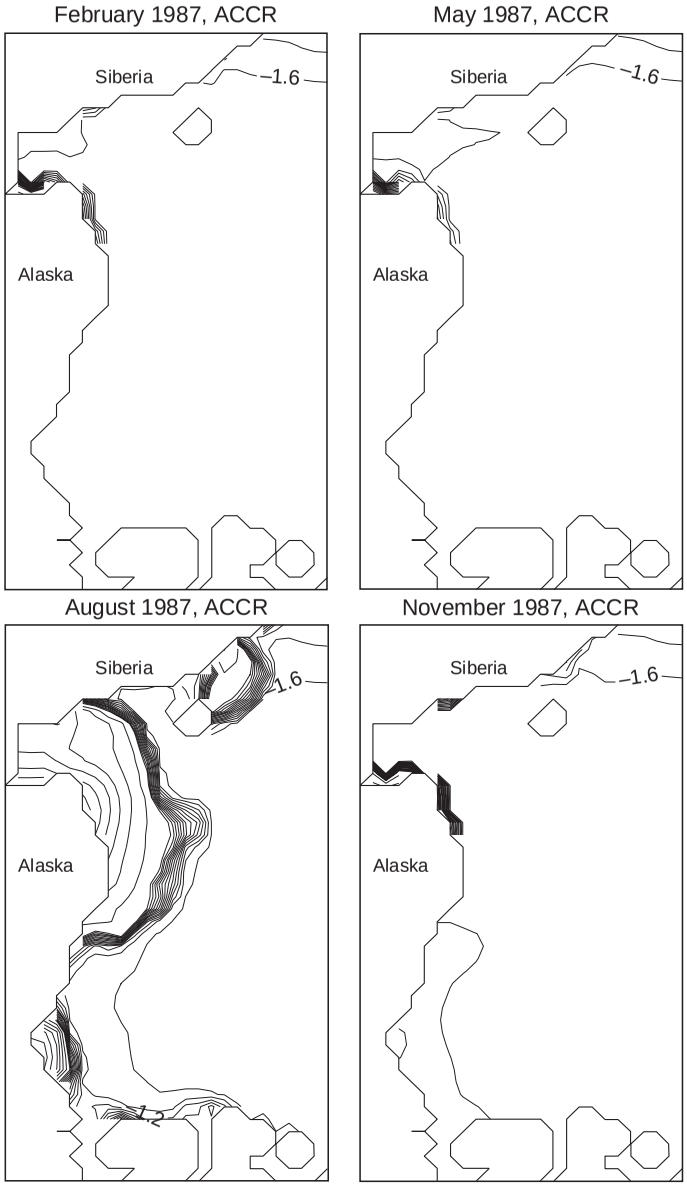

Figure 115. Simulated sea surface temperature in 1987 (ACCR).

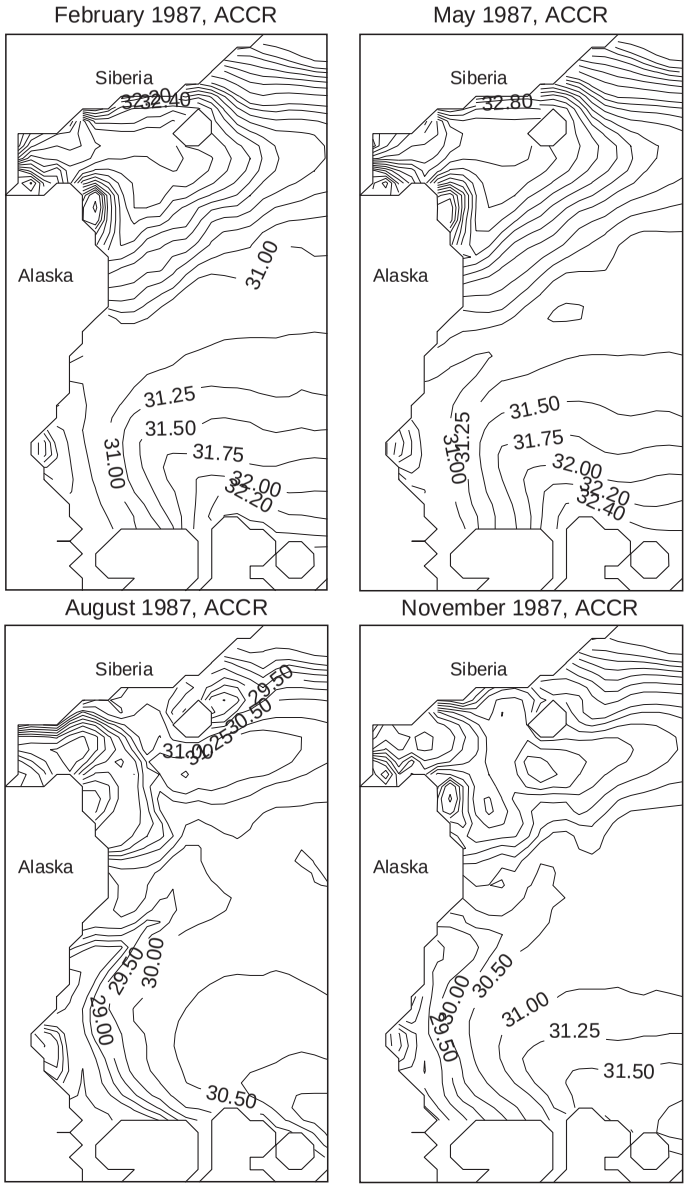

Figure 116. Simulated sea surface salinity in 1987 (ACCR).

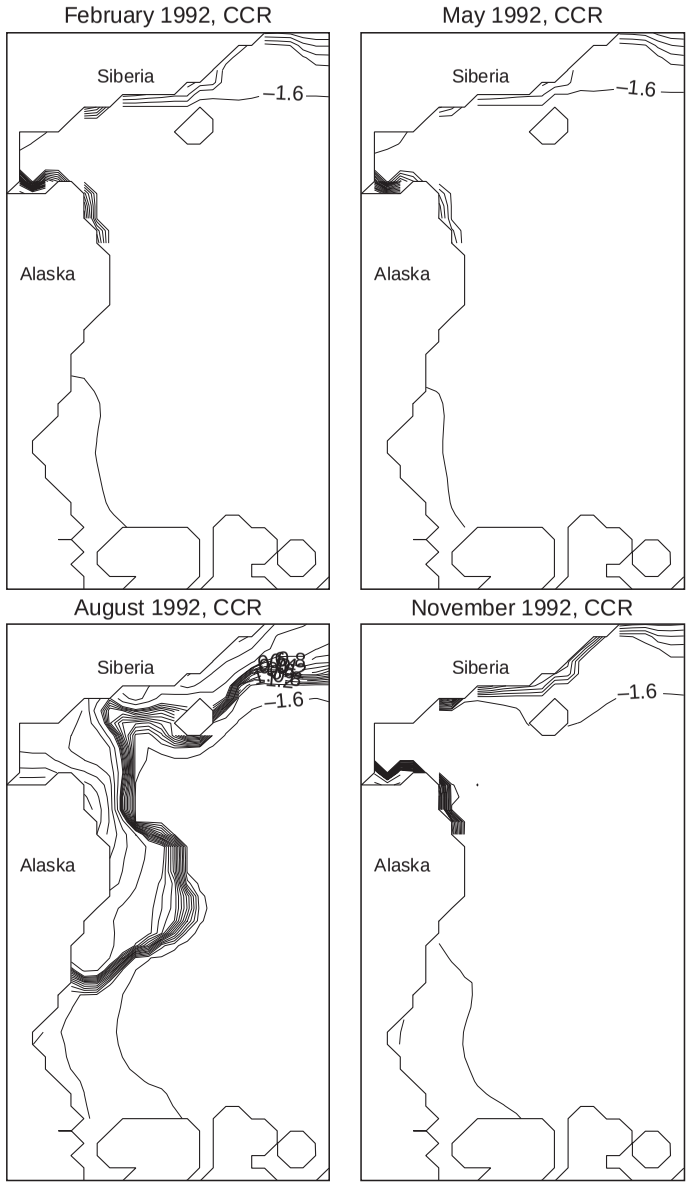

Figure 117. Simulated sea surface temperature in 1992 (CCR).

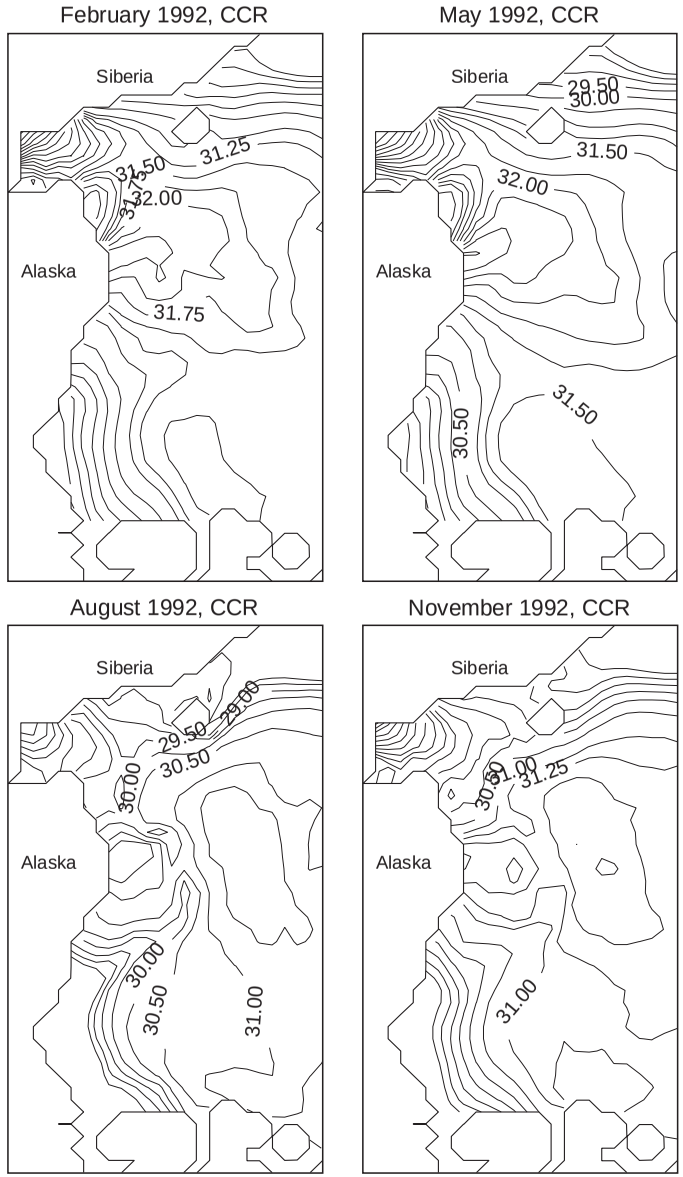

Figure 118. Simulated sea surface salinity in 1992 (CCR).

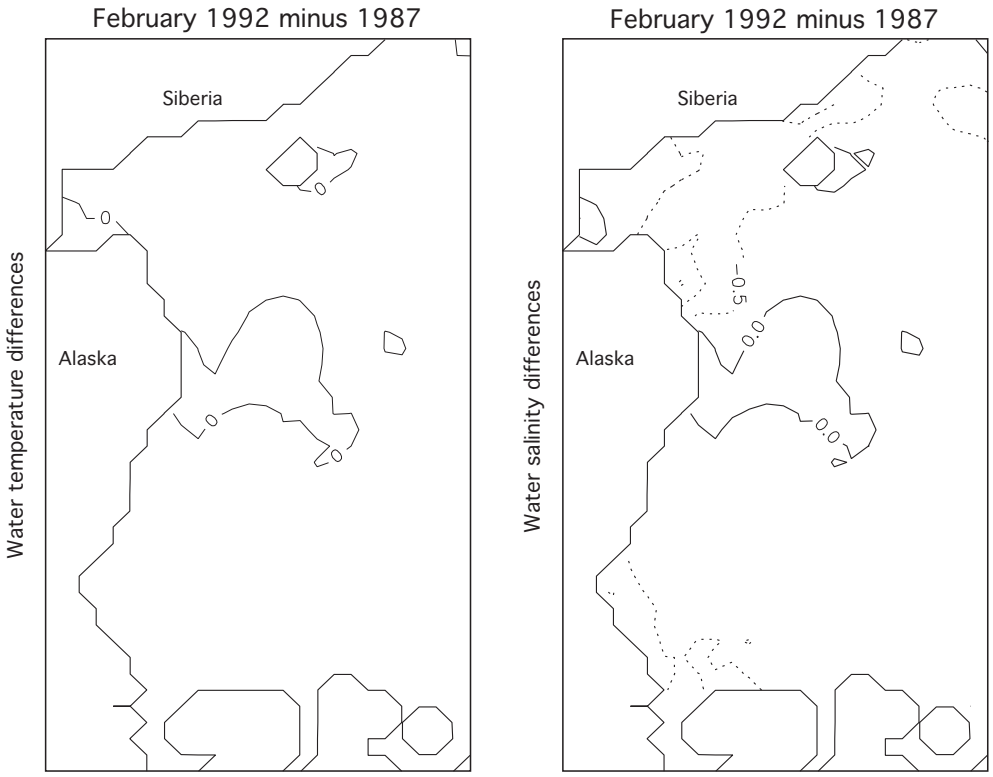

Figure 119. Differences in the surface water temperature (February).

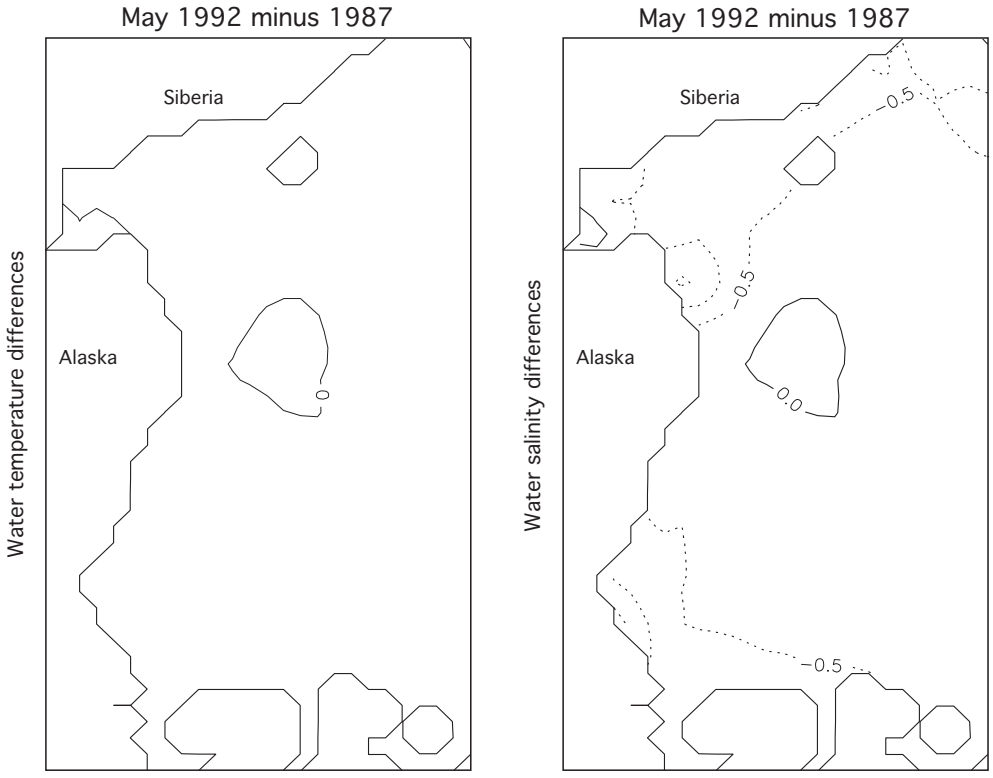

Figure 120. Differences in the surface water temperature (May).

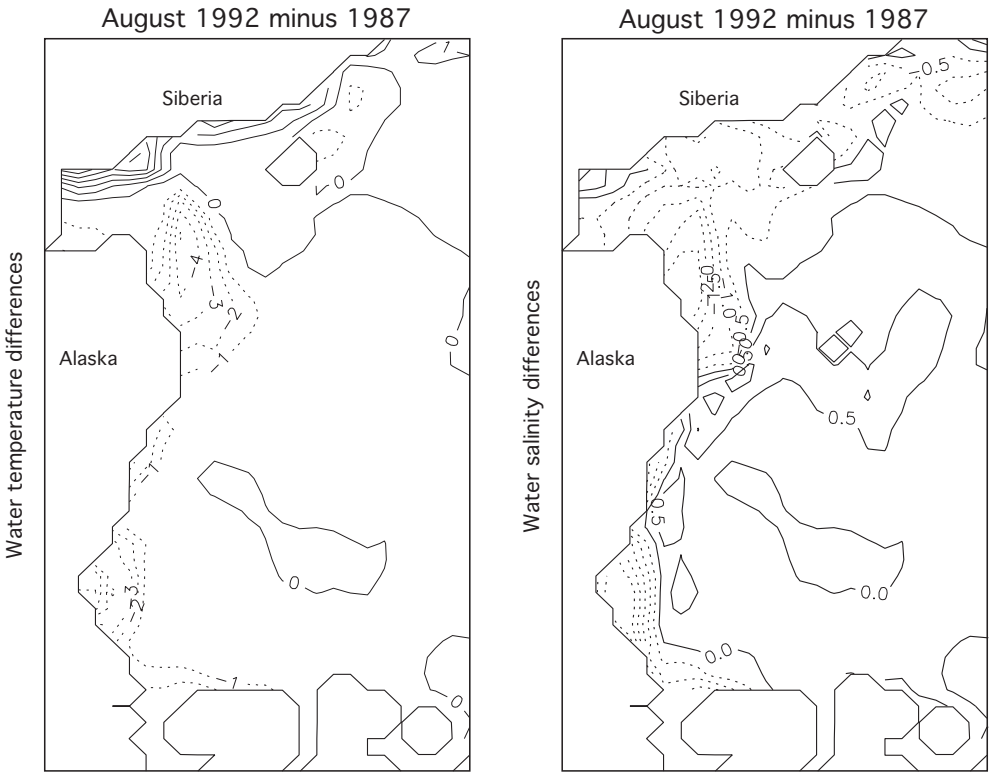

Figure 121. Differences in the surface water temperature (August).

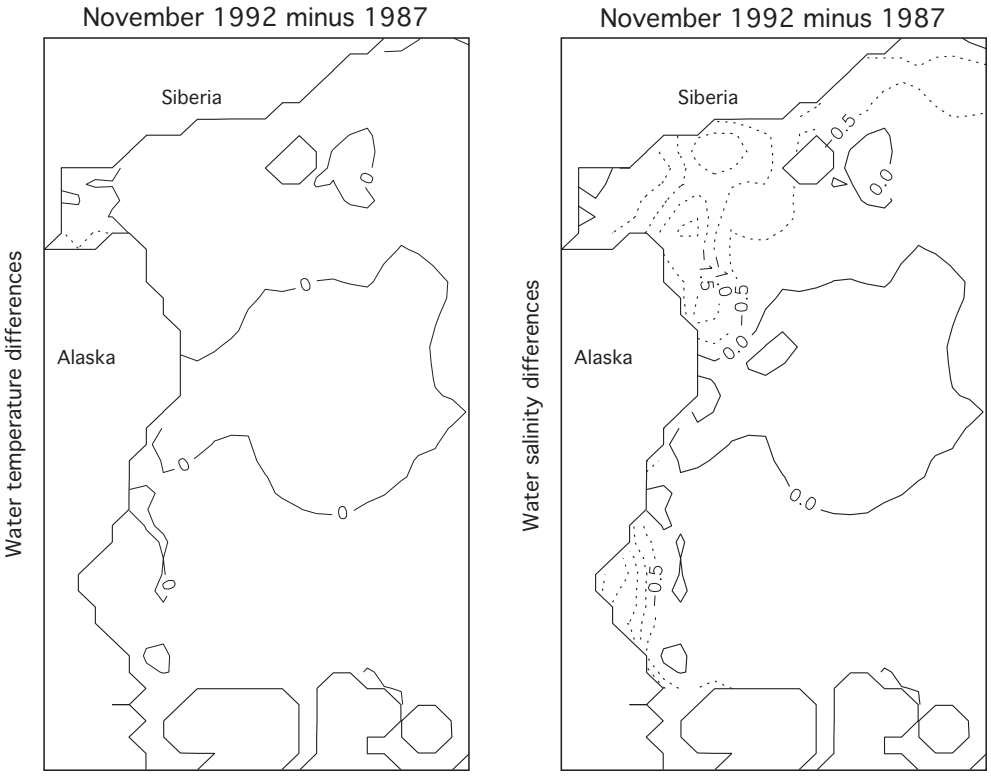

Figure 122. Differences in the surface water temperature (November).

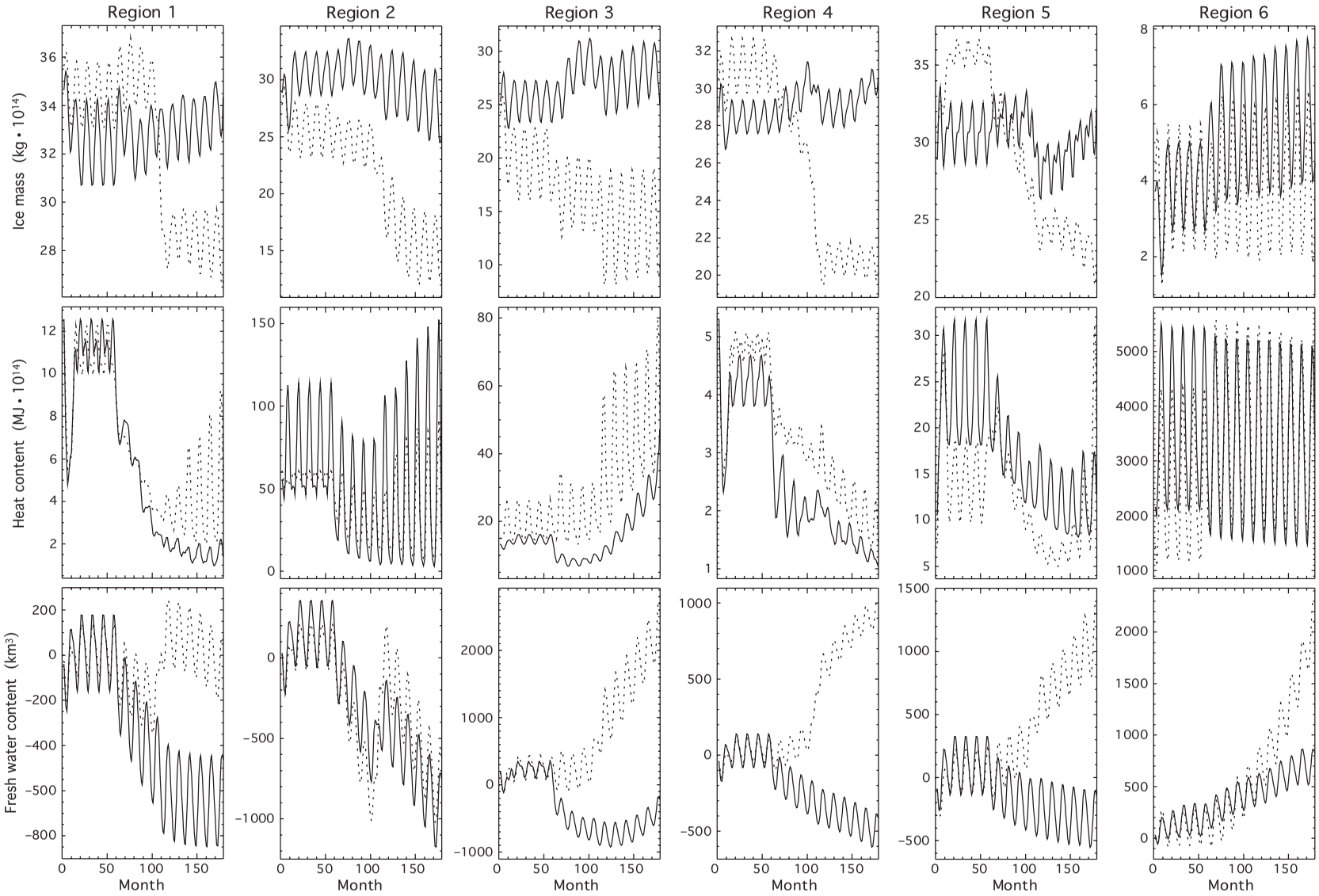

Figure 123. Temporal variability of the computed ice mass, heat, and freshwater content in the upper 50 m of the deep (depth is greater than 200 m) Arctic Ocean in ACCR (solid line) and CCR (dashed line). Note that vertical scales are different for different regions. Region locations are shown in Figure 55.

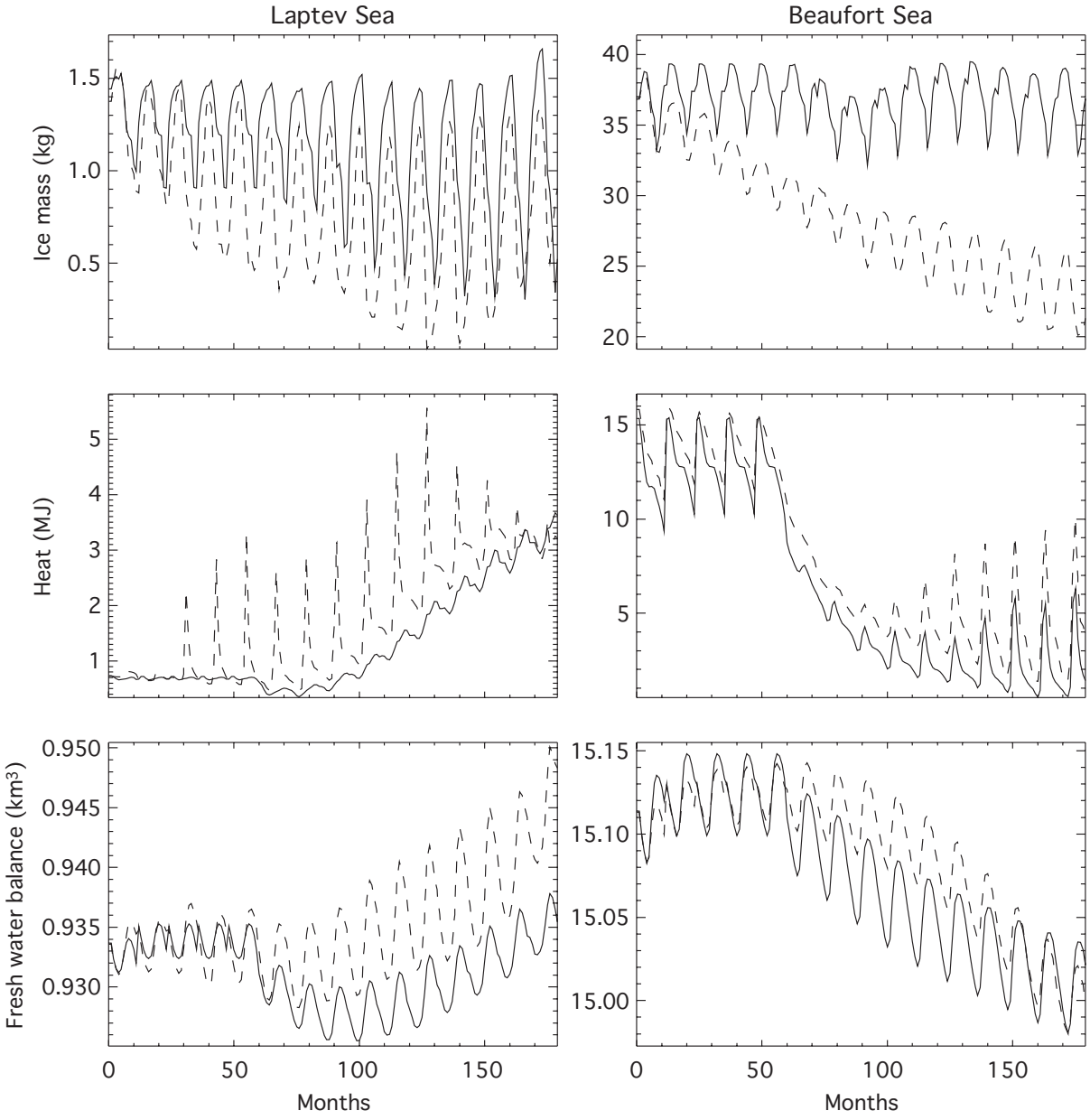

Figure 124. Temporal variability of the computed ice mass (10^{14}), heat (10^{14}), and freshwater content in the upper 50 m of the Laptev and Beaufort Seas in ACCR (solid line) and CCR (dashed line). Note that the vertical scales are different for different regions.

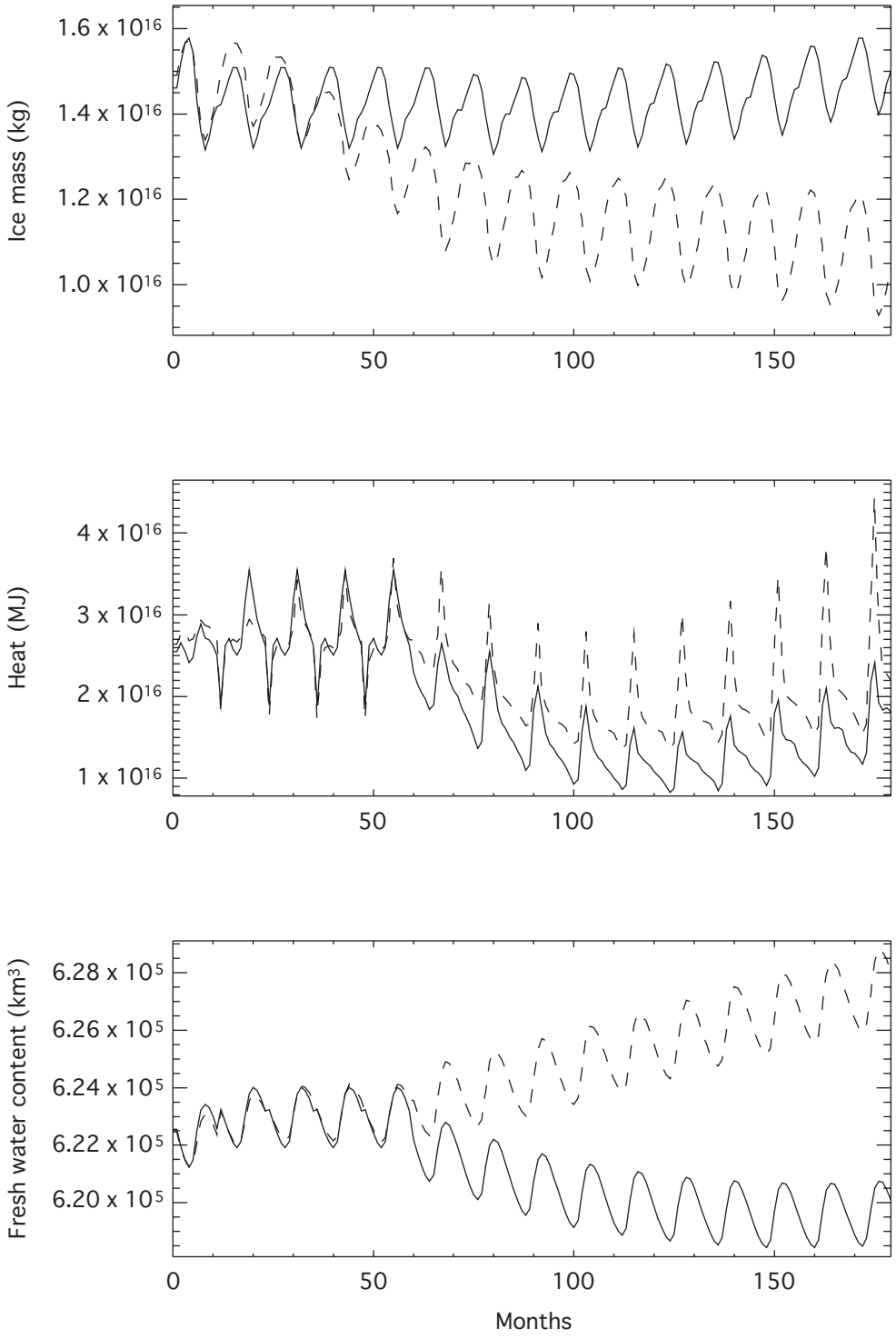

Figure 125. Temporal variability of the computed ice mass, heat, and freshwater content in the upper 50 m of the Arctic Ocean in ACCR (solid line) and CCR (dashed line).

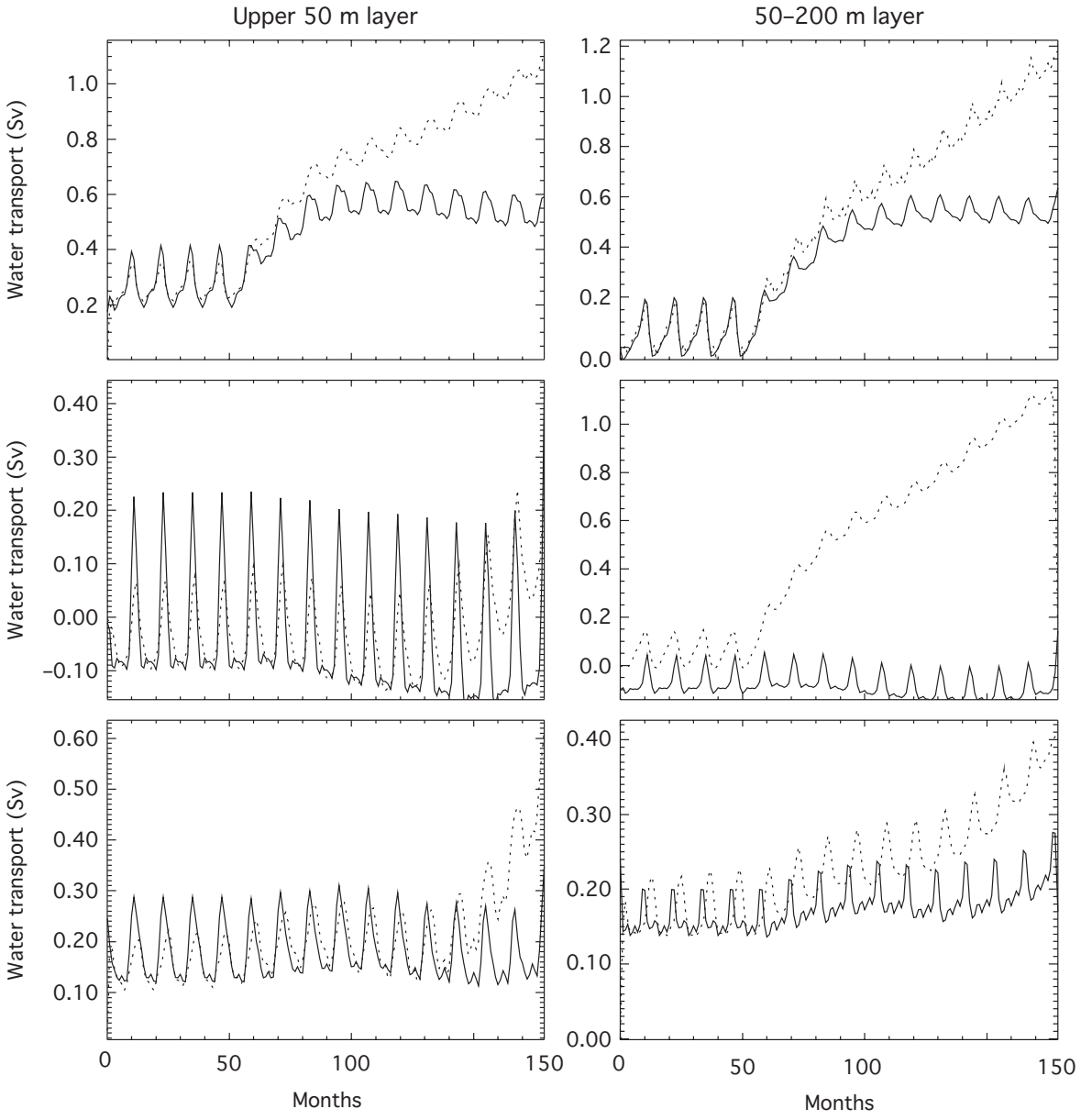

Figure 126. Water transport through Fram Straight (top), Franz Josef Land–Spitsbergen strait (middle), and Severnaya Zemlya–Franz Josef Land strait (bottom) in the upper 50-m layer (left) and in the 50–200-m layer (right) in 1987 (ACCR, solid line) and in 1992 (CCR, dotted line). Positive values are for transports from the Arctic Ocean for Fram Strait and into the Arctic Ocean for the two other straits.

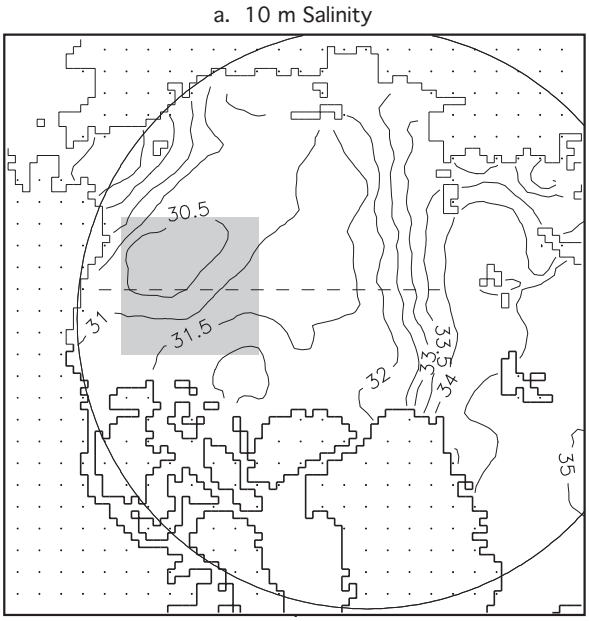

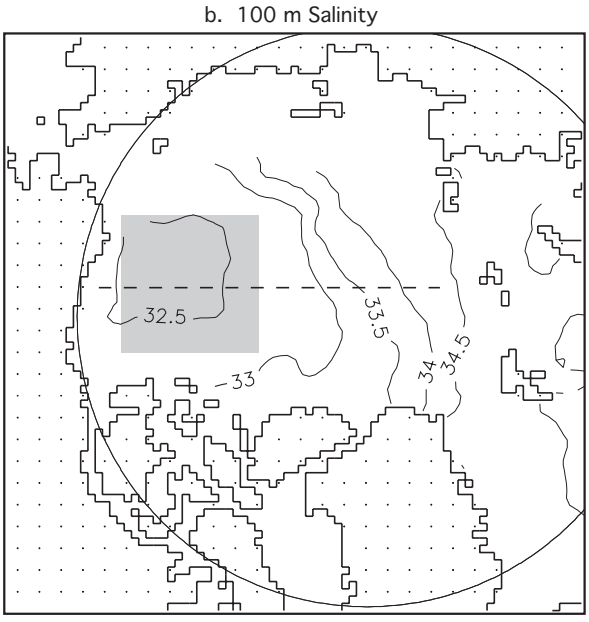

Figure 127. Winter water salinity at 10 meters (a). and 100 meters (b). The shaded box depicts the central area of the Beaufort Gyre. All data are from the U.S.–Russian Atlas of the Arctic Ocean for the winter period [EWG 1997].

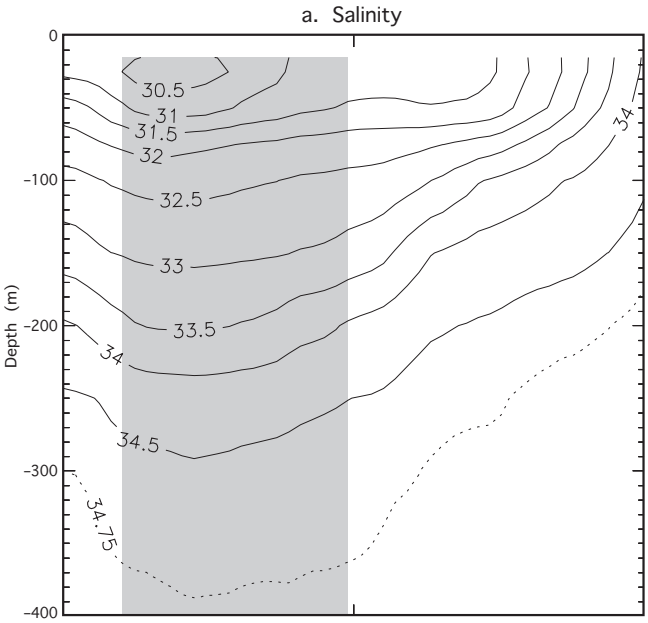

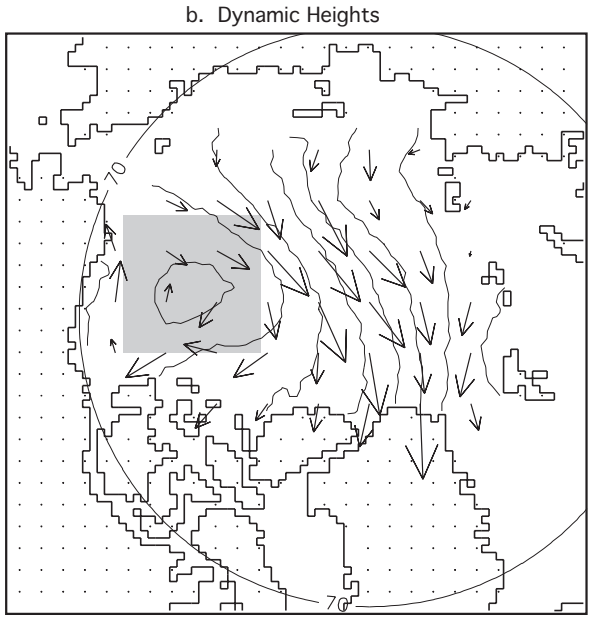

Figure 128. Salinity distribution along the dashed line in Figure 127 (a), and dynamic heights relative to 200 db and the direction of geostrophic circulation (b).

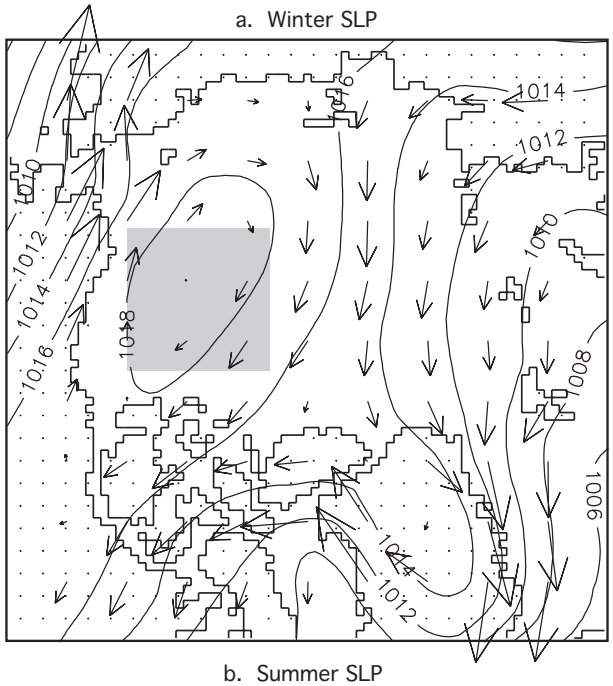

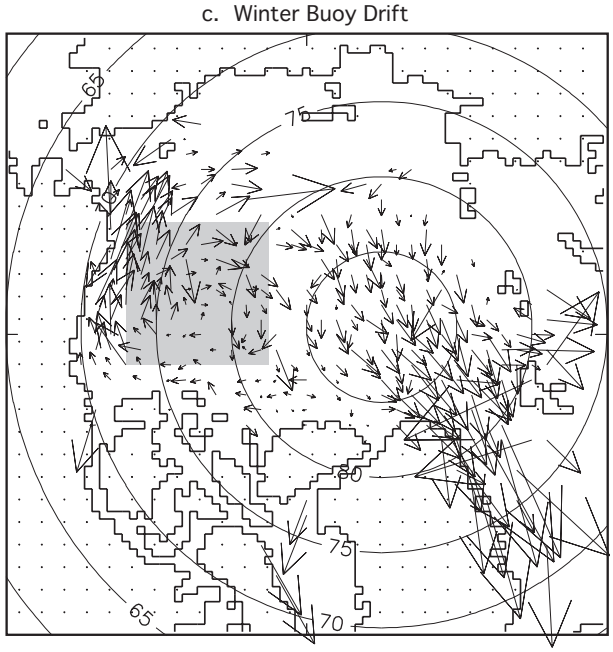

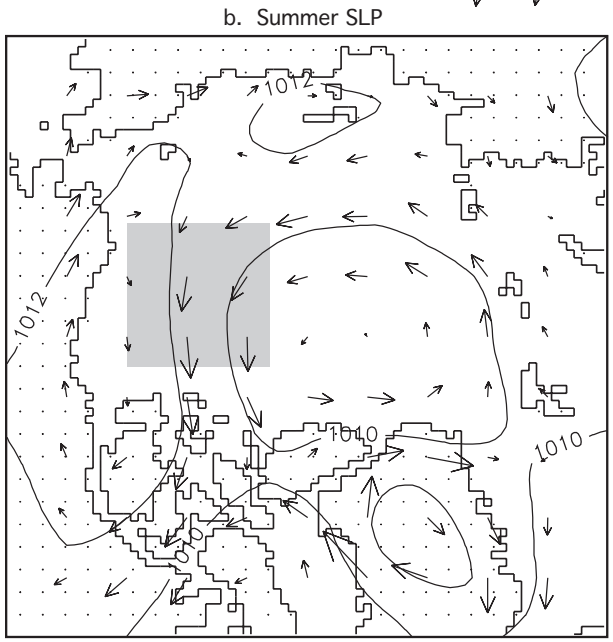

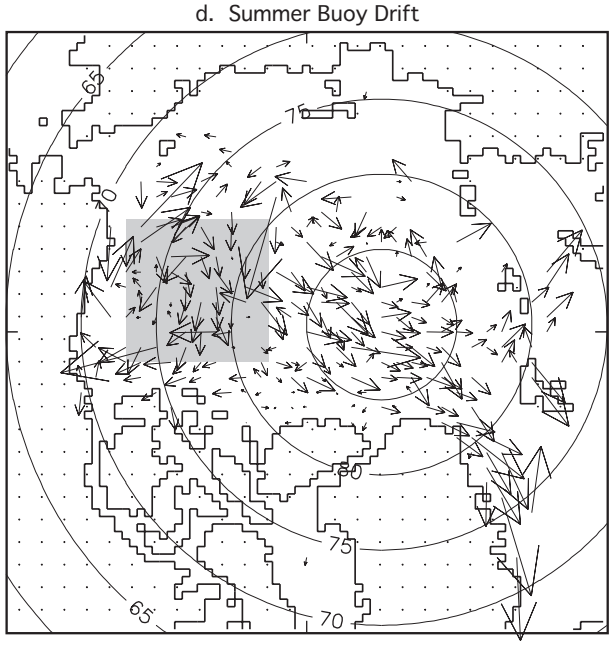

Figure 129. 1979–1997 winter (a) and summer (b) averaged SLP and geostrophic winds.

Figure 130. IABP buoy drift.

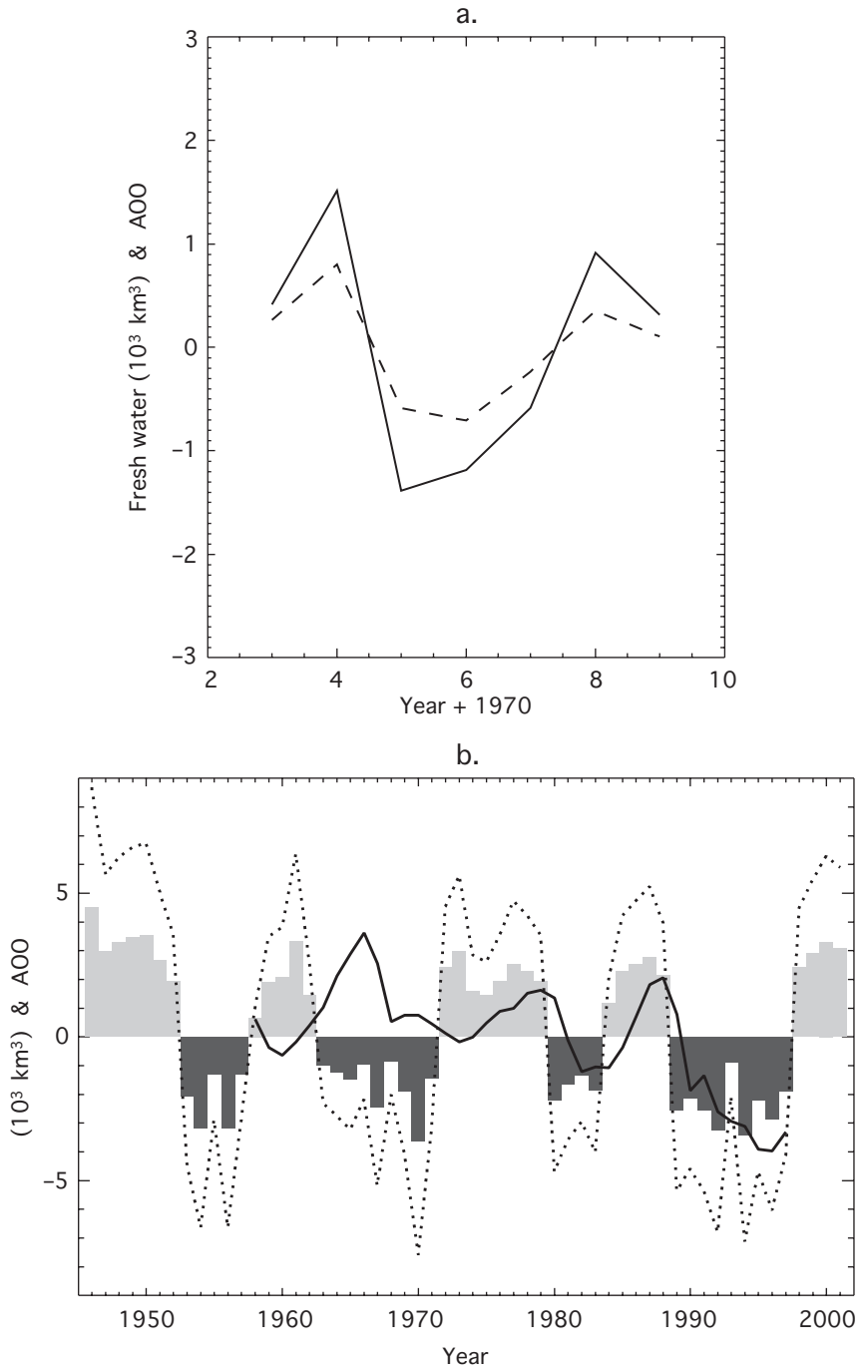

Figure 131. a) Correlation between the freshwater content anomaly (solid line) in the Beaufort sea (shaded box in Figure 127) and AOO (dashed line) for 1973–1979, and b) correlation between the sea ice volume anomaly from three models (solid line) and the AOO index (bars). After the 1970s, the sea ice volume increases during the anticyclonic circulation regime (positive index) and decreases during the cyclonic circulation regime (negative index). The dotted line depicts the variability of the reconstructed freshwater content in the box shown in Figures 128–130.

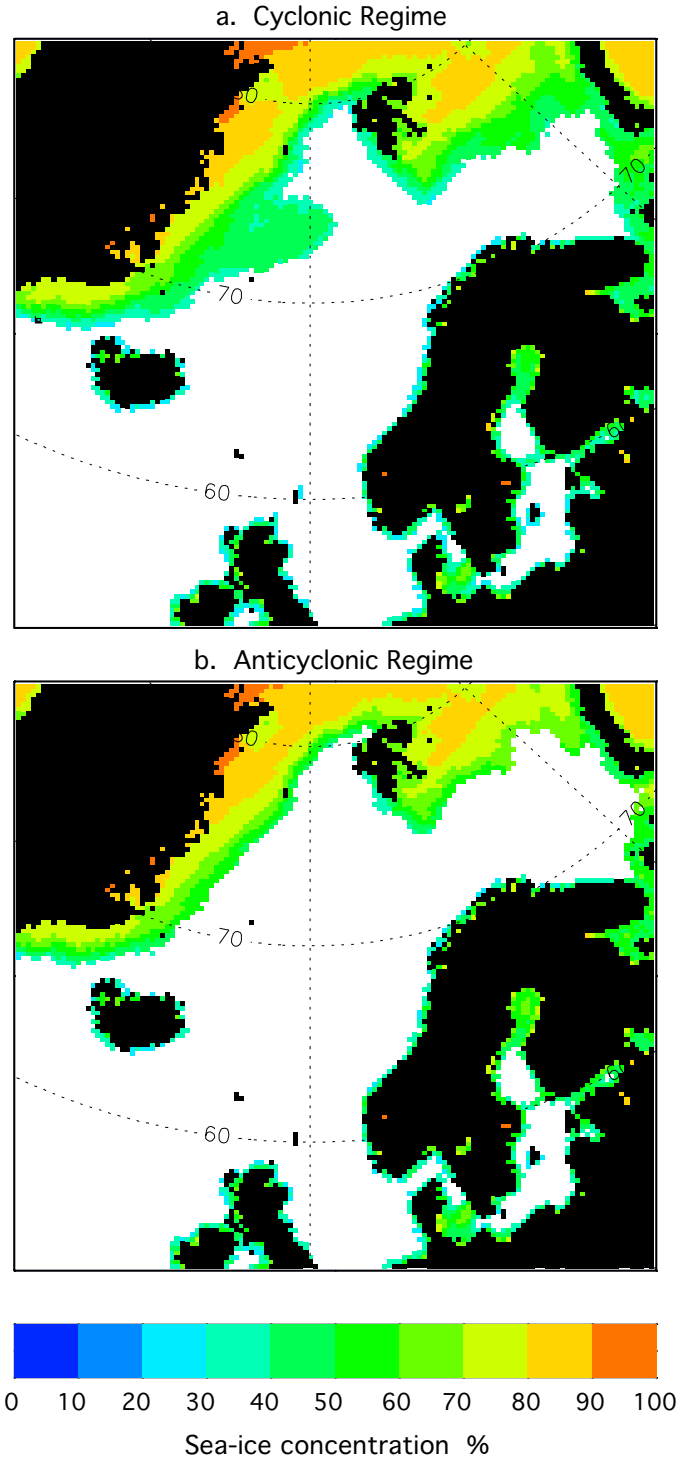

Figure 132. Sea ice concentration averaged for a) cyclonic: 1980–1983 and 1989–1997, and b) anticyclonic: 1984–1988 and 1998–2000 regimes. Note that much more ice is present in the Greenland Sea during cyclonic regimes because of enhanced development of the Odden ice tongue in the region of the Greenland Sea deep ocean convection during cyclonic regimes [Comiso et al. 2001].

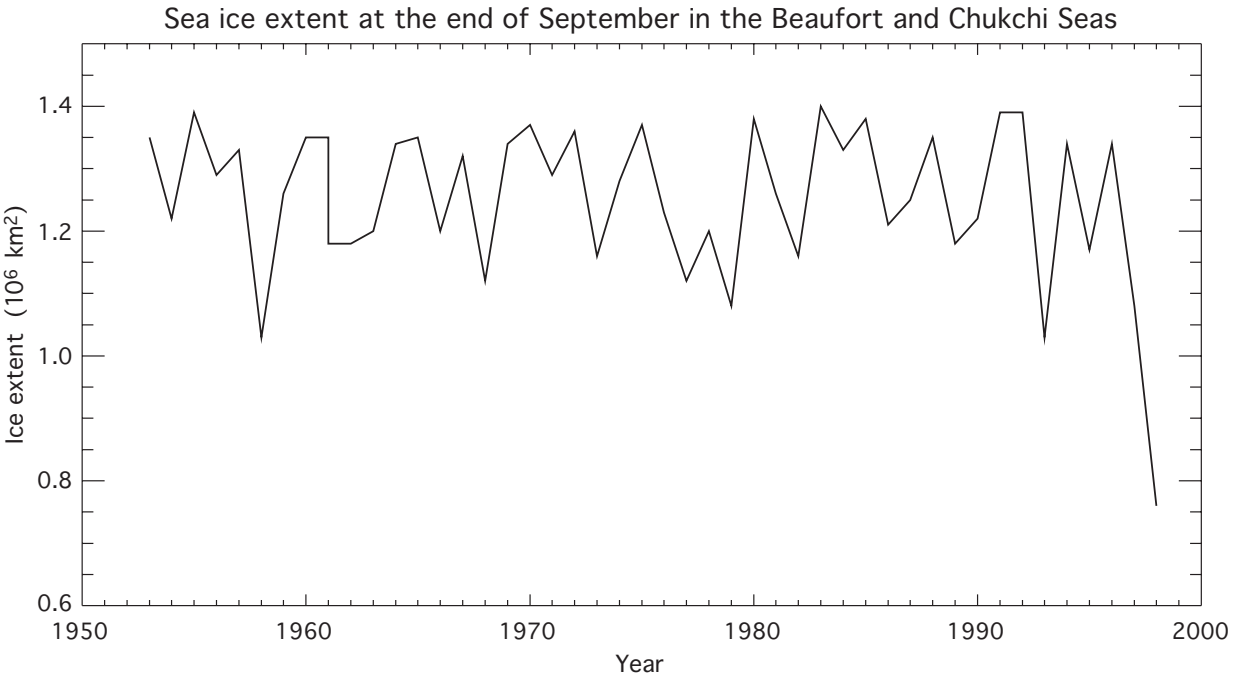

Figure 133. Sea ice extent at the end of September in the Beaufort and Chukchi Seas.

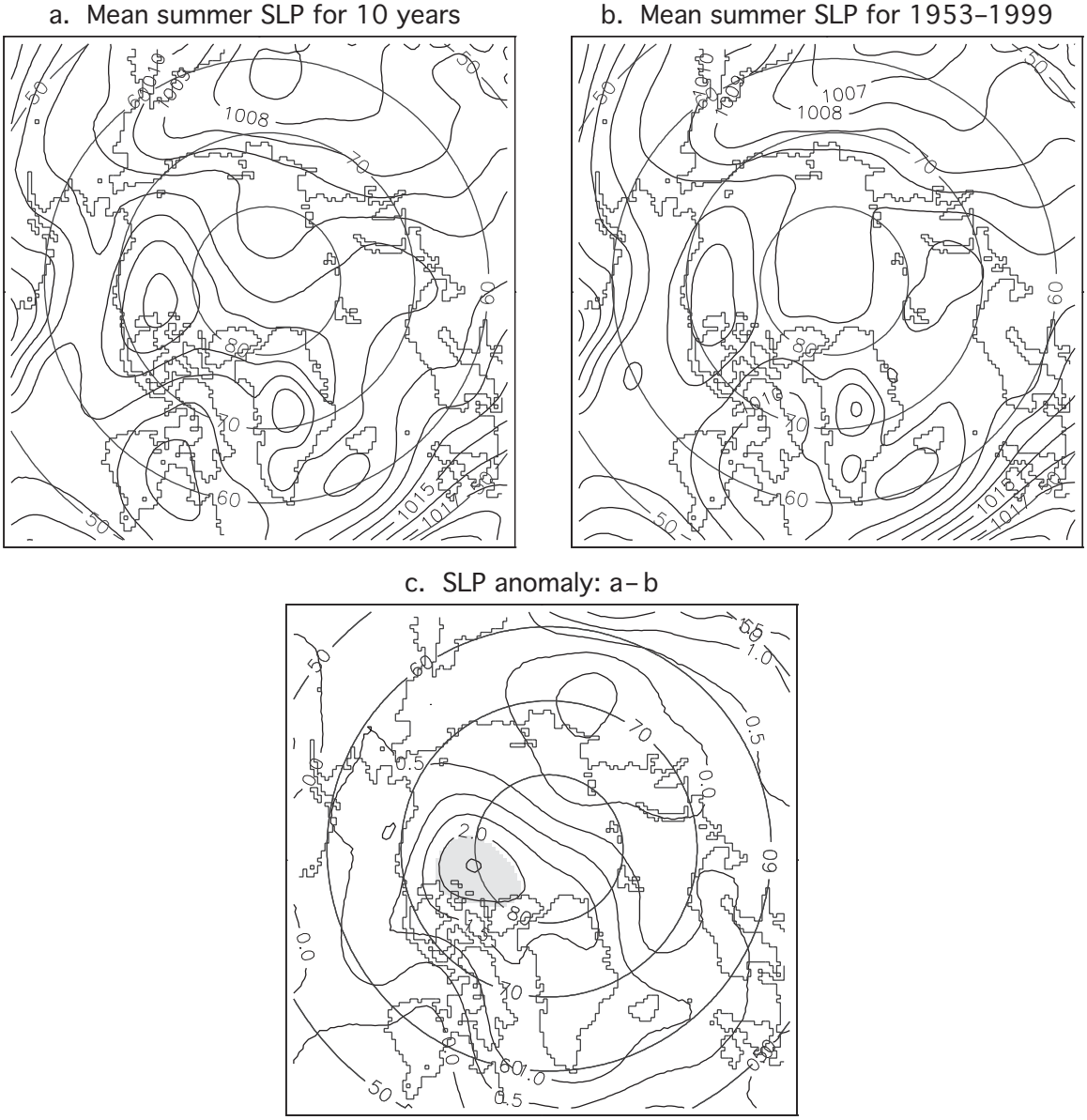

Figure 134. (a) Mean summer SLP for the 10 years with the lowest ice extent in the western Arctic (Figure 133), and (b) mean summer SLP for the period 1953–1999; (c) SLP anomalies (a minus b). The shaded area indicates anomalies greater than 2 hP. Contour intervals are 1 hPa in (a) and (b), and 0.5 hPa in (c).

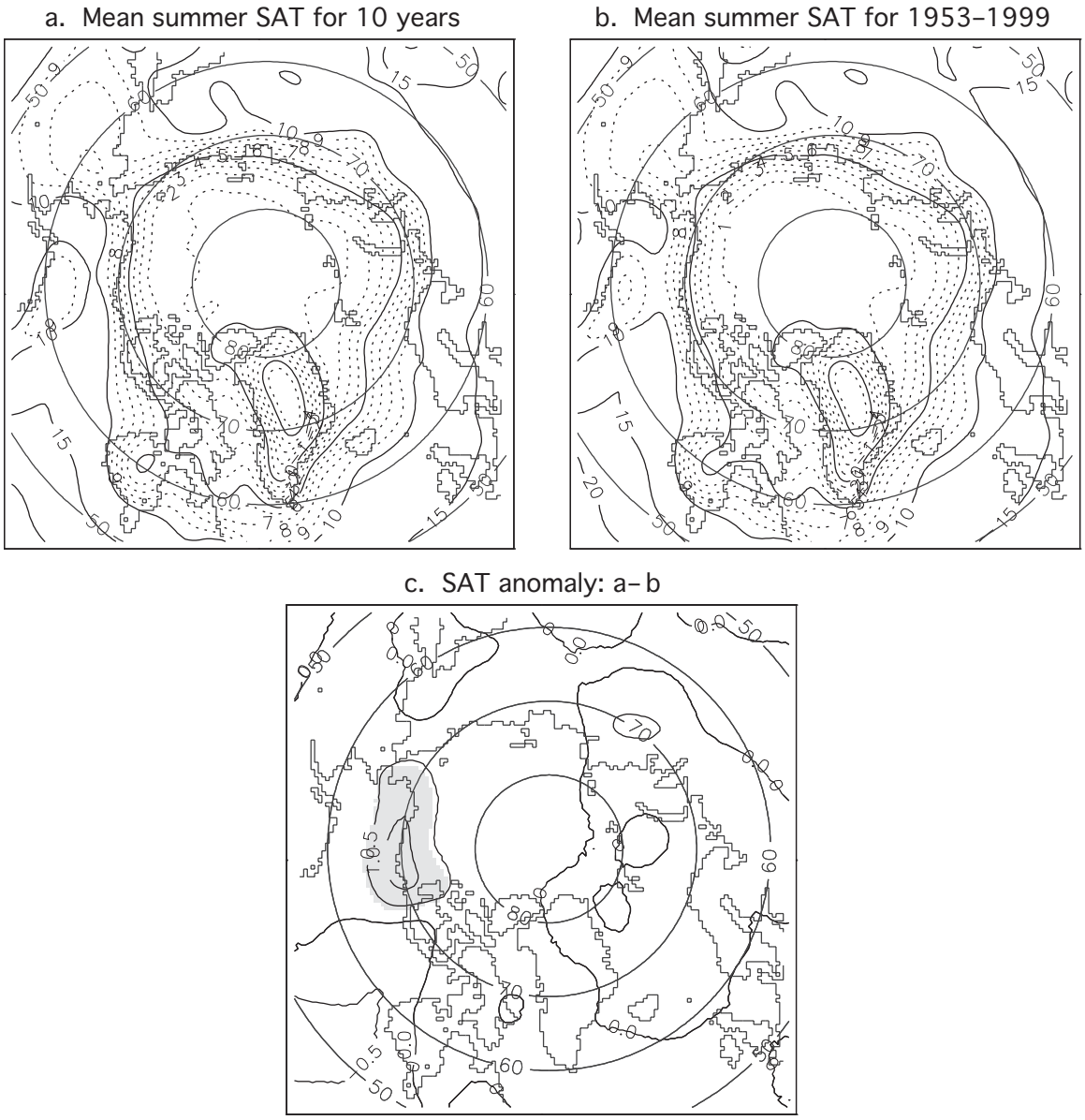

Figure 135. (a) Mean summer SAT for the 10 years with the lowest ice extent in the western Arctic (Figure 133), and (b) mean summer SAT for the period 1953–1999; (c) SAT anomalies (a minus b). The shaded area indicates anomalies greater than 2 °C. Contour intervals are 1 °C in (a) and (b), and 0.5 °C in (c).

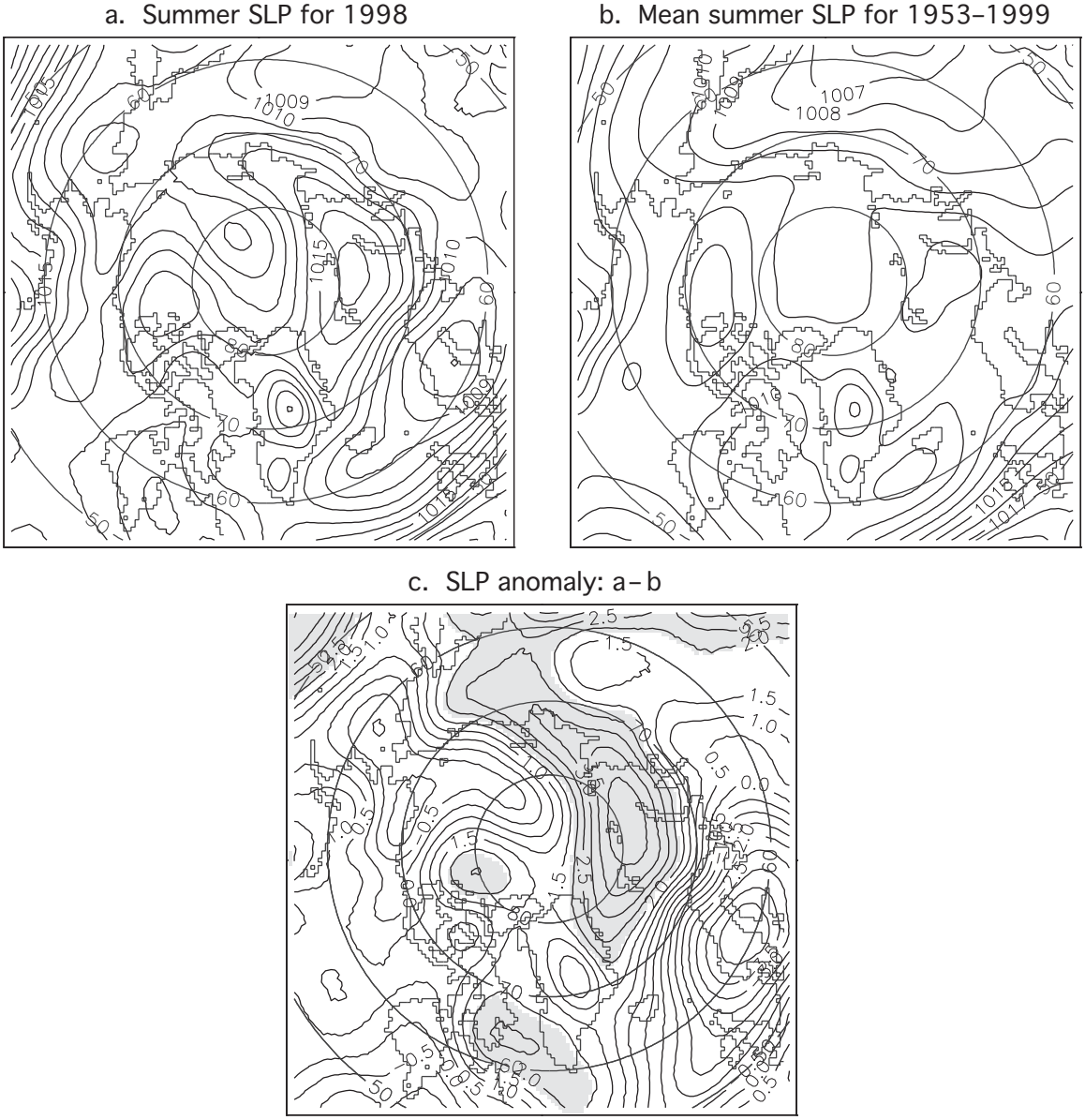

Figure 136. (a) Mean summer SLP in 1998, and (b) mean summer SLP for the period 1953–1999; (c) SLP anomalies (a minus b). The shaded area indicates anomalies greater than 2 hP(a). Contour intervals are 1 hPa in (a) and (b), and 0.5 hPa in (c).

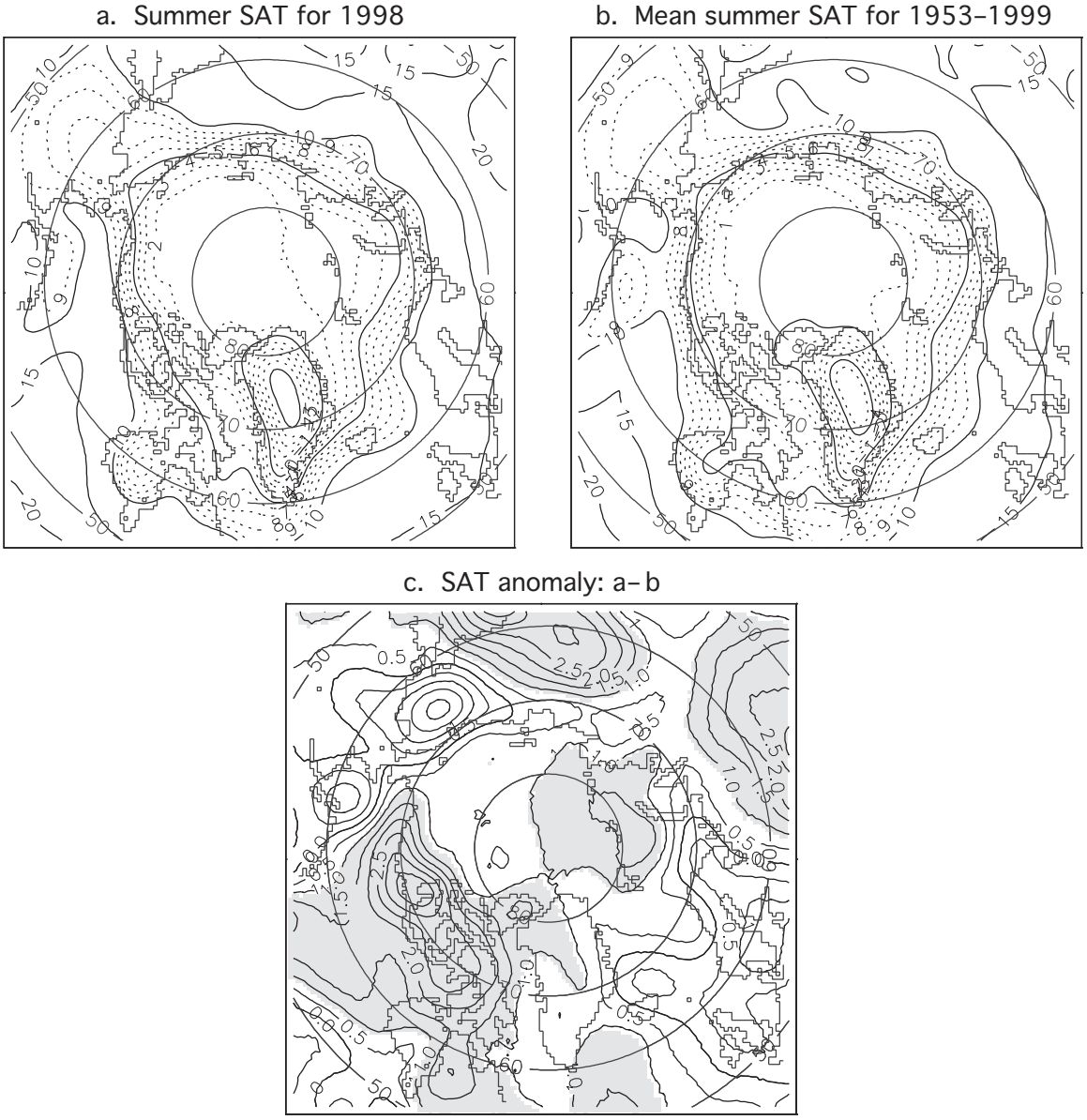

Figure 137. (a) Mean summer SAT in 1998, and (b) mean summer SAT for the period 1953–1999; (c) SAT anomalies (a minus b). The shaded area indicates anomalies greater than 2°C. Contour intervals are 1°C in (a) and (b), and 0.5°C in (c).

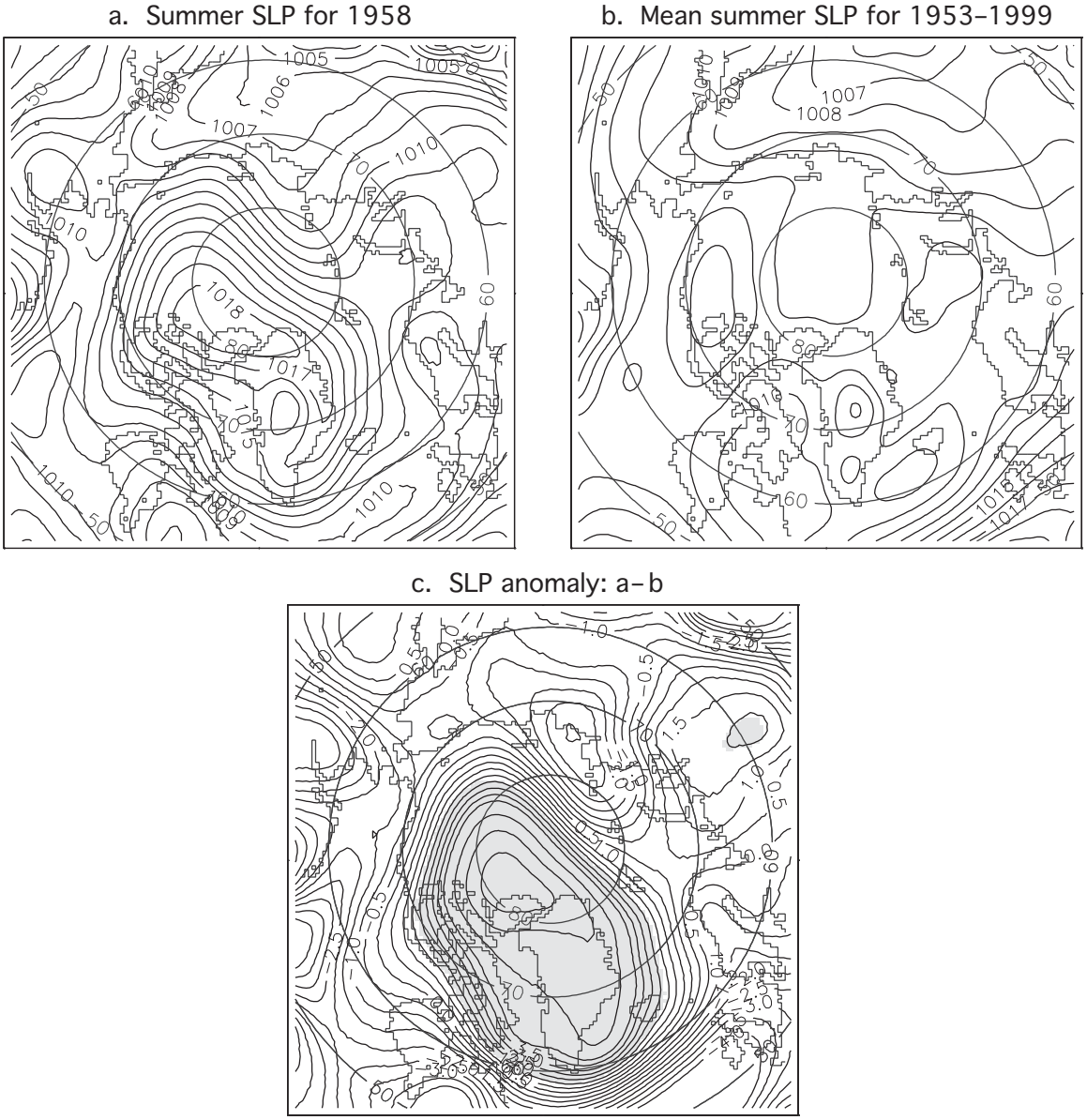

Figure 138. (a) Mean summer SLP in 1958, and (b) mean summer SLP for the period 1953–1999; (c) SLP anomalies (a minus b). The shaded area indicates anomalies greater than 2 hP(a). Contour intervals are 1 hPa in (a) and (b), and 0.5 hPa in (c).

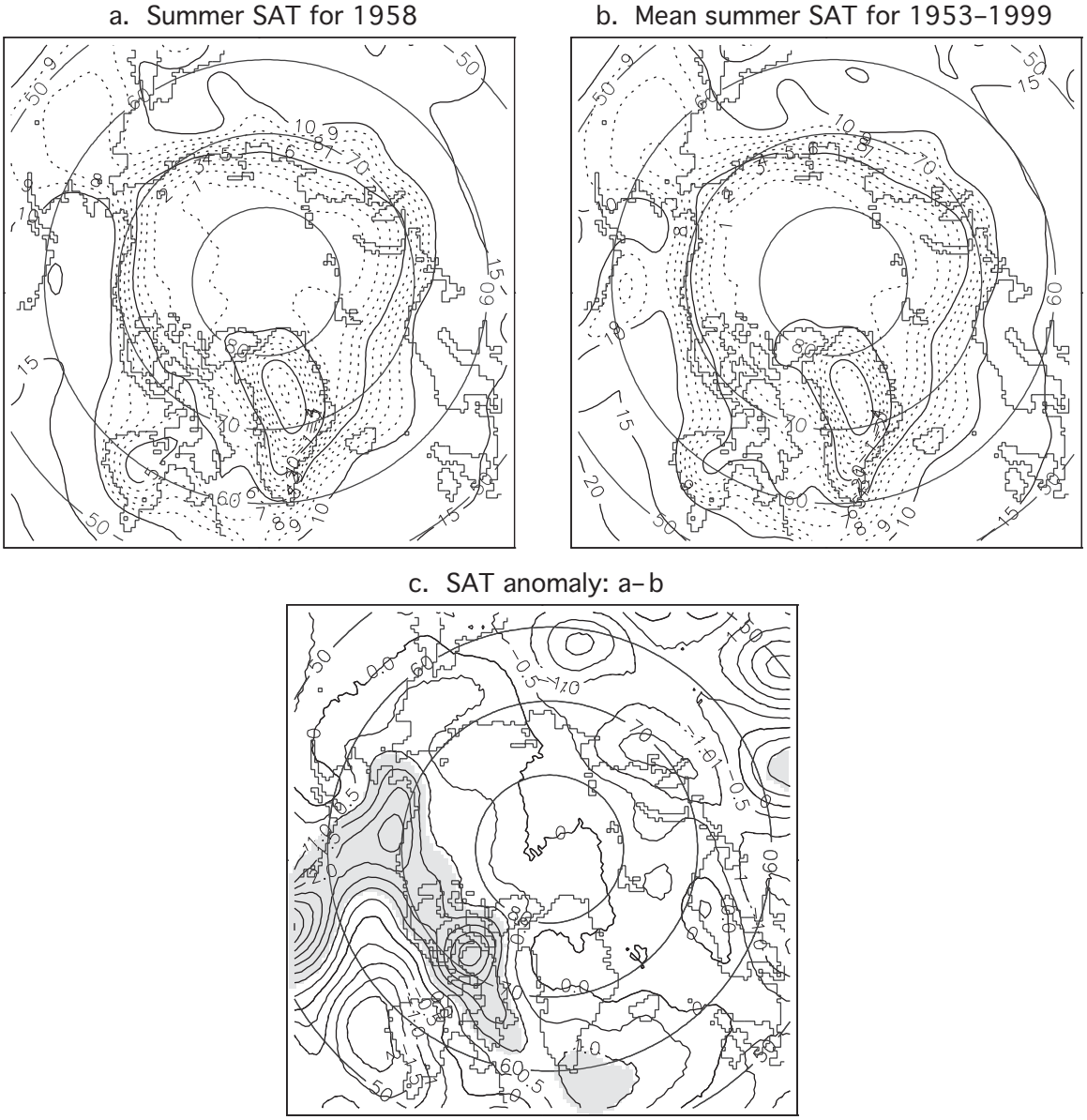

Figure 139. (a) Mean summer SAT in 1958, and (b) mean summer SAT for the period 1953–1999; (c) SAT anomalies (a minus b). The shaded area indicates anomalies greater than 2°C. Contour intervals are 1°C in (a) and (b), and 0.5°C in (c).

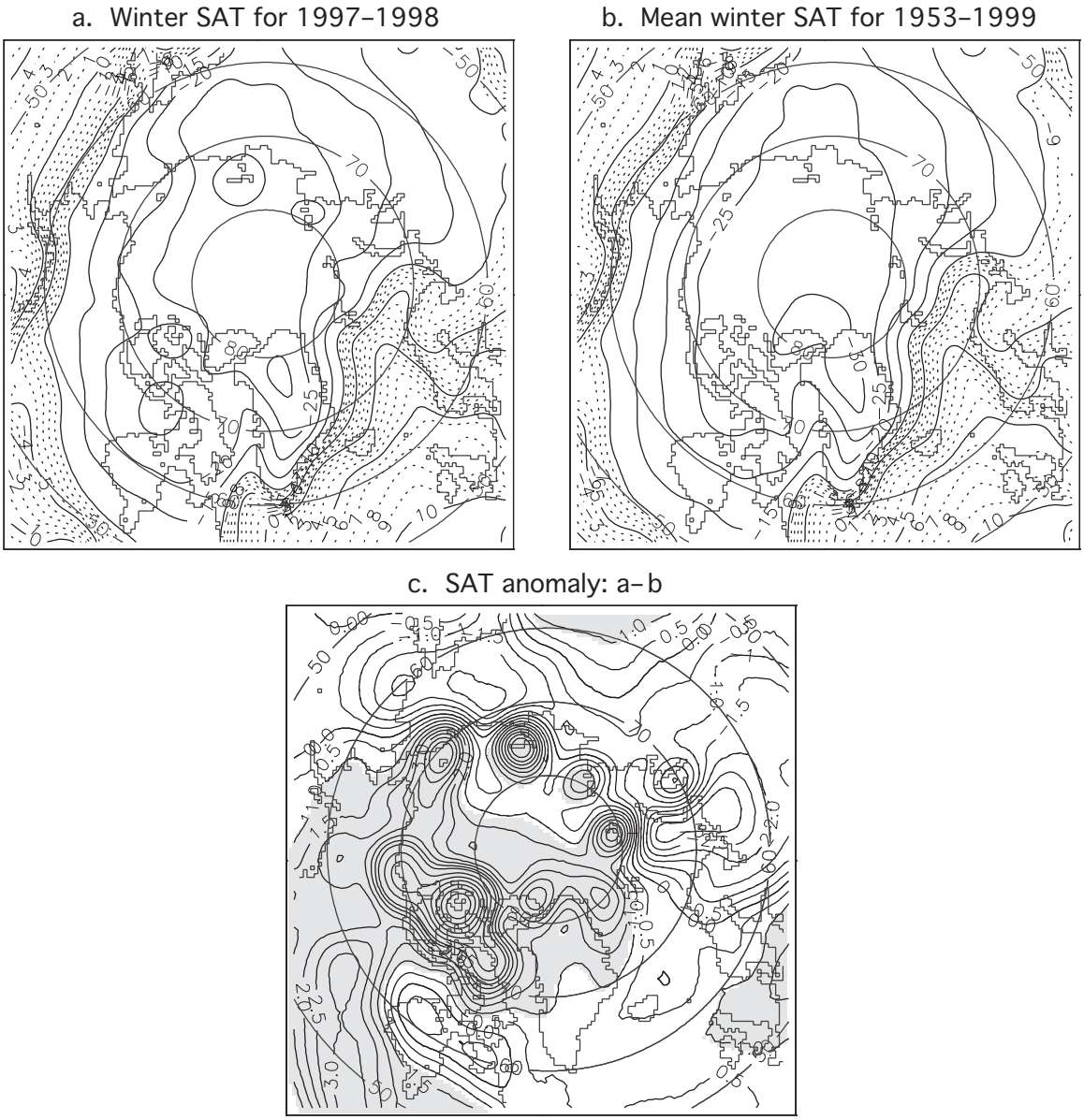

Figure 140. (a) Mean winter SAT in 1997–1998, and (b) mean winter SAT for the period 1953–1999; (c) SAT anomalies (a minus b). The shaded area indicates anomalies greater than 2 °C. Contour intervals are 1 °C in (a) and (b), and 0.5 °C in (c).

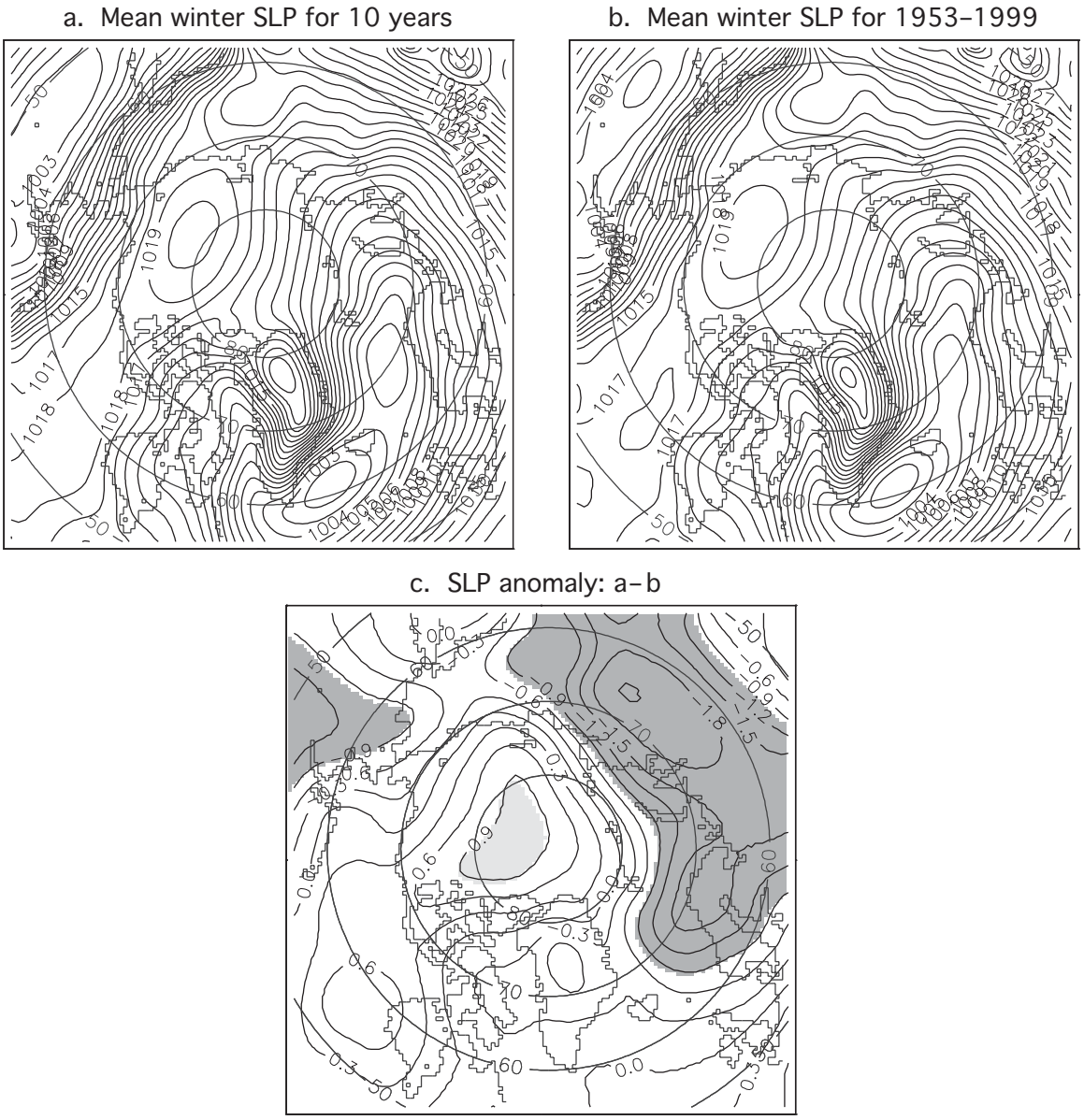

Figure 141. (a) Mean winter SLP for the 10 years with the lowest ice extent in the western Arctic (Figure 133), and (b) mean winter SLP for the period 1953–1999; (c) SLP anomalies (a minus b). The light shaded area indicates anomalies greater than 2 hP(a). Contour intervals are 1 hPa in (a) and (b), and 0.5 hPa in (c).

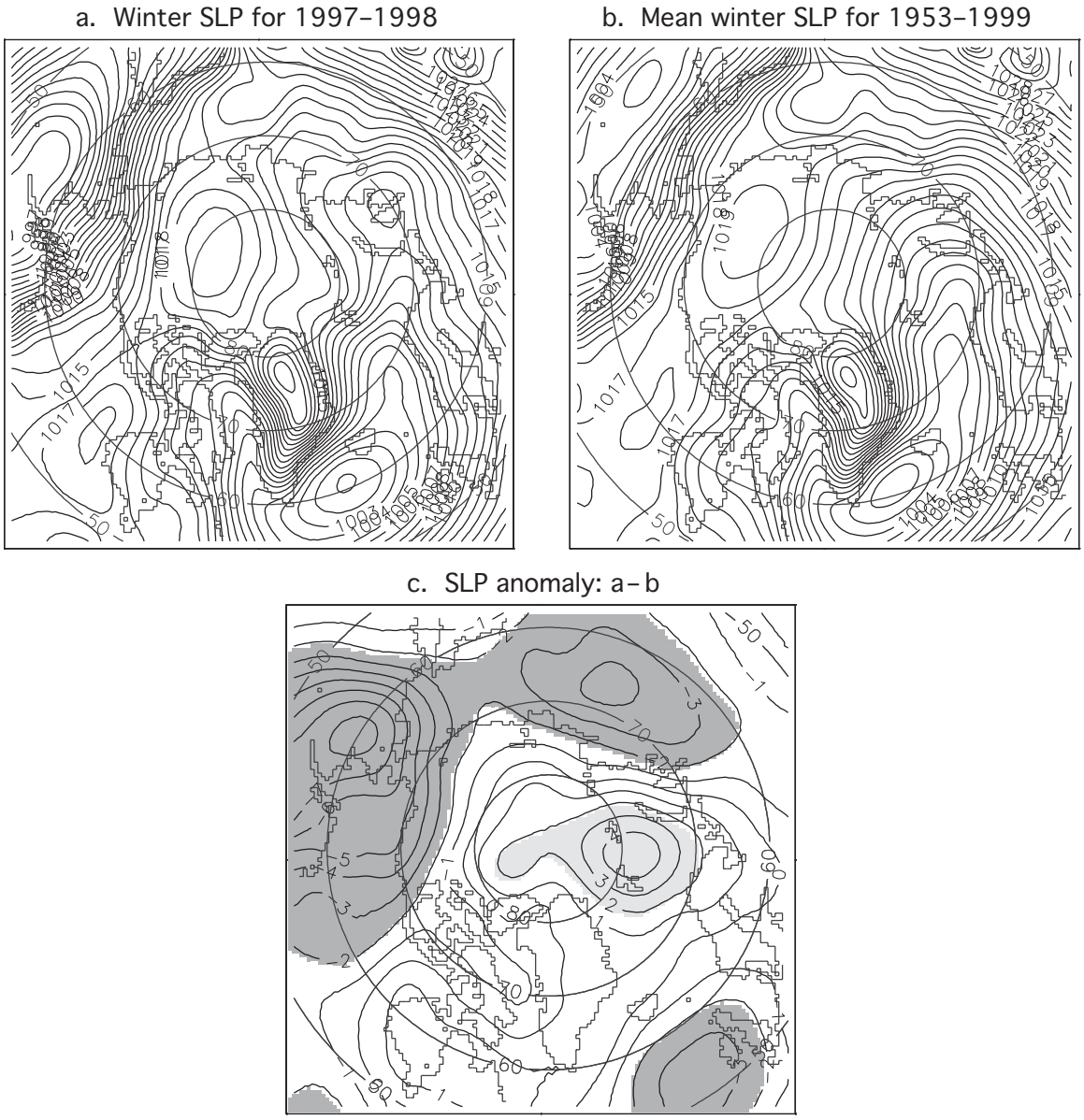

Figure 142. (a) Mean winter SLP in 1997–1998, and (b) mean winter SLP for the period 1953–1999; (c) SLP anomalies (a minus b). The light shaded area indicates anomalies greater than 2 hP(a). Contour intervals are 1 hPa in (a) and (b), and 0.5 hPa in (c).

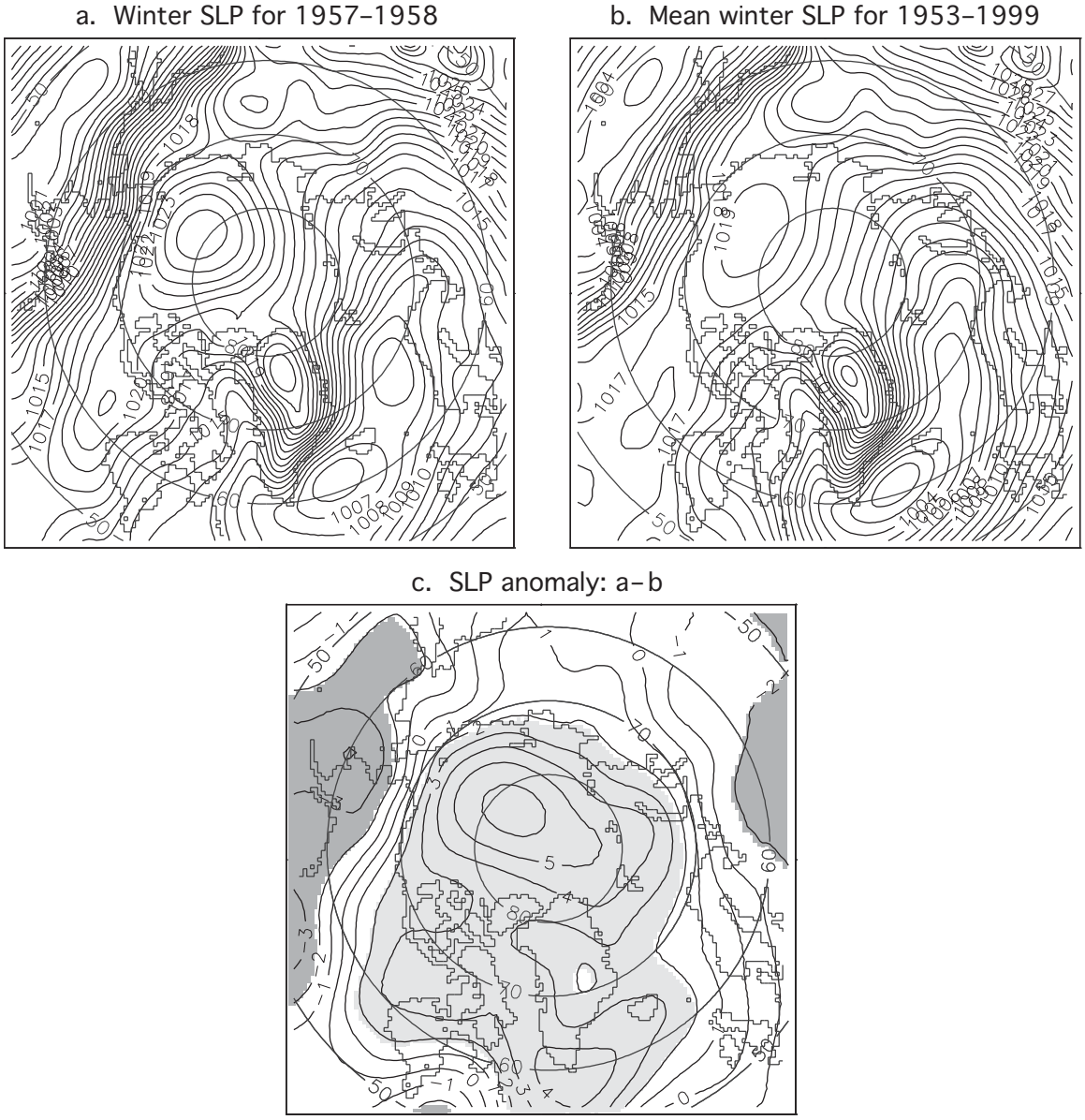

Figure 143. (a) Mean winter SLP in 1957–1958, and (b) mean winter SLP for the period 1953–1999; (c) SLP anomalies (a minus b). The light shaded area indicates anomalies greater than 2 hP(a). Contour intervals are 1 hPa in (a) and (b), and 0.5 hPa in (c).

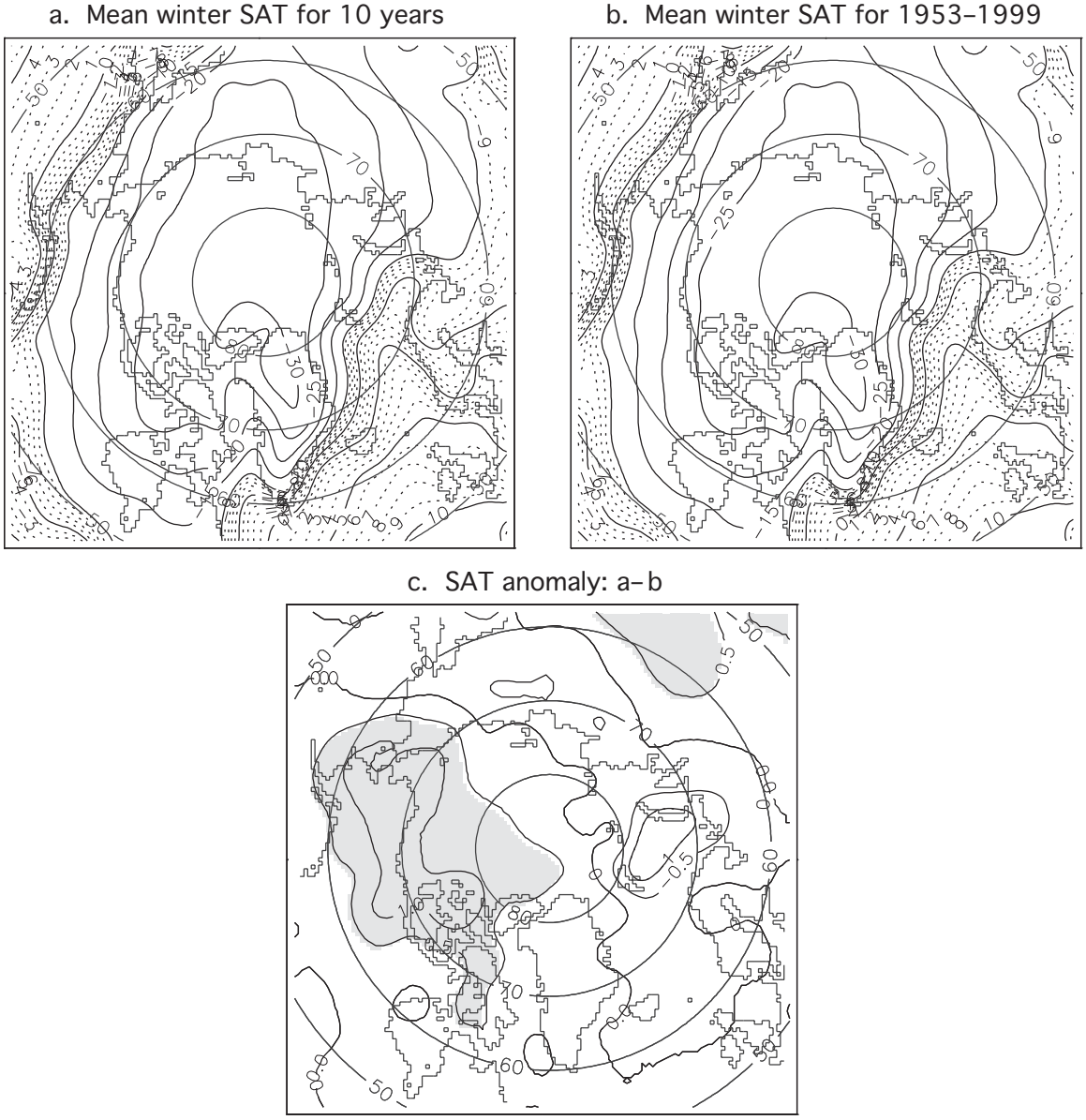

Figure 144. (a) Mean winter SAT for the 10 years with the lowest ice extent in the western Arctic (Figure 133), and (b) mean winter SAT for the period 1953–1999; (c) SAT anomalies (a minus b). The shaded area indicates anomalies greater than 2 °C. Contour intervals are 1 °C in (a) and (b), and 0.5 °C in (c).

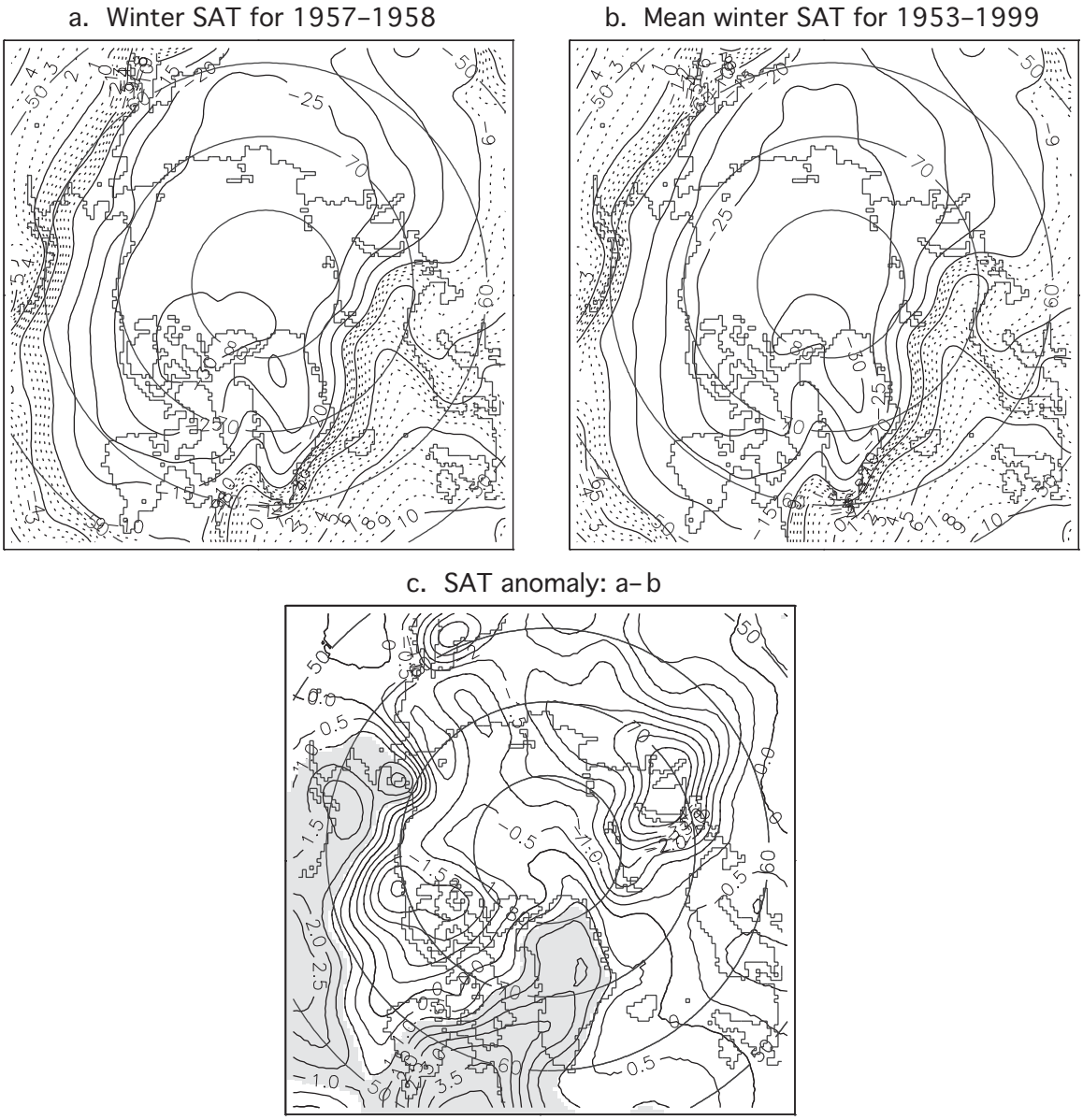

Figure 145. (a) Mean winter SAT in 1957–1958, and (b) mean winter SAT for the period 1953–1999; (c) SAT anomalies (a minus b). The shaded area indicates anomalies greater than 2 °C. Contour intervals are 1 °C in (a) and (b), and 0.5 °C in (c).

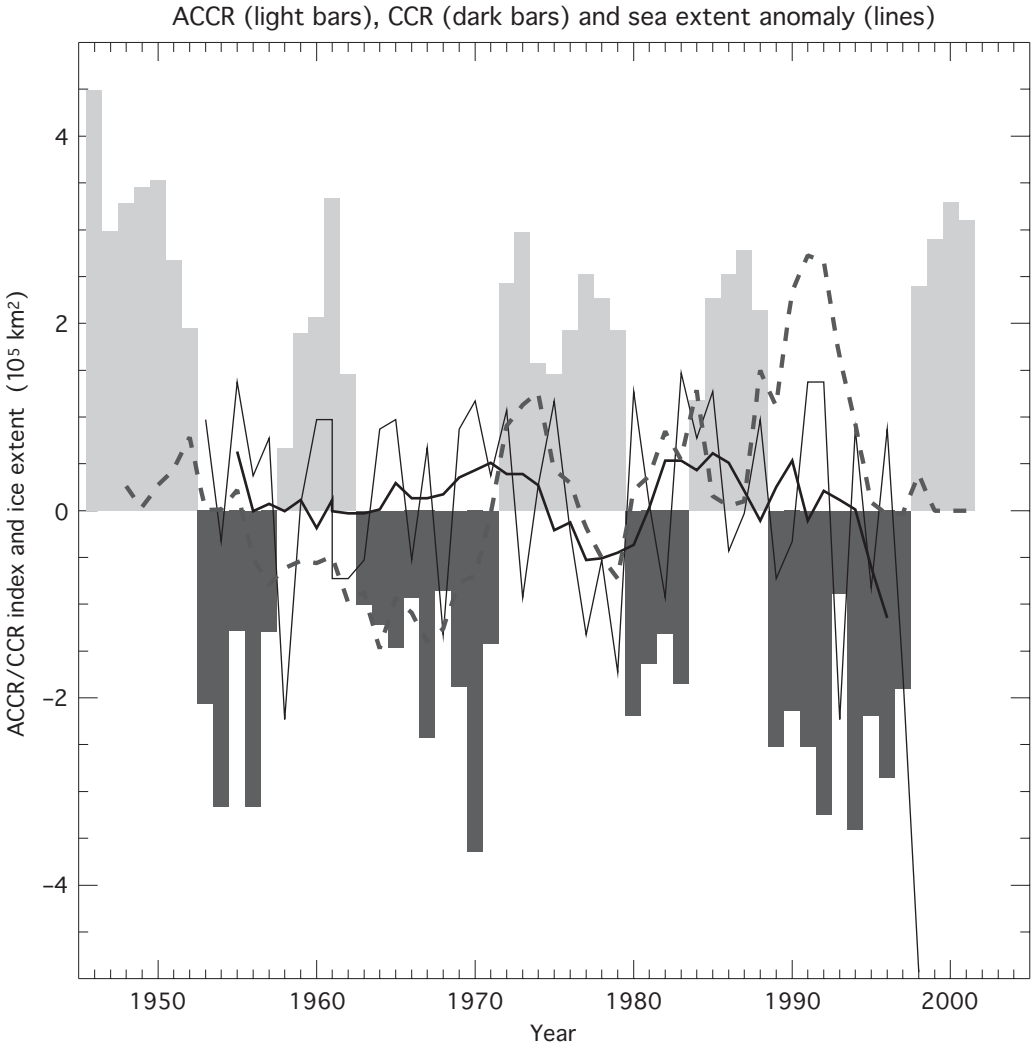

Figure 146. Time series of the Arctic Ocean Oscillation (AOO) index (bars), sea ice extent anomaly (solid lines; thin line shows annual mean and thick line depicts 5-year running mean), and North Atlantic Oscillation index (NAO) (dashed line).

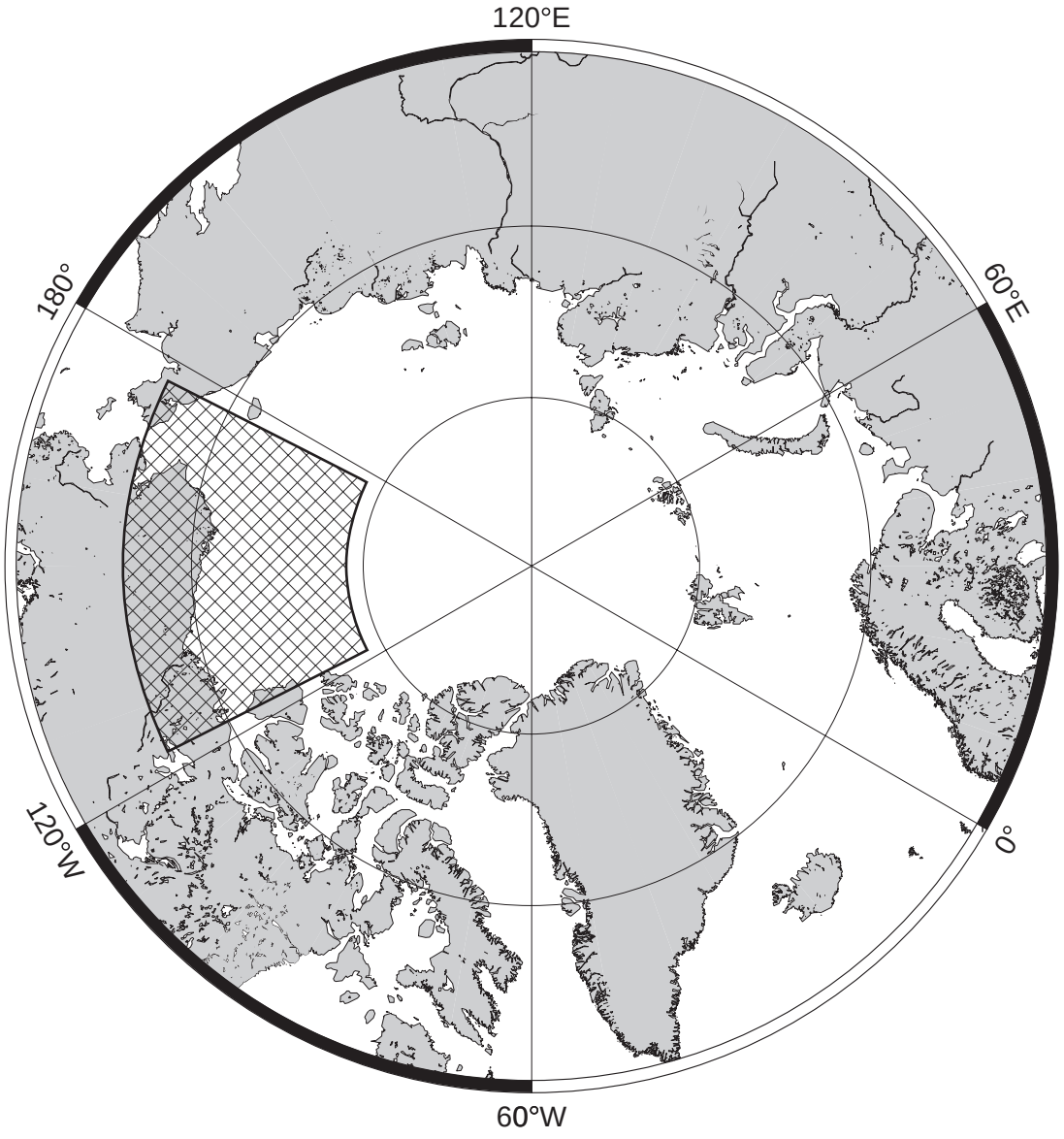

Figure 147. Beaufort and Chukchi Sea region (cross-hatched sector) where sea ice extent and sea ice area were calculated.

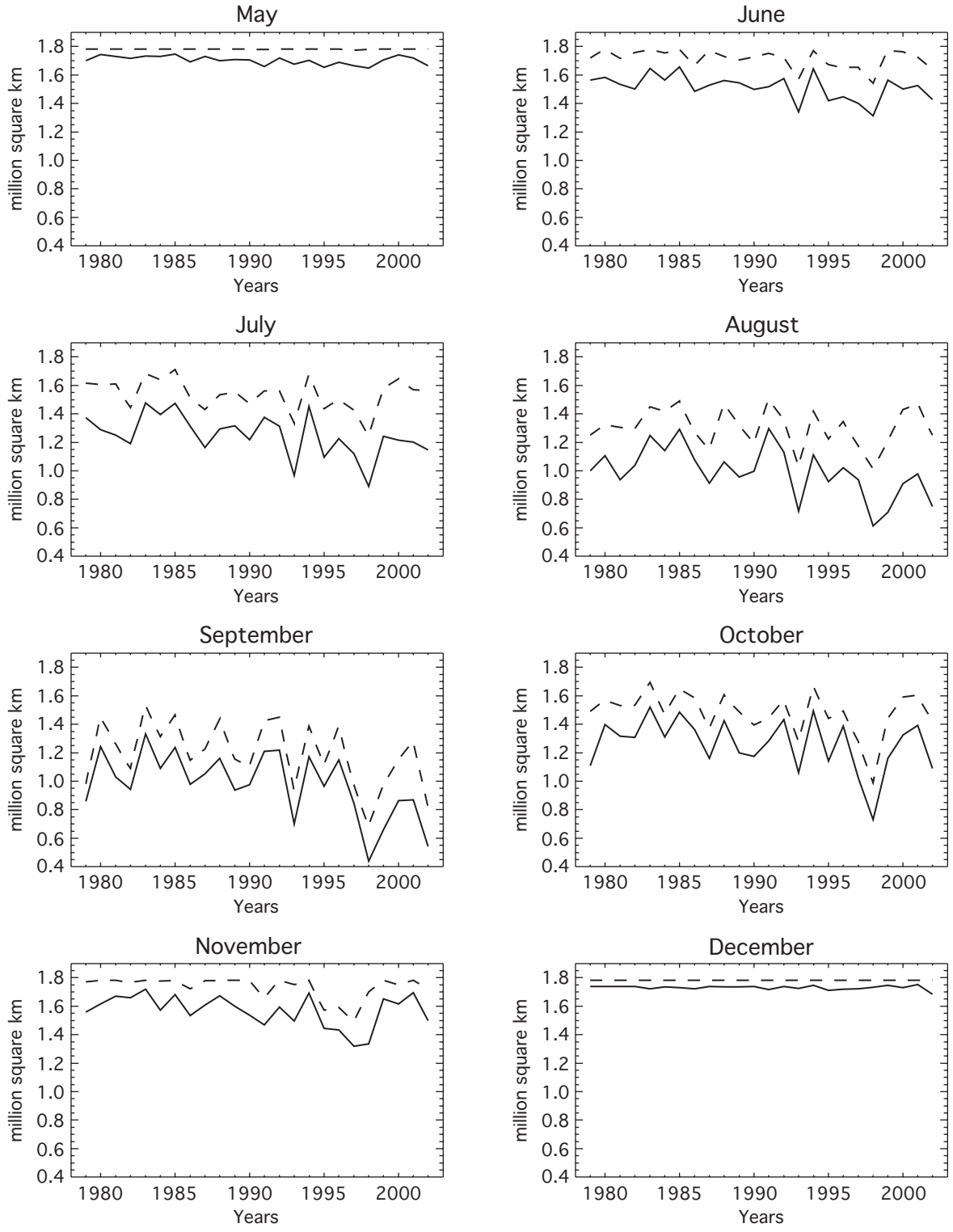

Figure 148. Time series of monthly mean sea ice area (solid line) and sea ice extent (dashed line) in the Beaufort and Chukchi Seas (see also Figure 147). Area is in million square kilometers.

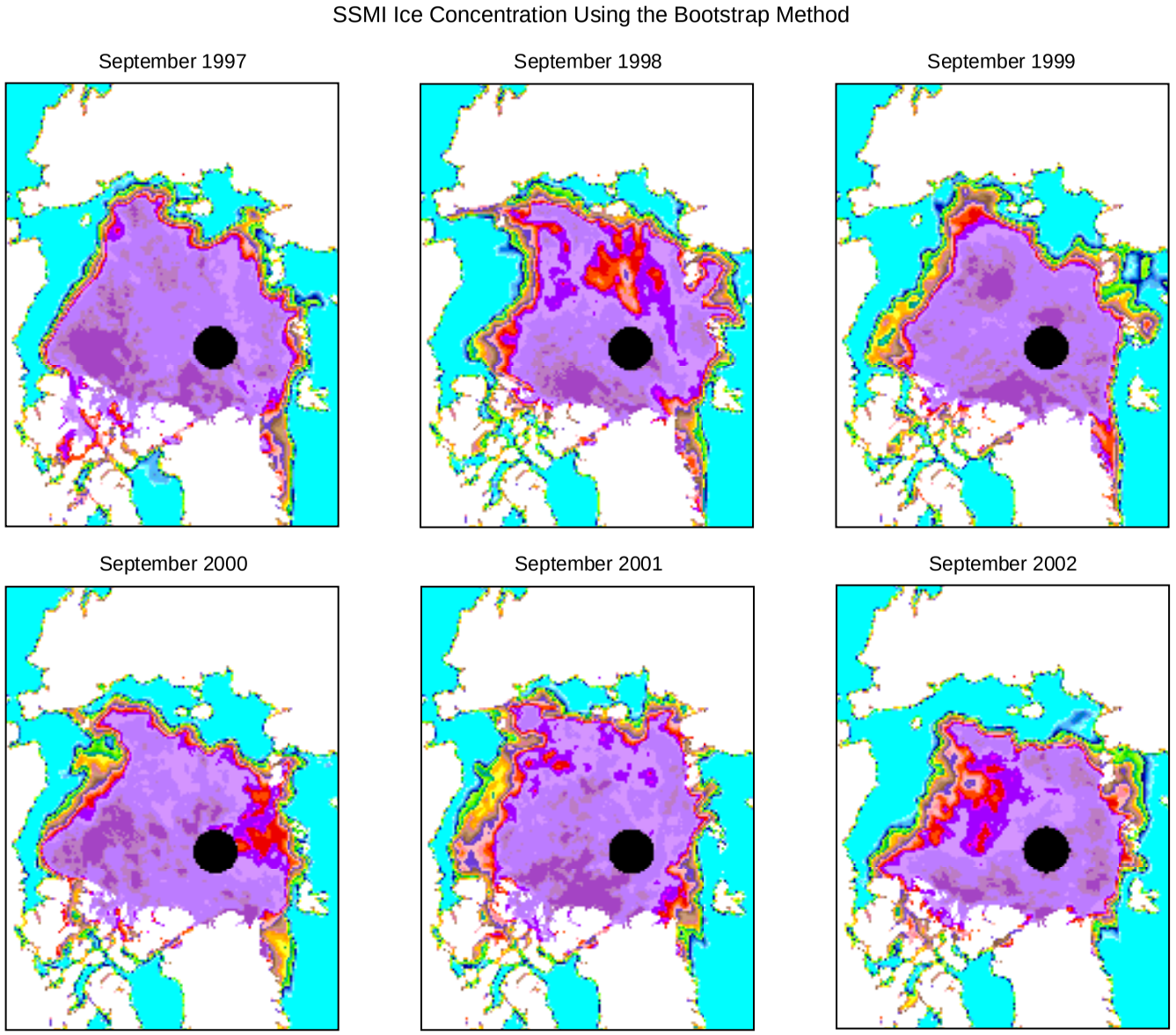

Figure 149. Mean sea ice concentration in the Arctic Ocean in September from 1997 through 2002.

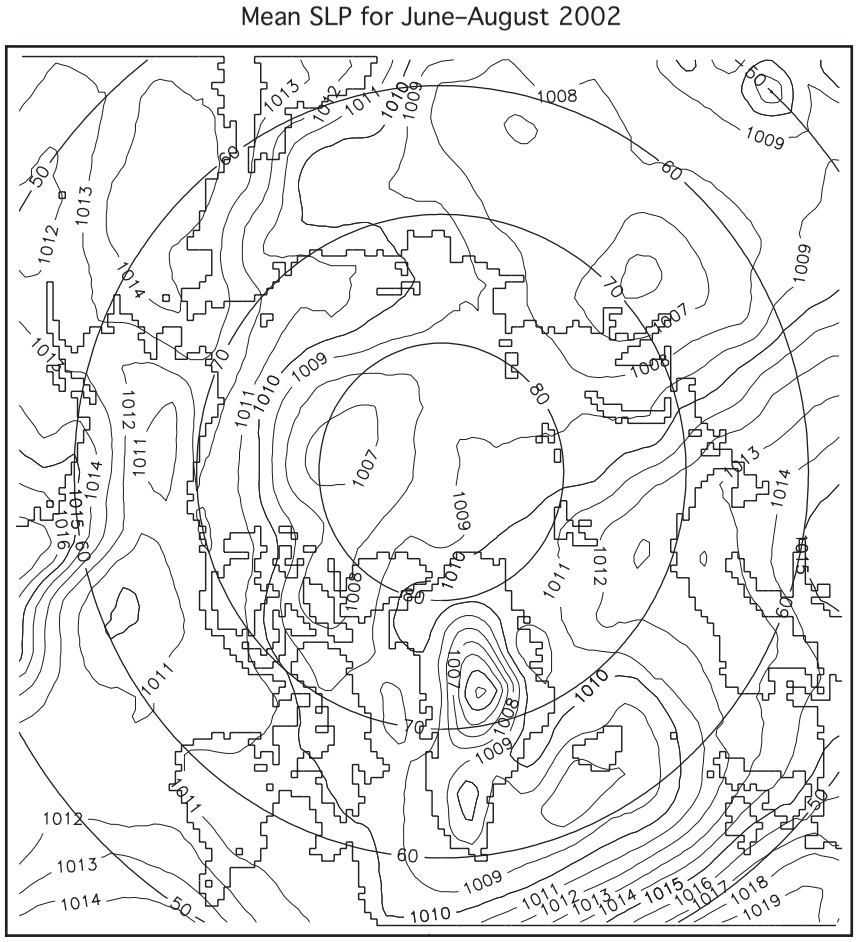

Figure 150. Mean (June–August) sea level atmospheric pressure (hPa) in 2002.

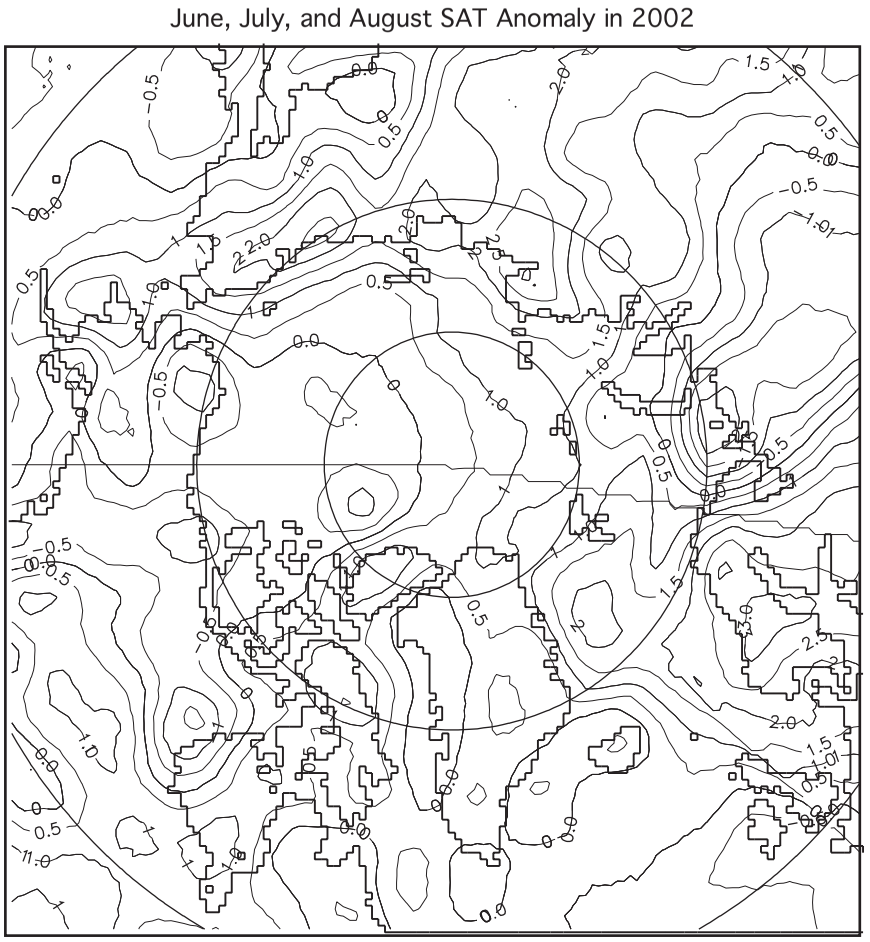

Figure 151. Sea surface air temperature anomaly (relative to 1948–2002) in June–August 2002.